Functionalization of a Ti-based Alloy with Synthesized Recombinant Fibronectin Fragments to Improve Cellular Response

Carolina Herranz Díez

PhD Thesis

Doctoral program of Biomedical Engineering

Supervised by

Dr. JM. Manero Planella

Dr. Jordi Guillem Martí

Department of Materials Science and Metallurgical Engineering

Universitat Politècnica de Catalunya · Barcelona Tech (UPC)

July 2014

Cuando me planteé realizar un doctorado, nunca pensé que el tiempo podría pasar tan rápido y tan lento a la vez. Tras cuatro años de trabajo me encuentro escribiendo las últimas líneas. Esta tesis es el producto del trabajo realizado durante estos cuatros años y no habría sido posible sin la colaboración y dedicación de muchas otras personas.

En primer lugar, querría dar las gracias a mis directores de tesis, el Dr. José María Manero y el Dr. Jordi Guillem.

También me gustaría darle las gracias a los miembros del grupo de Biomaterials, Biomechanics and Tissue Engineering (BBT) del Departamento de Ciencia de los Materiales e Ingeniería Metalúrgica de la ETSEIB porque cada uno de ellos ha participado de una forma u otra en esta tesis. Mención especial merecen Sara Gallinetti y Maria Godoy, sin ellas nada hubiera sido igual.

Otro pilar importante en la consecución de esta tesis ha sido el Instituto de Bioingeniería de Cataluña (IBEC) que me abrió sus puertas y puso a mi alcance todos sus recursos.

No puedo olvidarme de los investigadores de otros centros o departamentos que se prestaron a colaborar. Gracias al Dr. Benjamin Thierry y a la Dra. Lorena Diéguez del Ian Work Research Institute; a la Dra. Christine Selhuber-Unkel de la Universidad de Kiel; al Dr. Jeremy Schaffer de Fort Wayne Metals Corporation y al Dr. Emilio Jiménez y al Dr. Joan Josep Roa del Departamento de Ciencia de los Materiales e Ingeniería Metalúrgica de la UPC.

Gracias a mis padres y a mi hermano por haber estado siempre apoyándome y gracias también a Gonzalo por embarcarse conmigo en esta aventura sin dudarlo ni un segundo.

ABSTRACT

According to a study of the European Commission, approximately one million hips are replaced by prostheses worldwide every year. The interaction of the human body with foreign materials that are subjected to alternating mechanical load in a highly corrosive environment still provides challenges. The main factors affecting prosthesis failure are stress shielding effect and poor osseointegration.

In this thesis the problem of prosthesis failure has been approached from the material and from the osseointegration point of view trying to give a global solution to the problem.

Niobium and hafnium, which are demonstrated to be totally biocompatible, were used to design a Ti-based alloy. The effect of the alloying elements regarding microstructure and elastic modulus was studied and the best composition was deeply characterized in terms of microstructure, elastic modulus, corrosion resistance and superficial energy.

Recombinant fragments of fibronectin were synthesised spanning the cell attachment site and the heparin binding domain which are important for cell viability. These motifs were used to functionalise the surface of the TiNbHf alloy. Two tethering methods were studied: physisorption and silanisation. Silanisation was not used before to immobilise fibronectin recombinant fragments onto metallic substrates and in this thesis, its good performance was demonstrated.

In vitro studies were made with each fragment and with different combinations of the fragments, which showed the importance of the heparin binding domain to obtain a cell response equivalent to that of fibronectin in terms of cell adhesion, proliferation and differentiation.

Key words: stress shielding effect, titanium alloy, osseointegration, fibronectin, recombinant protein, biofunctionalisation, *in vitro* cell culture.

RESUMEN

De acuerdo con un estudio de la Comisión Europea, aproximadamente un millón de caderas son remplazadas por prótesis en el mundo anualmente. La interacción del cuerpo humano con materiales externos sujetos a una carga mecánica alternante en un medio altamente corrosivo todavía presenta ciertos desafíos. Los factores que contribuyen principalmente al fallo de una prótesis son el apantallamiento de cargas y la pobre osteointegracion.

En la presente tesis el problema de la fallida de prótesis ha sido abordado desde el punto de vista del material y de la osteointegracion en un intento de dar una solución global al problema

El niobio y el hafnio, cuya total biocompatibilidad ha sido demostrada, se han utilizado para diseñar una aleación de titanio. El efecto de dichos aleantes respecto a la microestructura y el módulo elástico ha sido estudiado y la mejor composición ha sido profundamente caracterizada en términos de microestructura, módulo elástico, resistencia a la corrosión y energía superficial.

Fragmentos recombinados de fibronectina han sido sintetizados abarcando la zona de adhesión celular y la unión de heparina, las cuales son esenciales para la viabilidad celular. Dichos motivos han sido utilizados para funcionalizar la superficie de la aleación TiNbHf. Dos métodos de unión diferentes han sido estudiados: fisisorción y silanización. La silanización es un método que no se ha utilizado hasta el momento para inmovilizar fragmentos de fibronectina sobre superficies metálicas y en la presente tesis su idoneidad ha sido demostrada.

Finalmente, estudios celulares in vitro se han llevado a cabo con cada fragmento y con diferentes combinaciones de ambos, lo cual ha mostrado la importancia de la zona de unión de heparina para obtener una respuesta celular equivalente a la obtenida con la molécula de fibronectina en cuanto a adhesión celular, proliferación y diferenciación.

THESIS OBJECTIVES

The main objective of this thesis is on one hand, study the ternary system TiNbHf as a potential substitute for the alloys used in total hip replacement and on the other hand, synthesise a fibronectin recombinant fragments spanning the III_{8-10} and III_{12-14} domains to improve osseointegration.

The specific objectives of the present thesis are:

1. To design a titanium alloy based on optimization of molecular orbital calculations of electronic structures towards low modulus of elasticity and the potential for super elasticity and study the effect of niobium and hafnium alloying elements in terms of microstructure and elastic modulus.

2. To select the appropriate TINbHf composition, fabricate a bar and characterise its microstructure, determine its elastic modulus, determine its corrosion resistance and study its superficial energy.

3. To fabricate, by recombinant protein techniques, the fibronectin fragments $FNIII_{8-10}$ (CAS) and $FNIII_{12-14}$ (HBII) and characterise the fuctionalisation of the TiNBHf alloy with such fragments.

4. To study cell response to the biofunctionalised material in terms of adhesion force and cell adhesion, proliferation and differentiation.

CONFERENCE CONTRIBUTIONS

C. Herranz, J. Schaffer, T. Trifonov, J. Portillo, S. Estrade, Ll. Yedra, J. Mendoza, FX Gil, J.M. Manero. "Microstructural characterization of a potential superelastic Nickel-free titanium alloy". **III Microscopy at the Frontiers of Science Conference**, September 2013, Tarragona, Spain (Poster Presentation).

C. Herranz, J. Schaffer, J.M. Manero. "Potential Superelastic nickel-free titanium alloy". **2013 Shape Memory and Superelastic Technology Conference**, May 2013, Prague, Czech Republic (Poster Presentation)

C. Herranz, M. González, J. Guillem-Martí, J. Peña,J.C Rodríguez-Cabello, F.J. Gil, J.M. Manero. "New nickel-free titanium alloys design and functionalization for implantology". **XXXIII Iberian Society de Biomechanics and Biomaterials Conference**, November 2010, Valencia, Spain (Oral Presentation).

I

Introduction

Chapter 1

Introduction

1. BONE

Bone plays an important role in the human body giving support, protecting soft tissues and participating in mineral metabolism. Bones are the framework were soft organs are supported and anchored. Bones are also a reservoir for minerals that are released to the blood stream and distributed to other parts of the body and the responsible of production of blood cells.

1.1 Bone composition

Bone is composed of 70% mineral (mostly hydroxiapatite), 22% organic matrix and 8% water, approximately. The organic matrix is composed of collagen in a 95% and the remaining 5% is composed of osteocalcin, osteonectin, proteoglycans, bone morphogenetic protein, proteolipids and phosphoproteins. Bone structural properties such as strain, strength, etc. are influenced by the different components of bone.

Each component of bone contributes in a different way to bone structural properties. Depending on the percentage of each part the physical properties (strain, strength, etc.) can be modified.

Depending on the shape of the bones they are classified in long, short, flat and irregular but all of them are formed for two basic osseous tissue:

- Cortical bone: is compact, dense and forms the outer surface of bones, contributing 80% of the weight of a human skeleton (Fig.1).
- Trabecular bone: is a porous lattice of bony struts called trabeculae (Fig.2). It has low density and strength but very high surface area, that fills the inner cavity of bones. The external layer of cancellous bone contains redbone marrow where the production of blood cells (known as haematopoiesis) takes place.

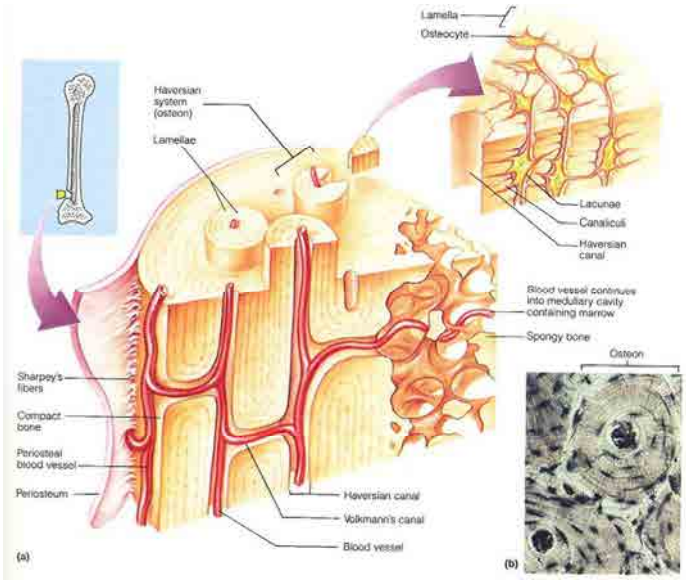

Fig.1 Microscopic structure of compact bone. A) Section of compact bone illustrating the osteons and the irrigation system. In the magnified section the osteocytes and the lamella are shown. B) Photomicrograph of a cross-sectional view of one osteon and portions of others. (90x). Adapted from [1].

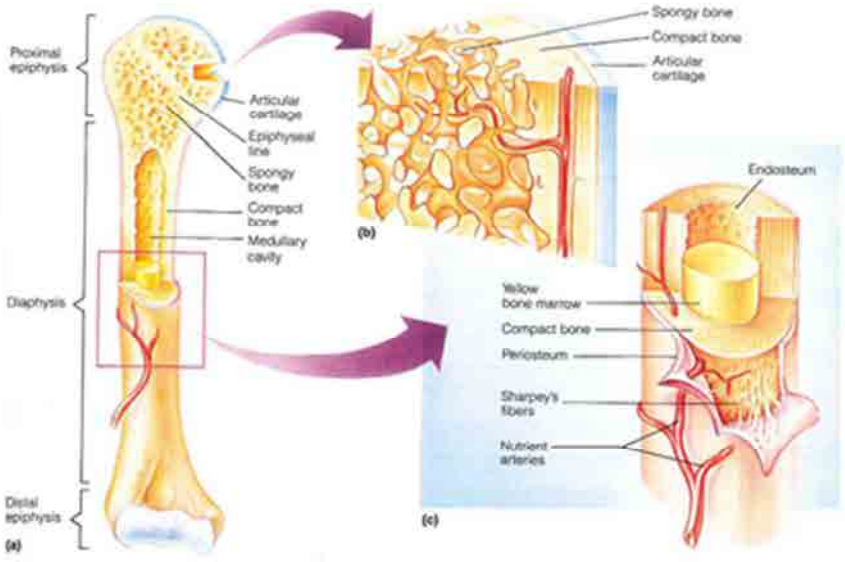

Fig.2 Long bone structure. A) Description of the parts of the long bone with a longitudinal cut showing the cortical and the trabecular bone. B) View of the trabecular and cortical bone present in the epiphysis. C) Cross section of the diaphysis showing the main components. Adapted from (1)

1.2 Bone mechanics

Bone is a dynamic tissue that changes morphology depending on the stresses applied and their direction; this is translated in different mechanical properties depending on the area of bone we are focusing on. We can say bone is an anisotropic material with special characteristics.

For this reason bone mechanics may be studied with two different perspectives: the material one and the structural.

As a material, tensile and compression tests can be performed obtaining the results showed in Table 1.

Bone type	Direction and type of load	Apparent density (g/cm^2)	Ultimate strength (MPa)	Modulus of elasticity (10^6 MPa)
Cortical (midfemur)	Longitudinal tension	1.85	133	17
	Longitudinal compression	1.85	193	17
	Longitudinal shear	1.85	68	3.000
	Transverse tension	1.85	51	11.500
	Transverse compression	1.85	33	11.500
Travecular (vertebral body)	Compression	0.31	6	76

Table 1. Values of some mechanical parameters when testing bone under different conditions. Adapted from [2]

1.2.1 Creep and stress relaxation

Collagen biochemistry of bone may change among different bone regions and there are also microcracks that make bone to deform over time when a constant loading is applied [3–5]. This phenomenon is known as creep. Together with creep another phenomenon takes place, the stress relaxation. That means the diminishment of the stress necessary to

maintain certain strain over time [6,7]. Creep helps the bone to cope with the stress and avoid fractures.

Creep and stress relaxation processes take place at both bone tissue types, cortical and trabecular. Collagen is responsible for these phenomena in both bone tissues, but microcracking is the main responsible for creep process in trabecular bone.

1.2.3 Viscoelasticity

Some materials have viscous and elastic properties and show this two behaviours when are deformed. This is what is it called viscoelasticity.

When bone is subjected to low strain rates no elastic deformation is appreciated, bone behaves like a viscous liquid. But at high strain rates bone shows a brittle elastic behaviour [2].

1.3 Bone cytology

Bone cells are generated in the fibrous membrane that covers the bone, called periosteum. The structural unit of compact bone is the osteon. The system is formed by vascularised concentric rings of hard bone matrix (Fig.2). The system host the cells needed for bone formation and regeneration: preosteoblastic cells, osteoblast, mature bone cells, osteocytes, macrophages and monocytes [1,8].

1.3.1 Mesenchymal Stem Cells (MSC)

The different types of bone cells originate from a progenitor cells called mesenchymal stem cells (MSCs) located in the bone marrow.

The progenitor cells have the ability to differentiate in the so called daughter cells, or stem cells, which have restricted developmental potentials. Depending on those developmental potentials, different stem cells are found: totipotent zygote, embryonic stem cells, hematopoietic stem cells and MSCs.

In our case the stem cells of interest are the MSCs because they give rise to a spectrum of specialized cells of tissues such as bone, cartilage, muscle, marrow, stroma, tendon, fat and others (see Fig.3). MSCs became specialized cells after differentiation. This

differentiation is affected by a number of intrinsic as well as extrinsic factors that regulate and guide the molecular and cellular pattern of expression [9].

MSCs also play an important role in the remodelling, repair and wound healing [10,11].

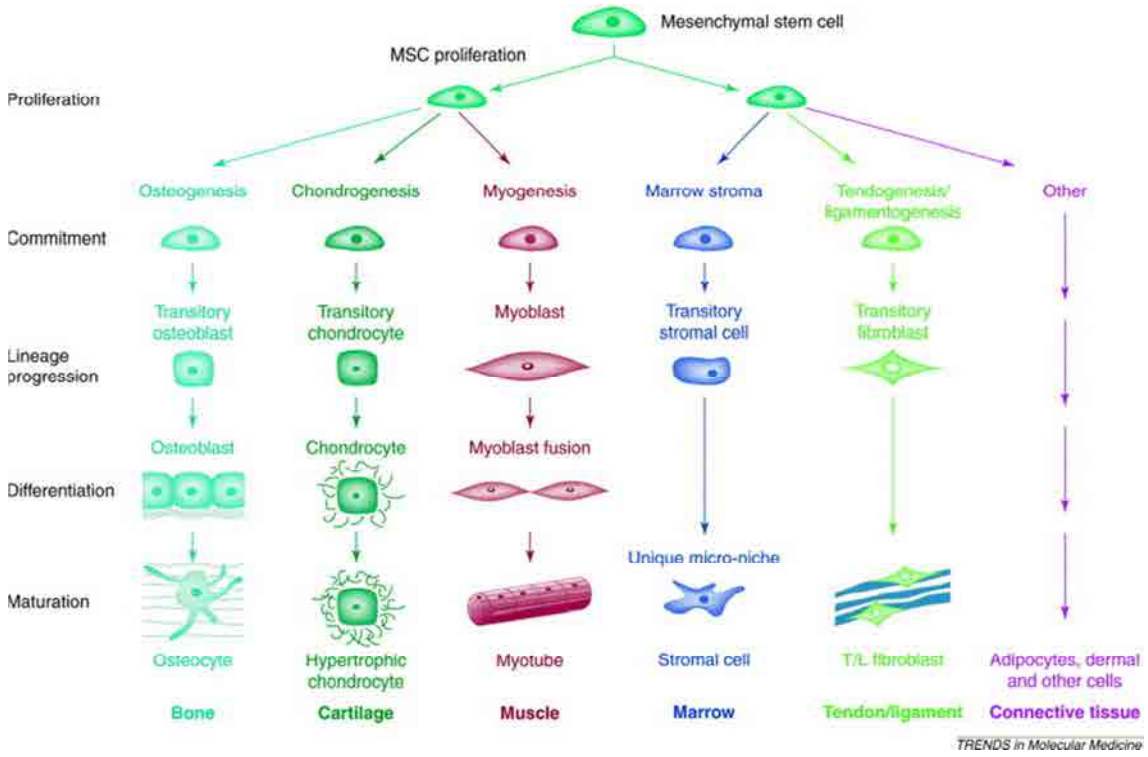

Fig.3 The mesengenic process. The stepwise cellular transitions from the putative mesenchymal stem cell (MSC) to highly differentiated phenotypes are depicted schematically. This scheme is oversimplified and does not represent all of the transitions or all of the complexities of single lineage pathways, nor does it represent the potential interrelationships of cells moving between pathways. Adapted from [10]

1.3.2 Osteoblasts

Osteoblasts are bone builders. They secrete the extracellular matrix (ECM) proteins needed to form the bone matrix. These mature cells generate the osteon and are fundamental for bone mineralization because they are the cells that regulate the quantity of calcium and phosphate to produce hydroxyapatite.

Osteoblasts are big cells with a large quantity of rough endoplasmic reticulum and Golgi apparatus in their cytoplasm. They originate from the mesenchymal stem cells of the bone marrow, endosteum, periosteum and perivascular pericytes.

1.3.3 Osteoclasts

Osteoclasts are mature bone cells whose principal function is to resorb mineralized bone matrix.

Osteoclasts are bigger than osteoblasts, multinucleated and with a cytoplasm with many vacuoles and mitochondria. They originate from the bone marrow hematopoietic stem cells, which differentiate into monocytes. Monocytes are activated by macrophages and osteoblasts through the RANK pathway and fused forming the multinucleated cells called osteoclasts.

This type of cells has two special traits: a ruffled border and a clear area rich in filaments. Both characteristics are essential for resorption to take place.

1.3.4 Osteocytes

Osteocytes are osteoblasts trapped in the mineralized matrix that they secrete. During matrix mineralization some osteoblasts become trapped within it in a space called lacunae. But they are not isolated; they are in contact between them through tiny canals called canaliculi where the extensions of osteocyte plasma membrane go through. In addition, the canaliculi are used to transport the nutrients required for cells [12–14].

The canaliculi play an important role in osteocytes function. Through the canaliculi circulate hormones, such as estrogen and glucocorticoids, fundamental for the osteocytes survival. If there is any change due to mechanical forces such as fractures, osteoporosis, etc., the amounts of hormones that reach the osteocyte vary affecting the osteocytes network. When this signal induces osteocyte apoptosis, bone mechanical integrity is compromised. Is because of that, osteocytes are called bone mechanotransductors. The osteocytes sense stresses applied to bone and guide the activity of osteoblasts and osteoclasts in a process called bone remodelling [1,8,15].

1.4 Bone remodelling process

1.4.1 Cell processes during bone remodelling

Bone is a tissue that is continuously remodelling due to its highly regenerative capacity. During life, bone suffer damage due to microdamage induced by cyclical loads and aging, but it has de ability to repair this damage resorbing and producing new bone in a process called bone remodelling.

Bone remodelling is carried out by bone cells. Each cell, as it was stated in section 1.3, takes part in different processes of bone remodelling. During the resorption process osteoclasts eliminate the non-functional bone matrix. The released growth factors stimulate the proliferation of preosteoblastic cells that differentiate into osteoblasts. During bone matrix mineralization some osteoblasts are trapped within the matrix and become osteocytes.

The process is divided into four stages: resting phase, resorption, formation phase, reversal phase and mineralization. The entire process is controlled by hormones and local factors that determine the role of each cell involved in each phase. Skeletal cells are responsible for synthesizing the local factors (growth factors, cytokines, and prostaglandins). Bone remodelling takes place in small groups of cells called basic multicellular units (BMUs) that are independent with each other [14,16,17].

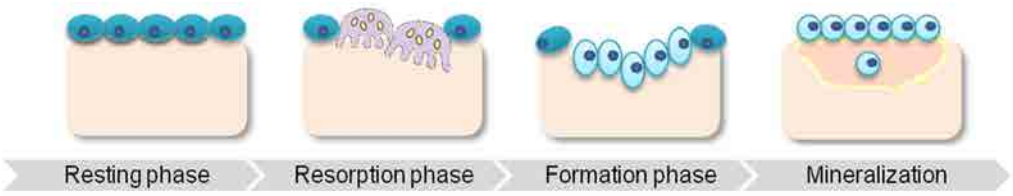

Fig.4 Fig. 1 Stages of bone remodelling. In the resting phase, bone is in a quiescent stage. After activation the osteoclasts suffer a shape change and the ruffle border appear. The degradation of the bone matrix starts. The next phase is bone formation. Preosteoclasts adhere to bone matrix, differentiate to osteoblasts and bone formation starts. The last stage of the bone remodelling process is bone mineralization. During this process the osteoid is formed and some osteoblasts that were trapped into the bone matrix become osteocytes [14].

1.4.1.1 Resting phase

The BMU's are in a quiescent phase, in other words, no degradation or generation of new bone take place.

1.4.1.2 Resorption phase

The resorption is a complex process where osteoclast membrane plays a fundamental role. In the membrane there is an area that attaches to the bone matrix and delimits the area to be resorbed. The bone area to be resorbed is exposed to an acidic environment, and then the matrix components are dissolved and endocytosed by the osteoclast [12–14].

This phase starts with the enrolment and spreading of osteoclast progenitors to bone which interact with osteoblast stromal cells and the result of such fusion are osteoclasts.

After fusion, the αvβ3 integrin receptor binds to osteopontin at a tripeptide arginine-glycine-aspartic acid (RGD) recognition site. Therefore, osteoclasts are polarized [13,14,17] and suffer a rearrangement of the cytoskeleton which forms multiple focal adhesions. After this rearrangement, osteoclasts present a sealing zone, a ruffled border and a functional secretory domain. The sealing zone presents many focal adhesions that seal a zone beneath the cell in contact with bone matrix forming the resorption lacunae. After the sealing, the ruffled border secretes vacuolar-type H^+-ATPase and cysteine protease cathepsin K. The purpose of the former is to acidify the lacunae to enable bone mineral dissolution and the purpose of the latter is to degrade organic phase.

The resorption products contained in the resoption lacunae (mainly collagen fragments, calcium and phosphate) are endocytosed by the osteoclasts and released to the functional secretory domain, from where they will be released to the blood stream.

1.4.1.3 Reversal phase

During the resorption phase there is a high concentration of calcium in the lacunae that triggers the retraction of the osteoclasts ruffled border and the enzyme release. Moreover, during bone resorption the growth factor TGF- β is released inducing osteoblast proliferation. Both phenomena contribute to the inactivation of osteoclast and thus, the end of resorption phase. This leads to a reversal phase in which osteoclasts disappear and macrophage-like cells appear on bone surface.

1.4.1.4 Formation phase

The formation phase took place simultaneously with the resorption process. The growth factors released by the matrix attract preosteoblastic cells and stimulate their proliferation. The preosteoblastic cells synthesize a cementing substance and morphogenic proteins (BMP family) which stimulate differentiation of preosteoblastic cells into osteoblastic cells. The osteoblasts synthesize osteoid materials which fill the resorbed areas.

1.4.1.5 Mineralization phase

About thirty days after osteoblasts start depositing the osteoid the mineralization phase starts. Some of the osteoblast differentiate into osteocytes and become embedded in the matrix and some others gradually flatten and become quiescent lining cells. The extracellular matrix surrounding osteocytes is formed by proteins, minerals, sugars and fluids. The most abundant protein is collagen which serves as a support for mineralization. Calcium and inorganic phosphate contained in blood plasma react and form amorphous calcium phosphate which eventually forms hydroxyapatite crystals (Ca_{10} $(PO_4)_6(OH)_2$). These crystals nucleate and grow onto the collagen fibrils of the bone matrix. Noteworthy, the noncollagenous proteins play also an important role during the mineralization phase..

The mechanism of bone remodelling is not the same for both types of bone. In cortical bone, osteoclasts dig tunnels that are filled by osteoblasts. However, osteoclasts move across the surface of trabecular bone resorbing a trench in damaged areas that is filled by osteoblasts [18].

1.4.2 Bone functional adaptation

In the 19th century, the German surgeon Julius Wolff, postulate a theory about the relationship between bone geometry and the loads applied to bone. According to the so called Wolff's Law, bone took its form depending on the tension applied. In other words, the trabeculae are not a messy tissue, they are organized depending on the load applied to bone and this organization also affects cortical bone [19]. Wolff's model is a very strict model that only takes into account loading, but there are other factors that affect bone remodelling.

Recent theories have added a new vision to Wolff's law keeping in mind that loading in bone remodelling process is important. It seems that all the scientists involved in such investigations agreed with the fact that is not the stress but the strain the key factor for the initiation of the process [20]. Another important idea of the new conception of Wolff's law is that the organisms possess the ability to adapt their structure to new living conditions.

In Figure 5(a) the strict Wolff model for bone remodelling is represented. Under Wolff vision, bone was ruled by mathematical equations. On the other hand, in Figure 5(b) it is showed a schematic representation of the modern vision of bone remodelling. The model is very simplified, because it does not take into account the age, the shape or the living conditions.

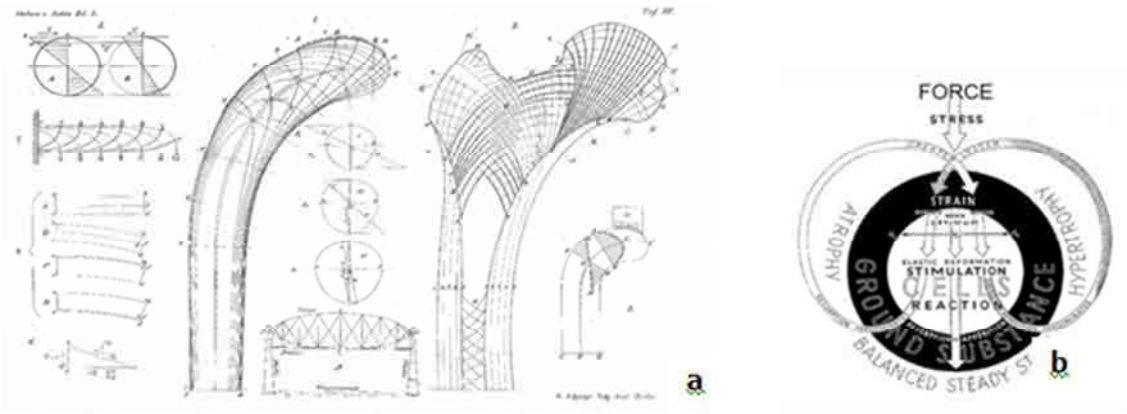

Fig.5 a) Wolff mathematical model of bone remodelling. b) Representation of the modern theory of bone remodelling. Adapted from [19].

1.5 Bone diseases

The organism is always looking for homeostasis, and so does bone by means of remodelling. But there are some situations in which bone is not able to maintain the homeostasis by itself, and requires a replacement.

Bone can be affected by different diseases or conditions that have as a result pain, malfunction, structural degeneration or a combination of them and the only way to alleviate them is replacement of the affected part. The disease can be caused by

bacteria, virus, fungus, autoimmunity, sclerosis, neoplasia, bone section missing or age related degeneration [21,22]

The options to replace/repair bone are:

- **Allografts**: the material used for the replacement is from another patient. The risks associated to this substitute are infection, rejection and loosening of stiffness due to sterilization.
- **Autografts**: the material used is from the same patient, but from a different site (such as the pelvis). Despite reducing the chances of rejections, there is a limited amount of material available and more pain and risk of infection because of the two surgeries needed.
- **Synthetic materials**: are materials developed in a laboratory which allows bone to regrow and fill the space or substitute the bone..

When dealing with age related degeneration, the solution is not as easy as in the replacement of missing parts case and it is necessary to replace the damage tissue with an alternative structure able to provide a degree of function equivalent to that of the damage tissue and also able to take the role of the affected tissue.

Two of the most common age-related diseases of bone are arthritis and osteoporosis. The arthritis degrades joint's cartilage and thus, the bones at joint rub against each other resulting in pain and decreased mobility. The osteoporosis is a phenomenon that makes bones brittle and it is also translated in a loss of bone mass. This brittleness and loosening of bone mass make bones prone to fracture [22]. In these situations, it is impossible to repair the bone and the joints and a replacement is needed.

2. MATERIALS USED FOR BONE REPLACEMENT

2.1 Biomaterials

2.1.1 Definition

There are many different definitions for a biomaterial:

"*Any substance (other than a drug), synthetic or natural, that can be used as a system or part of a system that treats, augments, or replaces any tissue, organ, or function of the body; especially, material suitable for use in prostheses that will be in contact with living tissue*". *Miller-Keane Encyclopaedia and Dictionary of Medicine, Nursing, and Allied Health, Seventh Edition. © 2003 by Saunders, an imprint of Elsevier, Inc. All rights reserved.*

"*Any synthetic material or device–eg implant or prosthesis-intended to treat, enhance or replace an aging or malfunctioning–or cosmetically unacceptable—native tissue, organ or function in the body. Cf Bioengineering, Breast implants, Hybrid artificial pancreas, Shiley valve, Teflon, Total hip replacement 2. A biomaterial used for its structural, not biological, properties–eg, collagen in cosmetics, carbohydrates modified by biotechnology to be used as lubricants for biomedical applications or as bulking agents in food manufacture*" *McGraw-Hill Concise Dictionary of Modern Medicine. © 2002 by The McGraw-Hill Companies, Inc.*

"*A synthetic or semi synthetic material used in a biologic system to construct an implantable prosthesis and chosen for its biocompatibility*." *Farlex Partner Medical Dictionary © Farlex 2012*

"*A systematically and pharmacologically inert substance designed for implantation within or incorporation with living systems*". Clemson University Advisory Board for Biomaterials

Despite of the different definitions, there is one common characteristic: a biomaterial is a material that doesn't belong to the body and is used to replace a specific function or a part of the body in a safe and physiologically acceptable way.

2.1.3 Use of biomaterials

Biomaterials have been used for humans since more than 2000 years ago. Ancient civilizations as Aztecs used gold and silver to repair trephination defects, wood and

animal bones for dental substitution or fibres and tendons for sutures. During history man tried to replace damage parts with other devices made with gold, silver, iron, wood, etc. But they were unsuccessful because of the use of incorrect materials and infection after implantation due to no aseptically procedures. In the 1860's the aseptic surgery technique was developed and since then there were an improvement in implanting devices. Thus, the use of stainless steel and engineered materials for biomedical applications increased.

Many different materials are currently used as biomaterials: metals, ceramics, polymers, glasses and composite materials. These materials are not used as raw materials, depending on where they are going to be placed or the needed feature, they are moulded or machined and in a form of coatings, fibres, films or foams. The biomaterials are also used to replace many different parts in the body. In Figure 6 the different biomaterials, their principal properties and some of the medical devices made with them are shown [23,24].

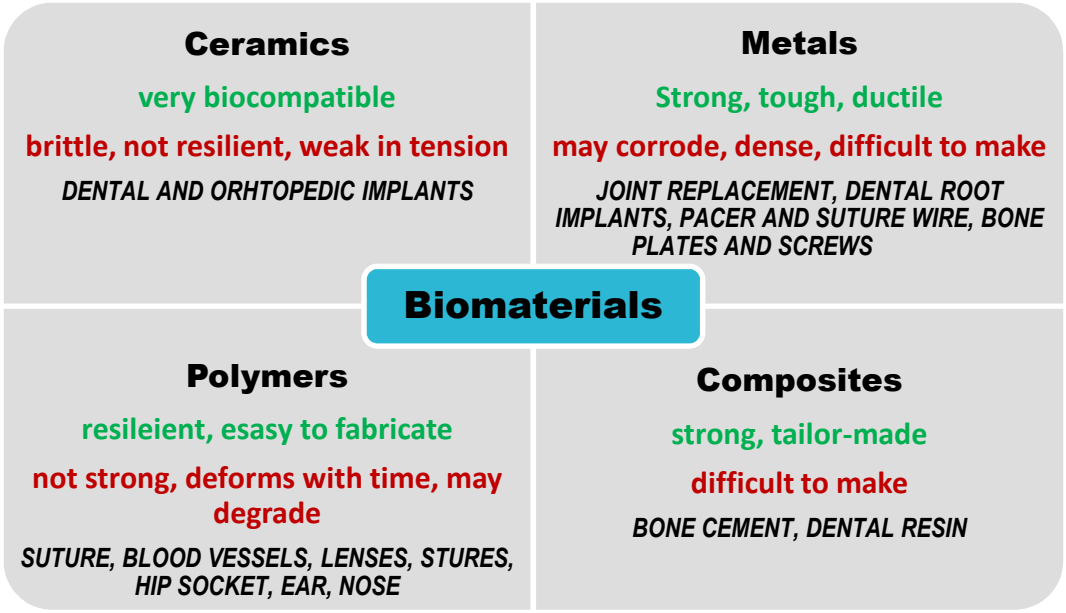

Fig.6 Different biomaterials with the pro's and con's and their applications in medicine.

2.2 Metals used as biomaterials for prosthesis

2.2.1 Introduction

As it was stated in point 2.1.3, with the development of the aseptic surgery technique in the 1860's, there were an improvement in implanting devices and many efforts were done to improve the materials properties and their biocompatibility.

1900: Lane of England designed a fracture plate using steel. This fracture plate was improved by Sherman of Pittsburgh by eliminating sharp corners and adding vanadium to enhance toughness and ductility.

1924: Zierold discover Stellite (Co-Cr-based alloy) as the most inert material for implantation.

1929: Two new stainless steels were developed, 18-8 (18 w/o Cr, 8 w/o Ni) and 18-8sMo (2-4 w/o Mo). They present high corrosion resistance, in particular the 18-8sMo to saline environments.

1932: A 19 w/o Cr, 9 w/ o Ni alloy named Vitallium was used for medical practice because of his light weight and resistance to corrosion.

1939: Tantalum was used in neurological and plastic surgery. Their poor mechanical properties and difficulties in processing devices with it made the material not suitable for orthopaedics.

Late 1940's: Initial commercial development of Ti as implant material.

Late 1970's: The use of Ti6Al4V in prosthesis grow quickly because of the high strength, light weight, formability and corrosion resistance. The alloys also presented good tissue tolerance.

2.2.2 Stainless Steels.

Stainless steels were the first material used as a biomaterial. During history this material has been improved to be used as an implantable material. The first stainless steel used for implantation was 18-8 (18 w/o Cr, 8 w/o Ni). The addition of chromium enhanced the corrosion resistance [25]. Another stainless steel used is the 18-8sMo (2-4 w/o Mo). The addition of molybdenum improved corrosion resistance to salt water [26]. This

characteristic is very important because the body acts as a saline environment. The corrosion resistance to chloride solution of the alloy was enhanced by reducing carbon content to a 0.03 w/o.

The 18-8 and 18-8sMo materials are the AISI 316 and 316L, respectively. They are the most widely used stainless steel for implants. The ASTM (American Society of Testing and Materials) recommends type 316L for implant fabrication. In table 2 the composition of the main stainless steel used for biomedical devices is shown.

ELEMENT	COMPOSITION (w/o)
Carbon	0.03 max
Manganese	2.00 max
Phosphorus	0.025 max
Sulfur	0.010 max
Silicon	0.75 max
Chromium	17.00-19.00
Nickel	13.00-15.00
Molybdenum	2.25-3.00
Nitrogen	0.10 max
Copper	0.50 max
Fe	Balance

Table 2. Composition in w/o of the AISI 316L stainless steel used for biomedical applications according to the ASTM [24].

The elements with more presence in the alloy are chromium, nickel and molybdenum. Chromium is a reactive element, but if it is passivated is able to give high corrosion resistance. Nickel is used to stabilize the austenitic phase and enhances corrosion resistance. And molybdenum increases resistance to pitting corrosion in a saline environment.

Despite of their good corrosion properties, stainless steel may corrode inside the body if they are exposed to high stress and/or hypoxia. For these reasons, the stainless steel is used for temporary devices such as fracture plates, screws and hip nails.

2.2.3. Co- Based Alloys

There are two basic types of Co-based alloys:

- CoCrMo: used to cast a product. Used in dentistry and in artificial joints.
- CoNiCrMo: wrought by forging. Used for making stems of prosthesis subjected to high loads such as knee or hip joints.

The ASTM recommends four types of Co-Based alloys for surgical implant applications.

	Co28Cr6Mo Castable		Co20Cr15W10Ni Wrought		Co28Cr6Mo Wrought		Co35Ni20Cr10Mo	
Element	Min	Max	Min	Max	Min	Max	Min	Max
Cr	27.2	30.00	19.00	21.00	26.0	30.0	19.0	21.0
Mo	5.0	7.0	-	-	5.0	7.0	9.0	10.5
Ni	-	2.5	9.0	11.0	-	1.0	33.0	37.0
Fe	-	0.75	-	3.0	-	0.75	9.0	10.5
C	-	0.35	0.05	0.15	-	0.35	-	0.025
Si	-	1.0	-	1.0	-	1.0	-	0.15
Mn	-	1.0	-	2.0	-	1.0	-	0.15
W	-	0.2	14.0	16.0	-	-		
P	-	0.02	-	0.04	-	-	-	0.015
S	-	0.01	-	0.03	-	-	-	0.01
N	-	0.25	-	-	-	0.25	-	-
Al	-	0.3	-	-	-	-	-	
Bo	-	0.01	-	-	-	-	-	0.015
Ti							-	1.0
Co				Balance				

Table 3. Chemical composition of the Co-based alloys approved by the ASMT for biomedical applications [24].

Although the ASMT recognizes this four Co-based alloys as good biomaterials, just two of them are mainly used in implant fabrications: CoCrMo and CoNiCrMo.

Cobalt and chromium form a solid solution and the addition of molybdenum produce finer grains increasing strength after casting or forging. CoNiCrMo has a high degree of corrosion resistance to saline environment. However, implants of CoNiCrMo can only be fabricated by hot forging due to difficulties of cold working.

Both alloys have similar abrasive wear properties although the CoNiCrMo is not suitable for joint prosthesis because it shows low frictional properties with itself and with other materials. Some studies suggest that this ions release due to friction might be harmful for the body [27].

The CoCr alloys were used in cast stem prosthesis but the stiffness of the alloy make the bone around the implant to resorb and there were also many stem fractures due to fatigue. Therefore, these alloys should be used for applications that require a long service life without fracture or stress fatigue.

2.2.4 Ti and Ti-Based Alloys

In the late 1930s, the tolerance of titanium in cat femurs was discovered and since then, titanium has been used for implant fabrication. It was found that titanium had some advantages over stainless steel and Co-based alloys: it was lighter and had better mechanic-chemical properties. When compared to other metals used for medical devices, titanium and Ti-based alloys have lower elastic modulus, high strength and reduced ductility. However, the poor shear strength make titanium and Ti-based alloy not able to fabricate bone screws, plates, etc.

The unalloyed titanium used for implant applications is classified in four grades depending on the impurities that it contains. Oxygen impurities are important because they play an important role in the ductility and the strength.

The main Ti-based alloys used for implant fabrication are listed in the table below.

Element	Ti6Al4V	Ti8Al17Nb	Ti13Nb13Zr	Ti12Mo6Zr2Fe
N	0.05	0.05	0.05	0.05
C	0.08	0.08	0.08	0.05
H	0.0121	0.009	0.012	0.020
Fe	0.25	0.25	0.25	1.5-2.5
O	0.13	0.20	0.15	0.08-0.28
Al	5.5-6.5	5.5-6.5	-	5.5-6.75
V	3.5-4.5	-	-	-
Ta		0.5	-	-
Zr		-	12.5-14.0	5.0-7.0
Nb		6.5-7.5	12.5-14.0	-
Mo		-	-	10.0-13.0
Ti		Balance		

Table 4. Chemical composition of the Ti-based alloys approved by the ASMT for biomedical applications [24].

Depending on the alloying elements, the properties of the alloys can be controlled. Aluminium is an α-stabilizer that increases the transformation temperature from α to β phase. On the other hand, V, Nb, Mn, Co, Ta, Cr and Cu are β-stabilizers that stabilize the beta-cubic phase and decrease the α-β transition temperature. Since oxygen

embrittles the alloy, the synthesis requires an inert atmosphere for high temperature processing or be forged below 925ºC.

2.2.5 Other metals

Ni-Ti alloys: NiTi presents a special characteristic named shape memory effect (SME). This means that the material is able to return to its original shape when is deformed by heating above the transformation temperature or by releasing the load. The equiatomic NiTi alloy presents SME near room temperature. This special feature of Ni-Ti alloys makes them useful in applications such as stents and arrow intraortic balloon catheter amongst others. In the former application the transformation temperature feature plays a key role expanding the stent when placed into the arteries due to body temperature. In the latter application, the deformation capacity because of the loads exerted is crucial to allow movement through the meandering paths into the hart chamber. NiTi have been used in medicine since the late sixties [21].

In addition to SME, NiTi alloy also exhibits ductility, high biocompatibility, super-plasticity and high damping properties. All this make NiTi an attractive material for stents, tailored compressive fixation of bone fragments, vena cava filters, intracranial aneurysm clips, orthodontic dental arch wires, etc. Despite these promising features and applications, there is an increasing concern about Ni allergy [28–30].

Tantalum: As titanium, this metal forms an oxide layer that makes them biocompatible [26,31] and prevents further oxygen penetration. Tantalum presents poor mechanical properties and high density. Is because of that, the uses of tantalum are restricted to wire sutures and arterial stents. Moreover, studies are being done with porous tantalum as bone graft substitute for the femoral head [32,33].

2.3 Titanium as a biomaterial

2.3.1 History

Titanium was discovered in 1791 by William Gregor. In the 1940s Bothe et al. and Leventhal conducted animal experiments with stainless steel, CrCoMb and Ti to test their bioactivity. Titanium showed the best results. Since then the use of Ti as implant material increased.

Titanium is the most widely used metal for medical devices. In the mid-1950s titanium started to be used in low-stress implants as heart valves. In the 1970s titanium was introduced for orthopaedic applications as an alternative of the CoCr. The lower elastic modulus, the elasticity and the good biocompatibility of titanium made him the perfect material for prosthesis [21,24,26].

2.3.2 What makes titanium biocompatible?

Many materials oxidize in contact with liquids, such as body fluids. The zone in contact with the fluid is oxidized in a process called ionization. The bond between the oxidized layer and the non-oxidized layer gets weaker inducing the detachment of atoms. Atoms are released to the body fluids where they attach to proteins modifying them [21]. This triggers the activation of defensive mechanism of the immune system and the metal is rejected.

Titanium doesn't present this behaviour; the bond between the oxidized layer and the non-oxidized one is stronger than in other metals. This peculiarity, avoid massive release of ions to the body minimizing the immune system response.

This special feature of Ti makes the difference with the other metals used as biomaterials.

2.4 Titanium alloys

In an attempt to improve the Young's modulus, strength/ductility balance, fatigue strength, fracture toughness and wear resistance, titanium was alloyed with other elements. Table 5 show some of the titanium alloys developed for medical applications.

Titanium alloys have better properties regarding low modulus, strength and corrosion resistant than stainless steel and Co-based alloys. The field of application of the titanium alloys is also superior. They are used in dental implants, joint replacement parts for hip, knee, shoulder, spine, elbow and wrist; and for bone fixation materials [28].

1. Pure Ti (ASTM F67-89) Grade 1, 2, 3 and 4 Purity → Decrease (add N_1Fe and O) Strength → Increase Ductility → Decrease	○ 7. Ti-15Sn-4Nb-2Ta-0.2Pd: $\alpha + \beta$ type (Japan) ○ 8. Ti-15Zr-4Nb-2Ta-0.2Pd: $\alpha + \beta$ type (Japan) ○ 9. Ti-13Nb-13Zr (ASTM F1713-96): near β type (U.S.A.), Low modulus
2. Ti-6Al-4V ELI (ASTM F136-84, F620-87): $\alpha + \beta$ type	○ 10. Ti-12Mo-6Zr-2Fe (ASTM F1813-97): β type (U.S.A.), Low modulus
3. Ti-6Al-4V (ASTM F1108-88): $\alpha + \beta$ type	○ 11. Ti-15Mo: β type (U.S.A.), Low modulus
○ 4. Ti-6Al-7Nb (ASTM F1295-92, ISO5832-11): $\alpha + \beta$ type (Swiss)	12. Ti-16Nb-10Hf: β type (U.S.A.), Low modulus
	13. Ti-15Mo-5Zr-3Al: β type (Japan), Low modulus
○ 5. Ti-5Al-2.5Fe (ISO5832-10): $\alpha + \beta$ type (Germany)	14. Ti-15Mo-2.8Nb-0.2Si-0.26O: β type (U.S.A.), Low modulus
○ 6. Ti-5Al-3Mo-4Zr: $\alpha + \beta$ type (Japan)	○ 15. Ti-35Nb-7Zr-5Ta: β type (U.S.A.), Low modulus
	○ 16. Ti-29Nb-13Ta-4.6Zr: β type (Japan), Low modulus
	○ 17. Ti-40Ta, Ti-50Ta: β type (U.S.A), High corrosion resistance
○:Developed for biomedical applications	

Table 5. Relation of the different Ti alloys for biomedical applications [28].

Although the superiority of the titanium alloys is patent, the scientific community is concerned about the ions release to the organism and the effect in human's health. For these reason, in the last years many efforts have been done to minimize the use of some alloying elements to avoid toxic debris [26,34]. These elements and its effect in human's health are explained in more detail in the following lines.

2.4.1 Ti-6A-l4V

This alloy was first used in the aeronautic industry and was proposed as a biomaterial. The main application of this alloy was total joint prostheses but in the 1980s high levels of Ti, Al and V were found in the surrounding tissue of the implant showing the low wear resistance of the material and the potential health problems [28,35]. Trying to solve the wear resistance the material wasn't used to replace hip heads or knees. Concerning the debris release, the vanadium was substituted by iron or niobium. From these modifications the Ti-5A-l2.5Fe and Ti-6Al-7Nb alloys were developed.

2.4.2 TMZF^{TM} Alloy

The TMZF^{TM} (Ti-12Mo-6Zr-2Fe) alloy improves the wear resistance of the Ti-6Al-4V, the tensile strength, the elastic modulus and the fracture toughness. The TMZF is a metastable alloy which beta-transus temperature is 754ºC. The strength can be increased with aging above beta-transus temperature, but the elastic modulus also increases and this is not desirable. Because of the good mechanical properties the TMZF alloy is used in orthopaedic applications and is approved by de FDA (Food and Drug Administration).

2.4.3 Ti-13Zr-13Nb

As the TMZF alloy, this alloy has higher wear resistance, higher tensile strength, higher fracture toughness and low elastic modulus than the Ti-6Al-4V. But in this case, the alloy is a near-β alloy. After aging, the microstructure is composed of martensite and beta precipitates which give strength and hardness to the material [21]. The alloy is used for hip and knee replacement.

2.4.4. Tyadine 1610

Is an alloy composed of Ti-(15.5-16.5)Nb-(9-10Hf) developed by Teledyne Wag Chang Albany for medical applications in the early 1990s [36]. It was the first time to use hafnium as an alloying element. The elastic modulus of the alloy is 81 GPa, lower than that of Ti6Al4V. Other advantage of the alloy is the higher tensile strength.

2.4.5 Ti-24Nb-4Zr-7.9Sn

The alloy was developed by Hao et al. for biomedical applications [37] .The alloy differentiate from the other titanium alloys because of the elastic modulus which match that of bone (33 GPa) and the unstable and plastic deformation behaviour [37]. The alloy presents a high recoverable elastic strain (~3.3%) and this made it useful also to reduce noise or vibration for other applications.

3. PROBLEMS DERIVED FROM THE INTERACTION PROSTHESIS-BODY

In the 20th century, the use of metals was introduced in medicine to replace damaged body parts. Since then the number of different materials and the quantity of applications have increased. The increase in population life expectancy is translated into an increase on degenerative diseases due to degradation of the mechanical properties of the bone. This is attributed to an excessive loading or absence of normal biological self-healing process. Approximately the 90% of people over 40 years old suffer some kind of disease related to bones [28].

However, the increase in replacement surgeries has been accompanied by a dramatically increase in the revision surgery. The main factors that contribute to implant failure and thus to revision surgery are: host response, allergy, stress shielding effect and poor osseointegration.

3.1 Host response

When an implant is placed in the body it triggers a response called foreign body reaction. There is a wound to be healed and also a foreign body which lymphocytes try to neutralise. Any alteration during the healing process of implant integration could result in an impaired tissue repair causing pathologic inflammation and leading to the implant failure.

3.1.1 Wound healing process

The process is driven in four integrated and overlapped stages: haemostasis, inflammation, proliferation and tissue remodelling. If one of the stages is interrupted, aberrated or prolonged in time the process is affected and that might result in a chronic wound.

In adults, the wound healing process involves the following events [38]:

- Haemostasis: starts immediately after wounding. There is a vascular constriction and fibrin clot formation. In the affected area, there is a release of pro-inflammatory cytokines and growth factors that control the bleeding.
- Inflammation: Inflammatory cells migrate to the wound and promote inflammation. During inflammation, there is an accumulation of neutrophils, macrophages and lymphocytes.
- Mesenchymal stem cell differentiation, proliferation and migration to the wound site
- Angiogenesis: in this phase new capillaries are formed and the vascular density of the wound is restored.
- Re-epithelialisation: new epithelial tissue grows over the wound surface. There is an epithelial proliferation and migration over the provisional matrix within the wound.
- Synthesis, cross-linking and alignment of collagen to provide strength to the healing tissue. This is the last phase of the healing process and can last for years.

3.1.2 Foreign body reaction

After implantation of biomaterial or device in the body there is an inflammatory and wound healing responses in which foreign body reaction is the end-stage response. The foreign body reaction is composed of macrophages and foreign body giant cells and may impact the biocompatibility of the implant medical device.

The host response depends on the physical and chemical nature of the implant or device and starts within 2 or 3 weeks after implantation although this reaction is always present at the tissue/material interface. Pure metals trigger a severe tissue reaction because of its oxidation, although pure titanium shows minimum tissue reaction due to its stable oxide layer, as stated in point 2.3.2.

After implantation, a layer of proteins adhere to the implant or the medical device. The type, level and surface conformation of the adsorbed proteins onto the implant surface might determine the tissue reaction. Albumin, fibrinogen, fibronectin and vitronectin amongst other proteins, modulate host inflammatory cell interactions and adhesion playing an important role in inflammation and wound healing responses [39] .

The events in the foreign body reaction include protein adsorption, monocyte/macrophage adhesion, macrophage fusion to form foreign body giant cells and cross-talk between macrophages/foreign body giant cells and inflammatory/wound healing cells.

Mainly, host response can be classified in inflammation and fibrous encapsulation [38,39].

3.1.2.1 Inflammation

As it was claimed before, the physic-chemical characteristics of the implant can induce a host response at the surrounding tissue unchaining the inflammatory response in the implant site.

The healing process starts with inflammation. The extent of injury in the implantation procedure and the location where the implant or the device is placed determine the extent or degree of the inflammatory response. The process is mediated by chemicals from the plasma, cells and injured tissue. During the process different cells play a role. In the first days after the injury, neutrophils predominate and after a few days, they are replaced by monocytes. These cells produce the provisional matrix consisting of fibrin, and inflammatory products released by the complement system. The aim of the matrix is activate platelets, inflammatory cells and endothelial cells that will restore the damaged tissue [40].

If after three or five days of inflammation there is no healing of the wound, the inflammatory [40,41] process turn into a chronic inflammation [40]. In this scenario, monocytes, lymphocytes, macrophages and foreign body giant cells are present at the biomaterial interface [39]. This type of inflammation may produce prolonged reactions causing extensive tissue destruction and delaying the natural healing process, resulting in granular tissues [24]. In some cases necrosis of tissues can be done by chemical, mechanical and thermal trauma.

3.1.2.2 Fibrous encapsulation

Granular tissues are constituted by macrophages, fibroblasts and vascular vessels. The macrophages are able to destruct small particles harmful for the body. When this is not possible, the macrophages and the polymorphonuclear leukocytes produce pro-fibrogenic factors which enhance fibrogenesis by fibroblasts around the material after

implantation. That generate a thin layer of collagenous tissue at the tissue-implant interface which encapsulates the implant or medical device [39,40]. Excessive collagen production and tissue contraction is translated in a reduced tissue function and fibrosis that might interfere in the implant of medical device functions [42].

3.2 Toxicity and Allergy

When using metals for implants it is very important to select the ones that are not toxics and do not trigger allergy in the surrounding tissue.

3.2.2 Toxicity

In figure 7 the toxicity of some pure metals is shown. The toxicity was measured as the growth rate of L-929 cells and fibroblast [24,39,43]. It is important to know the toxicity of the metals to avoid their use in implant devices or just to know the preliminary effect they may cause in the body. Due to wear in the implant during their life, ions are released to the blood stream. If the material is toxic, this ions release could produce several injuries in other tissues compromising the health of patients.

The ions release from the Co-Based alloys is the cause of skin related diseased due to Ni [26] and numerous animal studies reported carninogenity due to Co [29]. Despite the good properties of Ti-based alloys and the wide use of the Ti-6Al-4V alloy, the release of Al and V ions to blood stream are found to be associated with some serious diseases such as Alzheimer, neuropathy and ostemomalacia [27,28].

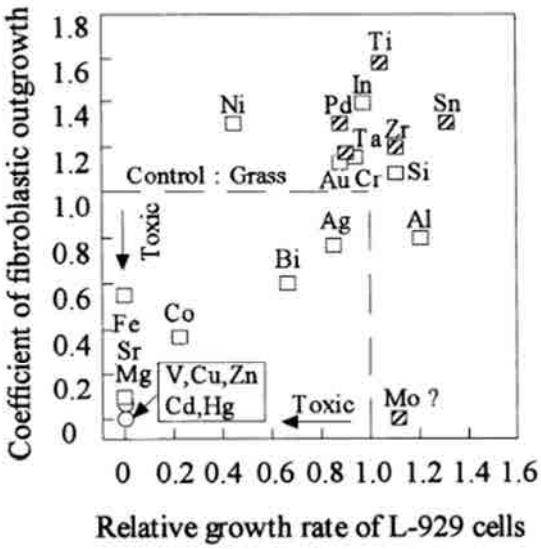

Fig.7 Toxicity of some pure metals regarding the growth of two different types of cells when in contact with them. Adapted from 35.

3.2.1 Allergy

However, not all the ions are toxic. The ions released through sweat and other body fluids to the body may act as allergens.

Allergy to metal ions is of high concern in Europe during the last decades. In figure 8 the percentage of allergy for some common metals is represented. One of the allergies that have increased more is the allergy to Ni. As it can be seen in figure 8 during the last years the increase has been dramatic. About the 20% of young females and 4% of young males suffer from it [26].

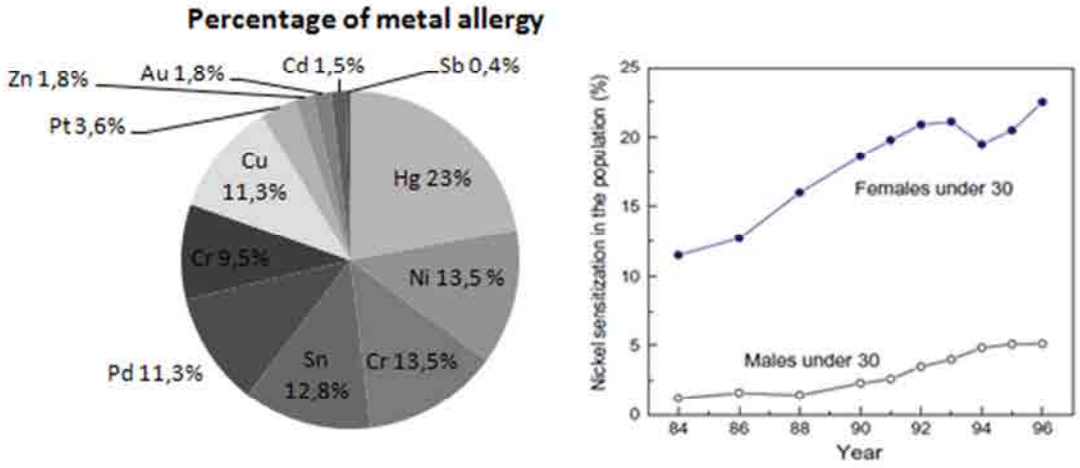

Fig.8 Percentage of allergy caused for each metal and the evolution of Ni allergy in population. Adapted from 26.

There are few reports stating the effects of Ni release and their consequences, but above certain concentrations Ni triggers severe local tissue irritation, necrosis and toxic reactions [26,28,30]. Studies made with NiTi dental implants, reported that the amount of ions released to the body are very low, and thus, the organism is capable to resorb it [29]. Although Ni dental implants allergy has not been demonstrated in a clear way, Ni should be treated as a potential allergen and thus, be avoided in future biomaterials.

3.3 Stress shielding effect

The properties of the materials used to bone replacement don't match those of bone. In Fig 9, the elastic moduli of the different alloys used for bone replacement are shown. It is easy to see that all of them have greater elastic modulus than bone.

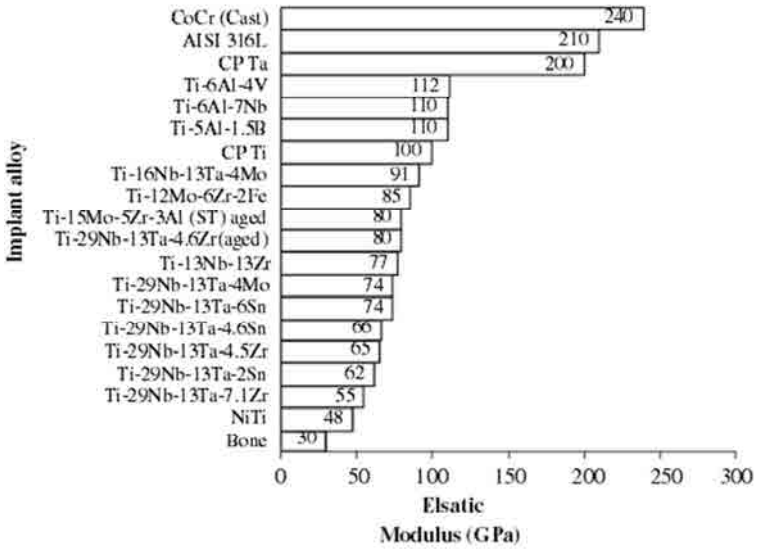

Fig.9 Modulus of elasticity of the most common biomedical alloys. Adapted from 44.

Because of this higher modulus, the implant takes some of the loads that should be going to the bone. This phenomenon is called stress shielding effect. In replacement prosthesis, the stem is introduced into the bone canal and as the stem is stiffer, it shares the load and carrying capacity of bone. According to bone remodelling process explained in point 1.4, bone remodels depending on the loads applied. If fewer loads are applied, bone suffers a resorption, adapting itself to the new loads demand. In Fig. 10 b, the zone of bone with more stress demand is darker than the one at which the implant shares the loads.

The consequence of the stress shielding effect is a reduction of bone density around the implant which leads to implant loosening. To avoid this non desirable effect, alloys with elastic modulus lower than the currently used ones are being developed and investigated [28].

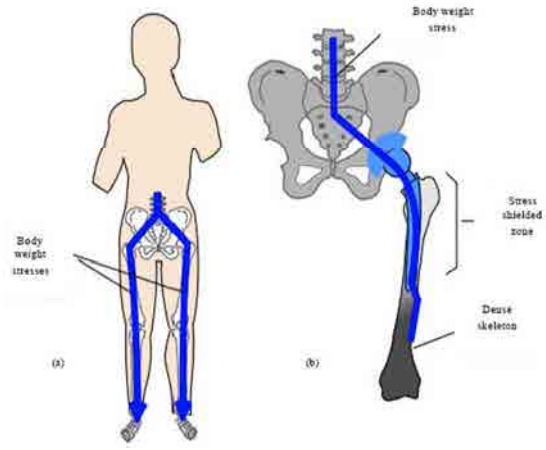

Fig.10 Scheme of the loads transferred to bone and bone behavior during stress shielding effect. Adapted from 28.

3.4 Poor osseointegration

The success of an implant depends on the degree of osseointegration. This concept was first introduced by Professor Per-Ingvar Branemark in the 1950's when he discovered the ability of bone to grow on titanium.

Osseointegration is defined as "the formation of a direct interface between an implant and bone, without intervening soft tissue" [45].

In a poor osseintegration scenario, the implant is not integrated with the surrounding bone and results in loosening of the implant with the consequent revision surgery. Revision surgery is not desirable for three reasons: a) is expensive; b) causes pain to the patient; c) the ratio of success is low [46].

An appropriate surface chemistry, roughness and topography of the implant are of paramount importance to achieve good osseointegration. Implant should be designed with the aim to avoid fibrin adhesion, blood vessel growth and micromotions. Micromotions are understood as relative movements between the implant and the bone with which it has direct contact.

4. MIMICKING EXTRACELLULAR MATRIX

The extracellular component of bone is very important for the bone remodelling process. Bone healing related to implants involves many cellular and extracellular biological events taking place at bone-implant interface that end when the implant is covered with newly formed bone. This phenomenon is called osseointegration.

The biological events that take give rise to osseointegration are similar to those of bone healing process at least in terms of initial host response. The process is regulated by growth and differentiation factors released by the activated blood cells at bone-implant interface.

After one day of implantation, osteoblasts and mesenchymal stem cells migrate and attach to the implant surface. These cells release bone-related proteins and create a non-collagenous matrix layer on the implant material that regulates cells adhesion and binding of minerals [28].

The early deposition of bone on the implant surface is called peri-implant trabecular bone and ensures the biological fixation of the implant.

4.1 Extracellular matrix

The extracellular matrix (ECM) is secreted by cells to create a proper environment where grow and communicate between them. This environment is formed by proteins, minerals, sugars and fluids. Once the cells are settled on the ECM, they can by themselves make new ECM according to their necessities or remodel the one is already made [47].

4.1.1 Functions

The ECM is a non-cellular component of all tissues and organs, gives physical support for the cellular constituents and initiates biochemical and biomechanical cues needed for tissue morphogenesis, differentiation and homeostasis.

Bone ECM gives tissue's chemical and mechanical properties, regulates bone cells and is a reservoir for ions [48]. Tensile and compressive strength and also elasticity, depends

on the ECM. Protection is mediated by the ECM as well. The ECM has a buffering action that maintains extracellular homeostasis and water retention.

The morphological organization and the physiological function of the tissue are also directed by the ECM. It binds growth factors (GFs) and interacts with cell-surface receptors to elicit signal transduction and regulate gene transcription.

On the ECM one can find specific protein sequences recognized by cell membrane receptors such as integrins, discoidin domain receptors and syndecans that mediate cell adhesion. Adhesion plays an important role in cytoskeletal coupling to the ECM and in cell migration through the ECM.

4.1.2 Composition

Bone ECM is formed of osteoid. The osteoid is an organic phase which constitutes approximately the 20% of bone mass and a mineral phase. In bone ECM there are growth factors and bone morphogenic proteins (BMP).

In table 6, there is a scheme on which the type of molecule of the ECM and its role in ECM function is represented.

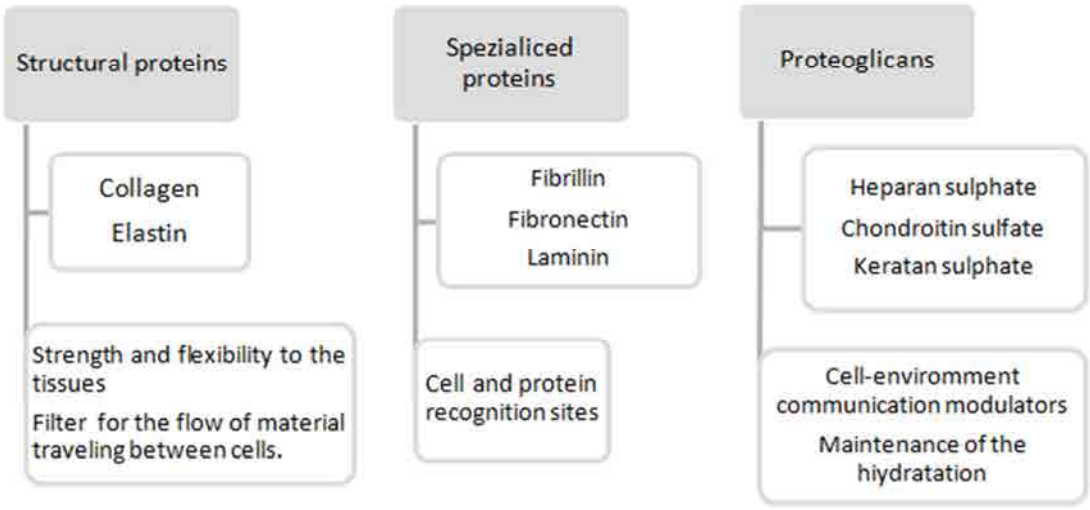

Table 6. Scheme of the constituents of the ECM and their functions 49.

4.1.2.1 Collagen

Amongst structural ECM proteins, collagen is the most abundant one. In mammalians there are up to 28 triple helical proteins called collagens. Collagens are present in many parts of the body and they are important for a many different functions such as tissue scaffolding, cell adhesion, cell migration, cancer, angiogenesis, tissue morphogenesis and tissue repair.

Collagen associates with elastin to recover its coiled structure after being stretched. The stretching properties of elastin are limited by tight association with collagen fibrils. The way collagen fibrils are aligned is determined by connective tissue cells. They apply tension on the matrix organizing collagen fibrils into sheets and cables. In a tissue there is a mix of different types of collagen, although one type usually predominates.

The different types of collagens are classified by function and domain homology [48,50]. Mainly there are two big groups of collagens: heterotrimerics and homotrimerics. The former are collagens with two identical α chains and a third chain that differs; the latter have three identical α chains.

The collagen predominant in bone is collagen type I which is heterotrimeric and fibril-forming. This type of collagen has an important role in tissue. It is the principal tensile element of tendon, cartilage, bone and skin.

As can be seen in Fig. 11, collagen type I is formed by three polypeptide α chains linked by hydrogen bonds, exhibiting an extended polyproline-II conformation, a right-handed supercoil and a one-residue stagger between adjacent chains [51]. Fibroblasts, condroblasts and osteoblasts synthesise collagen type I.

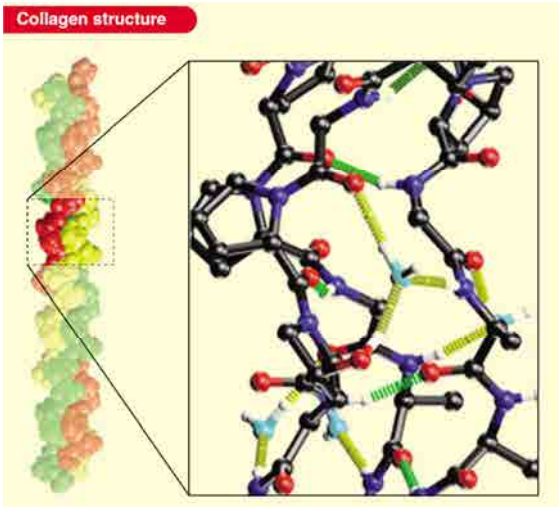

Fig.11 Image of the collagen structure. Adapted from 51.

The integrin recognition adhesion sequences of collagen are located in the triple helical domain. The adhesion sequence for collagen is the peptide -Phe-O-Gly-Arg (GFOGER), where the O is hydroxyproline which signals the A-domain α1 integrins [51].

4.1.3.2 Fibronectin

Fibronectin (FN) is a protein found in plasma and other body fluids and is a part of the ECM as well. FN mediates many different cellular interactions with the ECM and is necessary in cell adhesion, migration, growth and differentiation [52]. Most of cell types express FN.

Fibronectin is composed of two equal subunits of approximately 250kDa linked covalently near the C-terminus by a pair of disulphide bonds. There are three domain types of repeating units that form each monomer. The repeats are named type I, II and III.

Fibronectin molecule presents in the domain I and III an heparin fixation zone (Heparin binding) and also in the domain III a zone for cell adhesion (See Fig.12).

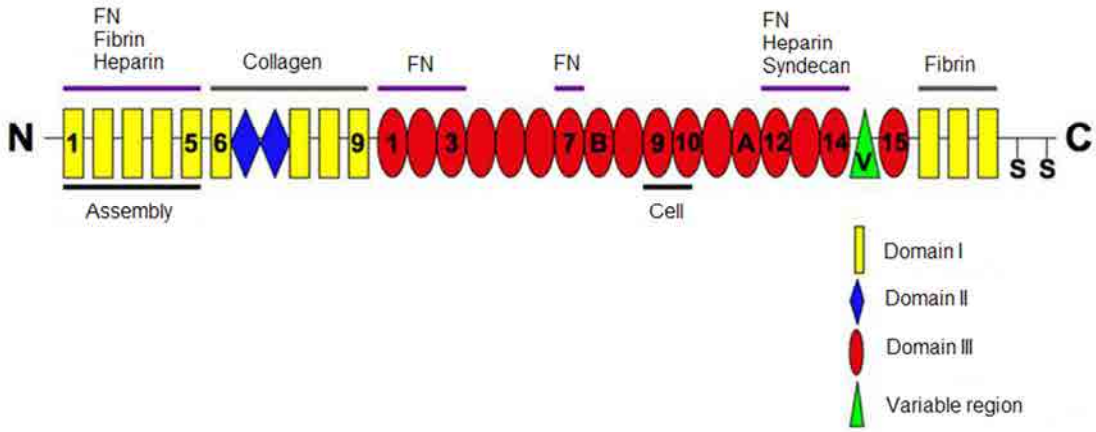

Fig.12 Simplified molecule of Fibronectin. Each domain of FN is represented and the main characteristic of each domain. Adapted from 53.

FN can be a ligand for a dozen members of the cell-surface heterodimeric receptors that link the ECM with the intracellular cytoskeleton which are called integrins (see Fig.13). Integrins bind to the FN Arg-Gly-Asp (RGD) sequence, which is located in the FN repeat III10.

RGD is the most common sequence for cell adhesion through integrin signalling. However, it is not a specific sequence since it is recognized for several integrin types signalling only some aspects of cell behaviour (Dee et al). The presence of additional sequences is required for specifically recognition by concrete integrin types. For instance, FN presents a PHSRN (Pro–His–Ser–Arg–As) sequence belonging to the III_9 domain [53]. The PHSRN is necessary to bond RGD to the integrin α5β1 which increase its affinity forty-fold compared to RGD alone [54,55]. RGD and PHSRN together give a stable adhesion to the integrin α5β1.

Fibronectin also interact with heparan sulfate proteoglycans (HSPGs) via the heparin binding domains [49]. HSPGs take part in the focal adhesions and stress fibres formation. When syndecan-4 (a membrane HSPG) binds to FN, interacts with integrins and induces the formation of focal adhesions and stress fibres. The syndecan-4 and syndecan-1 also play a role in the regulation of the activation of the αvβ3 and αvβ5. The extracellular domain of the proteoglycan interacts with the β-integrin subunit [53].

Some studies have shown that i) the FN heparin binding domain enhances cell adhesion and proliferation of osteoblasts and ii) the RGD-containing central cell-binding domain of FN together with the Heparin binding domain of FN enhances cell adhesive and spreading activities [56].

4.1.4 Adhesion process

To make adhesion possible, cell membrane integrins must recognize a concrete amino . Briefly the mechanism of how RGD binds to integrins can be explained as follows (see Fig.13): the interface between the α and β subunits is the area of RGD recognition. The R residue must fit into a cleft located in the α subunit, whilst the D coordinates a cation bound in a von Willebrand factor domain in the β subunit.

The process of integrin adhesion is very important for cell survival. Integrins are important for cellular processes establishing the unions between the ECM and the cytoskeleton. This linking acts as a mechanotransductor that regulate cell adhesion and spreading [54,57].

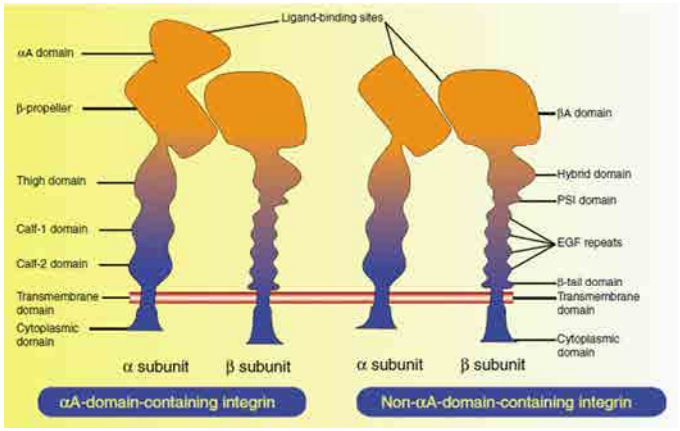

Fig.13 Integrin domain structure. Adapted from 54.

4.1.4.1 Integrins

The interactions between cells and cell-extracellular matrix are essential to cell motility, proliferation, differentiation, regulation of gene expression and cell viability.

Integrins are composed of two units: the α and the β unit. There are 11 variations of α and 6 of β (see Fig.14). This makes a great variety of integrins, and thus cells are able to recognize different adhesion proteins (ligands) and different adhesion motifs [58].

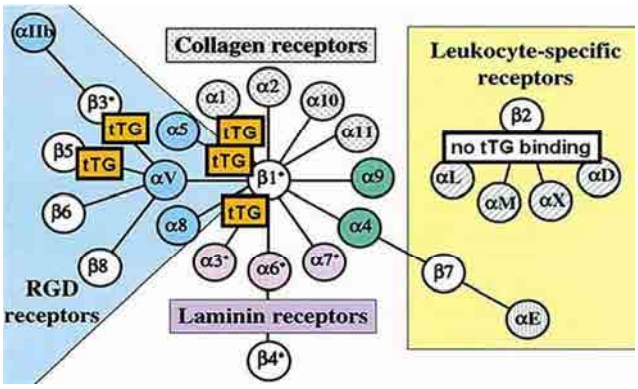

Fig.14 Display of the different dimmers belonging to integrins and the corresponding receptors. Adapted from 52.

Integrins show a bidirectional linkage: on the cytoplasmic membrane and on the extracellular matrix (see Fig.13).

On the cytoplasmic membrane integrins are in charge of coordinating the assembly of cytoskeletal polymers and signalling complexes. On the extracellular matrix, they engage extracellular matrix macromolecules or counter receptor on adjacent cell surfaces. Because of this bidirectional linkages there are spatial restrictions on signalling and extracellular assembly.

Once integrins have interact with the ECM substrates, or after the stimulation of growth factors, they cluster and form focal adhesions in the plane of the membrane by means of the β-chain cytoplasmic region. During this phase, focal adhesion kinase (FAK), tensin, talin and vinculin are recruited and the formation of the multi-molecular complex focal contacts starts [59]. Finally, focal complexes anchor the cytoskeleton to the membrane.

4.1.4.2 RGD motif

RGD was claimed as the adhesive peptide sequence found in many ECM molecules including fibronectin, vitronectin, sialoprotein and osteopontin. That makes RGD the most used sequence in biomaterial strategies to mimic ECM. due to ist ability to bind to many integrins such as αvβ3, αvβ1, α8β1, αvβ8, αvβ6, αvβ5 and αIIbβ3. Integrin binding is of paramount importance for cell survival, considering that it regulates cell adhesion and spreading.

4.2 Biofunctionalisation of surfaces

As was stated in the previous points, usually the material we place in the body to restore some function or to replace damage parts is artificial and metallic in a great extent. In other words, they are artificial materials with no biofunction as the material or function replaced. This, in combination with problems regarding implant-tissue interactions previously explained, contributes to the implant failure. To avoid that, is necessary to confer biocompatibility to the materials used and one way to do that is by biofunctionalisation of their surface. This type of surface modification changes the material's surface composition, structure and morphology but the bulk material properties are not modified [60].

This problems and the necessity to make materials bioactive, led to the development of ECM-derived motifs (described in point 4.3). Functionalization with ECM proteins, favours adhesion and it is expected that also integration will be favoured. The new motifs contain the functional parts of the ECM proteins, but they are more stable, less costly to produce and may be tailored in composition for specific applications.

4.2. 1 Physisorption

Most proteins are large amphipathic molecules, in other words, they possess both a polar and a non-polar region and exhibit both hydrophilic and hydrophobic properties. That special feature makes them innate surface-active molecules.

Protein adsorption is driven by intermolecular forces, such as Coulomb forces, van der Waals forces, Lewis acid-base forces, and more entropically based effects such as hydrophobic interactions, conformational entropy and restricted mobilities. Intramolecular forces within protein molecules are also important because they might lead to an alteration of protein conformation [61].

The extent protein adsorbed on a solid substrate and its mechanism of adsorption is affected by various factors such as protein properties, solid substrate surface and environmental conditions.

Influence of protein properties on protein adsorption

The charge, size, stability of the structure, amino acid composition, and steric conformation may affect the adsorbed protein amount. Charged proteins preferentially

adsorb on substrate surfaces of the opposite charge. On most surfaces, however, proteins adsorb the most at their isoelectric point where they are at neutral charge. Size also affects protein adsorption due to the fact that smaller proteins diffuse more quickly and arrive at the substrate surface faster, but they form fewer contact points with the material surface than larger proteins. Protein hydrophilic domains make proteins tend to adsorb to polar material surfaces, while hydrophobic domains tend to adsorb to hydrophobic material surfaces. Structural stability of proteins play a role on protein adsorption as well. Less structural stable proteins exhibit greater unfolding upon adsorption onto a material surface and form more contact points/bonds.

Most proteins change their conformation upon adsorption to a solid interface [62]. This is because the conformation of a protein that corresponds to the free energy minimum in solution usually does not correspond to the free energy minimum of this protein when contacts with the surface.

For instance, glycoproteins have the hydrophobic domains buried inside a shell of glycans. This conformation determines its behaviour to hydrophobic planar surfaces [62,63].

Influence of surface substrate surface properties on protein adsorption

The materials surface owns a specific surface energy, polarity, charge and morphology. Non polar surfaces favour protein adhesion as well as high surface tension or charged substrates. In glycoproteins this rule does not apply because they adhere better on hydrophilic planar surfaces. Opposite charges between the surface and protein promote increased protein adsorption, while like charges tend to reduce protein adsorption. The type of bonds between proteins and material surface are dictated by the chemical composition of the surface.

Roughness is another important surface property affecting protein adsorption. Increased surface roughness and topological features provide increased material surface area for protein adsorption. Although, it was shown that nanometre scale roughness do not have a considerably effect on protein adsorption [64].

Influence of external parameters on protein adsorption

The equilibrium state and the kinetics of protein adsorption are affected by temperature. Elevated temperatures enhance protein adhesion [62].

The pH plays an important role on determining the electrostatic state of proteins. Adsorption rates are high when protein and substrate bear opposite charges since electrostatic attractions accelerate the migration towards the surface. However, the total mass load is generally observed to be maximized at the isoelectric point [62–64]

The concentration of ions in the protein solution might also affect protein adhesion. The adsorption of charged proteins or protein domains to oppositely charged substrates is hampered whereas the adsorption to like-charged substrates is enhanced [62]. The hydrophobic peptide moiety in the protein molecule assembles to interact with a hydrophobic region of the surface, resulting in a multipoint attachment with more interacting points. Some studies indicated that the higher the bulk concentration, the greater the amount of protein adsorbed, showing a saturation curve. These two statement results are opposed, which leads us to think that there is no a protein concentration dependency in protein adhesion [63].

4.2.2 Covalent bonding. Silanization

Silanisation is a common method to attach biomolecules onto hydroxylated surfaces. After silanisation, the surface of the material is covered with alkoxysilane molecules. These types of molecules are able to form strong bonds with titanium oxide layer TiO_2. The TiO_2 layer contains hydroxyl groups that attack and displace the alkoxy groups of the silane forming covalent -Si-O-Si bonds. Silanes are silicon chemicals with hydrolysable groups and organic substitution allowing permanent property modification. These modifications include hydrophobicity, release, absorption, orientation and charge conduction.

Aminosilanes are special members of the alkoxysilanes group. They carry the catalysing amine function, required for chemical bonding with the surface, inside the molecule. This makes them more reactive than other silanes. The most commonly used aminosilane is the 3-Aminopropyltriethoxysilane (APTES) which have three ethoxy groups per molecule (see Fig.15).

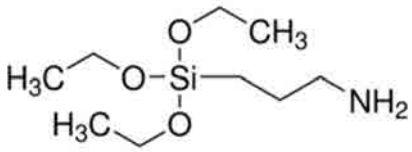

Fig.15 Structural formula of APTES.

Proteins interact with APTES at the primary amino groups or the carboxyl groups, but specific attachment at a defined site is very difficult with these functionalities. It is because of that a crosslinker is in need. Adding a crosslinker, the biomolecules used to biofunctionalisation will find a single functional site and moderate reaction conditions [65].

One of the crosslinkers used is the N-Succinimidyl 3-maleimidopropionate which is a short, sulfhydryl and amino reactive heterobifunctional crosslinking reagent (see Fig.16).

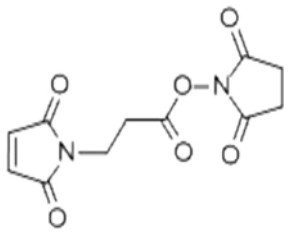

Fig.16 Structural formula of the N-Succinimidyl 3-maleimidopropionate.

Silanisation of the surfaces can be done in solution (APTES diluted in an anhydrous solvent) or in vapor phase [66].

The guidelines to follow when dealing with APTES in solution are:

- The extent of polymerisation of animosilanes at the interface and in solution should be controlled using an anhydrous solvent.
- Silane concentration should be low to avoid formation of oligomers and polymers in solution.
- Run the reaction at moderate temperature to help disruption of hydrogen bonds and reduce the number of weakly bonded silane molecules in silane layers.

- Cleaning of the substrates after silanisation with the anhydrous solvent, ethanol and water to facilitate the displacement of weakly bonded silane molecules and the hydrolysis of residual alkoxy groups in silane layers.

4.3 Motifs for biofunctionalisation

4.3.1 ECM proteins

The use of full ECM proteins seems to be the best strategy to biofunctionalisation, because the whole protein gives all their functionality and not only their adhesion capacity. The coating methods used are protein adsorption from solution, injection of protein solution into the implant, dip coating and covalent boding.

Despite the possibility to do the biofunctionalisation with full-length ECM proteins and the verification by scientific studies of the osseintegration improvement [49,67], the use of these proteins has been hindered by several factors. Amongst many others we can mention low solubility, costly obtaining methods, immunogenicity and a narrow range of optimal conditions to be active.

4.3.2 Mimetic peptides

In an attempt to avoid the limitations of full-length ECM proteins, in the last decades the use of ECM-derived peptides have been studied [68,69]. These are short chains of peptides containing the functional sites of the ECM protein of interest. These motifs are able to trigger the same cell response as the imitated functional sites of the full protein which means they are able to trigger cell adhesion, proliferation and signalling. Moreover, this motifs are more stable and easy to synthesize that the ECM proteins [70].

The spacing and the conformation of the peptides is crucial to trigger the proper cell response [49,57,71]. Is because of that some different strategies in presenting those motifs are being use. Some of the peptide's sequences are in a linear form; others are cycled in a loop trying to improve ligand specificity for integrins and in other cases, different peptides targeting integrin and non-integrin receptors are mixed [43,72–75].

4.3.3 Recombinant proteins

Despite the efforts made to mimic ECM and its synergy sites with short chains of peptides, the bond is not as stable as with the full ECM proteins. This is because of two reasons: i) the high sensitivity of integrin's bond to conformation and orientation of the bonding motifs, ii) the less integrin specificity of the short peptides.

The recombinant protein technique [57,71] arises as a potential solution to the weak points of peptides. When dealing with recombinant proteins the signalling zone of the ECM protein of interest can be spanned and thus, their properties and functions [76]. With these type of motifs, the antigenicity of the full ECM proteins is reduced and the domains that may trigger undesirable cell responses as well. Another strong point of recombinant proteins is that some characteristics as protein immobilization, orientation or activity may be modulated by modification of some amino acids without affecting their integrin bond effectiveness. Moreover, there is the possibility of combine sequences, join different fragments, etc.

5. BIBLIOGRAPHY

1. Marieb, E. N. *Human anatomy and physiology*. 995, 60 (The Benjamin/Cummings, 1989).

2. Raisz, L. G., Rodan, G. A. & Bilezikian, J. P. *Principles of bone biology*. **2,** 1696 (Academic Press, 2002).

3. Kopperdahl, D. L., Roberts, A. D. & Keaveny, T. M. Localized damage in vertebral bone is most detrimental in regions of high strain energy density. *J. Biomech. Eng.* **121,** 622–8 (1999).

4. Nagaraja, S., Couse, T. L. & Guldberg, R. E. Trabecular bone microdamage and microstructural stresses under uniaxial compression. *J. Biomech.* **38,** 707–16 (2005).

5. Taylor, D. A crack growth model for the simulation of fatigue in bone. *Int. J. Fatigue* **25,** 387–395 (2003).

6. Ruimerman, R., Hilbers, P., van Rietbergen, B. & Huiskes, R. A theoretical framework for strain-related trabecular bone maintenance and adaptation. *J. Biomech.* **38,** 931–41 (2005).

7. Schaffler, M. Fatigue and repair in bone. *Int. J. Fatigue* **22,** 839–846 (2000).

8. Knothe Tate, M. L., Adamson, J. R., Tami, A. E. & Bauer, T. W. The osteocyte. *Int. J. Biochem. Cell Biol.* **36,** 1–8 (2004).

9. Deans, R. J. & Moseley, A. B. Mesenchymal stem cells: Biology and potential clinical uses. *Exp. Hematol.* **28,** 875–884 (2000).

10. Caplan, A. I. & Bruder, S. P. Mesenchymal stem cells: building blocks for molecular medicine in the 21st century. *Trends Mol. Med.* **7,** 259–264 (2001).

11. Maxson, S., Lopez, E. A., Yoo, D., Danilkovitch-Miagkova, A. & LeRoux, M. A. Concise Review: Role of Mesenchymal Stem Cells in Wound Repair. *Stem Cells Transl. Med.* **1,** 142–149 (2012).

12. Manolagas, S. C. Birth and Death of Bone Cells: Basic Regulatory Mechanisms and Implications for the Pathogenesis and Treatment of Osteoporosis. *Endocr. Rev.* **21,** 115–137 (2000).

13. Crockett, J. C., Rogers, M. J., Coxon, F. P., Hocking, L. J. & Helfrich, M. H. Bone remodelling at a glance. *J. Cell Sci.* **124,** 991–998 (2011).

14. Hill, P. A. Bone remodelling. *J. Orthod.* **25,** 101–107 (1998).

15. Noble, B. S. & Reeve, J. Osteocyte function, osteocyte death and bone fracture resistance. *Mol. Cell. Endocrinol.* **159,** 7–13 (2000).

16. Fernández-Tresguerres Hernández-Gil, I., Alobera Gracia, M. A., del Canto Pingarrón, M. & Blanco Jerez, L. Physiological bases of bone regeneration I. Histology and physiology of bone tissue. *Med Oral Patol Oral Cir Bucal.* **11,** E–147–E–151 (2006).

17. Fernández-Tresguerres Hernández-Gil, I., Alobera Gracia, M. Á., del Canto Pingarrón, M. & Blanco Jerez, L. Physiological bases of bone regeneration II. The remodeling process. *Med Oral Patol Oral Cir Bucal.* **11,** E–151–E–157 (2006).

18. Van Oers, R. F. M., Ruimerman, R., Tanck, E., Hilbers, P. A. J. & Huiskes, R. A unified theory for osteonal and hemi-osteonal remodeling. *Bone* **42,** 250–9 (2008).

19. Wolff, J. The Classic: On the Inner Architecture of Bones and its Importance for Bone Growth. *Clin. Orthop. Relat. Res.* **468,** 1132–1528 (2010).

20. Ruff, C., Holt, B. & Trinkaus, E. Who's afraid of the big bad Wolff?: ?Wolff's law? and bone functional adaptation. *Am. J. Phys. Anthropol.* **129,** 484–498 (2006).

21. *Titanium in medicine :material science, surface science, engineering, biological responses, and medical applications*. (Springer, 2001).

22. Cambridge, U. of. Structure of bone and implant materials. Bone replacement. at <http://www.doitpoms.ac.uk/tlplib/bones/bone-replacement.php>

23. University of Washington. An introduction to biomaterials. (2004). at <http://www.uweb.engr.washington.edu/research/tutorials/introbiomat.html>

24. Park, J. B. & Lakes, R. S. *Biomaterials :an introduction*. **3,** 561 (Springer, 2007).

25. Ratner, B. D. *Biomaterials science :an introduction to materials in medicine*. **2,** 851 (Elsevier Academic, 2004).

26. Niinomi, M. Recent Metallic Materials for Biomedical Applications. *Metall. Mater. Trans. A* **33,** 477 (2002).

27. Swierenga, S. H. H., Gilman, J. P. W. & McLean, J. R. Cancer risk from inorganics. *Cancer Metastasis Rev.* **6,** 113–154 (1987).

28. Geetha, M., Singh, A. K., Asokamani, R. & Gogia, A. K. Ti based biomaterials, the ultimate choice for orthopaedic implants – A review. *Prog. Mater. Sci.* **54,** 397–425 (2009).

29. Uo, M., Watari, F., Yokoyama, A., Matsuno, H. & Kawasaki, T. Dissolution of nickel and tissue response observed by X-ray scanning analytical microscopy. *Biomaterials* **20,** 747–755 (1999).

30. Yang, K. & Ren, Y. Nickel-free austenitic stainless steels for medical applications. *Sci. Technol. Adavanced Mater.* **11,** 1–13 (2010).

31. Matsuno, H., Yokoyama, A., Watari, F., Uo, M. & Kawasaki, T. Biocompatibility and osteogenesis of refractory metal implants, titanium, hafnium, niobium, tantalum and rhenium. *Biomaterials* **22,** 1253–1262 (2001).

32. Cohen, R. A porous tantalum trabecular metal: basic science. *Am. J. Orthop. (Belle Mead. NJ).* **31,** 216–217 (2002).

33. Levine, B. R., Sporer, S., Poggie, R. A., Della Valle, C. J. & Jacobs, J. J. Experimental and clinical performance of porous tantalum in orthopedic surgery. *Biomaterials* **27,** 4671–4681 (2006).

34. Wang, K. The use of titanium for medical applications in the USA. *Int. Symp. Metall. Technol. Titan. Alloy.* **213,** 134–137 (1996).

35. YUMOTO, S. *et al.* ALUMINUM NEUROTOXICITY IN THE RAT BRAIN. *Int. J. PIXE* **02,** 493–504 (1992).

36. Amick, D. D. Characterization of TiNbHf alloys for potential medical dental applications. (1993).

37. Hao, Y. L. *et al.* Super-elastic titanium alloy with unstable plastic deformation. **87,** (2005).

38. Guo, S. & DiPietro, L. A. Factors Affecting Wound Healing. *J. Dent. Res.* **89,** 219–229 (2010).

39. Anderson, J. M., Rodriguez, A. & Chang, D. T. Foreign body reaction to biomaterials. *Innate Adapt. Immune Responses Tissue Eng.* **20,** 86–100 (2008).

40. Anderson, J. M. Biological responses to materials. *Annu. Rev. Mater. Res.* **31,** 81–110 (2001).

41. The recombinant protein handbook. Protein amplification and simple purification.

42. Barbara Rolfe, J. et al. *Regenerative Medicine and Tissue Engineering - Cells and Biomaterials*. (InTech, 2011). doi:10.5772/837

43. Puleo, D. A. & Bizios, R. *Biological Interactions on Materials Surfaces*. (Springer, 2009). doi:10.1007/978-0-387-98161-1-7

44. Setcos, J. C., Babaei-Mahani, A., Silvio, L. Di, Mjör, I. A. & Wilson, N. H. F. The safety of nickel containing dental alloys. *Dent. Mater.* **22,** 1163–1168 (2006).

45. Ridzwan, M. I. Z., Shuib, S., Hassan, A. Y., Shokri, A. A. & Mohamad Ibrahim, M. N. Problem of Stress Shielding and Improvement to the Hip Implant Designs: A Review. *J. Med. Sci.* **7,** 460 (2007).

46. Miller, B. F., Keane, C. B., Klajn, D. S. & Boxaca, M. *Diccionario enciclopédico de enfermería*. **5ª,** 1524 (Panamericana, 1996).

47. Mavrogenis, A. F., Dimitriou, R., Parvizi, J. & Babis, G. C. Biology of implant osseointegration. *J. Musculoskelet. Neuronal Interact.* **9,** 61–71 (2009).

48. Cassimeris Lingappa, Vishwanath R., Plopper, George.,Lewin, Benjamin.,, L. *Lewin's cells.* (Jones and Bartlett Publishers, 2011).

49. Shekaran, A. & García, A. J. Extracellular matrix-mimetic adhesive biomaterials for bone repair. *J. Biomed. Mater. Res. Part A* **96A,** 261–272 (2011).

50. Alberts, B. & Walter, P. *Molecular biology of the cell*. **4th,** 1,36,49,1463 (Garland, 2002).

51. Kadler, K. E., Baldock, C., Bella, J. & Boot-Handford, R. P. Collagens at a glance. *J. Cell Sci.* **120,** 1955–1958 (2007).

52. Humphries, J. D., Byron, A. & Humphries, M. J. Integrin ligands at a glance. *J. Cell Sci.* **119,** 3901–3903 (2006).

53. Pankov, R. & Yamada, K. M. Fibronectin at a glance. *J. Cell Sci.* **115,** 3861–3863 (2002).

54. Sechler, J. L., Corbett, S. A. & Schwarzbauer, J. E. Modulatory Roles for Integrin Activation and the Synergy Site of Fibronectin during Matrix Assembly. *Mol. Biol. Cell* **8,** 2563–2573 (1997).

55. Wierzbicka-Patynowski, I. & Schwarzbauer, J. E. The ins and outs of fibronectin matrix assembly. *J. Cell Sci.* **116,** 3269–3276 (2003).

56. Sarrazin, S., Lamanna, W. C. & Esko, J. D. Heparan Sulfate Proteoglycans. *Cold spring Harb. Perspect. Biol.* **3,** (2011).

57. García, A. J., Schwarzbauer, J. E. & Boettiger, D. Distinct Activation States of α5β1 Integrin Show Differential Binding to RGD and Synergy Domains of Fibronectin†. *Biochemistry* **41,** 9063–9069 (2002).

58. Geiger, B., Spatz, J. P. & Bershadsky, A. D. Environmental sensing through focal adhesions. *Nat. Rev. Mol. Cell Biol.* **10,** 21–33 (2009).

59. Ruoslahti, E. Integrins. *J. Clin. Invest.* **87,** 1–5 (1990).

60. Petit, V. & Thiery, J.-P. Focal adhesions: Structure and dynamics. *Biol. Cell* **92,** 477–494 (2000).

61. Hlady, V. & Buijs, J. Protein adsorption on solid surfaces. *Curr. Opin. Biotechnol.* **7,** 72–77 (1996).

62. Rabe, M., Verdes, D. & Seeger, S. Understanding protein adsorption phenomena at solid surfaces. *Adv. Colloid Interface Sci.* **162,** 87–106 (2011).

63. Nakanishi, K., Sakiyama, T. & Imamura, K. On the adsorption of proteins on solid surfaces, a common but very complicated phenomenon. *J. Biosci. Bioeng.* **91,** 233–244 (2001).

64. Cai, K. *et al.* Surface functionalized titanium thin films: Zeta-potential, protein adsorption and cell proliferation. *Colloids Surfaces B Biointerfaces* **50,** 1–8 (2006).

65. Xiao, S.-J., Textor, M., Spencer, N. D. & Sigrist, H. Covalent Attachment of Cell-Adhesive, (Arg-Gly-Asp)-Containing Peptides to Titanium Surfaces. *Am. Chem. Soc.* **14,** 5507–5516 (1998).

66. Zhu, M., Lerum, M. Z. & Chen, W. How To Prepare Reproducible, Homogeneous, and Hydrolytically Stable Aminosilane-Derived Layers on Silica . *Langmuir* **28,** 416–423 (2011).

67. Hanawa, T. An overview of biofunctionalization of metals in Japan. *J. R. Soc. Interface* **6,** S361–S369 (2009).

68. Morra, M. Biomchemical Modification of Titanium Surfaces: Peptides and ECM Proteins. *Eur. Cells Mater.* **12,** 1–15 (2006).

69. LeBaron, R. G. & Athanasiou, K. A. Extracellular Matrix Cell Adhesion Peptides: Functional applications in Orthopedic Materials. *Tissue Eng.* **6,** 85–103 (2000).

70. Kim, H.-E., Kim, H.-W. & Jang, J.-H. Identification and characterization of a novel heparin-binding peptide for promoting osteoblast adhesion and proliferation by screening an Escherichia coli cell surface display peptide library. *J. Pept.* **15,** 43 (2008).

71. García, A. J. & Reyes, C. D. Bio-adhesive Surfaces to Promote Osteoblast Differentiationand Bone Formation. *J. Dent. Res.* **84,** 407 (2005).

72. Arnold, M. *et al.* Activation of Integrin Function by Nanopatterned Adhesive Interfaces. *ChemPhysChem* **5,** 383–388 (2004).

73. Cavalcanti-Adam, E. A. *et al.* Cell Spreading and Focal Adhesion Dynamics Are Regulated by Spacing of Integrin Ligands. *Biophys. J.* **92,** 2964–2974 (2007).

74. Keselowsky, B. G., Collard, D. M. & García, A. J. Integrin binding specificity regulates biomaterial surface chemistry effects on cell differentiation. *Proc. Natl. Acad. Sci. U. S. A.* **102,** 5953–5957 (2005).

75. Deber, C. M., Madison, V. & Blout, E. R. Why cyclic peptides? Complementary approaches to conformations. *Acc. Chem. Res.* **9,** 106–113 (1976).

76. Sørensen, H. P. & Mortensen, K. K. Advanced genetic strategies for recombinant protein expression in Escherichia coli. *J. Biotechnol.* **115,** 113–128 (2005).

77. Gonzalez, M., Peña, J., Manero, J. M., Arciniegas, M. & Gil, F. J. Desing and Characterization of New Ti-Nb-Hf alloys. *J. Mater. Eng. Perform.* **18,** 490 (2009).

II

Materials and Methods

Chapter 2

Materials and methods

1. DESIGN OF A NI-FREE B-TITANIUM ALLOY

1.1 Alloy properties prediction

We started from an alloy designed by Marta González which composition is Ti-24.8Nb-16.2Hf-1Zr with an elastic module of 68GPa and shape memory properties[1,2]. This alloy was designed based on a property map (Fig. 17) developed by Milena Arciniegas[3] which was based on the properties map developed by M. Morinaga[4].

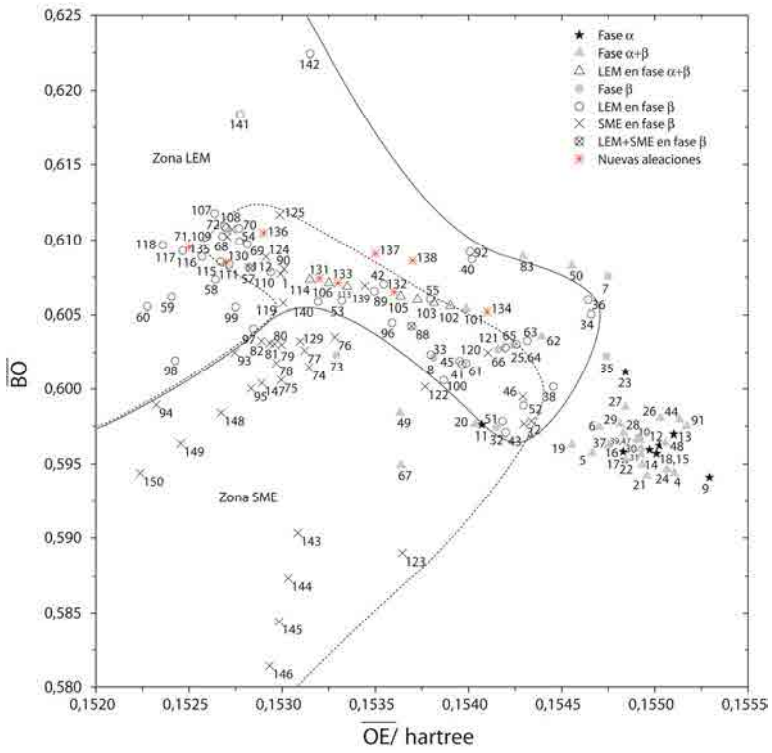

Fig.17 Alloy's properties map developed by Arciniegas3

The method designed by Morinaga is based on the effect of the alloying elements on the properties wanted to be predicted[5]. Two quantic parameters obtained from the calculations in a cluster using the "discrete Variational (DV)-Xα" were considered. These quantum parameters are the bond order (Bo) and the level of energy of the virtual orbital d (Md).

In view of the fact that the possible relation between the electronic affinity and the energy of the virtual orbitals not occupied is not well defined with the method conceived by Morinaga, Arciniegas implemented a new parameterization of the bond

order and the energy level. These new parameters are the bond order ($\overline{BO}$) and the orbital energy ($\overline{OE}$).

$\overline{BO}$ is the bond order calculated from a natural population analysis that presents a minimum dependence on the calculation basis chosen.

$\overline{OE}$ is the absolute value of the highest energy of the occupied molecular orbital centered in the alloying element known as HOMOAL.

$\overline{OE}$ values are expressed in atomic energy units, differing from the values of Md that are expressed in electron-volt, eV. The OE values calculated do not represent a parallel behavior with the values published by Morinaga.

Based on the chemical composition and BO and OE values shown, the $\overline{BO}$ and $\overline{OE}$ for each alloy were calculated with Eq.1.1 and Eq. 1.2, respectively.

$$\overline{BO} = \sum x_i(\mathrm{BO})_i \qquad \text{Eq. 1.1}$$

$$\overline{OE} = \sum x_i(\mathrm{OE})_i \qquad \text{Eq. 1.2}$$

According to the results obtained, the alloys with shape memory properties are in the range $0.4688 \leq \overline{BO} \leq 0.6117$; $0.1518 \leq \overline{OE} \leq 0.1543$. The alloys with low elastic modulus are in the range $0.5970 \leq \overline{BO} \leq 0.6224$; $0.1523 \leq \overline{OE} \leq 0.1546$. There is a range in which the BO and OE parameters for the shape memory and low elastic modulus properties are overlapped.

According to their position in the properties map, the high OE values and intermediate BO values mark out the region for α-phase alloys region on the map; whereas the low values of OE and a wide range of BO mark out the β-phase alloys region. Those alloys in which both phases coexist are scattered in the central area of the map (see Fig.17).

The basis alloy, Ti-24.8Nb-16.2Hf-1Zr, is located in the area of shape memory and low modulus according to Arciniegas' map. Each different chemical combination of the alloy was placed in the properties map (see Fig. 17).

The different alloy's composition is shown in Table 7.

Alloy	Formulation
1	Ti-20Nb-16.2Hf
2	Ti-22Nb-16.2Hf
3	Ti-23Nb-16.2Hf
4	Ti-26Nb-16.2Hf
5	Ti-27Nb-16.2Hf
6	Ti-29Nb-16.2Hf
7	Ti-24.8Nb-10Hf
8	Ti-24.8Nb-12Hf
9	Ti-24.8Nb-15Hf
10	Ti-24.8Nb-17Hf
11	Ti-24.8Nb-19Hf
12	Ti-24.8Nb-21Hf

Table 7. % w.t. of Nb and Hf for each alloy designed.

1.3 Fabrication process

The different alloys were fabricated from Titanium cp bars, Nb foil 99,8% purity and Hf shavings 99,7% from Sigma-Aldrich.

The raw material was set to make 20g buttons of the alloy. Before the melting of the buttons, the raw material was cleaned in an ultrasound bath for 3 minutes with acetone, ethanol and distilled water.

The buttons were melted in an arc melting furnace. Each button was melted 5 times and was turned 180ºC each time to avoid the segregation of elements and to homogenize the alloy. The buttons were then encapsulated, together with a piece of Ti cp2, in a quartz crystal capsule at vacuum atmosphere. The reason of add a Ti piece into the capsule is to reduce the oxidation of the material due to its great oxygen affinity.

The material was thermal treated above its β-transus temperature. Samples were homogenized at 1100ºC for 12ºC, followed by a solubilisation at 1100ºC for 1.5h and after that, quenched in water and ethanol at 0ºC. With such treatment a complete austenisation of the material was achieved and the metastable β-phase was retained.

2. MECHANICAL AND MICROSTRUCTURAL CHARACTERIZATION OF THE ALLOY

2.1 Nanoindentation

Nanoindentation[6] is a simple technique on which the forces applied are in the order of nano Newtons (nN) and the depth penetrations are in the order of nanometres. This technique is based on contact mechanics. The main objective of this kind of text is obtaining the elastic modulus and the hardness of a given material with unknown properties. One of the advantages of this technique is that it is a non-destructive assay and small samples are needed reducing costs.

The typical test consists on apply a stress on the indenter which is in contact with the sample surface. The load and the depth of indentation are recorded whilst the load goes from an initial value of zero to a maxim value and then returns to zero.

Depth indentation and indenter geometry give a direct measure of the contact angle at full loading. From this measurement, mean contact pressure can be obtained and therefore, material hardness. An estimation of the material elastic modulus can be obtained analysing the initial portion of the elastic response during unloading.

There is a great variety of indenter's geometry, although the spherical tip and the Berkovich tip are the most used for nanoindentation.

The determination of the contact area, the hardness and the elastic modulus is based on the Hertz elastic contact theory (Eq. 2.1).

$$P=\frac{4}{3}E^{*}\cdot\sqrt{R}\cdot\sqrt{h_e{}^{3}} \qquad \text{Eq. 2.1}$$

The most studied case and thus, the better know is the contact between a rigid sphere and a flat surface (Fig.18). According to Fisher-Cripps[6] approach, the maximum depth or total indentation (ht) is obtained at maximum load (Pmax). When this load is removed completely from the surface, a residual depth remains (hr). If maximum load is applied again, the loading is elastic until a distance (he) equal to the difference between the total indentation depth (ht) and the residual depth (hr). During the loading process

may be an elastic response at the beginning followed by an elastic-plastic deformation at high loads.

R is the radius of curvature combined with the indenter radius (Ri) and the radius of the residual indentation (Rr). This radius is higher than the indenter radius due to the deformation that takes place on it. E^* (Eq. 2.2) represents de effective modulus of the system, which combines the elastic properties of the indenter and of the sample under study taking into account the indenter's deformation.

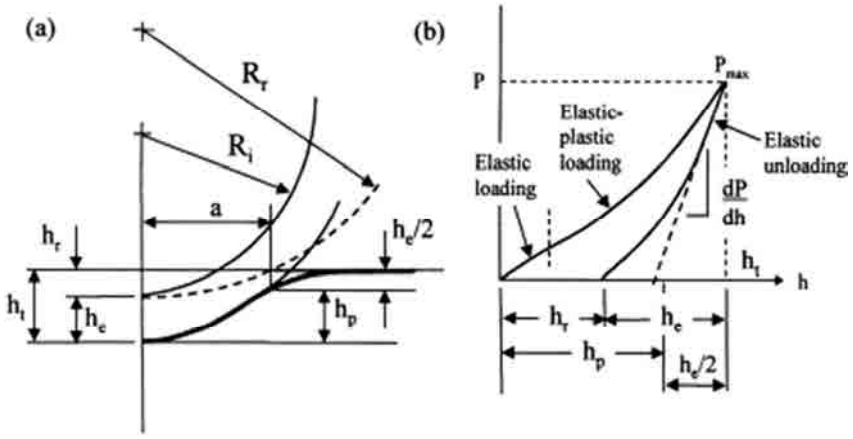

Fig.18 (a) Representation of the contact between a rigid spherical indenter and a flat surface. (b) Loading-displacement curve for an elastic-plastic sample loaded with an spherical indenter. Adapted from (14)

$$\frac{1}{E^*} = \frac{(1-\nu^2)}{E} + \frac{(1-\nu'^2)}{E'} \qquad \text{Eq. 2.2}$$

E and ν are the elastic modulus and the Poisson's coefficient of the material under study; E' and ν' are the elastic constants of the indenter. For a diamond indenter the values are 1140 GPa and 0.07, respectively.

The mean pressure contact is often called "indentation stress" and the relationship between contact area and contact radius (Eq. 2.3), "indentation deformation".

$$a = \sqrt{2R_i - h_p^2} \qquad \text{Eq. 2.3}$$

This relationship leads us to think in a response of similar nature than that obtained by means of a classic tensile test and compression test. In both cases a linear response is given for a totally elastic condition. Despite this, with nanoindentation it is possible to obtain data regarding the elastic-plastic properties of the material that cannot be obtained with the conventional tensile tests.

Depending on the parameters under study, different types of assay could be done.

To perform the experiments, 1mm thick slide of material was cut and mirror polished.

To determine the existence of phase transformation during loading and unloading process, 5 cycles of loading-unloading at an indentation depth of 300nm were done. To determine the elastic modulus and the hardness, 10 cycles of loading-unloading at an indentation depth of 2000nm were done. In this case, the first 100nm of the loading curve were taken and the resultant curve was fit with the Hertz curve.

2.2 Tensile testing

The tensile testing is the most commonly used method to determine different mechanical properties such as the Elastic modulus, the ultimate strength, elastic deformation, etc. One of the advantages of this test is its standardization that permits to achieve the most reliable results.

During the test, a cylindrical specimen is pulled for both sides until the sample changes its shape or fractures (Fig. 19).

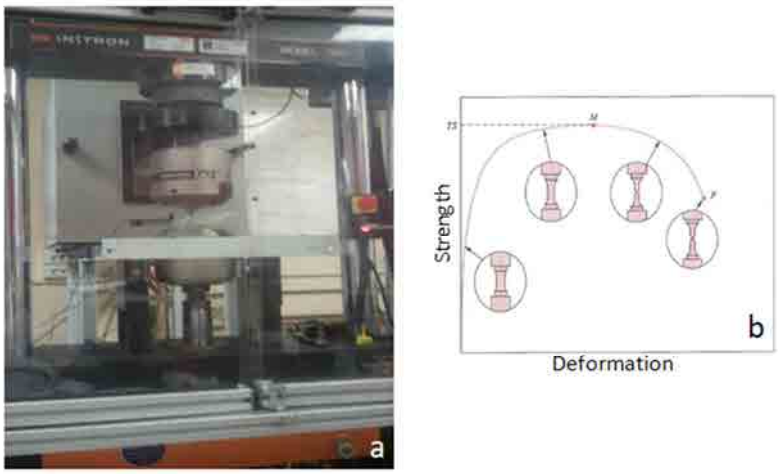

Fig.19 a) Image of the INSTRON 8500 DIGITAL CONTROL model 1342 used for testing. b) Evolution of the specimen test during tensile test[7].

Six samples were machined according to the ASMT E8M-04 standard (Fig. 20).

The tests were performed in an 8500 Digital Control testing machine model 1342 (Instron, Norwood, MA, USA). The specimens were pulled at $1.5 \bullet 10^{-4} s^{-1}$, according to the ASMT standard.

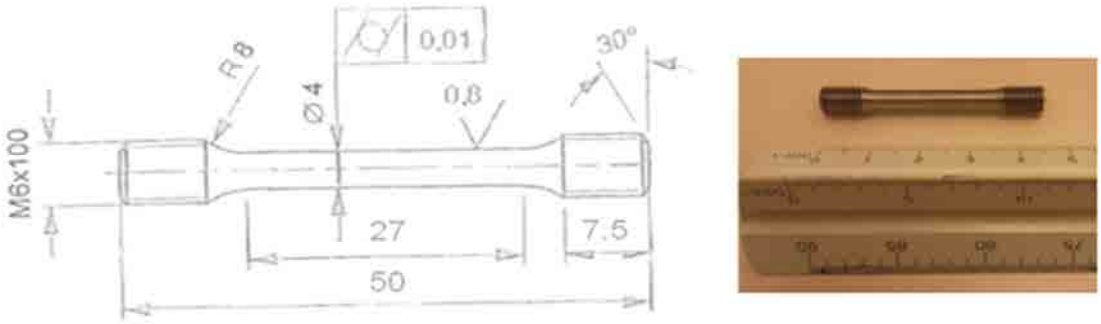

Fig.20 Dimensions of the tensile test specimen according to the ASMT E8M-04.

2.3 Optical microscopy

The determination of the grain size was carried out by means of a routine based on the ASTM E112 96 Standard Test Methods. The results were analyzed with Omnimet software (Buheler Company, Lake Bluff, IL, USA).

The alloy was cut into a 1mm thick slice and mechanically polished with colloidal silica suspension achieving a mirror polished surface. The etching of the samples was carried out using Kroll's reactive which composition is HF (48%), and HNO_3 (65%) in an aqueous solution.

A GX51 microscope (Olympus Corporation, Orangeburg, NY, USA) was used to study the microstructure of the material. Images were taken in a digital format and processed to eliminate the artifacts due to spots, corrosion points or polishing gridding pores, since these artifacts may lead to an error during the routine. To process the images the grain borders were drawn, then the background color was determined as well as the area to process. The outside frame was cleared out and the border grain eliminated. After that, the bit plane was thickened, filled and featured.

2.4 Transmission electron microscopy (TEM)

This technique is based on Bragg's Law. The source of light is an electron beam generated by a heated tungsten filament. The beam is exposed to a high voltage and accelerated. Beam's current density spans a range between 100 and 200 keV.

The beam passes through an ultrathin material sample. When trespassing, the electron beam interacts with the sample. Some of the electrons are absorbed and others are dispersed, loosing velocity and changing the trajectory. To visualize the electron beam after it passed through the sample, a magnetic lens is used. With the lens, the beam is focused, magnified and projected on a fluorescence display.

The dark field images are generated from the diffracted electrons and the bright field images are obtained from the electrons that have passed through the sample.

The samples to be studied must be transparent to the electron beam, between 10 and 500 nm thick, in order to obtain valid results.

TEM technique allows the possibility to obtain the diffraction patterns of selected areas of the sample. The existing diffraction patterns and the net parameters of the structures, permit to index the diagrams obtained. In other words, TEM allows us to know the crystallography of the material under study.

The microscope used was a JEM 1200 EXII (JEOL, Tokyo, Japan) (Fig.21) with a beam power of 120 kV and a calibrated chamber constant of λL=2.606 mm·nm. The chamber constant was calculated by TlCl powders (CsCl type, a=0.3841 nm).

Fig.21 a) Microscope JEOL 1200 EXII used in the assay. b)Electropolishing equipment Tenupol-3 by Struers. c) Sample after the electropolishing ready to be used in the TEM.

The alloy was cut into a 1 mm thick slice and mechanically polished with a 240 paper grid achieving a 100 µm thickness. Afterwards, 3mm diameter discs were die-cast with a Model 659 Disc Punch (Gatan, Inc. Pleasanton, CA, USA). Once the discs were cut, they were polished by the jet-polishing method with a Tenupol-3 equipment (Struers, Denmark) at 10ºC and at a voltage of 40 V. The electrolyte used was composed by 40% 2-butoxyethanol, 40% methanol and 10% mL perchloric acid in an aqueous solution. The jet polishing technique enables de polishing of metal disks simultaneously from both sides and automatically stops the polishing operation when perforation occurs.

2.5 X-Ray diffraction

The non-destructive X-Ray diffraction technique was used to determine alloy's crystallography.

When a laser beam comes into contact with a crystalline material, the beam diffraction takes place. By means of Bragg's Law ($n\lambda=2d\text{sen}(\theta)$ the X-Ray diffraction wave length and the interatomic distance are related with the incidence angle of the diffracted beam (Fig. 22).

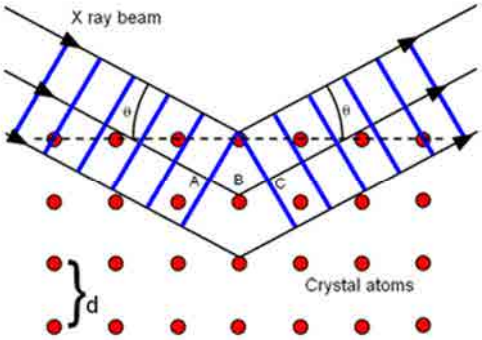

Fig.22 Scheme of the X-ray beam diffraction on a crystalline material and the relation with the inter-atomic distance. Adapted from http://tap.iop.org

Fig.23 Equipment used in the X-ray diffraction assays. Difractometer D8 Advance from Brueker.

The alloy was cut into a 1mm thick sheet of and polished for one side with a 1200grit paper. It is important that the samples have parallel sides for the proper running of the technique.

The samples were analyzed using a Difractometer D8 Advance (Bruker) equipment (Fig. 23). A Cu K_α (λ=1.542Å) radiation was applied because the wave length is similar to the distance between planes in the crystalline net. Measurements were taken with a step size of 0.05º and with an intensity normalized to the time of counting (counts per second). The Power Diffraction File (PDF) data base was used to identify and to index the phases present in the alloy. In the PDF the diffraction patterns of known materials are compiled and the crystalline structure, reticular parameters and diffraction plains are

detailed. The indexation of the phases is done by direct comparison between the PDF's spectra and the ones obtained experimentally. Due to the novelty of the alloy there are no diffraction patterns available. The patterns used where those from Ti (α and β), Nb and a quenched TiNb alloy with up to 12% content of Nb.

3. PHYSICO-CHEMICAL CHARACTERIZATION OF THE ALLOY

Some studies suggest that the type, quantity and conformation of the adsorbed proteins on a material, are influenced by the underlying substrate[8–10]. In other words, surface energy, roughness and chemistry are involved in the proteins adsorbed and thus, in the subsequent cell adhesion.

In this section, the different methods used to determine the physic-chemical properties of the developed alloy are described.

3.5 Contact angle

The solid surface tension of a given material can be determined by different methods, but one of the most extended ones is the contact angle.

The strong points of this method are the simplicity, the small volume of liquid needed and an accuracy of approximately ±2º. But it also possess weak points as the small angles are difficult to measure, the measurement relies on the consistency of the operator to assign the tangent line and impurities onto the surface of the sample can alter the measurements[11,12].

The technique is based on Young's equation. Young described in 1805 the contact angle of a liquid drop on an ideal solid surface by the mechanical equilibrium of the drop under the action of three interfacial tensions:

- γ_{lv}: liquid–vapor γ
- $_{sv}$: solid–vapor
- γ_{sl}: solid–liquid

Θγ is the so called Young's contact angle (Fig.24)

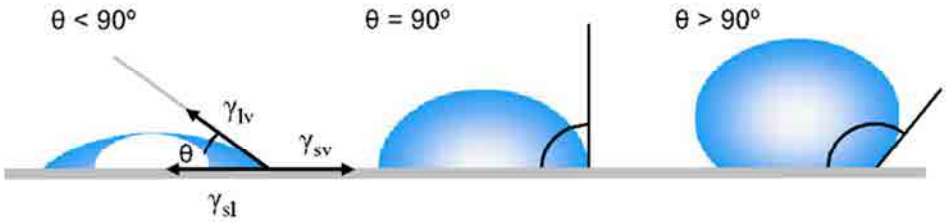

Fig.24 Representation of the angles formed between a liquid drop and a solid surface. Adapted from[12]

According to this, there is a correlation between the contact angle and the interfacial tensions (Eq. 1.1), but only two parameters can be measured; the contact angle and the liquid-vapor phase tension.

$$\gamma_{lv} \cos \theta\gamma = \gamma_{sv} - \gamma_{sl} \qquad \textit{Eq.3.1}$$

There are different methods that correlates contact angles with the surface energy of the sample[11]. In this thesis, the Owens and Wendt approach was used. According to Owens and Wendt, dispersion and hydrogen bonding forces may operate on a surface and the surface tension is being composed of two components: dispersive surface tension (γ^d) and surface tension due to hydrogen and dipole-dipole interactions (γ^h).

$$\gamma = \gamma^d + \gamma^h \qquad \textit{Eq.3.2}$$

Taking into account the forces that operate at the surface they postulated:

$$\gamma_{sl} = \gamma_s + \gamma_l - 2\sqrt{\gamma_s^d \gamma_l^d} - 2\sqrt{\gamma_s^h \gamma_l^h} \quad \text{Eq.3.3}$$

If equation 1.3 is combined with equation 1.1, the following relationship is obtained:

$$\gamma_l (1 + \cos \theta_\gamma) = 2\sqrt{\gamma_s^d \gamma_l^d} - 2\sqrt{\gamma_s^h \gamma_l^h} \quad \text{Eq. 3.4}$$

In equation 1.4 there are two unknown parameters: γ_s^d and γ_s^h, thus be having one equation with two unknown quantities. Is because of that, two different liquids should be used to make the contact angle measurements for the same surface. Having the

contact angle of the same material for different liquids, two simultaneous equations could be solved.

The equipment used to perform the assays was an *Oca 15+ (Dataphysics, Filderstadt, Germany)* (Fig. 25). It is provided with a horizontal stage to place the samples, an illumination source and a telescope with an incorporated protractor and a camera to take photographs of the drop profile.

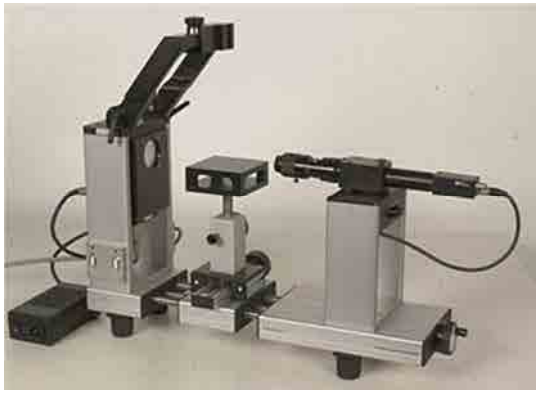

Fig.25 Contact angle measurement equipment Oca15+ from Dataphysics (www.dataphysics.de).

The materials tested were Ti cp, Ti6Al4V and the developed alloy in the thesis. All of them were cut into 2 mm thick discs and were mirror polished. Measurements were done in triplicate using three discs for each material type.. All measurements were made the same day and under the same conditions. The liquids used for the measurements were MilliQ water and Diiodomethane (Sigma-Aldrich, Germany). Droplets of 3 μl were dispensed at a speed of 1 μl/s.

Results were analyzed using the SCA20 Software (Dataphysics).

3.6 Zeta Potential

The electric surface properties of the material are the result of the chemistry and the ion distribution at the diffuse interface between substrate and solution. The ζ-potential, the scientific term for electrokinetic potential, is widely used for quantification of the magnitude of the electrical charge at the double layer. .

The technique used for ζ-potential quantification is based on the charge displacement in an electric double layer caused by an external force shifting the liquid phase tangentially

against the solid. Due to charge density, an electric field is formed drawing oppositely charged ions towards it and driving like-charged ions away.

The electrical double layer is the net charge density on a microfluidic substrate in contact with an aqueous solution. The net charge density is defined by equilibria reactions as protonation, deprotonation, adsorption and others.

The electric double layer is modeled based on the Gouy-Chapman Stern model. According to this model, the electric double layer is comprised of a diffuse layer and a Stern layer (see Fig. 26). The Stern layer is a layer of anions that attach to a charged surface. These ions are temporally bound and screen the surface charge.

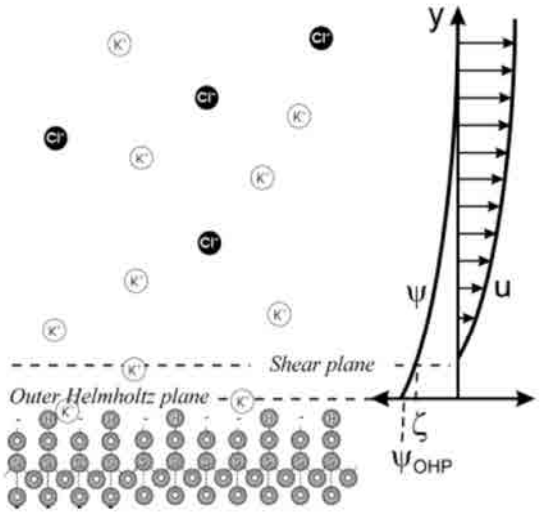

Fig.26 Conceptual representation of the electrical double layer at the intereface of silica and a weak KCl solution. ψ is the local potential. OHP is the outer Helmholtz plane. u is the local electroosmotic velocity. Shielding of this surface charge occurs due to adsorbed ions inside the OHP and by mobile ions in a diffuse layer. The shear plane is where hydrodynamic motion becomes possible. ξ is the potential at this plane. Extracted from[13]

There are three different methods to measure ζ-potential:

- Measuring the electrosmotic mobility.
- Measuring the streaming current of streaming potential generated by pressure-driven flow through a conduit.
- Measuring the response of a small spherical particle in an applied electric field.

In this thesis the streaming current of streaming potential generated by pressure-driven flow through a conduit was measured. A KCl 1mM electrolyte was forced to flow directly through a small gap formed by two sample surfaces with pressure. The equipment used was a SurPASS Electrokineic Analyzer for Solid Samples (Anton Paar GmbH, Graz, Austria). The calculations were made according to the Fairbrother-Mastin equation (Eq. 3.5). The materials tested were Ti cp, Ti6Al4V and the developed alloy in the thesis. All of them were cut into 2 mm thick discs and mirror polished.

$$\zeta = \frac{dU}{dp} \cdot \frac{\eta}{\varepsilon \cdot \varepsilon_0} \cdot k \quad \text{Eq. 3.5}$$

3.7 Corrosion resistance

When an implant or a medical device is placed into the body immediately interacts with body fluids. The body environment is very aggressive for the implant due to the presence of cations, anions, organic acids and proteins. The degradation products due to corrosion might be hazardous to body environment[14–21]. Hence the determination of the corrosion resistance of any new developed alloy is very important.

In medical devices different types of corrosion may occur:

Crevice corrosion: occurs in confined spaces to which the access of the working fluids from the environment is limited such as beneath the heads of fixing screws.

Pitting corrosion: occurs when the corrosion penetrates the mass of the metal with limited diffusion ions digging a hole. This type of corrosion is typical in the oral cavity due to the greater availability of oxygen and acidic fluids.

Fretting corrosion: is induced under load and in the presence of repeated relative surface motion as in load bearing metallic orthopedic implants such as the interface modular connection between implant components or the bone-stems interface.

To determine the corrosion resistance of the studied material, open circuit potential and cyclic voltammetry assays were conducted according to the ISO 10993-15:2009 Biological evaluation of medical devices standard.

Open circuit potential: is the potential of the working electrode relative to the reference electrode when no potential or current is being applied to the cell.

Cyclic voltammetry: the electrode potential is raised to a more negative potential and then, decreased in a reverse back to the starting voltage. These assays permit to establish the current intensity circulating through the material at different applied electric voltage ranges.

The equipment used for the assay was a *Parstat 2273 Advanced electrochemical system* potentiostat (Princeton Applied Research, Oak Ridge, TN, USA) controlled by the *PowerSuite* software (Princeton Applied Research). A Faraday cage was used to shield the test cell of interferences due to the presence of other equipment near the set up (Fig. 27).

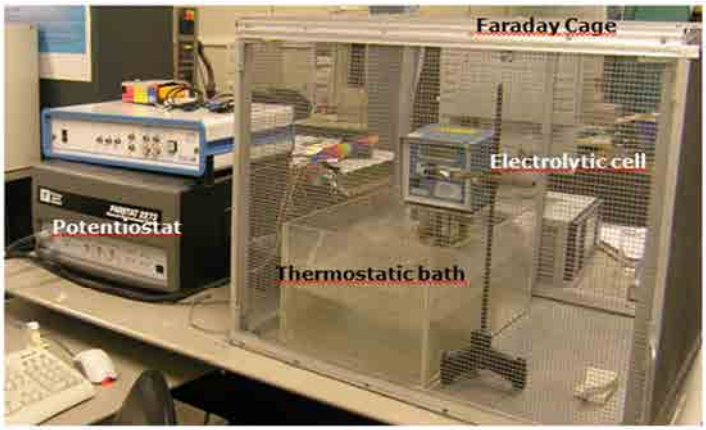

Fig.27 Set up used for the corrosion assays.

The materials tested were Ti cp, Ti6Al4V and the developed alloy in the thesis. All of them were cut into 2 mm thick discs and mirror polished.
A piece of electric cable was glued with colloidal silver to the unpolished face of the samples and isolated with Poly(methyl methacrylate) (PMMA). The area of the mirror polished face was 0,8 cm^2.

The electrolyte used to perform the tests was *HBSS Hank's Balanced Salt Solution* (Sigma-Aldrich). This solution mimics body environment in which the material will be implanted. In table 8 the composition of the electrolyte is detailed.

Chemical	Concentration (g/l)
$CaCl_2$ - H_2O	0.18
KCl	0.4
KH_2PO_4	0.06
MgO_2 - $6H_2O$	0.08
$MgSO_2$ – $7H_2O$	0.7
NaCl	8
$NaHCO_3$	0.35
Na_2HPO_4	0.48
D-glucosa	1

Table 8. Chemical composition of the *HBSS Hank's Balanced SALT Solution* (Sigma-Aldrich).

The electrolyte was kept at 37ºC during the assay using a thermal bath. For each experiment, the electrolyte was renewed.

In Fig.28 the scheme of the electrolytic cell set up during the assays is showed. As a reference electrode a saturated calomel electrode (SCE) was used. A graphite bar was used as cathode and the material to be studied was used as anode.

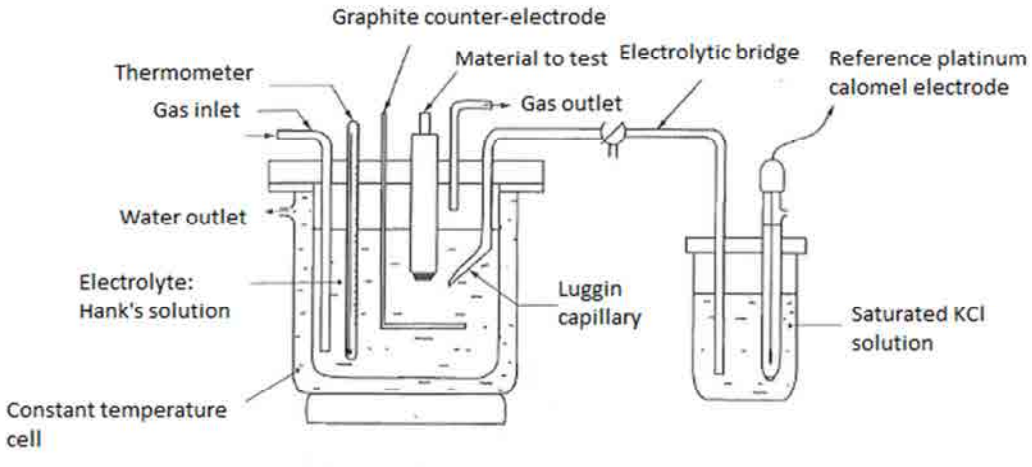

Fig.28 Schematin set up of the electrolytic cell during the assays. Adapted from ISO 10993-15:2009 Biological evaluation of medical devices standard.

Open circuit assays were performed for 3 hours with the purpose to study the system stability and check the proper preparation of the samples. During the assay, the evolution of the difference in the electric potential between the sample and the reference electrode subjected to time was recorded. The system was assumed as stabilized when the potential remained stable for 30 minutes with variations no higher than ±2 mV. This value of potential was used as the open circuit value.
The cyclic voltammetry assays were conducted incrementing the voltage from -0.3 to 4 V at a constant velocity of 1mV/s. After that the voltage was reversed back to the starting value.

4. SYNTHESIS OF THE RECOMBINANT FRAGMENTS OF FIBRONECTIN

4.1 RNA extraction and reverse transcription

4.2.1 RNA extraction

For being able to synthesize the desired fribronectin fragments, first of all the mRNA has to be isolated. The mRNA could be obtained from animal cells, animal tissue, bacteria or yeast. In our case, the mRNA was extracted from SAOS-2 cells, a cell line derived from a human osteosarcoma.

To extract the mRNA from SAOS-2 the RNeasy® Mini Kit (Qiagen, Maryland, USA) was used. The kit allows us to obtain up to 100 µg of mRNA from a small sample of material.

The technique combines in one hand the linkage properties of the silica membranes and on the other hand the speed of the micro centrifugation technique. The process is performed by means of the addition of buffers facilitated on the kit and following centrifugations.

The first process step is to lyse and homogenize the samples. For this purpose 600 µl of buffer containing Thiocynate of Guanidine was used. This compound is highly denaturing, inactivates the RNases and this way secures the intact RNA purification

With the aim of conditioning the sample for membrane adhesion, ethanol is added to the RNeasy® mini spin column. By means of a centrifugation the mRNA is adhered to the membrane and the waste pass through it and remains on the collector tube.

After several washes with manufacturer's provided buffers, a high quality mRNA remains in the membrane. The mRNA was eluted with 30 ul of RNase-free water.

Once de mRNA is purified it is necessary to know its concentration and purity with the aim to determine the quantity required in further processes. that the mRNA was quantified using the Nanodrop ND-1000 Spectrophotometer (Thermo Scientific, Massachusetts, USA). The Nanodrop is a spectrophotometer able to measure wave lengths (λ) from 220nm to 750nm. For nucleic acids the wave length used was λ=260 nm.

In addition, the purity of the sample can also be measured. Two ratios have to be taken into account: the 260/280 ratio and the 260/30 ratio.

- Ratio 260/280: is used to assess the nucleic acids purity. For pure DNA the ratio is approximately 1.8 and for pure RNA is approximately 2.0. The ratio is also used to assess protein contaminations.
- Ratio 260/230: is used as a secondary measure of nucleic acid purity. This value is often higher than the value obtained for the ratio 260/280. The expected values are commonly in the range of 2.0-2.2. Lower values of this parameter indicate sample contamination due to carbohydrates, phenols, HCl, ethanol etc.

4.2.2 RNA reverse transcription

The reverse transcription is based on the replication process of retroviruses. The process allows the generation of complementary DNA (cDNA) from an RNA template using a reverse transcriptase enzyme. The obtained cDNA can be used for molecular cloning, amplification, etc.

The QuantiTect Reverse Transcription kit (Qiagen) was used to obtain cDNA from mRNA. 1.12 µl of purified RNA were incubated in 2 µl of gDNA Wipeout buffer at 42ºC for 2 minutes with the aim to eliminate the genomic DNA. Then, it was mixed with 3 µl of Master Mix buffer, 1 µl of Quantiscript buffer and 1 µl of RT primer mix in

order to set the RT reaction. Retrotranscription was performed at 42ºC during 15 min and was inhibited at 95ºC for 3 min. The obtained cDNA was stored at -20ºC.

4.3 Primers design

The DNA sequences used to amplify the FNIII 8-10 and the FNIII 12-14 of Homo sapiens fibronectin were obtained from the nucleotide NCBI database (www.ncbi.nlm.nih.gov/). Primers were selected from the *Universal ProbeLibrary* by Roche (www.roche-applied-science.com) and ordered to *Invitrogen*.

For each fragment, CAS or HB II, the primer, the reading frame, the target, the added of the starting frame and the riding frame are given.

A cleavage site was added to both fragments. The cleavage site was cut by the restriction enzyme forming the sticky ends, thus the DNA sequence was inserted in the plasmid. With the aim to allow the restriction enzyme to attach and cut the target, two nucleotides were added. It is important not to lose the reading frame of the protein of interest after any of the previous DNA sequence modifications. In Fig. 29 and Fig. 30 the final sequence obtained for each CAS primer and HB II primers after the nucleotides addition is shown, respectively.

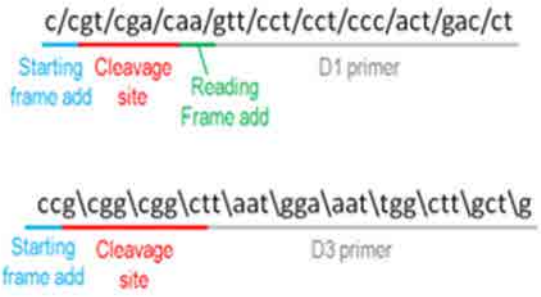

Fig.29 Primers D1 and D3 corresponding to the CAS sequence with the starting frame add, the cleavage site and the reading frame add.

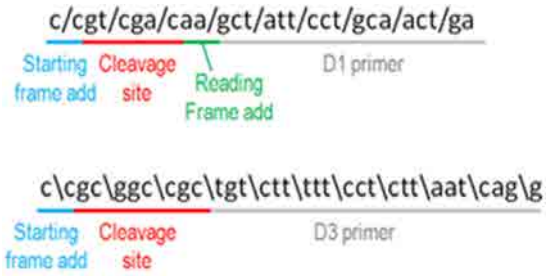

Fig.30 Primers D1 and D3 corresponding to the HB II sequence with the starting frame add, the cleavage site and the reading frame add.

4.4 PCR amplification

The polymerase chain reaction (PCR) is a biochemical technology in molecular biology to amplify a single or a few copies of a piece of DNA across several orders of magnitude, generating thousands to millions of copies of a particular DNA sequence.

Fig.31 Equipment to conduct the polymerase chain reaction.

The AmpliTaq Gold® 360 Master Mix (Invitrogen) was used. The kit contains thermostable polymerase, nucleotides, etc at the proper concentration and an enhancer called 360GC Enhancer.

Basically PCR consists in three steps: denaturation, annealing and extension.

Denaturation is a process that must not take more than 30 seconds and is initiated at a temperature of 95ºC. During this step, the DNA is opened and rendered in a single strand.

Anealling is the process on which the two primers bind the appropriate complementary strand. The temperature for this step varies depending on the size of the primer and its nucleotide sequence. The annealing temperature can go as high as 72°C. There is a temperature, called melting temperature, at which the 50% of the primer stops to attach the DNA, but it is not the temperature at which the primer is actually totally attached to DNA. In our case, the annealing temperature for each fragment was chosen regarding the melting temperature of the corresponding primer. For the CAS the annealing temperature was 70ºC and for the HB II, 67ºC.

Once the annealing is completed the **extension** starts. The primers act as a mold to start the extension process. During the extension phase, the fragment corresponding to the target is amplified. The reaction took place at 72ºC because it is the optimal working temperature of the Taq polymerase.

Three identical reactions were prepared for the PCR amplification. Each reaction was prepared mixing 25 µl of AmpliTaq Gold 360 Master Mix, 1 µl of each primer needed and 1 µl of DNA in aqueous solution.

The PCR cycle was conducted following the supplier's advice. In Tab. 9 the cycles, times and temperatures of the process are shown. During the cycling phase, the first 5 cycles were done at 65ºC to amplify the DNA fragment without the restriction target, the following cycles were done at 70ºC and the target and the DNA were both amplified.

State	Step	Temperature	Time
Holding	AmpliTaq Gold 360 Master Mix polymerase activation	95ªC	10 min
Cycling (40 cycles)	Denaturation	95ºC	30 s
	Annealing	65ºC	30 s
	Extend	72ºC	60s/kb
	Denaturation	95ºC	30 s
	Annealing	70ºC	30 s
	Extend	72ºC	60s/kb
Holding	Final extend	72ºC	7 min
Holding	Final hold	4ºC	∞

Table 9. Table with the cycles, times and temperatures of the PCR cycle for each step or the reaction.

4.4.1 Verification of the PCR amplification

The amplification of the different fragments was verified by electrophoresis. The electrophoresis permits to separate DNA molecules by weight. This method is based on the dynamics of proteolytic solutions[22]. The negative charge of the sugar-phosphate backbone of DNA is the cause of its migration towards the anode when a voltage is applied. The mobility of the DNA depends on molecule's size; longer molecules migrate more slowly because they experience more resistance within the gel. Because the size of the molecule affects its mobility, smaller fragments end up nearer to the anode than longer ones in a given period[23].

Electrophoresis was carried out in an acrylamide gel. These types of gels are formed by hydrogen bridges when they are in a cold aquose solution. The pore size depends on the acrylamide concentration and is inversely proportional to gel concentration. Molecules pass through the pores, thus it is of paramount importance to know the type of molecule to analyze. For low molecular weight molecules it is needed a high concentrated gel, whilst for high molecular weight molecules a low concentrated gel is needed.

The device used was a mini-PROTEAN 3by Bio-Rad.

The gel was at a concentration of 6% and was composed by acrylamide, TBE5X (0.445 M Tris-borate, 0.01 M EDTA at pH 8.2), distilled H_2O, TEMED and APS 10%. The

APS is the polymerizing agent and the TEMED is the reaction catalyst. A comb with wells was placed and the gel was set up for 30 min. .

The 10 µl of the PCR result were mixed with 1.1 ul of Blue Juice Gel Loading Buffer. This buffer contains bromophenol blue in order to monitor the electrophoresis. The dye has a slight negative charge in a moderated pH migrating in the same direction but faster than DNA.

The 100 bp DNA Ladder (Invitrogen) was used to identify the approximate size of the sample fragments. This molecular-weight size marker consists in 15 fragments from 100 to 1500 bp in multiples of 100 bp and an additional fragment of 2072 bp. The 600 bp band is 2 to 3 times more intense than the rest of the bands with the aim to give internal orientation. The ladder is not for quantification.

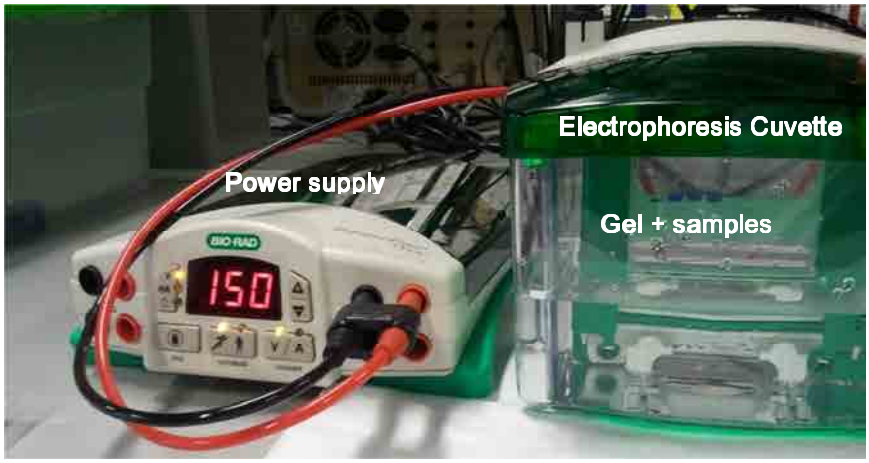

Fig.32 Set up for the electrophoresis assay.

The samples and the ladder were loaded into separate gel wells and electrophoresis was run at 150V in a Mini-Protean® 3 Cell (Bio-Rad) with no time set up.
The gel was stained with A dilution of 5µl SYBR® Safe DNA Gel Stain (Invitrogen) in 50 µl of TBE 1x and visualized with Gel DocTM XR+ Molecular Imager (Bio-Rad, California, USA).

4.4.2 Purification of the PCR amplification

During the amplification process the DNA as well as the primers was amplified. The components of the PCR such as primers, dNTPS, enzymes, salts, etc. must be eliminated, if not the plasmid might insert them and avoid the correct replication of the DNA.

The QIAquick PCR Purification kit (Qiagen) was used to carry on the purification.

The kit combines the technology of spin columns with the properties of the selective union to a silica membrane specifically designed for that purpose. The kit also has specific buffers optimized for an efficient recovery of DNA and elimination of contaminants. The DNA is absorbed by the membrane at high salt concentration whilst the contaminants pass through de column. The impurities are eliminated and the pure DNA is eluted in Tris buffer or water.

140 µl of the PCR product were mixed with 700 µl of PB buffer from the kit and added to the columns provided with the kit. The mixture was centrifuged and washed on-column several times following the manufacturer's instructions. Finally, 30 µl of EB buffer (10 mM Tris·Cl, pH 8.5) was added to the column and incubated for 1min at room temperature and centrifuged. The resulting 30 µl were the purified PCR product.

5. FRAGMENTS CLONNING PROCEDURE

5.1 E.coli transformation

5.1.1 E. coli strains used

On this thesis two different strains of E.coli were used:

- MAX Efficiency® DH5α™ Competent Cells
- One Shot® BL21 Chemically Competent E. coli, both from Invitrogen.

The MAX Efficiency® DH5α™ Competent Cells were used as libraries to amplify the inserted DNA.

The One Shot® BL21 Chemically Competent E. coli were used to express the proteins. This strain is deficient in proteases, reducing the degradation of the heterologous proteins expressed.

5.1.2 Plasmid

The cloning was carried out using plasmids, also called vectors. A plasmid is a synthetic small circular double helix molecule of DNA derived from larger plasmids that are formed naturally in bacterial cells[24].

Plasmids replicate independently of bacterial chromosomes. This means that are unnecessary for bacteria, but they might provide selective advantages. These intrinsic characteristics of plasmids make them an important tool in molecular biology, especially in genetic engineering. One application is recombinant proteins production. Since the plasmid replicates independently of the bacterial DNA, it is possible to obtain numerous copies of the DNA recombined molecule.

The plasmid used in this thesis was a pGEX-6P-1 (GE Healthcare, New Jersey, USA) (Fig.33). This plasmid has an ampicillin resistance marker, which confers resistance to 100 μg/ml ampicillin. Expression is under the control of the *tac* promoter, which is induced by the lactose analog isopropyl b-D thiogalactoside (IPTG). The plasmid is also engineered with an internal *lac*Iq gene. The *lac*Iq gene product is a repressor protein that binds to the operator region of the *tac* promoter, preventing expression until induction by IPTG (Isopropyl β-D-1-thiogalactopyranoside**)**, thus maintaining tight control over expression of the insert. In addition to offering chemically inducible, high-level expression, the plasmid allows mild elution conditions for release of fusion proteins from the affinity medium. Thus, effects on antigenicity and functional activity of the protein are minimized. The pGEX-P1-6 encodes the recognition sequence for site-specific cleavage by PreScission Protease, between the GST domain and the multiple cloning site.

Cleavage of pGEX-6P GST fusion proteins occurs between the Gln and Gly residues of the recognition sequence Leu-Glu-Val-Leu-Phe-Gln-Gly-Pro. Low temperature (5°C) digestion minimizes the degradation of the protein of interest. Because PreScission Protease has been engineered with a GST tag, it can also be removed from the cleavage mixture simultaneously with the GST portion of the fusion protein. The pGEX-6P

plasmid permits convenient site-specific cleavage and simultaneous purification on Glutathione Sepharose. The pGEX-6P series provides all three translational reading frames linked between the GST coding region and the multiple cloning sites.

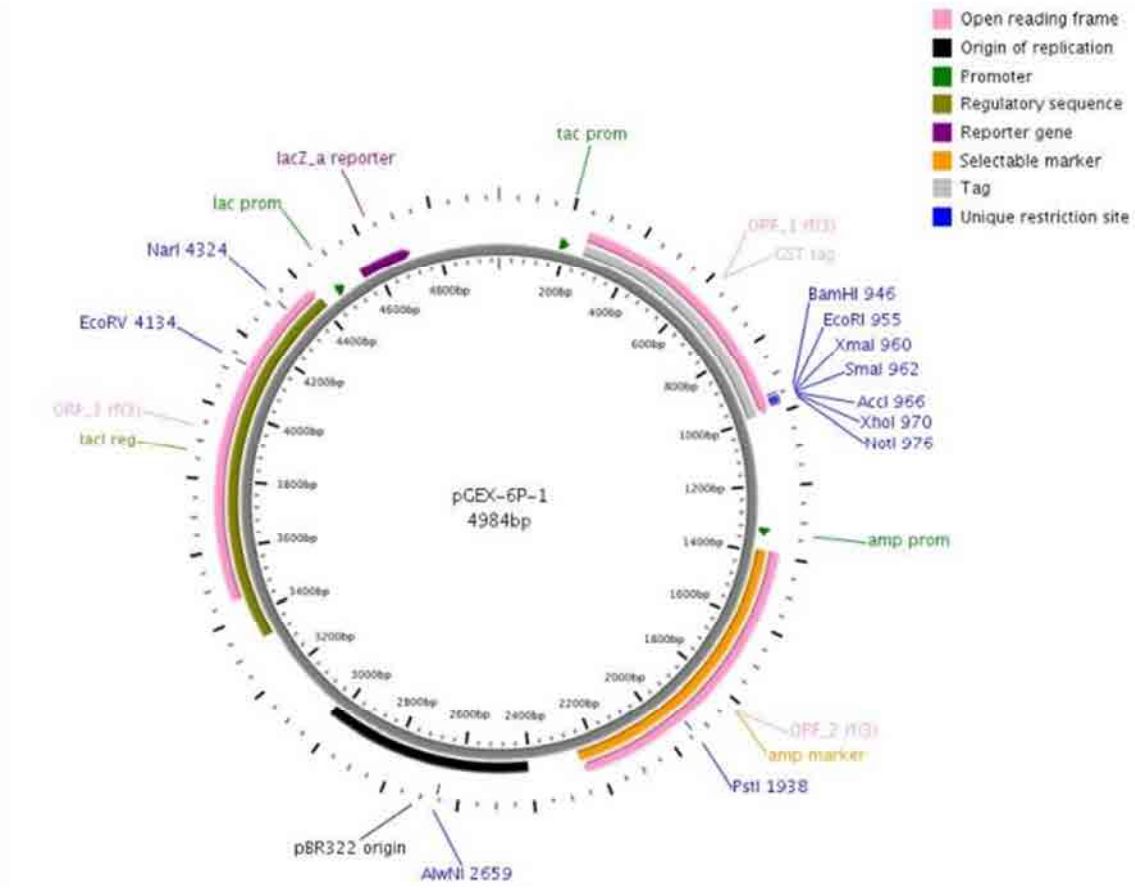

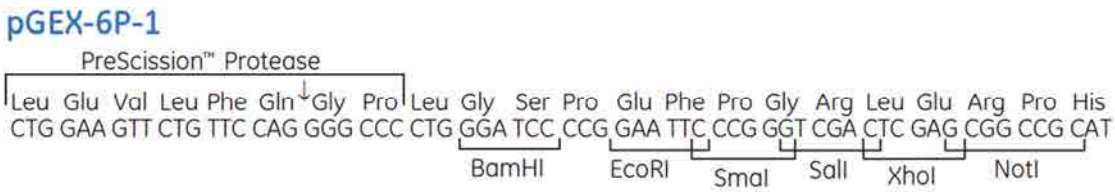

Fig.33 Map of the p-GEX-P6-1 glutathione S-transferase fusion plasmid showing the reading frames and main features. Adapted from www.gelifesciences.com

5.1.3 Plasmid and DNA digestion

In order to the plasmids to be used as a vector in the ligation it is important to cut the circular sequence with a restriction nuclease obtaining thus, a linear DNA molecule. This process is called digestion.

The same process is used for DNA. The DNA is cut with the same restriction enzyme in order to obtain the desired fragments for cloning.

The plasmid was digested by mixing 1ug of plasmid with 1 µl of SalI, 1 µl of NotI, 7 µl of NE Buffer 3, 0.7 µl of BSA. The mixture was incubated at 37ºC for 2h.

The DNA was digested adding to the 30 µl purified PCR, 1 µl of SalI, 1 µl of NotI, 7 µl of NE Buffer 3, 0.7 µl of BSA. The mixture was incubated at 37ºC for 2h.

After plasmid and DNA digestion, purification is needed with the aim to eliminate the fragments cut during digestion. The purification process was the same described in section 4.4.2. The aim of this purification is to eliminate the small target fragments which might be ligated again avoiding the fragment and plasmid ligation; the restriction enzymes, the buffer, etc.

5.1.4 Plasmid and DNA ligation

Once the DNA and the plasmid were purified, the ligation between them was carried out. In Tab. 10 the combinations of the different reaction mixture for ligation are shown.

COMBINATION 1	**COMBINATION 2**	**COMBINATION 3**
2 µl plasmid	3 µl plasmid	3 µl plasmid
2µl DNA	2 µl DNA	3 µl DNA
3 µl ligase buffer 1 µl ligase 22 µl H_2O RNAse free	3 µl ligase buffer 1 µl ligase 21 µl H_2O RNAse free	3 µl ligase buffer 1 µl ligase 20 µl H_2O RNAse free

Table 10. Quantities of each element that participate in the ligation for three different conditions.

When DNA and the plasmid get into contact they anneal through the sticky ends. After that, the DNA fragment and the plasmid are linked covalently by means of the T4 DNA Ligase (Roche, Manheim, Germany). The different combinations were left at 4ºC over night to alloy the reaction to took place. After that, all of them were mixed resulting in one reaction.

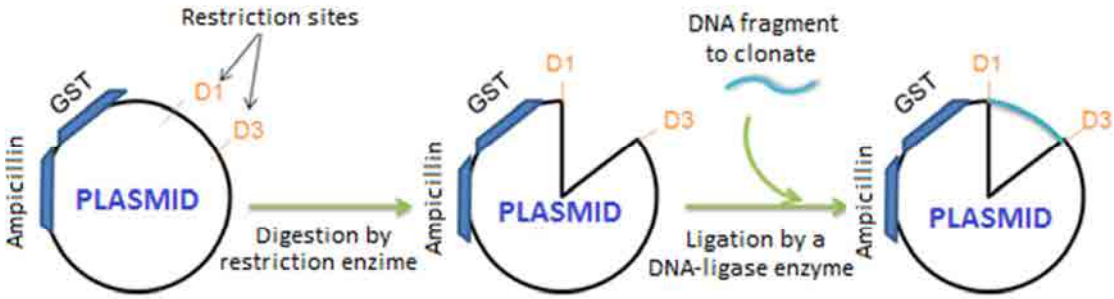

Fig.34 Scheme of the annealing mechanism between the plasmid and the DNA fragment.

5.1.5 Transformation of the E.coli with the result of the Plasmid and DNA ligation

Transformation is the incorporation of exogenous genetic material (e.g. plasmid with an inserted DNA fragment) into bacteria.

Transformation is a basic technique used in molecular biology. It consists of two phases:

- Union of the extracellular DNA with the cell.
- Insertion of the extracellular DNA into cytoplasm.

Some bacteria made this process naturally, although it is not frequent. To carry on the process in an artificial way, or in a forced way, a thermal shock was used.

When the bacteria (E. coli in this case), gets into contact with the DNA (in this case, ligations), the DNA binds to lipopolysaccharides receptors on the cellular surface. The application of a heat shock is conducted, the sample changes from 0ºC to 42ºC and a release of cell surface lipids takes place. This transport of lipids opens pores on the cell membrane and the DNA pass through the pores to the cytoplasm. After that, the sample is cooled to a 0ºC making the open pores of cell membrane to disappear (26).

5.1.5.1 MAX Efficiency® DH5α™ Competent Cells Transformation

50 ul of $DH5_{\alpha}$ cells were mixed with 10ul of each DNA-plasmid ligation made. The mixture was incubated for 30 minutes at 4ºC. A heat shock was made incubating cells for 45 seconds at 42ºC. After that cells are quickly brought to 4ºC and incubated for 2 minutes.

5.1.5.2 One Shot® BL21 Chemically Competent E. coli Transformation

50 ul de BL21 (DE3) cells were mixed with 10ul of DNA. The mixture was incubated for 30 minutes at 4ºC. A heat stroke was made incubating cells for 30 seconds at 42ºC. After that, cells are quickly brought to 4ºC.

5.2 Transformed E.coli culture

Since the plasmid is ampicillin resistant, agar plates with ampicillin were used for DH5α cells and for BL21 cell culture. The unique cells able to life and reproduce into the plate will be those who had inserted the plasmid.

The plate was made with Luria Broth (LB) medium Invitrogen, Agar Invitrogen and demineralized water.

In one liter of distilled water, 25g of LB medium and12.5g of Agarose were dissolved and autoclaved. Once the medium was tepid, 5ml of Ampicillin were added. Culture plates were filled with the resultant medium. Plates were let to cool until they were solid and then stored at 4ºC.

5.3 Verification of the transformation

Although all the colonies that had grown onto agar plates with ampicillin had inserted the plasmid, it was necessary to ensure that the DNA fragment was inserted in the plasmid, was inserted in the proper reading frame and was inserted without nucleotide errors.

Nine different colonies were picked from the plaque. Each colony is introduced into a falcon with 4ml of LB+Ampicillin medium and cultivated over night at 37ºC and 250

rpm. After incubation, inoculates were centrifuged at 1000rpm for 5 minutes in order to discard the medium.

In order to isolate DNA of the DH5α cells, the PureLink™ Quick Plasmid Miniprep Kit (Invitrogen) was used.

The cells were lysed using an alkaline/SDS buffer provided by the kit. Then, the lysate was placed in a spin column with silica membrane which trapped the plasmid. Contaminants were eliminated by cleaning buffers, also provided by the kit. Plasmid tethered to the column was eluted with 40 µl of a buffer containing Tis-HCl and EDTA provided by the kit.

To separate the plasmid and the DNA, the samples were digested using the digestion enzymes appropriated for each DNA sequence. The followed procedure was the same described at section 5.1.3.

Once the digestion was done, an electrophoresis was conducted following the steps described at section 4.4.1. Samples were stained with BLUE JUICE Gel Loading Buffer and 100bp LADDER was used as a guide.

Among the samples that had inserted the DNA sequence, that which showed the band with more intensity was chosen for sequencing.

5.4 Fragments sequencing

With sequencing it is possible to obtain the complete sequence of the inserted fragment. The result was checked to detect any change in the genetic sequence, because this might lead to another protein transcription or to a deficient protein.

The method used was the Sanger sequencing method. The Sanger method uses dideoxynucleotide triphosphates (ddNTPs) as DNA chain terminators. This chain-termination method requieres a single-stranded DNA template, DNA primers, DNA polymerase, normal deoxynucleotidephosphates (ddNTPs) and modified nucleotides (dideoxyNTPs) that terminate DNA strand elongation. These (ddNTPs will aso be radioactively or fluorescently labeled for detection in automated sequencing machines.

The sequencing was carried out at the Genomic Services of the UB (http://www.ccit.ub.edu/CA/tb06.html). To conduct the sequencing, 100 ng/kb of the entire construction (plasmid+inserted sequence) were needed.

6. PROTEIN EXPRESSION AND PURIFICATION

6.1 Conditions for protein expression

6.1.1 E. coli culture and induction of expression

The purified plasmid belonging to the colony with the correct insert was used to transform the BL21 cells as detailed in section 5.1.5.2.

Transformed BL21 cells were streaked on a LB+agar +Ampicillin culture plate and incubated overnight at 37ºC. After incubation, four colonies were picked and cultured overnight at 37ºC and at 250 rpm in falcons with 4ml of LB medium with Ampicillin.

The 4ml cell culture was added to a 1 liter of LB+Ampicillin medium to achieve great bacteria production and thus, great amount of protein. Cells were incubated at 37ºC and 250 rpm until they reached an optical density of 0.6-0.8 at 600 nm. 1mM IPTG was then added and cells were incubated for additional 4 hours at 37ºC and 250 rpm.

6.1.2 Recombinant protein isolation from other E.coli products

To isolate the protein of interest among the others synthesized by the bacteria, it is required to disrupt cellular membrane and thus, release all synthesized products.

Bacterial disruption is a critical step in the purification process. The disruption may affect the quantity of recombinant protein obtained during purification, its biological activity, its integrity and the way it is associated to other cellular components[25].

Sonication was selected from the different used methods for bacterial disruption. This method uses pulses of high frequency ultrasounds generated by a vibratory probe which is immersed in the liquid with bacteria suspended on it. Due to the great energy generated by the probe, microscopic vapor bubbles are formed on the liquid that

explode making the shock waves spread along the sample. *(Thermo Scientific. Pierce Protein Research products. Traditional methods of cell lysis.)*

When using this technique a number of aspects should be taken into account:

The heat produced by sonication when mechanical energy is transformed into thermal energy might denature the protein.

The foam generated by sonication might cause denaturation and oxidation of the protein.

An excessive sonication might produce many debris products that might interfere on the subsequent protein purification.

For all these reasons, it is necessary to maintain the samples cold during sonication and determine the minimum sonication time needed to obtain the maximum cell lysis.

Before cell disruption is necessary to isolate the cells from the culture media. To achieve that, the medium containing the cells was centrifuged at 7700 rpm for 10 minutes at 4ºC. After centrifugation, the supernatant was disposed and the pellet was frozen at -80ºC.

Then, the pellet was resuspended in 20ml of PBS 1X and sonicated on ice following 8 cycles at 30 kHz… for 30 seconds with a 60 seconds rest between each pulse.

Additionally, cell lysis was done by adding 20% Triton X-100.. The samples were incubated under mild agitation for 30 minutes at 4ºC. Therefore, samples were centrifuged at 12000g for 10 minutes at 4ºC. The obtained supernatant contained the products synthesized by the bacteria while the pellet contained the cellular debris.

6.2 Protein purification process

The purification was carried out in an ÄKTApurifier equipment with 1ml GSTrap™ affinity columns (GE Healthcare, USA).

The column was equilibrated with deionized water. The supernatant obtained after sonication, which contains the protein, was loaded into the equipment at a 5 ml/min flow rate. Once the sample to purify is on the equipment, 3 ml of the Prescission

cleavage buffer (50 mM Tris-HCl, 150 mM NaCl, 1 mM EDTA, 1 mM dithiothreitol (DTT), pH 7.0) were loaded. Immediately after, 40 µl of HRV3C Protease, Recombinant expressed in E.coli (Sigma-Aldrich, Germany) diluted in 960 µl of Prescission cleavage buffer were loaded in the equipment. The protein was cleaved at 4ºC over night. After cleavage, prescission cleavage buffer were loaded in the equipment which made the protein pass through the column. The eluted protein was collected and the, glutathione Elution Buffer (50 mM *TRIS-HCL*, *10 MM REDUCED GLUTATHIONE*, *PH 8.0)* was loaded in the column to remove the GST portion of the fusion protein.

6.3 Protein quantification

Different methods are used to determine the concentration of a protein in dissolution[26] . The most commonly used are:

Biuret reactive: it contains $CuSO_4$ which turn to violet when the peptidic bonds are broken. The handicap of this method is the low sensitivity and the amount of required protein to obtain reliable data.

Lowry Method: in this method the Biuret reactive and the Folin-Ciocalteau reactive for phenols detection are combined. The reactive is reduced by means of phenol groups present in the protein, turning the solution into blue. The problem with this method is the interference of most of the compounds used in the enzymatic reaction.

UV absorption at 280nm or 205-220 nm: proteins absorb UV light in the range of 280nm due to the tyrosine and tryptophan residues. The problem lies in the fact that this both amino acids vary considerably between different proteins, so the measurement of the concentration obtained is approximated. Only with pure proteins the measurements achieved are reliable.

Dye Binding: the dye used is Comassie Blue G-250. In a strong acid environment the stain shows a red-brown color, but when it bonds to a positive charged protein it turns into deep blue. It is one of the most popular methods due to its reliability, speed and simplicity. The main disadvantage lies on the high stain capability and the influence of the samples' pH, which can make the results to vary.

BCA reactive (bicinchoninic acid): it is a reactive patented by Pierce Protein Research Products. In this method the Cu reduction capability in presence of proteins is combined with the capability of BCA to react with the reduced Cu resulting in a deep purple color reaction.

The sensitivity of the method is higher than the one for the Dye Binding method and more over, is not affected by the differences between similar proteins. The method is not compatible with strong reducing agents.

In this thesis the BCA Protein Assay Reagent (Thermo Scientific) was used to quantify the obtained protein.

For quantification, a calibration curve with BSA (bovine serum albumin) was made. This protein has high stability, low cost and it doesn't interfere in a great variety of biochemical reactions. The curve was made with known dilutions of BSA in Prescission Buffer, as the behaviour is practically lineal for concentrations between 20-200 µg/ml. Knowing the linear equation of the calibration curve it is possible to know the concentration of the purified protein.

The purified protein was diluted in a proportion 1/5. The reagent mixture was prepared according to manufacturer's indications and the procedure followed as well. Triplicates for each measurement were done. The reaction was incubated at 37ºC for 30 min. After this time, the reaction was stopped lowering the temperature in ice. 225 µl of each sample were place in a 96 multiwell plate. The absorbance was read in a plaque spectrophotometer POWER WAVE XS (BioTek, Germany) at a λ=562 nm.

7. BIOFUNCTIONALIZATION

7.1 Physisorption

In the present work the physisorption of the FN fragments to the TiNbHf alloy was done according to the following protocol:

TiNbHf discs of 2 mm thick were mirror polished and cleaned in an ultrasound with cyclohexane (3x), isopropanol (3x), H_2O(3x), ethanol (3x) and acetone (3x) and dried

with nitrogen. All chemicals purchased from Sigma-Aldrich. FN fragments were prepared at a 100 µg/ml concentration diluted in PBS pH 7.4 (Invitrogen). A 100 µl drop of each fragment was placed on each sample and incubated overnight at room temperature.

7.2 Covalent binding. Silanisation

In the present work, the silanisation method was done in solution and toluene was used as the anhydrous solvent. The crosslinker used was N-Succinimidyl 3-maleimidopropionate.

Discs 2mm thick of the TiNbHf alloy were mirror polished and silanised according to the following procedure:

Samples were cleaned with O2 plasma for 5min at a 12 MHz frequency in a Expanded Plasma Cleaner PDC-002 (Harrick Scientific Corporation, New York, USA). The aim was to promote and increase the formation of –OH groups on the material surface. Next samples were immersed in a solution of 0.08M APTES (Aminopropyl-triethoxysilane, Sigma-Aldrich) in toluene (Sigma-Aldrich) at 70ºC for 1h under agitation in an inert atmosphere. After silanisation, the samples were sonicated in toluene for 5 minutes and cleaned with toluene (3x), acetone (1x), isopropanol (3x), distilled water (3x), ethanol (3x) and acetone (3x) afterwards. Subsequently aminosilanised samples were immersed in a 7.5 mM solution of N-succinimidyl-3-maleimidopropionate in DMF (N, N-dimethylformamide Sigma-Aldrich) for 1h under agitation at room temperature. The cross-linked samples were rinsed in DMF (3x), acetone (1x), distilled water (10x), ethanol (3x) and acetone (3x) and dried with nitrogen. Straightforward, 100 µl drop of the desired motif of functionalisation was placed on the samples and incubated for 1h at room temperature.

7.3 Protein adhesion characterization

7.3.1 Optical Waveguide Lightmode Spectroscopy System (OWLS)

The OWLS is a labelling-free technique used to investigate the interaction at the solid/liquid interface. With OWLS, the adsorption, binding and adhesion processes can

be studied. The technique is based on the coupling of a polarized light by a diffraction grating into the waveguide layer.

To carry on the experiments a sensor is needed (Fig. 35). The sensor is a glass substrate, made by the SOL-GEL technology, with a waveguide layer of thickness 200nm and with a refraction index 1.8. The waveguide layer is grated with a periodicity of 2400 lines/mm.

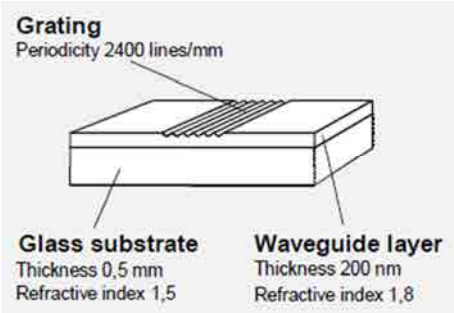

Fig.35 Sensor used for OWLS experiment. Extracted from www.microvacuum.com

The sensing principle is based on the incoupling phenomenon (see Fig.36). The incoupling is a resonance phenomenon, that occurs at a precise angle of incidence which depends on the refractive index of the medium covering the surface of the waveguide. In the OWLS system, a He-Ne laser is used as the source of light and the incoupling occurs at two-well defined angles of incidence: one for the transverse electric (TE) and the other for the transverse magnetic (TM) polarization mode of the laser. These angles depend on the refractive indices of the medium covering the surface of the waveguide.

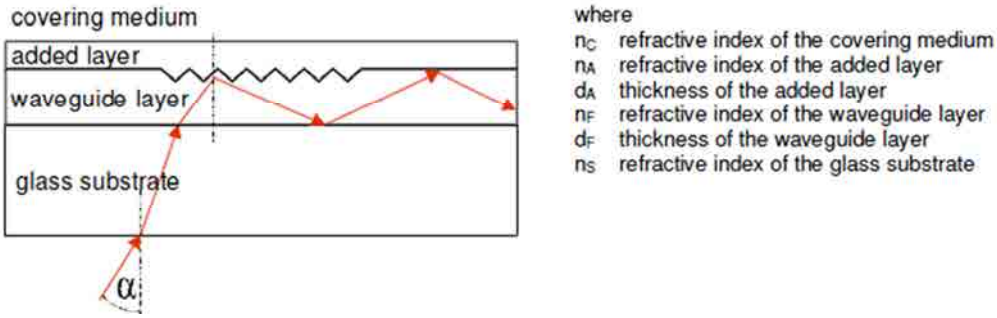

Fig.36 Representation of the OWLS equipment sensing principle. Extracted from www.microvacuum.com

In Fig. 37 a scheme of the optical system is showed. A He-Ne laser beam pass through a shutter, is reflected on a prism and arrives to the sensor surface at a certain angle. The sensor is placed into a holder and positioned on a rotator. The stepping motor controls the rotator angle at any time and the two photodiodes at the edges of the waveguide measure light intensity. Both the stepping motor and the photodiodes are controlled by a computer.

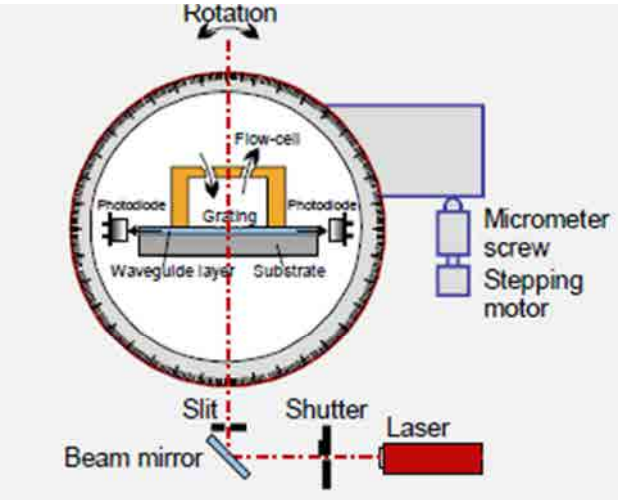

Fig.37 Representation of the optical set up of the OWLS system. Extracted from www.microvacuum.com

In the present work a *OWLS^{TM} 120 Optical Waveguide Lightmode Spectroscopy System Biosense 2.6 Software* (Micro Vacuum Ltd. Budapest, Hungary) was used.

Adsorption mode was selected from the different solid-liquid interface phenomenon that OWLS is able to measure. In Fig. 22 scheme of the process is shown.

To determine the amount of material adsorbed it was assumed that the adsorbed layer depended linearly on the concentration of the adsorbed material and a dynamic measurement was needed. Briefly, the procedure is as follows: the incoupling angles (TE and TM) for electric and magnetic modes are evaluated from the measured lightmode spectra. The effective refractive indices (N(TE), N(TM)) of the waveguide structure are calculated on the basis of incoupling condition. Once the effective refractive indices are calculated and assuming that the optical parameters of the waveguide layer (n_F, d_F), the substrate (n_S) and the covering medium (n_C) are known

(Fig. 38), the refractive index (n_A) and the thickness (d_A) of the added layer can be calculated.

The chips used had a waveguide layer coated with a TiO_2 10nm thin film which was the coating with closer characteristics to the TiNbHf alloy. Each chip was cleaned in an ultrasound bath with cyclohexane (3x), isopropanol (3x), H_2O (3x), ethanol (3x) and acetone (3X) and was dried with N_2. The chips used to determine the adsorbed amount of protein by a covalent bonding were silanised as explained in point 7.2. In this case, the biofunctionalisation motifs were CAS and HB II recombinant fragments of FN.

To conduct the adsorption measurements, the optical parameters of the chip were measured after injecting PBS on the flow cell. Taking these parameters of reference to make the calculation, the dynamic measurement started. This measurement was made with the buffer solution to achieve a base line. When the drift dN_{TM}/dt is less that 10^{-8} s^{-1}, the base line was considered stable and the protein fragment of study was injected in the flow cell with a syringe. The dynamic measurement of the protein adhesion was monitored for 1h. After 1h PBS was injected in the flow cell and the non-adsorbed protein onto the chip surface was eliminated.

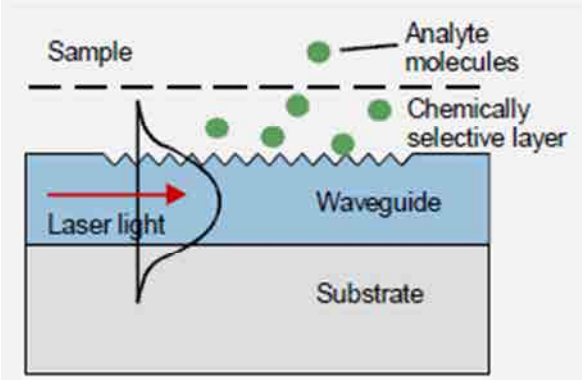

Fig.38 Scheme of the principle detection in an adhesion process. The refractive index changes by the binding of the analyte molecules. Extracted from www.microvacuum.com

7.3.3 Atomic Force Microscope (AFM)

The AFM basic principle is that a prove and a sample can interact and the forces involved in this interaction can be translated into images.

The AFM uses a cantilever that act as a spring. When the cantilever is close to the surface suffer from the interaction forces which can be attractive or repulsive. This attraction or repulsion produces the deflection of the cantilever. To detect the cantilever's deflection and translate it into an electrical signal a laser beam is used (see Fig.39). The laser beam is reflected from the back of the cantilever onto a photodetector. Depending on the cantilever deflection, the angle of the laser beam reflected changes, and the beam spot is reflected in a different area of the photodetector. The signals from the four quadrants of the photodetector are compared to calculate the deflection signal. The electronic signals given by the photoelectrode are translated into images by means of software.

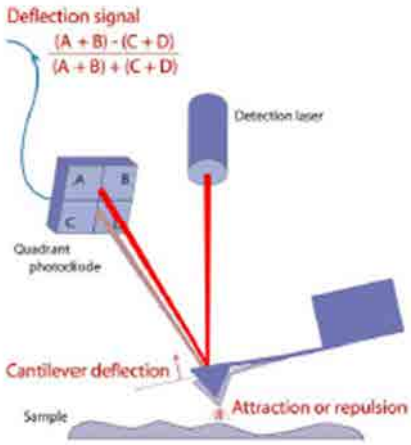

Fig.39 Scheme of the cantilever deflection photodetection.

AFM is a technique widely used when working with biological samples because there is no need of staining or coating the sample of study and the samples do not need to conduct electricity and they can be imaged in physiological conditions as well. This technique gives 3D topographical information of the samples as well as mechanical properties of adhesion.

In this thesis, the AFM technique was used to determine the topographical distribution of the protein under study in a TiNbHf samples and the adhesion force of cells when in contact with the protein functionalized TiNbHf samples. The equipment used was a *NanoWizar®III (JPK Instruments, Berlin, Germany)* (Fig. 40).

Fig.40 NanoWizar® III from JPK Instruments set up.

7.3.3.1 Surface imaging

The AFM was used to map the spatial distribution of the proteins either adsorbed or covalently bonded to the substrates.

AFM cantilever can interact with the surface in a contact imaging mode or in tapping mode. In the contact mode the scanning forces applied on the adsorbed protein layer might re-distribute the protein outside of at the edges of the scanning area [27]. To avoid this, the tapping mode was used. In the tapping mode the tip of the cantilever makes repulsive contact with the surface of the sample at the lowest point of the oscillation (Fig.41)

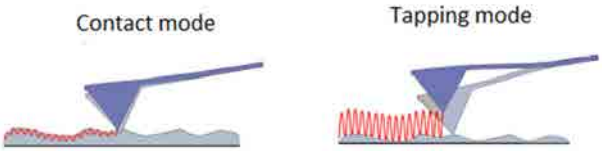

Fig.41 Representation of the contact and tapping mode of the cantilever during surface imaging. Adapted from NanoWizard® AFM Handbook. JPK Instruments.

The samples used in the assay were biofunctionalised with the CAS fragment as stated in point 7.1 for the physisorbed ones; and as in 7.2, for the silanised ones. All the experiments were conducted in PBS at 37ºC in an attempt to reproduce physiological conditions. Three images of each sample were taken and they were analyzed with the JPK SPM data processing software (JPK Instruments, Germany)

7.3.3.2 Cell adhesion force analysis

The single molecule force spectroscopy is used to perform mechanical assays with single molecules. These experiments can be done at ambient conditions or in a fluid and at a controlled temperature. Basically, the experiment is based on a tip in contact with the sample that is retracted from it. The cantilever is still attached to the sample due to some kind of adhesion and the cantilever is deflected downwards, but at some point the cantilever's force is able to overcome the adhesion and break free.

In the AFM force analysis conducted a cell was attached to a functionalized cantilever. In Fig.42 a visual description of the process and an image of the curve obtained is shown.

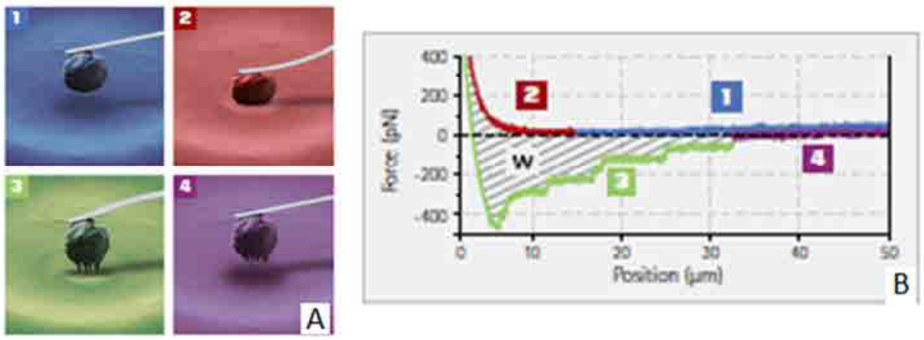

Fig.42 A) Visualization of a cell adhered to a cantilever being attached and retracted from a surface. B) Representation of a Force-Distance curve of the events taking places during cell attachment and retraction. Adapted from *www.jpk.com*

The tests were made with samples biofunctionalised with lRGD, cRGD and the CAS fragment as stated in point 7.2 immersed in culture medium at 37ºC.

The cells used were rat mesenchymal stem cells (rMSC). The cells were cultured in Advanced DMEM supplemented with 10% FBS (foetal bovine serum), antibiotics (50 U/ml penicillin and 50 µg/ml streptomycin), 2 mM L-glutamine and 20 mM HEPES buffer solution. All the chemicals were purchased from Gibco®.

The cantilevers were incubated in 0.5mg/ml BSA-biotin (Sigma-Aldrich, Germany) at room temperature overnight. After incubation, cantilevers were washed with PBS 1X three times and then, incubated in 0.5 mg/ml streptavidin (Sigma-Aldrich, Germany) at

room temperature for 10 min. After incubation, cantilevers were washed with PBS 1X three times. Immediately after, cantilevers were incubated in 0.2 mg/ml biotin-concanavalin A (Sigma-Aldrich, Germany) at room temperature for 10 min.

The samples were placed in a petri dish specific for the AFM equipment and immersed in culture medium Advanced DMEM without FBS. To avoid cell adhesion to the petri dish a layer of Polyethylene glycol was made on the surface at which the samples were attached.

10ul of cells were introduced into the petri dish and a unique cell was immobilised on the cantilever. To achieve the cell immobilisation the cantilever was attached to the cell with a force of few nano Newtons and inducing contact for a few seconds. Once the cell was immobilised, it was placed on the sample with a load varying between 300 and 800 pN. Cell was left for 5 seconds intereacting with the surface and straightforward was moved away with a retracting speed of 3um/s. Six different cells were tested in each sample and 20 adhesion assays were made with each cell. All curves were analyzed with the JPK SPM data processing software (JPK Instruments, Germany)

8. CELLULAR ASSAYS

8.1 General considerations

8.1.1 Cell type

In this thesis, the aim of the cell culture is to determine if cells are able to adhere, spread and differentiate in a device for bone applications. There are two cells involved in bone formation: mesenchymal stem cells and osteoblasts.

The cell type used in this thesis was rat mesenchymal stem cells (rMSCs). Primary cell culture reflects in a more accurate way the process that takes part when an implant is inserted in the body.

The cells were obtained from Sprague-Dawley rats in a process developed by Institute of Bioengineering of Catalonia (IBEC).

8.1.2 Culture medium

Advanced DMEM (Gibco®, Invitrogen) was used for rMSCs culture. Advanced DMEM (Dulbecco's Modified Eagle Medium) is a widely used basal medium that allows the culture of mammalian cells with reduced Fetal Bovine Serum (FBS) supplementation. This medium contains high glucose, essential amino acids, sodium pyruvate and phenol red, thus it has to be supplemented with FBS, antibiotics, L-glutamine and the organic buffer HEPES (all from Invitrogen). In table 11 the formulation of the medium used in the assays is shown.

COMPONENT	% IN THE TOTAL VOLUME
penicillin/streptomycin	1%
L-glutamine	1%
HEPES	2%
FBS	10%
Advanced DMEM	86%

Table 11. Formulation of the supplemented Advanced DMEM used in the cell assays.

8.1.3 Cell culture maintenance

rMSC cells were maintained in Advanced DMEM supplemented with 10% FBS (fetal bovine serum, *Invitrogen*), 20 mM HEPES Buffer solution (*Invitrogen*), antibiotics (50 U/ml penicillin and 50 µg/ml streptomycin, *Invitrogen*), 2 mM L-glutamine(*Invitrogen*) in an incubator with 5% CO_2 and 95% relative humidity at 37ºC. Cell medium was changed every 2 days to maintain the proper levels of nutrients, growth factors and hormones for cell growth as well as for the pH and the osmotic pressure of the culture.

Cells were kept at an optimal density for continued growth and to stimulate further proliferation. When cells reach confluence, cell proliferation is greatly reduced or ceases. Confluent cells were detached and seeded in a new flask.

Cells were detached using TrypLE™ Express (Invitrogen). TrypLE™ Express is composed of cell dissociation enzymes with similar kinetics and cleavage specificities to trypsin. Detached cells were centrifuged, resuspended in medium and seeded.

8.2 Adhesion assay

Cell adhesion assay was done to test the ability of the protein fragments developed to trigger or to enhance cell adhesion.

The number of cells adhered were measured by a lactate dehydrogenase (LDH) assay and the morphology, cytoskeletal assembly and focal contacts by means of immune fluorescence.

8.2.1 Lactate dehydrogenase LDH assay

The LDH assay is a non-radioactive colorimetric assay based on the measurement of the lactate dehydrogenase activity released from the cytosol of damaged cells.

Lactate dehydrogenase (LDH) catalyses the interconversion of pyruvate and lactate. The LDH activity is determined by a coupled enzymatic reaction, whereby the tetrazolium salt INT is reduced to formazan. An increase in the number of cells results in an increase of LDH enzyme activity in the culture supernatant after lysis. This increase in the amount of enzyme activity in the supernatant directly correlates to the amount of formazan formed during a limited time period.

The *Cytotoxicity Detection Kit ^{PLUS} (LDH)* from Roche was used. The kit is provided with a catalyst, a dye solution and a stop solution. The procedure to perform the assay was as follows:

Samples were prepared as stated in point 7.2 and seeded with 25000 cells/well. After 5h incubation 300 µl of *Mammalian Protein Extraction Reagent (M-PER)* purchased from Thermo Scientific were added to the samples. The LDH kit reaction mixture was prepared following the manufacturer guidelines. 100 µl of each sample and the calibration curve were added to a 96 well plate. 100 µl of the LDH kit reaction mixture were added to the wells with the M-PER solution and incubated protected from light for 10-15min. After the incubation time, 50 µl of the LDH Kit stop solution were added to each well and the absorbance was read in a multiwell plaque reader at a λ=492nm.

8.2.3 Immunofluorescence

Immunofluorescence is a technique based on the specificity of the interaction antigen-antibody. The technique is applied directly on the cells and is capable of identify the

sub-cellular localization of the protein of interest and the co-localization with other proteins using fluorescent dyes

At the end of the incubation time the cell culture medium was removed and each well rinsed three times with phosphate buffered saline (PBS, Gibco, Invitrogen), fixed with 4% paraformaldehyde (Sigma-Aldrich, Germany) for 30 min and then washed three more time to remove excess paraformaldehyde. Fixed cells were permeabilised with Triton X-100 (*Sigma*) at 0.05% in PBS at room temperature for 20 min and cleaned with a 20nM Glycine in PBS solution three times. With the aim to reduce non-specific background, samples were blocked with 5% BSA (Sigma-Aldrich, Germany) in PBS and incubated for 30 min at room temperature. The blocking solution was removed and a drop of 100 µl of mouse anti-vinculin (Sigma-Aldrich, Germany) at a dilution 1:100 in 1%BSA in PBS was added to each sample and incubated at room temperature for 1h. After incubation, samples were cleaned with a 20nM Glycine in PBS solution three times. A drop of 100 µl of secondary Alexa 488 goat anti-mouse antibody (Invitrogen, Madrid, Spain) at a dilution 1:1000 and TRITC-phalloidin (Invitrogen, Madrid, Spain) at a dilution 1:300 both in PBS were added to each sample and incubated at room temperature in the dark for 1 h. After incubation, samples were cleaned with 20nM Glycine in PBS solution three times. 300 µl of DAPI (Invitrogen, Madrid, Spain) at a dilution 1:1000 in PBS was added to each sample and incubated at room temperature in the dark for 2 min. After this time, samples were cleaned with 20nM Glycine in PBS solution three times. Samples were placed in a cover slide and a drop of 8 µl of Mowiol® 4-88 (Sigma-Aldrich, Germany) was added to the samples as an anti-fading agent.

8.3 Proliferation assay

Cell proliferation is the increase in cell number as a result of cell growth and division. Cell proliferation is a very sensitive indicator of cell stress because it requires intact cell structures and function to be achieved. To determine the proliferation of cells the number of surviving cells were determine by means of LDH assay.

Samples were prepared as stated in section 7.2 and seeded with 10000 cells. Cells were cultured for 4 hours, 7 days, 14 days and 21 days. After each incubation period, the procedure followed was as stated in section 8.2.1.

8.4 Differentiation assay

Cell differentiation is a multi-step procedure associated with the expression of a specific set of cellular markers. In osteoblast differentiation, ALP is involved in the initial steps of mineralization. Moreover, during bone development or bone-related diseases, the activity of the alkaline phosphatase (ALP) changes. ALP is a hydrolase enzyme responsible for removing phosphate groups from many types of molecules, including nucleotides, proteins, and alkaloids.

The *SensoLyte® pNPP Alkaline Phosphatase Assay Kit *Colorimetric** from ANASPEC was used.

This assay is based on measuring ALP activity by monitoring the colour change as para-nitrophenol phosphate (pNPP), which is colourless, is cleaved to paranitrophenol + phosphate which is yellow.

Samples were prepared as stated in section 7.2 and seeded with 1000 cells. Cells were cultured for 4 hours, 7 days, 14 days and 21 days. After each incubation period 300 µl of Mammalian Protein Extraction Reagent (M-PER) purchased from Thermo Scientific were added to the samples. The alkaline phosphatase dilution buffer and the alkaline phosphatase standard were prepared following the manufacturer guidelines. 50 µl of the sample were transferred to a 96-well cell culture plaque. Then, 50 µl of the Alkaline Phosphatase Yellow (pNPP) Liquid Substrate was added and the mixture was incubated at 37ºC for 30 min. After incubation, the absorbance was read in a multiplaque reader at a λ=405nm. Results were normalized versus cell number and time of incubation.

9. BIBLIOGRAPHY

1. González, M., Peña, J., Manero, J. M., Arciniegas, M. & Gil, F. J. Optimization of the Ti-16.2Hf-24.8Nb-1Zr Alloy by Cold Working. **18,** 506 (2009).

2. Gonzalez, M., Peña, J., Manero, J. M., Arciniegas, M. & Gil, F. J. Desing and Characterization of New Ti-Nb-Hf alloys. *J. Mater. Eng. Perform.* **18,** 490 (2009).

3. Arciniegas, M., Peña, J., Manero, J. M., Paniagua, J. C. & Gil, F. J. Quantum parameters for guiding the design of Ti alloys with shape memory and/or low elastic modulus. *Philos. Mag.* **88,** 2529 (2008).

4. Morinaga, M., Yukawa, M., Adachi, H. & Ezaki, H. in *Superalloys 1984* (Gell, M., Kortovich, C. S., Bricknell, R. H., Kent, W. B. & Radavich, J. F.) 523–532 (The Minerals, Metals & Materials Society, 1984).

5. Morinaga, M. *et al.* Theoretical design of beta-type titanium alloys. *Titan. '92 Sci. Technol. Proc. Symp. World Titan. Conf.* **San Diego,,** 217 (1993).

6. Fischer-Cripps, A. C. A review of analysis methods for sub-micron indentation testing. *Vacuum* **58,** 569–585 (2000).

7. Callister, W. D. & Rethwisch, D. G. *Materials science and engineering*. **8th,** (John Wiley & Sons, 2011).

8. Keselowsky, B. G., Collard, D. M. & García, A. J. Integrin binding specificity regulates biomaterial surface chemistry effects on cell differentiation. *Proc. Natl. Acad. Sci. U. S. A.* **102,** 5953–5957 (2005).

9. Phillips, J. E., Petrie, T. A., Creighton, F. P. & García, A. J. Human mesenchymal stem cell differentiation on self-assembled monolayers presenting different surface chemistries. *Acta Biomater.* **6,** 12–20 (2010).

10. Lavenus, S. *et al.* Behaviour of mesenchymal stem cells, fibroblasts and osteoblasts on smooth surfaces. *Acta Biomater.* **7,** 1525–1534 (2011).

11. Kwok, D. Y. & Neumann, A. W. Contact angle measurement and contact angle interpretation. *Adv. Colloid Interface Sci.* **81,** 167–249 (1999).

12. Yuan, Y. & Lee, T. R. in *Surf. Sci. Tech.* (Bracco, G. & Holst, B.) 3–34 (Springer Berlin Heidelberg, 2013). doi:10.1007/978-3-642-34243-1_1

13. Kirby, B. J. & Hasselbrink, E. F. Zeta potential of microfluidic substrates: 1. Theory, experimental techniques, and effects on separations. *Electrophoresis* **25,** 187–202 (2004).

14. Anderson, J. M., Rodriguez, A. & Chang, D. T. Foreign body reaction to biomaterials. *Innate Adapt. Immune Responses Tissue Eng.* **20,** 86–100 (2008).

15. Anderson, J. M. Biological responses to materials. *Annu. Rev. Mater. Res.* **31,** 81–110 (2001).

16. Park, J. B. & Lakes, R. S. *Biomaterials :an introduction*. **3,** 561 (Springer, 2007).

17. Puleo, D. A. & Bizios, R. *Biological Interactions on Materials Surfaces*. (Springer, 2009). doi:10.1007/978-0-387-98161-1-7

18. Swierenga, S. H. H., Gilman, J. P. W. & McLean, J. R. Cancer risk from inorganics. *Cancer Metastasis Rev.* **6,** 113–154 (1987).

19. Niinomi, M. Recent Metallic Materials for Biomedical Applications. *Metall. Mater. Trans. A* **33,** 477 (2002).

20. Geetha, M., Singh, A. K., Asokamani, R. & Gogia, A. K. Ti based biomaterials, the ultimate choice for orthopaedic implants – A review. *Prog. Mater. Sci.* **54,** 397–425 (2009).

21. Yang, K. & Ren, Y. Nickel-free austenitic stainless steels for medical applications. *Sci. Technol. Adavanced Mater.* **11,** 1–13 (2010).

22. Viovy, J.-L. Electrophoresis of DNA and other polyelectrolytes: Physical mechanisms. *Rev. Mod. Phys.* **72,** 813–872 (2000).

23. Brody, J. R. & Kern, S. E. History and principles of conductive media for standard DNA electrophoresis. *Anal. Biochem.* **333,** 1–13 (2004).

24. Alberts, B. & Walter, P. *Molecular biology of the cell*. **4th,** 1,36,49,1463 (Garland, 2002).

25. Glover, D. M. & Hames, B. D. *DNA cloning :a practical approach*. **2,** (IRL Press, 1995).

26. Scopes, R. K. *Protein Purification: Principles and Practice*. **3rd,** 404 (Springer, 1994).

27. Hlady, V. & Buijs, J. Protein adsorption on solid surfaces. *Curr. Opin. Biotechnol.* **7,** 72–77 (1996).

III

Results

Chapter3

Effect of the alloying elements in the Ti-24.8Nb-16.2Hf-1Zr alloy

1. DESIGN OF THE ALLOY COMPOSITION

The basis alloy, Ti-24.8Nb-16.2Hf-1Zr [1], was located in the area of shape memory and low modulus according with the Arciniegas' map[2]. Our aim was to remain in this area and to lower the elastic modulus without losing the β-phase properties of the alloy: high templability, high mechanical strength and conformability, plus low elastic modulus. Zirconium was eliminated because of its low proportion in the alloy (1%). The low amount of Zr in the base alloy made it more an impurity than a β-stabilizer affecting mechanical properties.

Niobium and Hafnium were maintained because of their properties.

- Niobium play two roles in the alloy: on one hand is a β-stabilizer, and on the other hand gives high corrosion resistance [3,4].
- Hafnium has the excellent oxidation resistance, corrosion resistance in a wide variety of media, and high stability of oxides, nitrides, carbides and other compounds and also acts as a beta stabilizer [3].
- The osteogenic and biocompatibility properties of both Nb and Hf [5].

The percentage in mass of each element was varied forming 12 different ternary alloys according to the values shown in Table 12.

ALLOY	Nb (w%)	Hf (w%)	Ti (w%)
1	20	16	Balance
2	22	16	Balance
3	23	16	Balance
4	26	16	Balance
5	27	16	Balance
6	29	16	Balance
7	25	10	Balance
8	25	12	Balance
9	25	15	Balance
10	25	17	Balance
11	25	19	Balance
12	25	21	Balance

Table 12. Variations in the composition of the ternary alloy Ti-25Nb-16Hf.

1.1 Effect of the alloying elements on the alloy's quantum parameters

Each alloying element has its own quantum parameters (Table 13). The value of the quantum parameters of the alloy is influenced by the quantum parameter of each alloying element and the amount of each element in the alloy.

Element	BO (eV)	OE (eV)	e/a
Ti	0.641	0.15454	4
Nb	0.6207	0,14741	5
Hf	0.6698	0.14857	4

Table 13. Quantum parameters BO and OE and e/a relation for each alloying element.

The quantum parameters calculated were the bond order (BO), the orbital free energy (OE) and the electron atom ratio (e/a). These values were calculated according to the following equations:

$$\overline{BO} = \sum x_i(\mathrm{BO})_i \qquad \text{Eq. 3.1}$$

$$\overline{OE} = \sum x_i(\mathrm{OE})_i \qquad \text{Eq. 3.2}$$

$$\overline{e/a} = \sum x_i(\mathrm{e/a})_i \qquad \text{Eq. 3.3}$$

The values obtained for each alloy are shown in Table 14.

Alloy	Formulation	BO (eV)	OE (eV)	e/a
1	Ti-20Nb-16.2Hf	0.60992	0.15311	4.1314
2	Ti-22Nb-16.2Hf	0.61021	0.15300	4.1463
3	Ti-23Nb-16.2Hf	0.61036	0.15294	4.1539
4	Ti-26Nb-16.2Hf	0.61082	0.15277	4.1773
5	Ti-27Nb-16.2Hf	0.61098	0.15271	4.1853
6	Ti-29Nb-16.2Hf	0.61130	0.15258	4.2017
7	Ti-24.8Nb-10Hf	0.60891	0.15312	4.1584
8	Ti-24.8Nb-12Hf	0.60945	0.15303	4.1613
9	Ti-24.8Nb-15Hf	0.61029	0.15290	4.1654
10	Ti-24.8Nb-17Hf	0.61087	0.15280	4.1692
11	Ti-24.8Nb-19Hf	0.61148	0.15270	4.1725
12	Ti-24.8Nb-21Hf	0.61212	0.15260	4.1760

Table 14. Values of BO and OE corresponding to each alloy composition.

As the wt % Nb increases, the BO and the e/a values increased whilst the the OE values decreased. The same behaviour was observed when the wt % Hf increased.

When the wt % Nb was increased from 20 to 29, the $\overline{BO}$ was in the range $0.60992 \leq \overline{BO} \leq 0.61130$; the $\overline{OE}$ was in the range $0.15311 \leq \overline{OE} \leq 0.15258$ and the e/a was in the range $4.1314 \leq e/a \leq 4.2017$.

When the wt % Hf was increased from 10 to 21, the $\overline{BO}$ was in the range $0.60891 \leq \overline{BO} \leq 0.61212$; the $\overline{OE}$ was in the range $0.15312 \leq \overline{OE} \leq 0.15260$ and the e/a was in the range $4.1584 \leq e/a \leq 4.1760$.

The $\overline{OE}$ values did not vary significantly depending on the addition of Nb of Hf, whilst the values that were affected more significantly were the e/a values. Although all of the values correspond to values comprising the low elastic

These quantum parameters were located in the Arciniegas' properties map (Fig. 43). The alloys are located in the region of shape memory and low modulus properties.

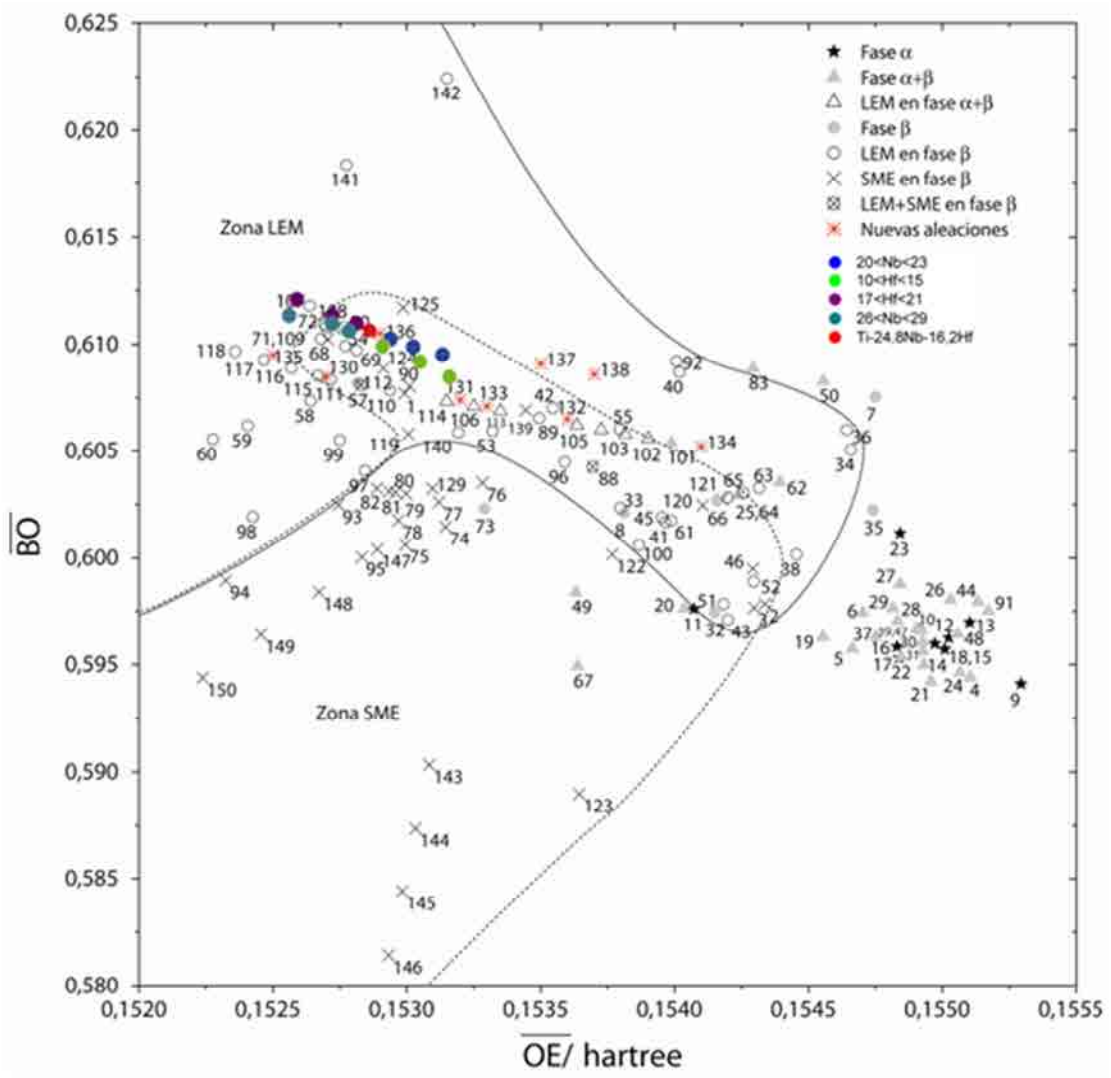

Fig.43 Alloys location in the properties map developed by Arciniegas.

According to Fig.43, all the alloys are located in the shared properties region, except for the alloys of composition Ti-29Nb-16.2Hf and Ti-24.8Nb-21Hf which are located in the region of low elastic modulus, but so close to the shared properties region. These two alloys are also the only ones in the β-region.

As long as the Nb and Hf are β-stabilisers and both have a high percentage in these alloys (29% and 21%) formulation, it makes sense the resulting microstructure was dominated by the β-phase.

The values of the parameter e/a obtained in each alloy range from 4.13 to 4.20. There are just two alloys that do not fulfill the requirements to present ultra-low elastic modulus, high strength, superelastic-like elastic deformability and superplastic-like cold

workability without work hardening at room temperature. These alloys are the ones containing 20% wt and 22% wt of niobium. The rest of alloys are potential candidates to accomplish with those special properties.

1.2 Alloys composition verification

Buttons of the designed alloys were fabricated in an arc melting furnace from Ti cp bars, Nb foil 99,8% purity and Hf shavings 99,7%. Once they were melted, the composition was verified by quantitave analysis using Energy Dispersive X-ray Spectroscopy (EDS). In Table 15 the values of experimental and theoretical chemical composition for each alloy are shown. The experimental values obtained are close to the theoretical values, with a slight deviation.

Alloy formulation	%w Element					
	Nb		Hf		Ti	
	Exp.	Theor.	Exp.	Theor.	Exp.	Theor.
Ti-23Nb-16.2Hf	22.98 ±0.21	23	15.62 ±0.18	16.2	61.4 ±0.24	57.8
Ti-22Nb-16.2Hf	19.82 ±0.2	22	19.91 ±0.24	16.2	60.27 ±0.18	61.8
Ti-20Nb-16.2Hf	20.53 ±0.2	20	16.02 ±0.18	16.2	63.45 ±0.24	63.8
Ti-24.8Nb-17Hf	23.69 ±0.045	24.8	18.39 ±0.17	17	57.92 ±0.2	58.2
Ti-24.8Nb-19Hf	24.126 ±0.46	24.8	19.46 ±1.81	19	56.41 ±1.37	56.2
Ti-24.8Nb-21Hf	21.41 ±0.65	24.8	21.50 ±0.28	21	57.09 ±0.63	51.2
Ti-26Nb-16.2Hf	25.91 ±0.15	26	16.35 ±0.085	16.2	57.73 ±0.21	57.8
Ti-27Nb-16.2Hf	26.73 ±0.45	27	16.62 ±0.09	16.2	56.62 ±0.35	56.8
Ti-29Nb-16.2Hf	28.56 ±0.035	29	16.85 ±0.22	16.2	54.58 ±0.19	54.8
Ti-24.8Nb-15Hf	23.56 ±0.42	24.8	15.8 ±0.11	15	60.64 ±0.25	60.2
Ti-24.8Nb-12Hf	23.76 ±0.15	24.8	13.15 ±0.28	12	63.08 ±0.39	63.2
Ti-24.8Nb-10Hf	22.32 ±0.49	24.8	9.11 ±0.39	10	68.58 ±0.76	65.2

Table 15. Values of the EDS analysis for each material composition and their standard deviations.

2. INFLUENCE OF THE COMPOSITION IN THE MICROSTRUCTURE

Diffraction database was used to identifying and indexing the phases present in the alloy. Due to the novelty of the alloy there are no diffraction patterns available. The patterns used where those from Ti (α and β), Nb and a quenched TiNb alloy with up to 12% content of Nb. Despite this, it was possible to relate each experimental peak with the close one on the reported spectra.

2.1 Effect of Nb in the microstructure

2.1.1 Optical microscopy results

Previous studies report a needle-shaped α phases in a β-dominated matrix in Ti-Nb alloys[6] and a dependence of the β-phase presence on the Nb content. High content of Nb favors the β-phase[7]. This microstructure is observed when the alloy is in an equilibrium state. In our case, the alloy is quenched and thus, not in equilibrium conditions.

In Fig. 44 the micrographies obtained by optical microscopy for alloys with Nb content from 20% w.t. to 29% w.t. are shown.

The microstructure is formed by martensitic plates. As the Nb content increases, the martensite plates become more organized until the microstructure is mainly beta with some isolated with some martensite. This martensite distribution might be due to the α'' proportion with respect to the α'.

Niobium is a beta stabilizer, therefore is logic that increasing niobium content makes the microstructure more beta. Nevertheless, this behaviour is not seen in the alloy with a 27% w.t. of Nb (Fig.44 e). This might be due to during polishing the martensite plaques were induced.

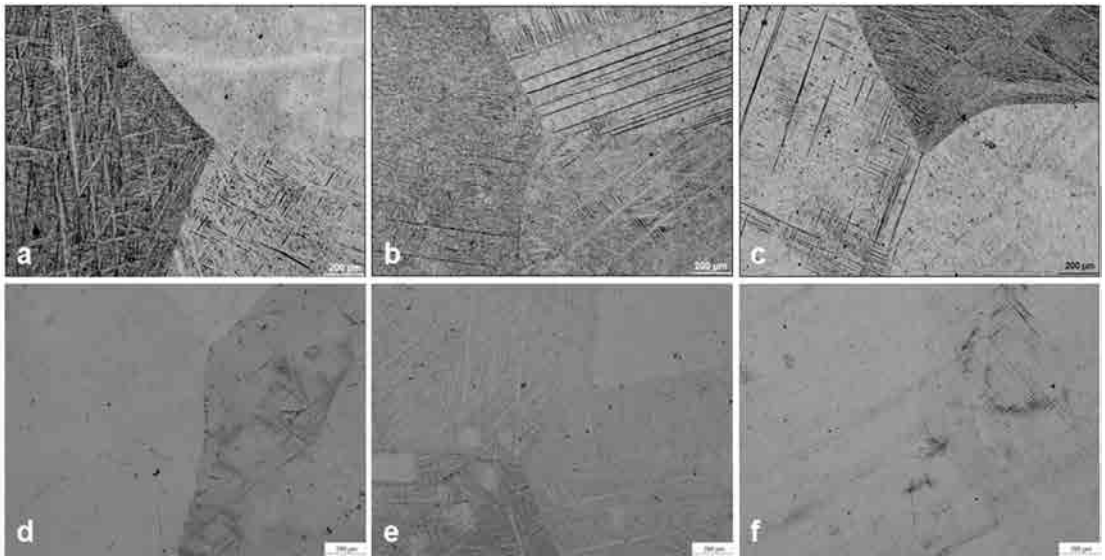

Fig.44 Micrographs obtained by optcal microscopy for the alloys Ti-20Nb-16.2Hf (a), Ti-22Nb-16.2Hf (b), Ti-23Nb-16.2Hf (c), Ti-26Nb-16.2Hf (d), Ti-27Nb-16.2Hf (e) and Ti-29Nb-16.2Hf (f).

2.1.2 XRD results

The diffractograms obtained for the Ti-(20-29)Nb-16Hf alloys (Fig.45) showed a gradually diminishing of the the α' and the α'' peaks as the Nb percentage increases in the alloys. From 26% wt of Nb, the microstructure formed by martesite (α' phase), thermo elastic martensite (α'' phase) and retained β phase became a microstructure formed by β-phase with areas of thermoelastic martensite.

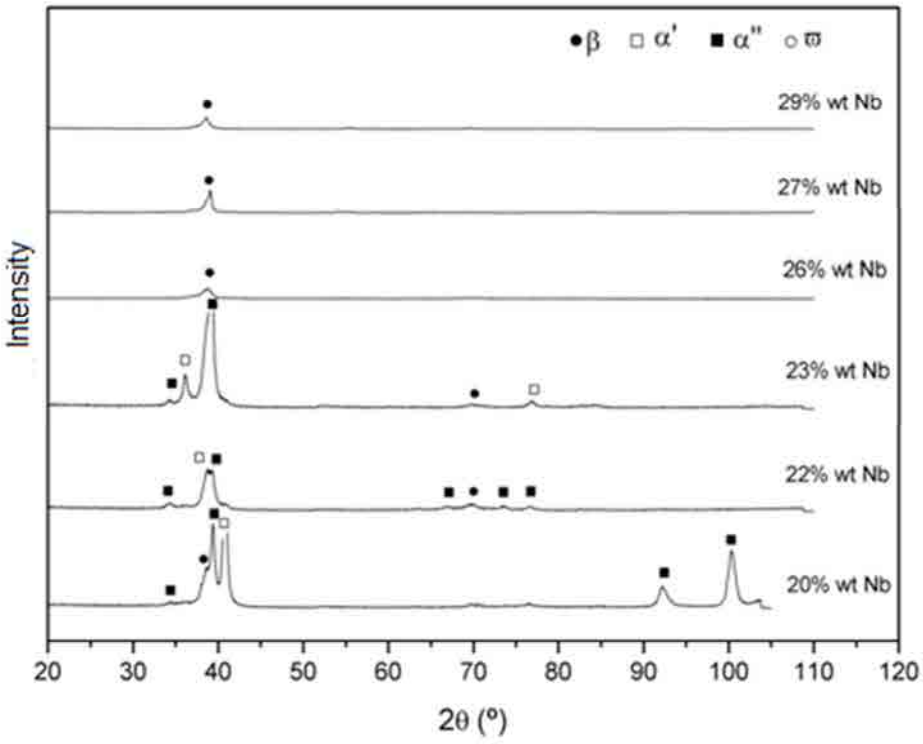

Fig.45 Normalized Diffractogram of the alloys Ti-(20-29)Nb-16Hf

2.1.3 TEM results

As the study made by Nobuhito et al.[8] suggested the presence of ω phase in Ti-Nb-Ta-Zr when the Nb mass percentage ranges from 15 to 25%, TEM images were done on the alloys with Nb mass ranging from 20 to 23% with the aim to verify absence of ω phase (Fig.46). Images demonstrated that no signs of ω phase were seen.

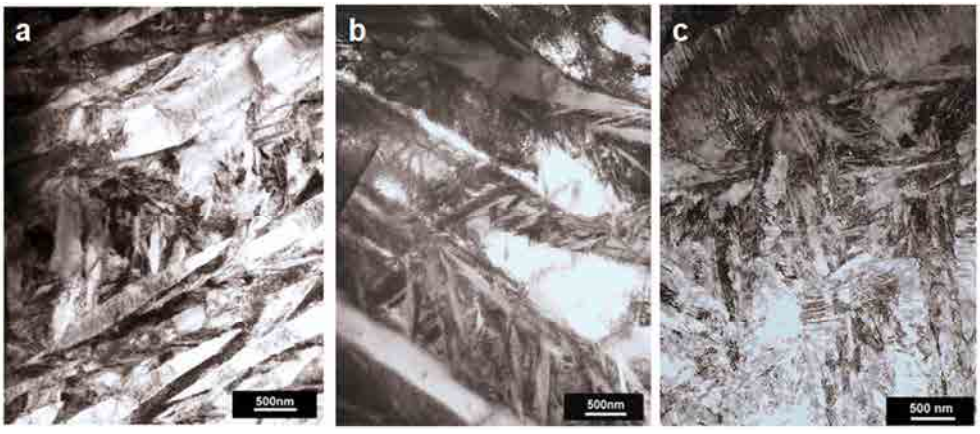

Fig.46 TEM images of the alloys Ti-xNb-16.2Hf with 23% Nb in (a), 22% Nb in (b) and 20% Nb in (c).

2.2 Effect of Hf in the microstructure

2.2.1 Optical microscopy results

For the Ti-24.8Nb-(10-21)Hf alloys group it can be seen that as the quantity of Hf increases, the martensite acicular plates became more woven (Fig. 47). The black dots correspond to small particles of Bakelite. The white spots with unrevealed microstructure are due to the polishing suspension attack. The spots were analyzed by SEM and no evidence of material impurities was found. This trend is interrupted for a 15% w.t. Hf as could be seen in Fig. 47 c.

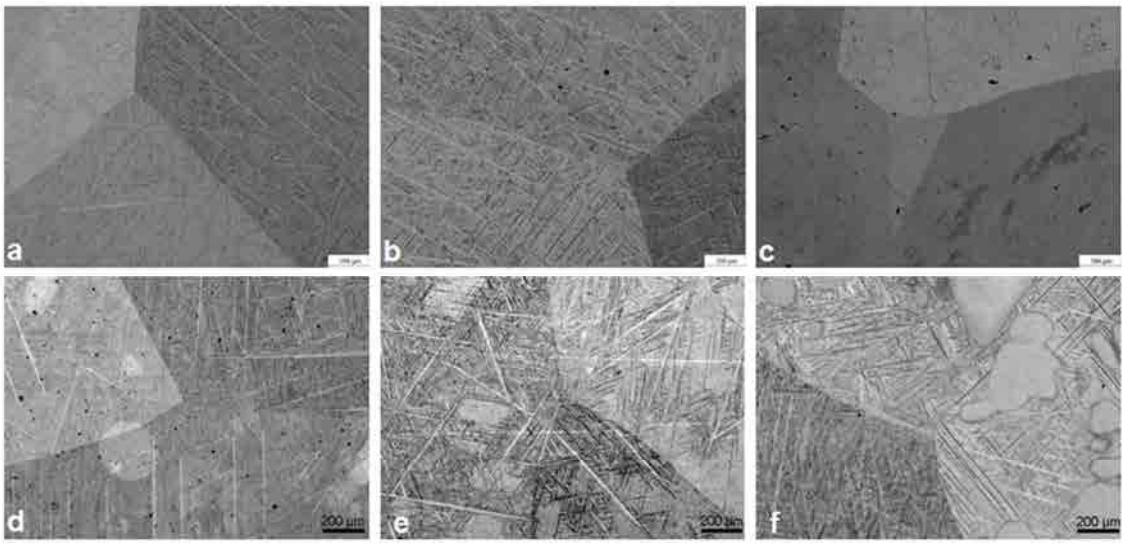

Fig.47 Micrographs obtained by optical microscopy for the alloys Ti-24.8Nb-10Hf (a), Ti-24.8Nb-12Hf (b), Ti-24.8Nb-15Hf (c), Ti-24.8Nb-17Hf (d), Ti-24.8Nb-19Hf (e) and Ti-24.8Nb-21Hf (f).

2.2.2 XRD results

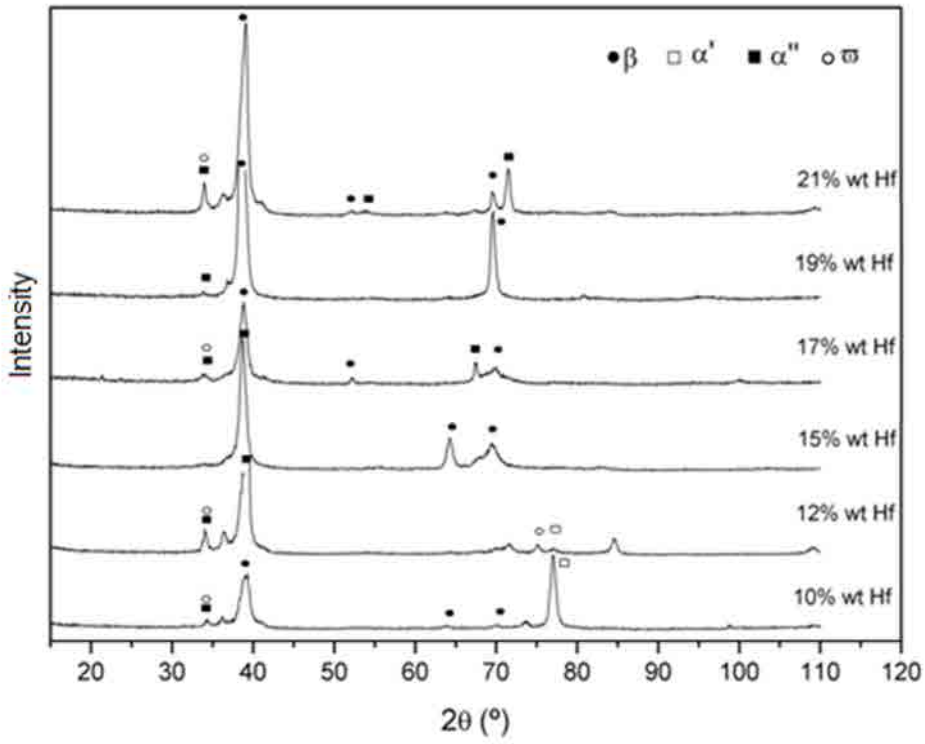

Fig.48 Normalized difractogram of the alloys Ti-24.8Nb-(10-21)Hf

In Fig.48 we can see ω phase is present in all the alloys except in those with a 15% w.t. and 19% w.t. of Hf. Omega phase is of difficult detection on diffractograms and it is possible its existence in both alloys, but not its detection with XRD.

In titanium alloys with beta-stabilizers which have been subjected to a quenching or aging treatment, the omega phase formation is common. The omega phase is metastable with respect to the quilibrium (α+β) or (α+ intermetallics). This is the case of our alloys and it is not estrange the presence of omega phase.

Comparing figures 45 and 48, it is observed that peaks appear in similar angles and with similar intensities. This might lead us to conclude that microstructure and thus, mechanical properties of the different materials, are similar with small variations.

2.2.3 TEM results

Omega phase was detected with XRD in all the alloys except in those with 15% wt and 19% wt of Hf. As the peak showing the ω-phase could be also identified as an α'' peak,

two alloys were studied by TEM to determine the proper peak. These alloys were those with 17% and 21% wt Hf.

The bright field images (Fig. 49) showed martensite plates in both alloys, but a great presence of β phase in the 17% Hf (Fig.49 a) alloy. The crystal diffraction pattern was tilted in a $[101]_{\beta}$. This morphology might be attributed to an α'' phase, which is characteristic of the thermoelastic martensite. The Diffraction pattern also revealed the presence of two variants [9,10] of the ω phase along the [101] zone axis (fig.7 a and b).

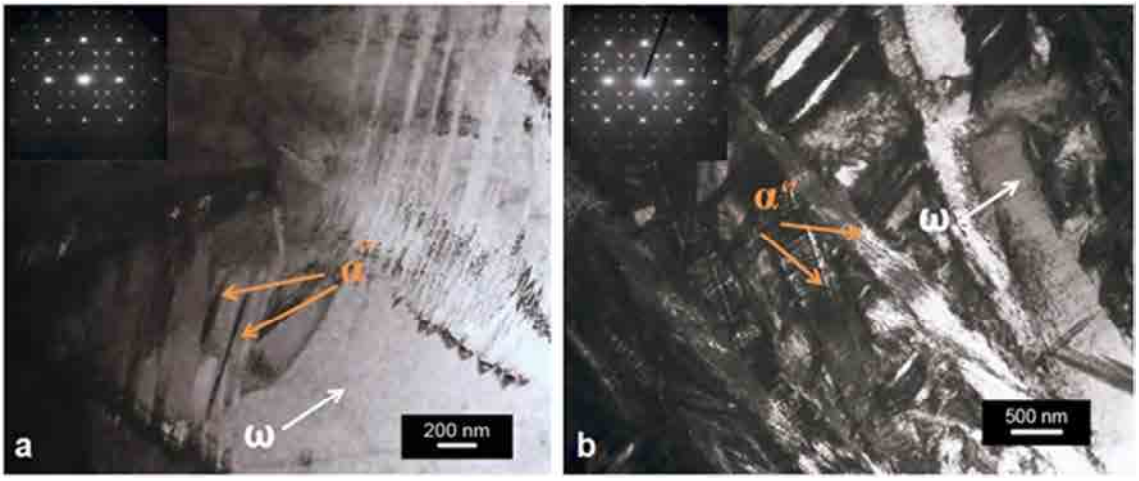

Fig.49 TEM images of the alloys Ti-24.8Nb-xHf with 17% Hf in (a) and 21% Hf in (b).

3. INFLUENCE OF THE COMPOSITION IN THE THERMOELASTIC PHASE TRANSFORMATION INDUCED BY STRESS

By means of P-h curves obtained by nanoindentation, the thermoelastic phase transformation induced by stress can be determined.

The thermoelastic phase transformation is shown by hysteresis loops on the loading (pop-in) or unloading curve (pop-out).

The wider the loops, the more reversibility of transformation will show the material. Pop-in's and pop-out's are an indicative of plastic deformation. These events are related to phase transformations induced under the indenter[11]. Materials with just a pure elastic deformation show loading-unloading curves practically equal[12].

3.1 Effect of niobium in the thermoelastic phase transformation

Looking at the Ti-(20-29)Nb-16.2Hf alloys group (see Fig. 50) we see that all of them present loops, but they are not equally wide in all cases. As the Nb content increases loops are being narrowed. This trend agrees with the change observed in the microstructure of the alloys: a high content in Nb is translated in a less martensitic structure.

The elastic recovery of the material is similar in all cases except for 23% Nb (Fig. 50 c) and 27% Nb (Fig. 50 e) alloys. As they show narrower loops, they should be alloys with less reversibility, but it is clearly observed how the recovery of the indenter trace is higher for both alloys.

It should be pointed out that for the alloys with 26% w.t. Nb (Fig. 50 d) and 27% w.t. Nb (Fig.50 e) pop-in's exist. We can conclude then that for these alloys there is a plastic deformation.

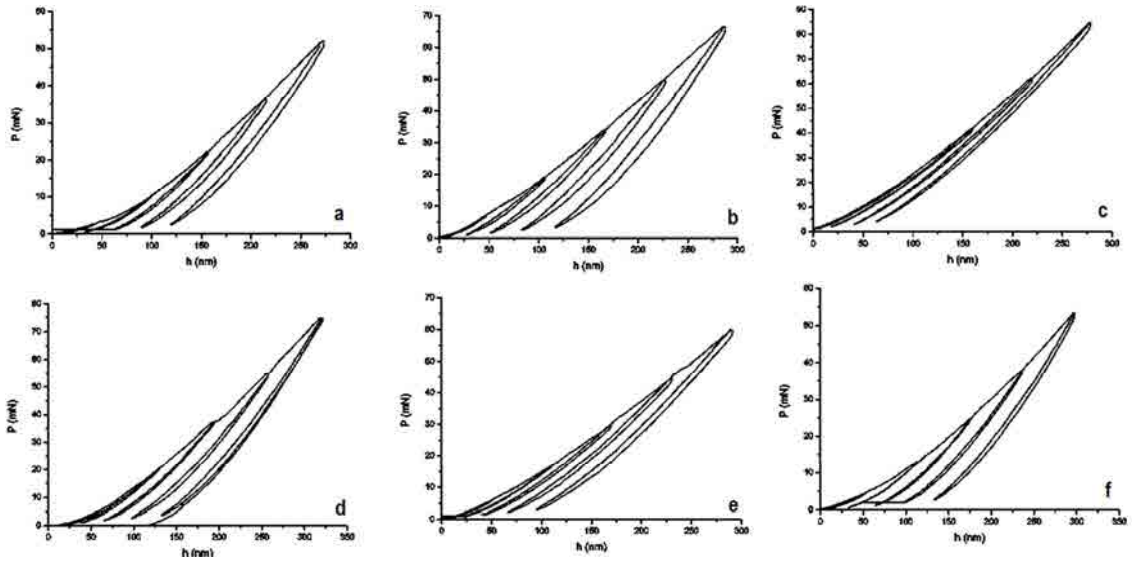

Fig.50 Nanoindentation curves obtained for 5 cycles of loading-unloading at an indentation depth of 300nm for the alloys Ti-20Nb-16.2Hf (a), Ti-22Nb-16.2Hf (b), Ti-23Nb-16.2Hf (c), Ti-26Nb-16.2Hf (d), Ti-27Nb-16.2Hf (e) and Ti-29Nb-16.2Hf (f).

3.1 Effect of hafnium in the thermoelastic phase transformation

In the manner of the Ti-(20-29)Nb-16.2Hf group alloys (Fig. 50), the Ti-24.8Nb(10-21)Hf group alloys (Fig. 51) also present the characteristic loops of hysteresis of phase transformation induced by stress.

As the Hf amount increases, the loops are becoming wider, except for the 15% w.t. Hf (Fig. 51 c). For this alloy, the same behavior as for the 23-27% w.t. Nb (Fig. 50 c and e) alloys is observed. This behaviour is similar to that of the austenitic NiTi[13].

The alloys with 17% w.t. Hf (Fig. 51 d) and 19% w.t. Hf (Fig. 51 e) pop-in's show pop-in's. As was said before, these events are indicators of plastic deformation.

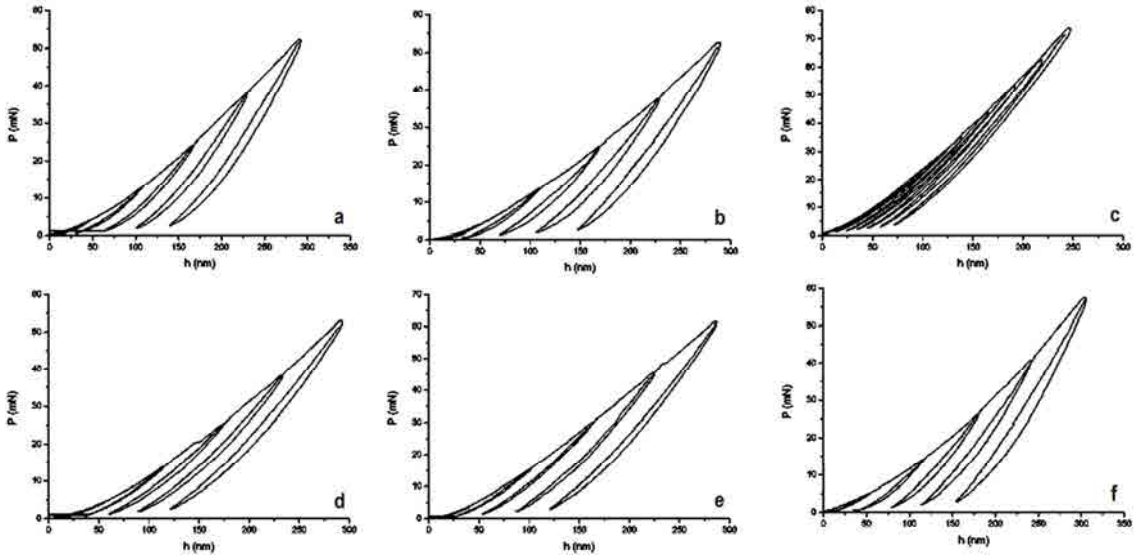

Fig.51 Nanoindentation curves obtained for 5 cycles of loading-unloading at an indentation depth of 300nm for the alloys Ti-24.8Nb-10Hf (a), Ti-24.8Nb-12Hf (b), Ti-24.8Nb-15Hf (c), Ti-24.8Nb-17Hf (d), Ti-24.8Nb-19Hf (e) and Ti-24.8Nb-21Hf (f)

4. INFLUENCE OF THE COMPOSITION IN THE ELASTIC MODULUS

To know the elastic modulus of the alloys the P-h curves at 2000 nm depth were used. The first is 100 nm of each curve was approximated to the Hertz's Equation. The slope of the curve determined the elastic modulus.

Nine nanoindentations were done on each sample and the obtained moduli and the average for each curve were calculated. .

4.1 Effect of niobium in the elastic modulus

According to Table 16, the modulus values for the Ti-(20-29)Nb-16.2 alloys group span from 38 to 77 GPa. In all the cases we are dealing with low elastic modulus alloys.

The elastic modulus values obtained show that for values of Nb percentage above 22% wt the modulus increases drastically, but for values above 27%wt Nb the value of the elastic modulus decreases again (Fig.52). As was shown in section 2.1, the increase in Nb content is translated in a β-phase microstructure.

Elastic Modulus (GPa)						
% wt Nb	**20**	**22**	**23**	**26**	**27**	**29**
Average	41,71	38,29	77,40	74,17	74,00	68,42
SD	5,62	9,01	2,51	4,58	7,30	2,31
Max	50,00	57,00	80,00	79,00	86,00	72,00
Min	36,00	32,00	75,00	69,00	68,00	65,00

Table 16. Modulus of elasticity according to the %wt of Nb on each alloy, with the maximum and minimum values obtained.

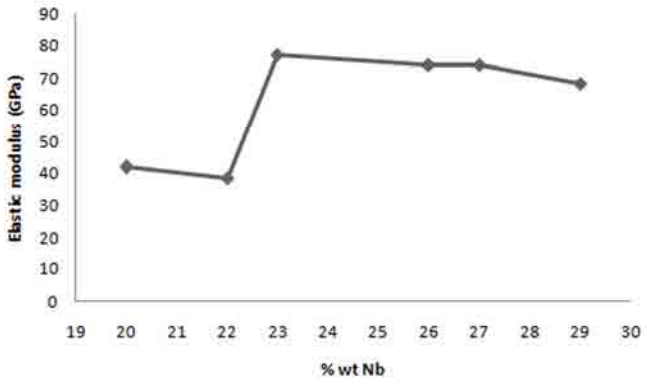

Fig.52 Graphic variation of the modulus of elasticity according to the %wt of Nb on each alloy, with the maximum and minimum values obtained.

Looking at the P-h curves for the first 100nm fitted to Hertz Equation (Fig.53), differences in slopes between the elastic and plastic zone can be observed. The change in the slope is an indicative of the transition from the plastic deformation to the elastic deformation.

The change from the elastic to the plastic behaviour, according to the curves, takes place for a 2 nN average applied force and with an approximately 34 nm penetration depth. This trend was seen for all the alloys except for the 23% wt Nb in which the force to pass from the elastic to plastic regime was 12 nN and the penetration depth 80 nm (Fig. 53c). In other words, the 23% wt Nb alloy can be deformed with higher loads keeping its elastic behavior.

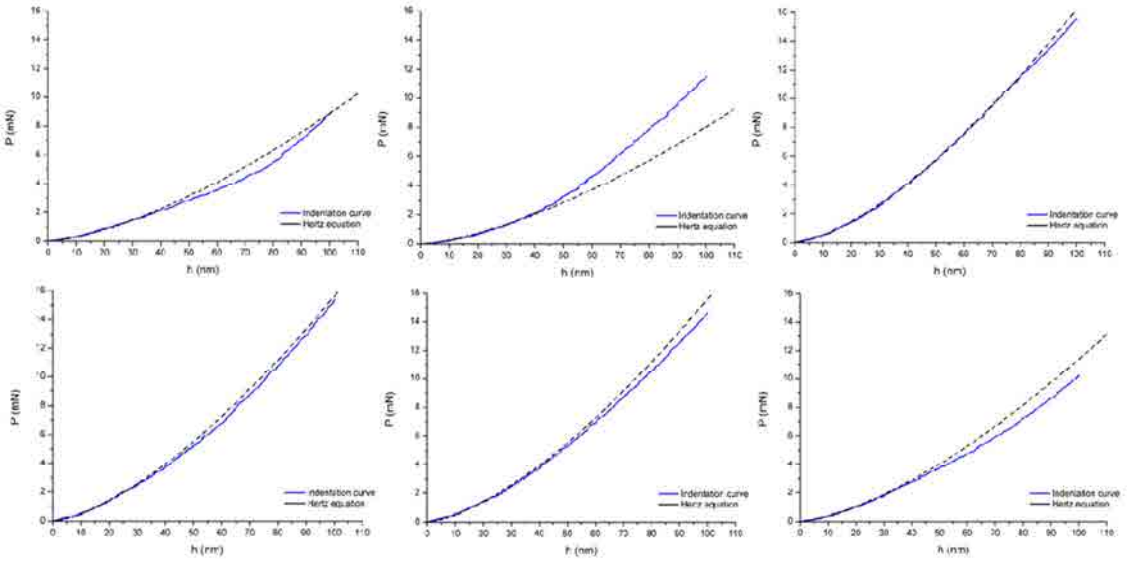

Fig.53 Nanoindentation curves obtained for the first 100nm for the alloys Ti-20Nb-16.2Hf (a), Ti-22Nb-16.2Hf (b), Ti-23Nb-16.2Hf (c), Ti-26Nb-16.2Hf (d), Ti-27Nb-16.2Hf (e) and Ti-29Nb-16.2Hf (f) and with the Hertz's Equation fitting. The change in the slope determines the transition from elastic to plastic deformation.

4.2 Effect of hafnium in the elastic modulus

Previous studies about the effect of Hf on the elastic modulus[14–16] reported low influence or an increase of the modulus with the addition of Hf.

According to Table 17, the obtained moduli are in a range of 45-77 GPa, that means there is a variation of modulus depending on the Hf amount in the alloy despite no trend is seen between Hf quantity and modulus (Fig. 54)

Elastic Modulus (Gpa)						
% wt Hf	**10**	**12**	**15**	**17**	**19**	**21**
Average	45,11	77,40	57,20	50,83	76,00	51,57
SD	3,74	6,58	1,10	2,41	8,91	5,62
Max	49,00	87,00	58,00	52,25	85,00	59,00
Min	38,75	70,00	56,00	46,00	60,00	42,00

Table 17. Modulus of elasticity according to the %wt of Hf on each alloy, with the maximum and minimum values obtained.

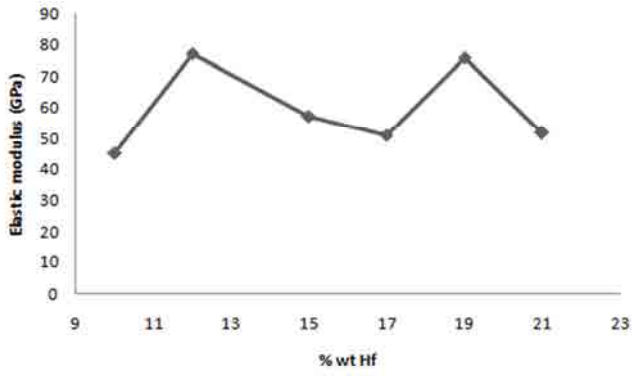

Fig.54 Graphic variation of the modulus of elasticity according to the %wt of Hf on each alloy, with the maximum and minimum values obtained.

The change from the elastic to the plastic behavior, according to the curves, took place for a 40 nN average applied force, but the penetration depth was not as constant as in the Nb alloys. For the Hf alloys it ranged from 1.5 to 5.4 nm. This trend was seen for all the alloys except for the 21% wt Hf in which the force to pass from the elastic to plastic regime was 7.5 nN and the penetration depth 79 nm.

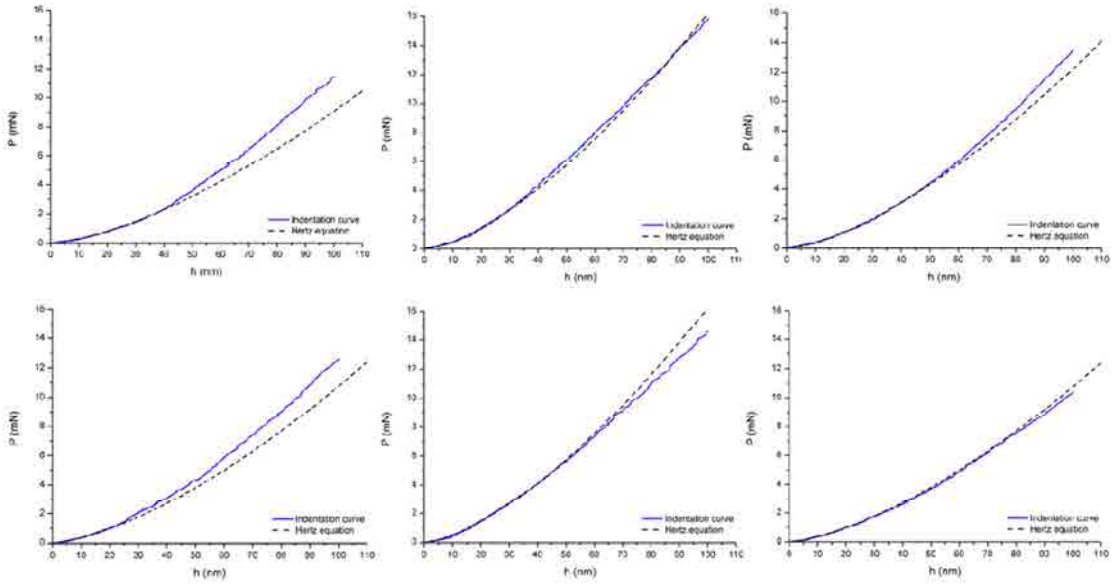

Fig.55 Nanoindentation curves obtained for the first 100nm for the alloys Ti-24.8Nb-10Hf (a), Ti-24.8Nb-12Hf (b), Ti-24.8Nb-15Hf (c), Ti-24.8Nb-17Hf (d), Ti-24.8Nb-19Hf (e) and Ti-24.8Nb-21Hf (f) and with the Hertz's Equation fitting. The change in the slope determines the transition from elastic to plastic deformation.

5. ALLOY'S SELECTION CRITERIA

Amongst the 12 alloys fabricated and studied, just one was chosen to work with and make further assays.

The criteria for determine the parameters to be considered in the material selection were:

- Quantum parameters as close as possible to the ones described for Gum Metal[17,18]
- High elastic deformation regime
- Low elastic modulus

The quantum parameters of interest were Bo=2.87 eV, Md=2.45 eV and e/a=4.24. The BO and OE calculated values can be easily translated into Bo and Md values to compare the values.

In Table 18 the values of Bo, Md and e/a for each alloy are displayed. There are two alloy compositions that showed quantum parameters close to the ones desired: 29% wt Nb and 21% wt Hf.

Formulation	Bo (eV)	Md (eV)	e/a
GUM METAL	**2.87**	**2.45**	**4.24**
Ti-20Nb-16.2Hf	2.848	2.473	4.1314
Ti-22Nb-16.2Hf	2.853	2.473	4.1463
Ti-23Nb-16.2Hf	2.855	2.473	4.1539
Ti-26Nb-16.2Hf	2.863	2.473	4.1773
Ti-27Nb-16.2Hf	2.865	2.473	4.1853
Ti-29Nb-16.2Hf	**2.871**	**2.473**	**4.2017**
Ti-24.8Nb-10Hf	2.849	2.460	4.1584
Ti-24.8Nb-12Hf	2.852	2.464	4.1613
Ti-24.8Nb-15Hf	2.858	2.470	4.1654
Ti-24.8Nb-17Hf	2.861	2.475	4.1692
Ti-24.8Nb-19Hf	2.865	2.479	4.1725
Ti-24.8Nb-21Hf	**2.869**	**2.483**	**4.1760**

Table 18. Values of the quantum parameters Bo, Md and e/a corresponding to each alloy composition.

The alloy elasticity is important for further processing. If the elastic regime is high the material could be easily machined.

In Fig.56 the different elastic-plastic behaviour of the alloys is shown. Comparing woth alloys it is clear that the elastic región of the 21 %wt Hf is higher than the one of the 29 %wt Nb.

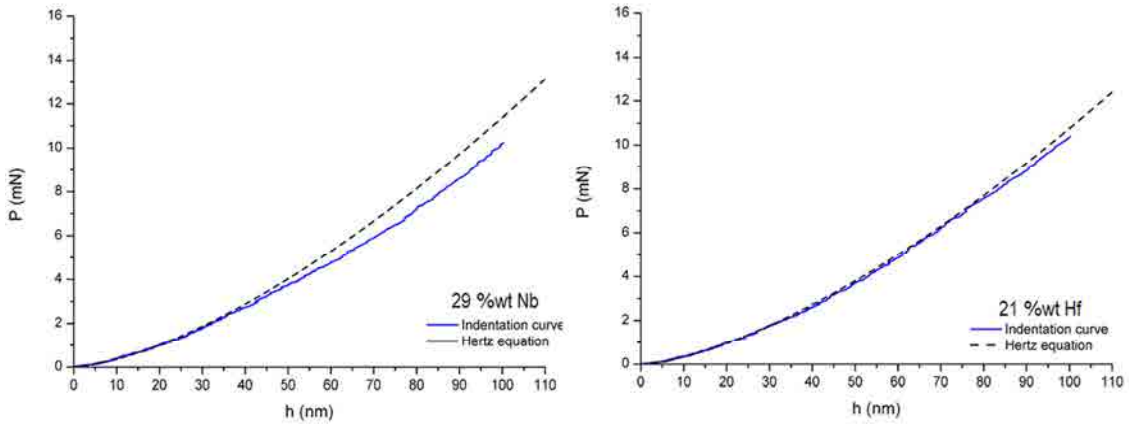

Fig.56 Nanoindentation curves obtained for the first 100nm for the alloys Ti-29Nb-16Hf and Ti-25Nb-21Hf with the Hertz's Equation fitting. The change in the slope determines the transition from elastic to plastic deformation.

The elastic modulus obtained by nanoindentation for the 29 %wt Nb has a value of 68.42 GPa which is higher than the modulus obtained for the 21 %wt Hf with value 51.57 GPa.

According to the values of quantum parameters, elastic behaviour and elastic modulus, the chosen alloy to work with was the Ti-25Nb-21Hf.

6. BIBLIOGRAPHY

1. Gonzalez, M., Peña, J., Manero, J. M., Arciniegas, M. & Gil, F. J. Desing and Characterization of New Ti-Nb-Hf alloys. *J. Mater. Eng. Perform.* **18,** 490 (2009).

2. Arciniegas, M., Peña, J., Manero, J. M., Paniagua, J. C. & Gil, F. J. Quantum parameters for guiding the design of Ti alloys with shape memory and/or low elastic modulus. *Philos. Mag.* **88,** 2529 (2008).

3. Amick, D. D. Characterization of TiNbHf alloys for potential medical dental applications. (1993).

4. Geetha, M., Singh, A. K., Asokamani, R. & Gogia, A. K. Ti based biomaterials, the ultimate choice for orthopaedic implants – A review. *Prog. Mater. Sci.* **54,** 397–425 (2009).

5. Matsuno, H., Yokoyama, A., Watari, F., Uo, M. & Kawasaki, T. Biocompatibility and osteogenesis of refractory metal implants, titanium, hafnium, niobium, tantalum and rhenium. *Biomaterials* **22,** 1253–1262 (2001).

6. Hon, Y. H. & Wang Y.N, J. Y. and P. Composition/Phase Structure and Properties of Titanium-Niobium Alloys. *Mater. Trans.* **44,** 2384 (2003).

7. Li, S., Hao, Y., Yang, R., Cui, Y. & Niinomi, M. Effect of Nb on Microstructural Characteristics of Ti-Nb-Ta-Zr Alloy for Biomedical Applications. *Mater. Trans.* **42,** 2964–2969 (2002).

8. Nobuhito, S., Niinomi, M., Toshikazu, A., Takashi, S. & Tadahiko, F. Effects os Alloying Elements on Elastic Modulus of Ti-Nb-Ta-Zr System Alloy for Biomedical Applications. *Mater. Sci. Forum* **449-452,** 1269–1272 (2004).

9. De Fontaine, D., Paton, N. . & Williams, J. . The omega phase transformation in titanium alloys as an example of displacement controlled reactions. *Acta Metall.* **19,** 1153–1162 (1971).

10. Sukedai, E., Hashimoto, H. & Tomita, M. Investigation of omega-phase in Ti–Mo alloys by high resolution electron microscopy, image processing and dark-field methods. *Philos. Mag. A* **64,** 1201–1208 (1991).

11. Bradby, J. E., Williams, J. S. & Wong-Leung, J. Nanoindentation-induced deformation of Ge. *Appl. Phys. Lett.* **80,** 2651 (2002).

12. Oliver, W. C. & Pharr, G. M. An improved technique for determining hardness and elastic modulus using load and displacement sensing indentation experiments. *Mater. Reserch Soc.* **7,** 1564 (1992).

13. González, M., Peña, J., Manero, J. M., Arciniegas, M. & Gil, F. J. Optimization of the Ti-16.2Hf-24.8Nb-1Zr Alloy by Cold Working. **18,** 506 (2009).

14. Zhou, Y.-L., Niinomi, M. & Akahori, T. Changes in mechanical properties of Ti alloys in relation to alloying additions of Ta and Hf. *14th Int. Conf. Strength Mater.* **483-484,** 153–156 (2008).

15. Zhou, Y.-L., Niinomi, M. & Akahori, T. Dynamic Young's Modulus andMchanical Properites of Ti-Hf alloys. *Mater. Trans.* **45,** 1549 (2004).

16. Hon, Y. H., Wang, J. Y. & Pan, Y. N. Influence of hafnium content on mechanical behaviors of Ti–40Nb–xHf alloys. *Mater. Lett.* **58,** 3182–3186 (2004).

17. Saito, T. *et al.* Multifunctional Alloys Obtained via a Dislocation-Free Plastic Deformation Mechanism. **300,** 464 (2003).

18. Hao, Y. L. *et al.* Super-elastic titanium alloy with unstable plastic deformation. **87,** (2005).

Chapter 4

Ti-25Nb-21Hf Alloy Characterization

1. ALLOY'S MICROSTRUCTURE

1.1 Optical microscopy and grain size

The microstructure observed by optical microscopy (Fig.57) showed an alloy formed mainly of β-phase with grains of different phase.

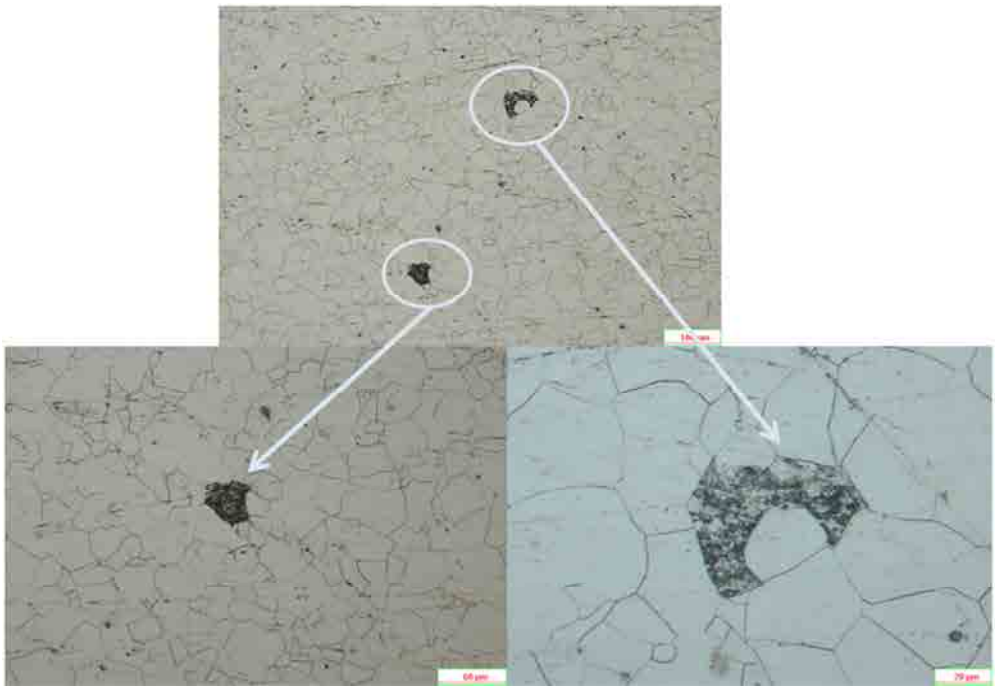

Fig.57 Micrographs obtained by optical microscopy for the Ti25Nb21Hf alloy at different augments showing the details of the grains shown.

The grain size was calculated for three different samples. Table 19 shows the values of grain size for each sample of the Ti25Nb21Hf alloy. In all the cases the grain size was less than 20 microns.

Sample	Grain size (Diameter in μm)
1	18.65 ± 14.7
2	10.74 ± 8.4
3	11.05 ± 9.2

Table 19. Values of the alloy's grain diameter obtained for three different Ti25Nb21Hf samples by means of a routine based on the ASTM E112 96 Standard Test Methods for determininig grain size which was ran in Buehler Omnimet software from registered trade mark Buheler Company, Lake Bluff, EE.UU.

1.2 X-ray diffraction (XRD)

According to the distance and the angles obtained by XRD for each peak identified in the alloy, the phases and the planes were identified (Table 20). The identification was done by means of comparison with the results for Ti, Nb and TiNb quenched alloy data available in the Power Diffraction File (PDF) data base and the values obtained according to software Carine v.3.0 by Ping et al. [1].

There are two peaks which couldn't be identified, a peak at 36,5º and a peak at 41,4º. On the other hand, some of the peaks identified can be related to more than one phase. The peak at 38,5º can be related to a α, α' α", β and ω phase. Taking a look to the diffractogram (Fig.58), the ω phase corresponds to a high peak. Usually ω phase is related to small peaks, for this reason, this phase was ruled out. The reticular parameter 'a' was calculated from the β peaks (at 55,3º and 69,5º) and a value of 3,319 Å was obtained.

Ti25Nb21Hf Diffraction angles and planes			
d	**2θ**	**Phase**	**Plane**
2,45198	36,5		
2,34656	38,5	β/α"/α/α'/ω/β	(1 1 0)/(0 0 2)/(0 0 2)/(0 0 2)/(2 -1 0)
2,18108	41,3		
1,65964	55,3	β	(2 0 0)
1,35074	69,5	β	(2 1 1)
1,17117	82,2	β/α/β	(2 2 0)/(0 0 4)/(2 2 0)
1,04588	94,8	α"	(1 3 3)

Table 20. Diffraction angles and planes obtained by comparison with the ones for Ti, Nb and TiNb quenched alloy for the Ti25Nb21Hf.

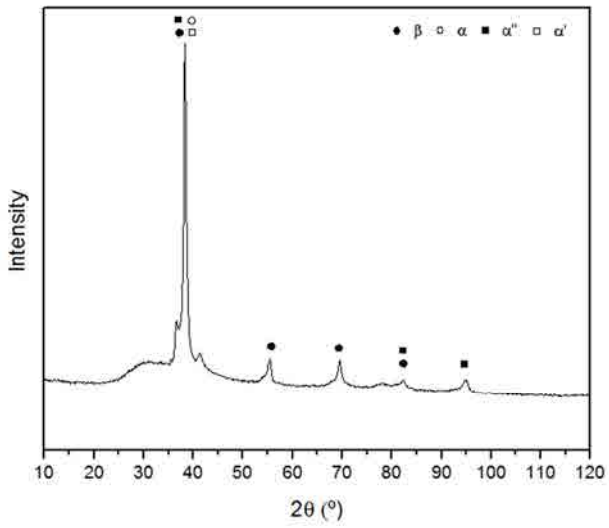

Fig.58 Diffractogram obtained for the Ti25Nb21Hf alloy. On each peak obtained, the possible phases are depicted.

1.3 Transmission electron microscopy (TEM)

TEM assays were conducted to elucidate which of the possible phases found by means of XRD were present in the alloy's microstructure.

According to Fig. 59a, the alloy's microstructure is mainly composed by equiaxial grains of β-phase with a high dislocations density. The diffraction diagram (Fig.59 a) shows a cubic centered structure in the body (BCC) with a zone axis [013]. This structure is typical of the β-phase. By means of the microscope's camera constant (2.606 mm.nm), the reticular parameter 'a' was obtained. The value of the 'a' parameter was 3.8 Å, which is also typical of the β-phase. An image of other area of the sample (Fig.59 b) showed martensite α´ or α´´ inside the β–phase grains.

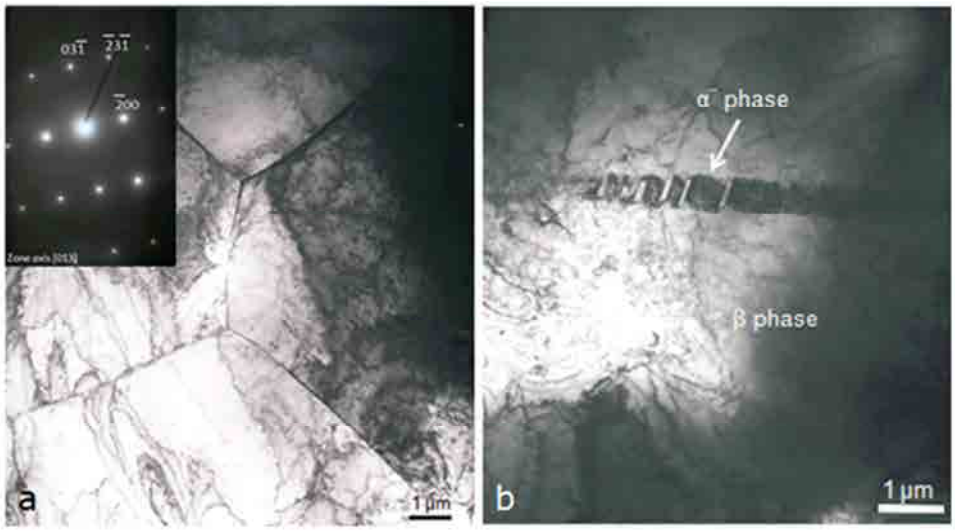

Fig.59 TEM images of the Ti25Nb21Hf alloy give evidence of a microstructure composed mainly of β-phase with thermoelastic martensite (α'').

2. DETERMINATION OF THE ELASTIC MODULUS

2.1 Elastic modulus by means of nanoindentation

Indentation load-displacement data contain a wealth of information. From the load displacement data many mechanical data such as hardness or elastic modulus can be obtained. Due to the fact that no evidence of phase transformation was shown by means of cyclic indentation, the elastic modulus was calculated by means of monotonic indentation. Fig.60 shows the values of elastic modulus as function of penetration depth at 100 nm (Fig. 60 a) and at 2000 nm (Fig. 60 b). In both conditions the modulus obtained for the Ti25Nb21Hf alloy was lower than the modulus obtained for the Ti6Al4V alloy.

Ti25Nb21Hf alloy had a value of elastic modulus of 96,7±7 GPa at 100 nm indentation depth whilst the value obtained at 2000 nm depth was 96,9±7 GPa. The elastic modulus values for the Ti6Al4V alloy were 123,3±20 GPa at 100 nm and 129,3±12 GPa at 2000 nm. The elastic modulus of the Ti25Nb21Hf alloy is clearly lower.

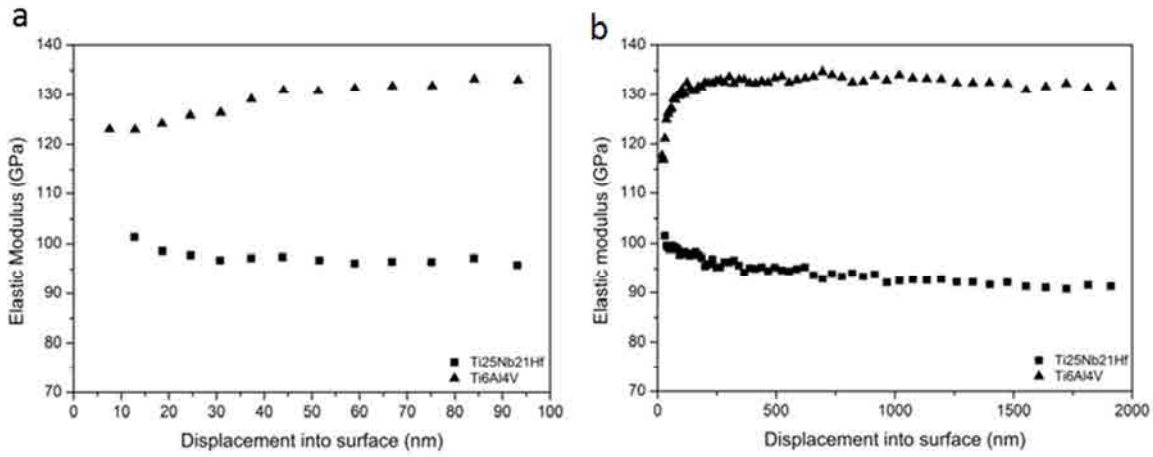

Fig.60 Elastic modulus evaluated using Berkovich nanoindentation as a function of penetration depth of indenter for the Ti25Nb21Hf and Ti6Al4V alloys at 100 nm (a) and 2000 nm (b).

2.2 Elastic modulus by means of tensile test

The representative stress-strain curves obtained during the tensile test for the Ti25Nb21Hf alloy and the control alloy Ti6Al4V are shown in Fig.61. The curve corresponding to the Ti6AL4V alloy showed a yield plateau that was not shown in the Ti25Nb21Hf alloy. In that region, the material continued deforming under a stress value which fluctuated around the yield limit. The Ti25Nb21Hf alloy showed an elastic zone and non-transition zone between the elastic and the plastic behaviour. The material kept deforming until reach the maxim stress.

The tensile strength shown for the Ti25Ng21Hf alloy was 906 MPa, which was less than the one shown for the Ti6Al4V that had a value of 951 MPa. The fracture stress observed for the Ti25Nb21Hf, 682 MPa, was also lower than the obtained for the Ti6Al4V alloy, 739 MPa.

According to the curves, the 25Nb21Hf alloy is less ductile than the Ti6Al4V alloy, but its elastic modulus is lower.

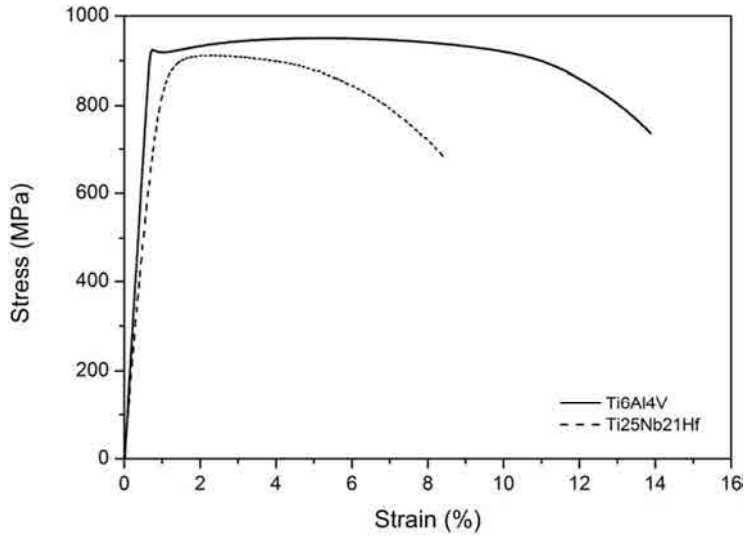

Fig.61 Stress-strain curves obtained from the tensile test for the study alloy Ti25Nb21Hf and the control alloy TI6Al4V.

The elastic modulus can be experimentally determined from the slope of the stress–strain curve created during tensile tests. In this thesis, the slope of the obtained curves for each specimen studied was calculated. The results are shown in Table 21. Test of the specimen 5 for the Ti25Nb21Hf alloy was ruled out due to the fact that the curve showed an abnormal behaviour. The values of the elastic modulus for the Ti25Nb21Hf alloy were lower than the ones obtained for the Ti6Al4V.

	Alloy	
	Ti6Al4V	**Ti25Nb21Hf**
Test	E (GPa)	E (GPa)
1	150	87,48
2	133,92	86,27
3	157,5	82,99
4	152,57	83,3
5	162,18	118,89
6	171,84	88,25
Mean	158,82	85,66
Std.	8,65	2,15

Table 21. Elastic modulus obtained from the tensile test curves for the study alloy Ti25Nb21Hf and the control alloy TI6Al4V.

3. ALLOY'S CORROSION RESISTANCE

3.1 Open circuit potential

The open circuit potential assay consists in measure the corrosion potential depending on time (E vs t). The electrochemical corrosion potential (E_{corr}) was measured for two hours and the data was registered each second.

Fig. 62 shows the curves measured for the open circuit assay for Ti cp, Ti6Al4V and Ti25Nb21Hf samples. The results show a long-term trend of cp Ti and Ti25Nb21Hf samples to more positives values than the Ti6Al4V samples. The more positive value was achieved by cp Ti samples followed by Ti25Nb21Hf alloy samples.

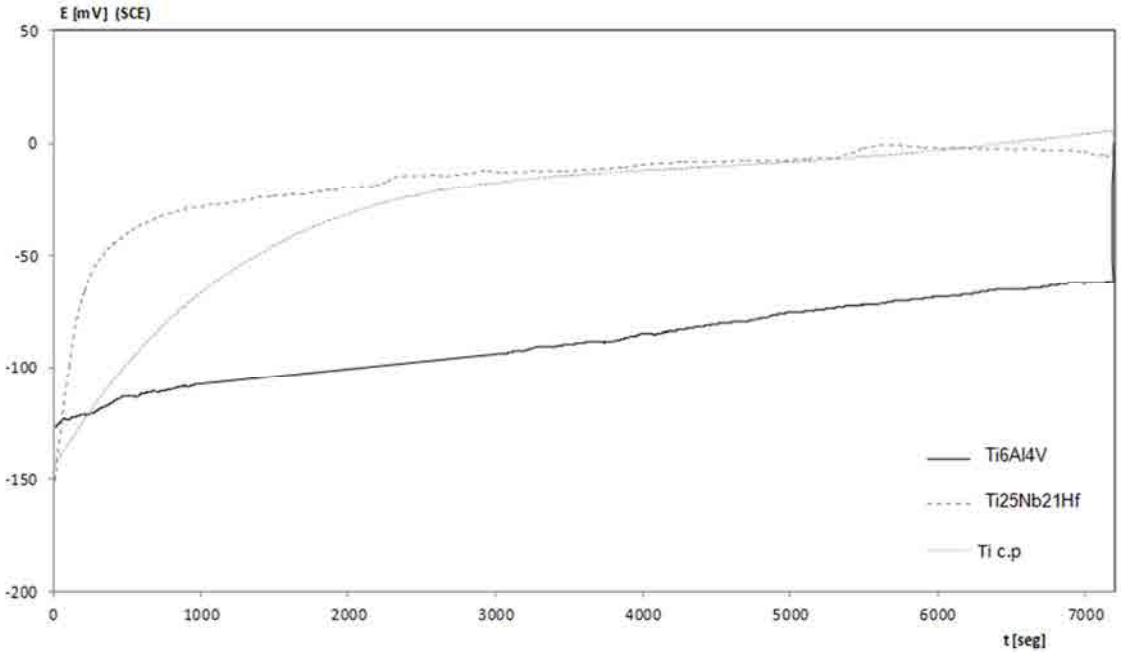

Fig.62 Open-circuit electrode potential as a function of time for the three materials under study in Hanks balance salt solution at 37ºC.

The positive slope of the Ti cp and Ti25Nb21Hf alloy is higher than that of the Ti6Al4V alloy. This result suggests a quicker reaction on the former samples when they get in contact with Hanks solution. These alloys create a protective layer of oxide which increases the electrochemical resistance of the material. The open circuit potential measured for each sample relative to the SCE electrode is shown in Table 22. Higher values of open circuit potential (E_{open}^{o}), indicates a higher resistance to corrosion under the assay conditions.

Material	E open circuit [mV]
Ti6Al4V	-58 ± 4
Ti25Nb21Hf	-6 ±15
Ti c.p	25 ± 15

Table 22. Open circuit potential for each material tested related to the calomel electrode. The potential of the calomel electrode vs the Standard hydrogen Electrode is 0,242V at 37ºC.

3.2 Cyclic voltammetry

The cyclic voltrammetry curves obtained for Ti cp, Ti6Al4V and Ti25Nb21Hf are shown in Figures 63, 64 and 65 respectively. The corrosion potential (E_{corr}) observed for cp Ti was E_{cor} ≈-59 mV, Ti6Al4V showed a E_{cor} ≈-39 mV, whereas the Ti25Nb21Hf alloys showed a E_{cor} ≈-124 mV (Table 23). The corrosion current density (I_{cc}) values for cpTi and Ti6Al4V alloy are equivalent, whilst the value for Ti25Nb21Hf alloy showed a lower value. All three materials reach their respective stable passive current densities as the potential increases, indicating the existence of a passive layer. No breakdown was observed in either of the materials under study.

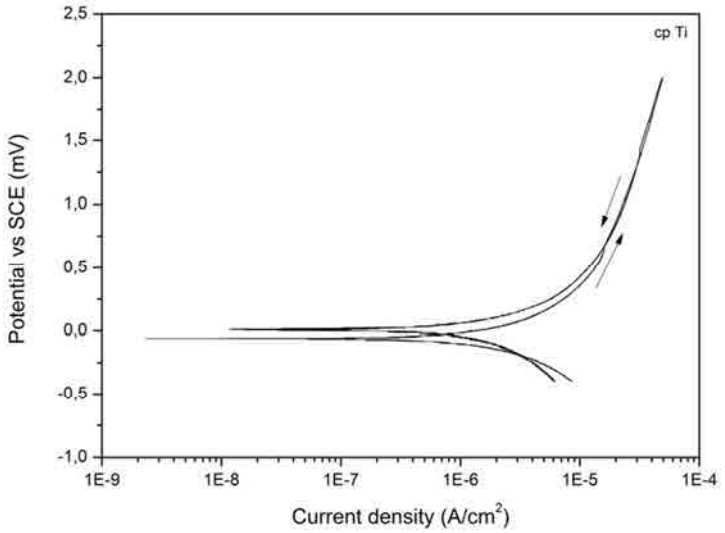

Fig.63 Cyclic voltammetry curve of cp Ti in Hanks solution.

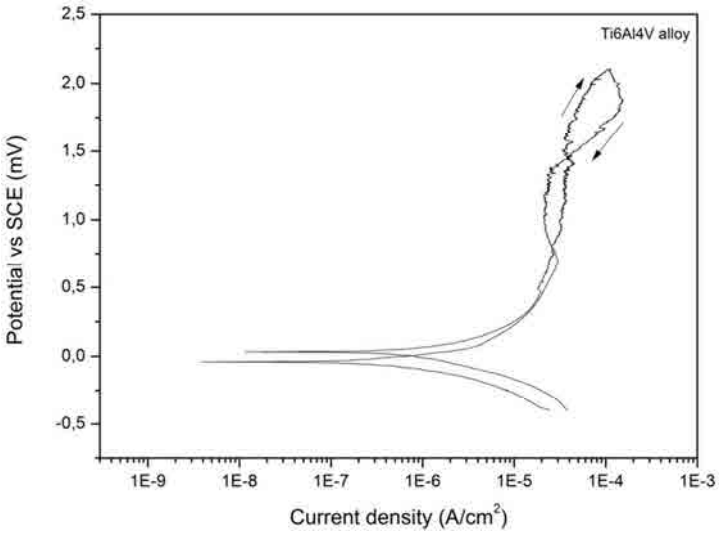

Fig.64 Cyclic voltammetry curve of Ti6Al4V in Hanks solution.

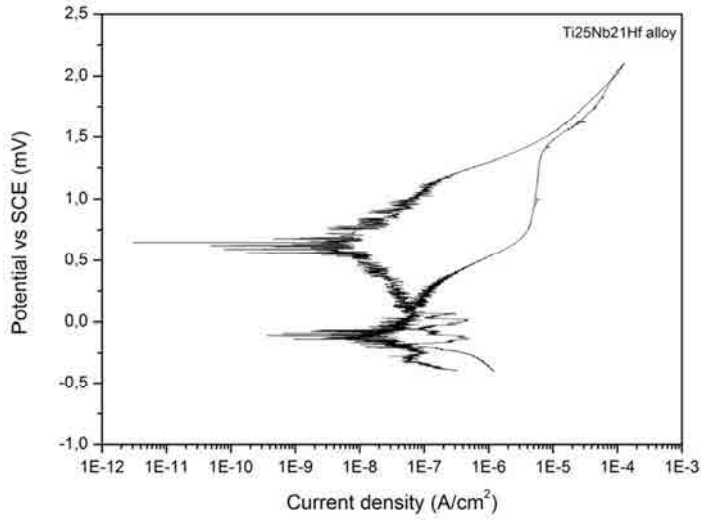

Fig.65 Cyclic voltammetry curve of Ti25Nb21Hf in Hanks solution.

Material	E_{corr} [mV]
Ti6Al4V	-39 ± 8
Ti25Nb21Hf	-124 ±35
Ti c.p	-59 ± 15

Table 23. Corrosion potential values obtained for each material tested with cyclic polarization.

When a metallic implant is placed in the body it could sustain electric potentials in the range of 0 to 500 mV. For these reason, the current density for potentials ranging to 0 to 500 mV and 500 to 1000 mV were also calculated (Table 24).

Material	Current [A/cm^2]	
	0-500 mV	500-1000 mV
Ti6Al4V	$1{,}58.10^{-6} – 2{,}18.\ 10^{-4}$	$2{,}39.\ 10^{-4} – 3{,}58.\ 10^{-4}$
Ti25Nb21Hf	$7{,}46.10^{-8} – 6{,}91.\ 10^{-7}$	$7{,}46.10^{-7} – 5{,}43.\ 10^{-6}$
cp Ti	$9{,}45.10^{-7} – 1{,}39.\ 10^{-5}$	$1{,}71.10^{-5} – 3{,}59.\ 10^{-5}$

Table 24. Current intensity measured for various potentials.

The values are shown in table 24. All samples tested exhibit a good electrochemical behaviour in the electrochemical working range for an implant inserted in a human body (0-500 mV). The Ti25Nb21Hf alloy also possess an excellent corrosion resistance (Ecorr = -124 mV) in a wide range of potentials (0-1000 mV) corresponding to the working range.

4. ALLOY'S SUPERFICIAL ENERGY

4.1 Contact angle measurements and SFE calculation

Fig. 66 shows the contact angles obtained by the sessile drop method on the different materials after a mechanical polishing to reach a roughness less than 100 nm. The contact angle observed for the alloy of study was 56º. This value is far from the 85º observed in cp Ti and slightly higher than the 45º observed for the Ti6Al4V alloy. The contact angles observed for diiodomethane are similar for cp Ti and Ti25NbHf alloy, whereas the values observed in Ti6Al4V alloy are lower.

The surface free energy (SFE) values and their dispersive and polar components are shown in Fig.67. SFE and polar and dispersive components grouped the samples into two differentiated groups: cp Ti in one hand and Ti6Al4V and Ti25Nb21Hf in the other hand. There are neither significant differences between the SFE nor between the polar SFE of Ti6Al4V and Ti25Nb21Hf alloys. Although the value of total SFE for cp Ti is

lower than for the other alloys, the dispersive component in all the samples is of the same order of magnitude. The differences are explained by the differences in the polar component being the one for cp Ti the lower one. The values of the total SFE, Γ_t, and the values of its polar, Γ^p, and dispersive, Γ^d, components, according to Owens and Wendt's model (Fig.67), show that in all three materials the molecular interactions are mainly dispersive

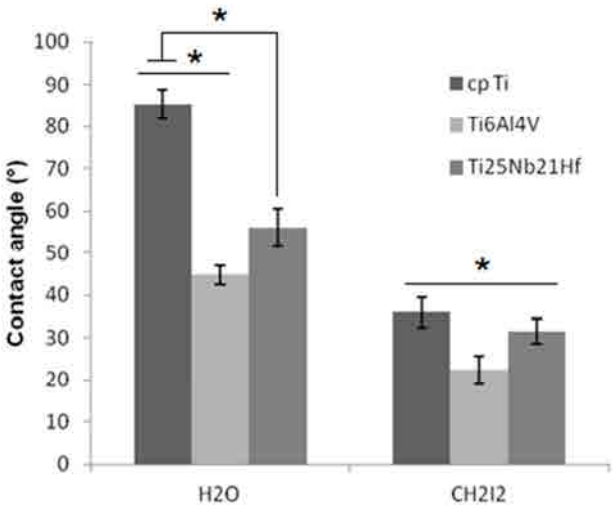

Fig.66 Contact angles for the different studied materials (Ti cp2, Ti6Al4v and TiNbHf) obtained with for distilled water (H_2O) and diiodomethane (CH_2I_2). Error bars represent a standard deviation for n=9. The asterisk means differences between samples with p<0,05.

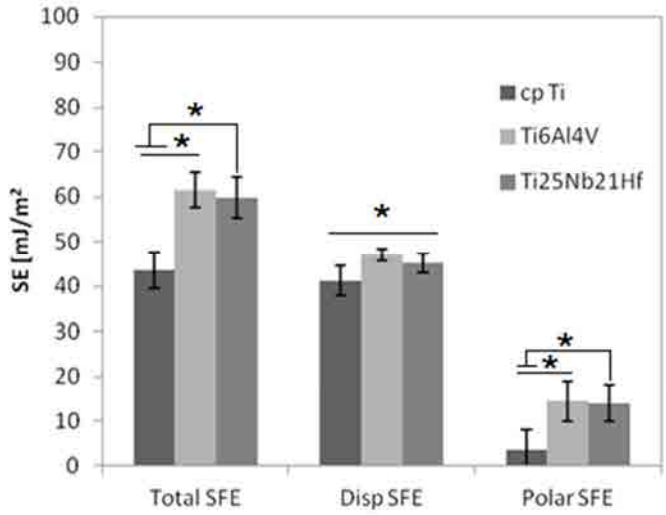

Fig.67 Total surface free energy (γ), polar (γp) and dispersive (γd) components of surface free energy calculated using the Owens-Wendt approach. Error bars represent a standard deviation for n=9. The asterisk means differences between samples with p<0,05.

4.2 Zeta potential results

The calculations were made using the Fairbrother and Mastin approach. This approach determines the length and cross-section of the rectangular slit between adjacent membrane samples from resistance and (electrolyte) conductivity measurements under conditions where interfacial conductance becomes negligible (e.g. at an ionic strength of 0.1 mol/L).

Zeta-potential measurements showed different electrokinetic behavior in the interactions at the interface between aqueous electrolyte and each material surface studied. Fig.68 shows zeta-potential versus pH for a standard 1mM KCl solution for cp Ti, Ti6Al4V and Ti52Nb21Hf. All samples showed zeta-potential/pH curve behavior between pH 2 and 8. The isoelectrical point (IEP) is the point where the curve crosses pH axis. For cp Ti an IEP of 3.2 was detected. In the case of Ti6Al4V and Ti25Nb21Hf alloys the IEP was found at pH 2.4 and 2.1 respectively. Slightly difference was shown in the IEP for the Ti6Al4V and Ti25Nb21Hf samples. The zeta-potential versus pH curves for these two materials showed no significant differences.

The zeta-potentials for each material at pH 7 are shown in Fig.69. The higher zeta-potential belongs to the Ti25Nb21Hf alloy

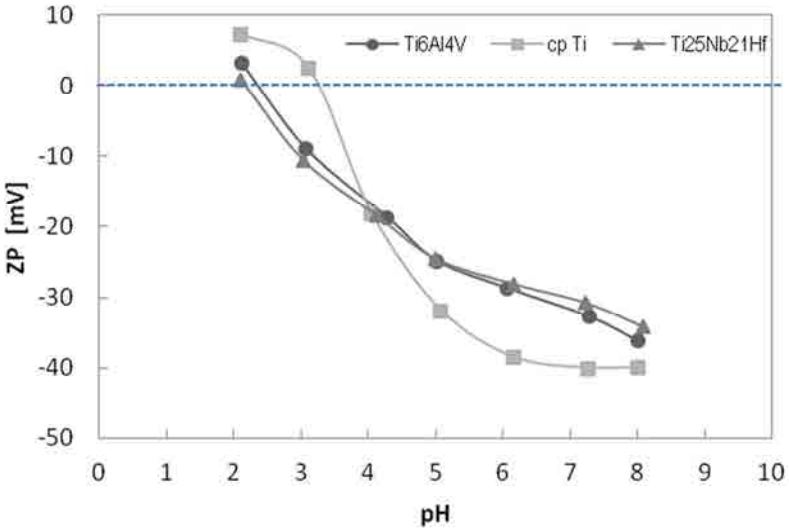

Fig.68 pH dependence of the zeta-potential for Ti cp2, Ti6Al4V and TiNbHf in a KCl electrolyte with a concentration 1mM. Different zeta-potential between the materials studied was demonstrated.

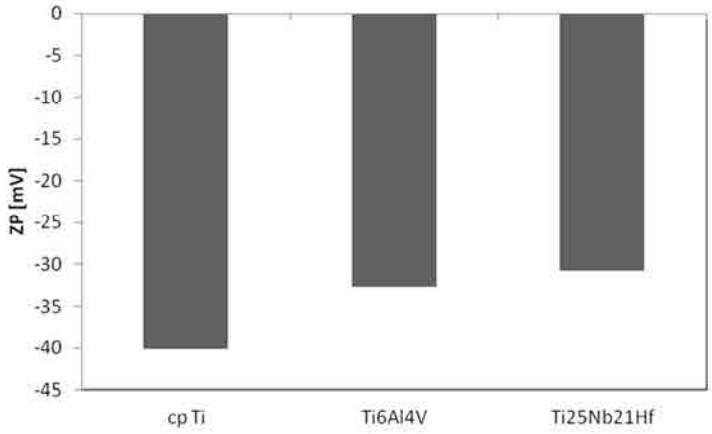

Fig.69 Zeta-potentials of the different samples at pH 7.

5. BIBLIOGRAPHY

1. Ping, D. H., Cui, C. Y., Yin, F. X. & Yamabe-Mitarai, Y. TEM investigations on martensite in a Ti–Nb-based shape memory alloy. *Scr. Mater.* **54,** 1305–1310 (2006).

2. Zhou, Y.-L., Niinomi, M. & Akahori, T. Changes in mechanical properties of Ti alloys in relation to alloying additions of Ta and Hf. *14th Int. Conf. Strength Mater.* **483-484,** 153–156 (2008).

3. Zhou, Y.-L., Niinomi, M. & Akahori, T. Dynamic Young's Modulus andMchanical Properites of Ti-Hf alloys. *Mater. Trans.* **45,** 1549 (2004).

4. Hon, Y. H. & Wang Y.N, J. Y. and P. Composition/Phase Structure and Properties of Titanium-Niobium Alloys. *Mater. Trans.* **44,** 2384 (2003).

5. Hon, Y. H., Wang, J. Y. & Pan, Y. N. Influence of hafnium content on mechanical behaviors of Ti–40Nb–xHf alloys. *Mater. Lett.* **58,** 3182–3186 (2004).

Chapter 5

Recombinant fibronectin fragments production

1. AMPLIFICATION OF THE FN FRAGMENTS

After RNA purification, its quality was determined by the nucleic acids/protein ratio and the acids/alcohol ratios. The obtained values are shown in Table 25.

CONCENTRATION µg/µl	0.89
RATIO 260/280	1.9
RATIO 260/230	1.4

Table 25. Values obtained by a nanodrop equipment regarding RNA extraction quality.

The ratios 260/280 had a value of 1.9 and the value of the ratio 260/230 was 1.4. Both values are between the values stated as ideal for RNA purity. (www.nanodrop.com. Wilmington, Delaware USA ©2007 NanoDrop Technologies, Inc).

RNA was retrotranscribed to cDNA and specifically amplified using the primers for each fragment. After the amplification the molecular weight of each fragment was checked by means of electrophoresis. The CAS d1-d3 fragment consists of 832 pair of bases and the HBII fragment, of 831 pair of bases. As could be seen in Fig.70, the molecular weight is the correct one in both cases.

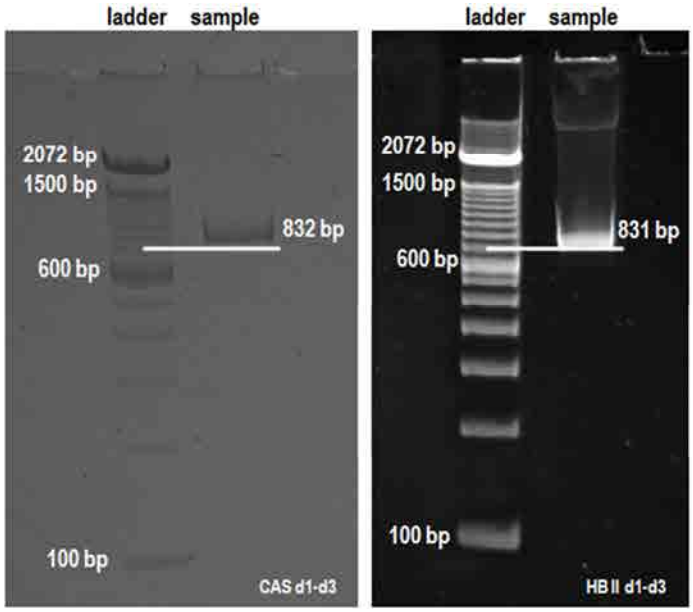

Fig.70 Electrophoresis of the amplified fragments CAS d1-d3 and HBII d1-d3 showing the pair of basis for each fragment.

2. PLASMID-DNA LIGATION

After fragments insertion in the pGEX plasmid, colonies of the DH5α E.coli strain were grown and it was checked which of them had inserted the correct fragment. To determine this, the molecular weight was determined by electrophoresis.

Figure 71 and figure 72 show the molecular weight of the DNA sequences inserted in each colony for the $CAS_{d1\text{-}d3}$ fragment and $HbII_{d1\text{-}d3}$ respectively.

Only five of the nine colonies (1, 2, 5, 7 and 9) picked with the $CAS_{d1\text{-}d3}$ fragment had inserted the DNA fragment in the plasmid (Fig. 71). According to the ladder, all of the inserted fragments exhibited the theoretical molecular weight, approximately 830 bp. The inserted fragment that gave the highest signal in the electrophoresis was number 5, which was selected for DNA sequencing.

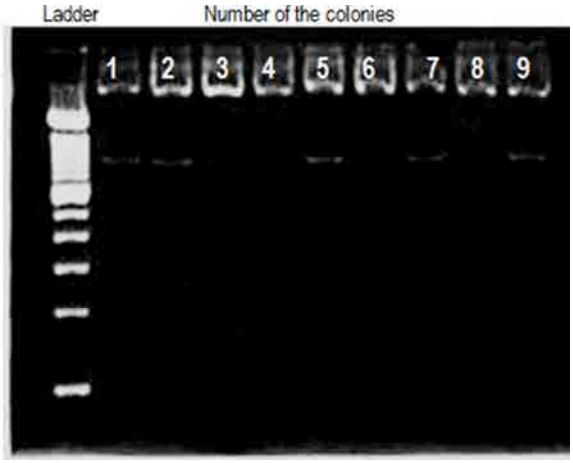

Fig.71 Electrophoresis gel showing the pair of basis of each picked colony with the inserted CAS d1-d3 sequence.

Only seven of the nine colonies transformed with $HbII_{d1\text{-}d3}$ grow and only four of them inserted a DNA sequence (see Fig.72). The colony 1 inserted a higher molecular weight fragment, while the other 3 colonies (2, 4 and 6) inserted the fragment with the theoretical molecular weight; approximately 831 bp. Amongst them, the colony 2 was selected for DNA sequencing.

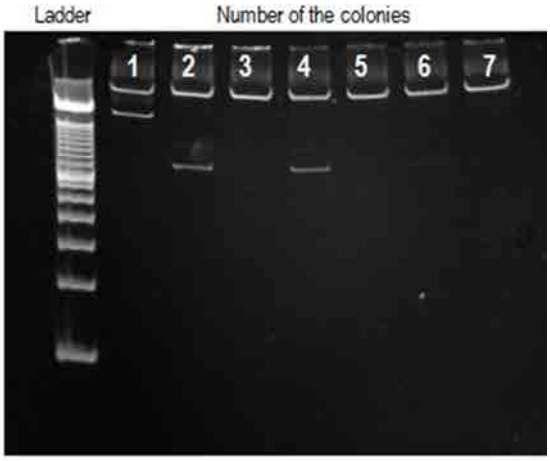

Fig.72 Electrophoresis gel showing the pair of basis of each picked colony with the inserted HbII d1-d3 sequence.

3. DNA FRAGMENTS SEQUENCING

Owing to the fact that a minimum amount of DNA is needed for the sequencing, the concentration of the inserted sequences was calculated. Table 26 show the results obtained for colony seven of the DH5α cells transformed with the $CAS_{d1\text{-}d3}$ fragment and for the colony two of the $HBII_{d1\text{-}d3}$.

FRAGMENT	CONCENTRATION (ng/µl)
CAS d1-d3	70.92
HB2 d1-d3	103,75

Table 26. Concentration of the DNA fragments obtained after plasmid insertion and cell transformation.

As it was said in Chapter 2 section 5.4, the sequencing was done at the Genomic Services of the UB (http://www.ccit.ub.edu/CA/tb06.html). The sequence obtained was in the 5' direction and in the 3' direction. To check the sequence in the 3' direction the DNA sequence obtained was transformed into the complementary form and was read in the reverse direction. First of all the primers were identified, then the targets and finally the DNA fragment sequence. Since the amplification process can introduce mutations, the nucleotides obtained were compared with the original ones. If there has been any

change in the DNA sequence, this could lead to an amino acid substitution or to a truncated protein. Sometimes this mutation leads to no error in transcription because there is more than one amino acid that codifies the same protein as could be seen in table 27.

Second base in codon

First base in codon	U	C	A	G	Third base in codon
U	Fen	Ser	Tir	Cis	U
	Fen	Ser	Tir	Cis	C
	Leu	Ser	STOP	STOP	A
	Leu	Ser	STOP	Trp	G
C	Leu	Pro	His	Arg	U
	Leu	Pro	His	Arg	C
	Leu	Pro	Gln	Arg	A
	Leu	Pro	Gln	Arg	G
A	Ile	Tir	Asn	Ser	U
	Ile	Tir	Asn	Ser	C
	Ile	Tir	Lis	Arg	A
	Met	Tir	Lis	Arg	G
G	Val	Ala	Asp	Gli	U
	Val	Ala	Asp	Gli	C
	Val	Ala	Glu	Gli	A
	Val	Ala	Glu	Gli	G

Table 27. Codon chart.

3.1 CAS_{d1-d3} fragment sequencing

The original sequence for the CAS_{d1-d3} fragment is:

CAAGTTCCTCCTCCCACTGACCTGCGATTCACCAACATTGGTCCAGACACCATGCGTGTCACCTGGGCTC
CACCCCCATCCATTGATTTAACCAACTTCCTGGTGCGTTACTCACCTGTGAAAAATGAGGAAGATGTTGC
AGAGTTGTCAATTTCTCCTTCAGACAATGCAGTGGTCTTAACAAATCTCCTGCCTGGTACAGAATATGTA
GTGAGTGTCTCCAGTGTCTACGAACAACATGAGAGCACACCTCTTAGAGGAAGACAGAAAACAGGTCTTG
ATTCCCCAACTGGCATTGACTTTTCTGATATTACTGCCAACTCTTTTACTGTGCACTGGATTGCTCCTCG
AGCCACCATCACTGGCTACAGGATCCGCCATCATCCCGAGCACTTCAGTGGGAGACCTCGAGAAGATCGG
GTG**CCCC**ACTCTCGGAATTCCATCACCCTCACCAACCTCACTCCAGGCACAGAGTATGTGGTCAGCATCG
TTGCTCTTAATGGCAGAGAGGAAAGTCCCTTATTGATTGGCCAACAATCAACAGTTTCTGATGTTCCGAG
GGACCTGGAAGTTGTTGCTGCGACCCCCACCAGCCTACTGATCAGCTGGGATGCTCCTGCTGTCACAGTG
AGATATTACAGGATCACTTACGGAGAGACAGGAGGAAATAGCCCTGTCCAGGAGTTCACTGTGCCTGGGA

GCAAGTCTACAGCTACCATCAGCGGCCTTAAACCTGGAGTTGATTATACCATCACTGTGTATGCTGTCAC
TGGC**C**GTGGAGA**C**AGCCCCGCAAGCAGCAAGCCAATTTCCATTAATTACCGAACA.

The underlined zones correspond to the primers' sequence. The primer, the reading direction, the target, the added of the starting guideline and of the riding guideline are detailed in Chapter 2 section 4.1. The d1 primer is marked in red; the d3 primer is marked in green and the targets in blue. The $CAS_{d1\text{-}d3}$ sequence is underlined in grey and the mutations are in black.

The sequence for the pGEX 5' direction was:

TCTCAATGGATCTGGAGTTCTGTTCCAGGGGCCCCTGGGATCCCCGGAATTCCCGGGTCGACAAGTTCCT
CCTCCCACTGACCTGCGATTCACCAACATTGGTCCAGACACCATGCGTGTCACCTGGGCTCCACCCCCAT
CCATTGATTTAACCAACTTCCTGGTGCGTTACTCACCTGTGAAAAATGAGGAAGATGTTGCAGAGTTGTC
AATTTCTCCTTCAGACAATGCAGTGGTCTTAACAAATCTCCTGCCTGGTACAGAATATGTAGTGAGTGTC
TCCAGTGTCTACGAACAACATGAGAGCACACCTCTTAGAGGAAGACAGAAAACAGGTCTTGATTCCCCAA
CTGGCATTGACTTTTCTGATATTACTGCCAACTCTTTTACTGTGCACTGGATTGCTCCTCGAGCCACCAT
CACTGGCTACAGGATCCGCCATCATCCCGAGCACTTCAGTGGGAGACCTCGAGAAGATCGGGTGCCCCAC
TCTCGGAATTCCATCACCCTCACCAACCTCACTCCAGGCACAGAGTATGTGGTCAGCATCGTTGCTCTTA
ATGGCAGAGAGGAAAGTCCCTTATTGATTGGCCAACAATCAACAGTTTCTGATGTTCCGAGGGACCTGGA
AGTTGTTGCTGCGACCCCCACCAGCCTACTGATCAGCTGGGATGCTCCTGCTGTCACAGTGAGATATTAC
AGGATCACTTACGGAGAAACAGGAGGAAATAGCCCTGTCCAGGAGTTCACTGTGCCTGGGAGCAAGTCTA
CAGCTACCATCAGCGGCCTTAAACCTGGAGTTGATTATACCATCACTGTGTATGCTGTCACTGGCCGTGG
AGACAGCCCCGCAAGCAGCAAGCCAATTTCCATTAAGCGGCCGCATCGTGACTGACTGACGATCTGCCTC
GCGCGTTTCGGTGATGACGGTGAAAACCTCTGACACATGCAGCTCCCGGAGACGGTCACAGCTTGTCTGT
AAGCNGGATGCCGGGAGCAAANAAGCCCGTCAGGGCGCGTCANCGGGTGTTGGCGGGTGTCGGGGCCCAN
CCATGANCCNAGTCCCGTANCGNATAGGGGAAGNGTATAATTNTTGAAAAAAAAAANGGGCCCCNGGAAA
CCCCTATTTTTNTAAGGGTNAAGGTCNNGAAAAAAANGGGTTTTTNAAACGNCNGGGGGGCCNTTTTNCG
GGGAAAANGGGGCNGGNAACCCNANTTNGTTTTTTTTTNCAAAAANNTTTAAAANTGTTTCCCCCNNAGG
AAAAAAAAACCCGGAAAAAGGGTTCNTNANNTTTGNAAANGGGAAGNGGGNGGTTTTNNNNTTTCGGGGG
CCCCNNTTTCNTTTTTN

The sequence for the pGEX 3' direction was:

NTCTNCGAACGCGCGAGGCAGATCGTCAGTCAGTCACGATGCGGCCGCTTAATGGAAATTGGCTTGCTGC
TTGCGGGGCTGTCTCCACGGCCAGTGACAGCATACACAGTGATGGTATAATCAACTCCAGGTTTAAGGCC
GCTGATGGTAGCTGTAGACTTGCTCCCAGGCACAGTGAACTCCTGGACAGGGCTATTTCCTCCTGTTTCT
CCGTAAGTGATCCTGTAATATCTCACTGTGACAGCAGGAGCATCCCAGCTGATCAGTAGGCTGGTGGGGG
TCGCAGCAACAACTTCCAGGTCCCTCGGAACATCAGAAACTGTTGATTGTTGGCCAATCAATAAGGGACT

TTCCTCTCTGCCATTAAGAGCAACGATGCTGACCACATACTCTGTGCCTGGAGTGAGGTTGGTGAGGGTG
ATGGAATTCCGAGAGTGGGGCACCCGATCTTCTCGAGGTCTCCCACTGAAGTGCTCGGGATGATGGCGGA
TCCTGTAGCCAGTGATGGTGGCTCGAGGAGCAATCCAGTGCACAGTAAAAGAGTTGGCAGTAATATCAGA
AAAGTCAATGCCAGTTGGGGAATCAAGACCTGTTTTCTGTCTTCCTCTAAGAGGTGTGCTCTCATGTTGT
TCGTAGACACTGGAGACACTCACTACATATTCTGTACCAGGCAGGAGATTTGTTAAGACCACTGCATTGT
CTGAAGGAGAAATTGACAACTCTGCAACATCTTCCTCATTTTTCACAGGTGAGTAACGCACCAGGAAGTT
GGTTAAATCAATGGATGGGGGTGGAGCCCAGGTGACACGCATGGTGTCTGGACCAATGTTGGTGAATCGC
AGGTCAGTGGGAGGAGGAACTTGTCGACCCGGGAATTCCGGGGATCCCAGGGGCCCCTGGAACANAACTT
CCAGATCCGATTTTGGAGGATGGTCGCCACCACCAAACGTGGCTTGCCAGCCCTGCAAAGGCCATGCTAT
ATACTTGCTGGATTTCAAGTACTTATCAATTTGTGGGANAGCTTCAATACGTTTTTTTAAACAAACTANT
TTGGGAACNCATCCNGCCCATNGGGTCCATGTANAAAAACNTCANNAGCGTCTAAAACNGAANTCNGGAN
GGGTTANTGATNCCNTTTAAATTGTTTTATNAAAAAAACAATTTTCNAAATTTTNNNCATTTNGGNANTT
GNTAAAAAAANNACTTTAAANTTTCAAATNTTTNNTTTNNAATTTNNAAAACCCNNNNTNAAANNNAAAC
CCCCNNTNAAAAN

The results obtained showed an error during the RT-PCR for the CAS $_{d1\text{-}d3}$. An A codon base was mutated into a G codon base. In this case this mutation did not affect the translation, because according to the codon chart both GAA and GAG translate the same amino acid: Glutamate.

3.2 HbII$_{d1\text{-}d3}$ fragment sequencing

The original sequence for the HbII$_{d1\text{-}d3}$ fragment is:

GCTATTCCTGCACCAACTGACCTGAAGTTCACTCAGGTCACACCCACAAGCCTGAGCGCCCAGTGGACAC
CACCCAATGTTCAGCTCACTGGATATCGAGTGCGGGTGACCCCCAAGGAGAAGACCGGACCAATGAAAGA
AATCAACCTTGCTCCTGACAGCTCATCCGTGGTTGTATCAGGACTTATGGTGGCCACCAAATATGAAGTG
AGTGTCTATGCTCTTAAGGACACTTTGACAAGCAGACCAGCTCAGGGAGTTGTCACCACTCTGGAGAATG
TCAGCCCACCAAGAAGGGCTCGTGTGACAGATGCTACTGAGACCACCATCACCATTAGCTGGAGAACCAA
GACTGAGACGATCACTGGCTTCCAAGTTGATGCCGTTCCAGCCAATGGCCAGACTCCAATCCAGAGAACC
ATCAAGCCAGATGTCAGAAGCTACACCATCACAGGTTTACAACCAGGCACTGACTACAAGATCTACCTGT
ACACCTTGAATGACAATGCTCGGAGCTCCCCTGTGGTCATCGACGCCTCCACTGCCATTGATGCACCATC
CAACCTGCGTTTCCTGGCCACCACACCCAATTCCTTGCTGGTATCATGGCAGCCGCCACGTGCCAGGATT
ACCGGCTACATCATCAAGTATGAGAAGCCTGGGTCTCCTCCCAGAGAAGTGGTCCCTCGGCCCCGCCCTG
GTGTCACAGAGGCTACTATTACTGGCCTGGAACCGGGAACCGAATATACAATTTATGTCATTGCCCTGAA
GAATAATCAGAAGAGCGAGCCCCTGATTGGAAGGAAAAAGACA

The underlined zones correspond to the primers' sequence. The primer, the reading direction, the target, the added of the starting guideline and of the riding guideline are

detailed in Chapter 2 section 4.1. The d1 primer is marked in red; the d3 primer is marked in green and the targets in blue. The HB $II_{d1\text{-}d3}$ sequence is underlined in grey and the mutations are in black.

The sequence for the pGEX 5' direction was:

ATCTAATGGATTGGAGTTCTGTTCCAGGGGCCCCTGGGATCCCCGGAATTCCCGGGTCGACAAGCTATTC
CTGCACCAACTGACCTGAAGTTCACTCAGGTCACACCCACAAGCCTGAGCGCCCAGTGGACACCACCCAA
TGTTCAGCTCACTGGATATCGAGTGCGGGTGACCCCCAAGGAGAAGACCGGACCAATGAAAGAAATCAAC
CTTGCTCCTGACAGCTCATCCGTGGTTGTATCAGGACTTATGGTGGCCACCAAATATGAAGTGAGTGTCT
ATGCTCTTAAGGACACTTTGACAAGCAGACCAGCTCAGGGTGTTGTCACCACTCTGGAGAATGTCAGCCC
ACCAAGAAGGGCTCGTGTGACAGATGCTACTGAGACCACCATCACCATTAGCTGGAGAACCAAGACTGAG
ACGATCACTGGCTTCCAAGTTGATGCCGTTCCAGCCAATGGCCAGACTCCAATCCAGAGAACCATCAAGC
CAGATGTCAGAAGCTACACCATCACAGGTTTACAACCAGGCACTGACTACAAGATCTACCTGTACACCTT
GAATGACAATGCTCGGAGCTCCCCTGTGGTCATCGACGCCTCCACTGCCATTGATGCACCATCCAACCTG
CGTTTCCTGGCCACCACACCCAATTCCTTGCTGGTATCATGGCAGCCGCCACGTGCCAGGATTACCGGCT
ACATCATCAAGTATGAGAAGCCTGGGTCTCCTCCCAGAGAAGTGGTCCCTCGGCCCCGCCCTGGTGTCAC
AGAGGCTACTATTACTGGCCTGGAACCGGGAACCGAATATACAATTTATGTCATTGNCCTGAAGAATAAT
CAGAAGAGCGAGCCCCTGATTGGAANGAAAAAGACAGCGGCCGCATCGTGACTGACTGACGATCTGCCTC
GCGCGTTTCGGTGATGACGGTGAAACCTCTGACACATGCAGCTCCCGGAGACGGTCACAGCTTGTCTGTA
AGCGGATGCNGGANCAAANAANCCCGTCAGGGCCCNTCACNGGTGTTGGCGGGGTGTCGGGGCCCACCCT
GACCCATTCCGTACGANAGGGANTGTNAATTTTTGAAANAAAAGGCCNCNGAAACCCCNTTTTTAAGGTA
AGNCNGNAAAAANGGNTTNTNAANCCNGGGGGCNTTTTGGGNAAGGGGGGNANCCCCTTTNTTTTTTTTT
AAAANTNAAANGNTNCCCCCGGNAAAAACCCGGNAAGGTTTTANTTNAAAGGGAANAAGATTNAATTCGG
GGCCCNTTCTTTTNGGGTTTTTTTTNTTTTCCCNANCCGGNAAAAAAAAAAAATTGGGGGGGGGTTTNTN
TNTNNCCNAAAATTTNTTTCCNAAATTAAAAAATTTTGGGGGGGGGGGGGGGNCNCCCCNTTTTTTTNNN
NNNNAAAAANNNNNNNNNNNNNNNNNN

The sequence for the pGEX 3' direction was:

CNTGNNTNCGNAACGCGCGAGGCAGATCGTCAGTCAGTCACGATGCGGCCGCTGTCTTTTTCCTTCCAAT
CAGGGGCTCGCTCTTCTGATTATTCTTCAGGGCAATGACATAAATTGTATATTCGGTTCCCGGTTCCAGG
CCAGTAATAGTAGCCTCTGTGACACCAGGGCGGGGCCGAGGGACCACTTCTCTGGGAGGAGACCCAGGCT
TCTCATACTTGATGATGTAGCCGGTAATCCTGGCACGTGGCGGCTGCCATGATACCAGCAAGGAATTGGG
TGTGGTGGCCAGGAAACGCAGGTTGGATGGTGCATCAATGGCAGTGGAGGCGTCGATGACCACAGGGGAG
CTCCGAGCATTGTCATTCAAGGTGTACAGGTAGATCTTGTAGTCAGTGCCTGGTTGTAAACCTGTGATGG
TGTAGCTTCTGACATCTGGCTTGATGGTTCTCTGGATTGGAGTCTGGCCATTGGCTGGAACGGCATCAAC
TTGGAAGCCAGTGATCGTCTCAGTCTTGGTTCTCCAGCTAATGGTGATGGTGGTCTCAGTAGCATCTGTC
ACACGAGCCCTTCTTGGTGGGCTGACATTCTCCAGAGTGGTGACAACACCCTGAGCTGGTCTGCTTGTCA
AAGTGTCCTTAAGAGCATAGACACTCACTTCATATTTGGTGGCCACCATAAGTCCTGATACAACCACGGA
TGAGCTGTCAGGAGCAAGGTTGATTTCTTTCATTGGTCCGGTCTTCTCCTTGGGGGTCACCCGCACTCGA
TATCCAGTGAGCTGAACATTGGGTGGTGTCCACTGGGCGCTCAGGCTTGTGGGTGTGACCTGAGTGAACT

TCAGGTCAGTTGGTGCAGNAATAGCTTGTCGACCCGGGAATTCCGGGGAATCCCAGGGGCCCCNTGGAAC
AGAACTTCNANATCCGATTTNGAAGANGGTCNCCACCACCAAACGTGGCTTGCCANCCCTGCAAAGGCCA
TGCTAAAAACTNGCTGAATTCAATACTTATCAATTNGNGGGAANCTTCANACGTTTTTTAAAANAANTAA
TTTTGGNANCCATCCAGCCNATTGGGTCCATGTAAAAAANACNTCAANAGGTCTAACAANTGAAGTCNGG
AGGGGTANAGATCCCNTTTAAATGNTTNAAANAAANCATTTTCAAAATTTNNCCATTNCGGGACTGNAAA
AAAAAATTNAANTTNAANNNTTAANATGCAATNCNAAACCNAATTANACAAACNCCCTTAAATAAAACCC
CCCCCTTTGAANNCCCANNGTGGTTNNNCCTAANNGAAGGCCAAAGGTTTTCCCCCCAAAAAGGAGGGAA
CCCCCCCCNTTTTTCCTTTCCNCNCCAANGCNTTTTTNAAAAAAAAAGGGGGGCCCTNTAAAAAANAAAGGG
GNTTCCCCCCCNNGNGNTTTTTNTTATNNNNAANNNNNNNNNNNNNNNNNNN

The HB II $_{d1\text{-}d3}$ sequencing showed also a mutation in one of the nucleotides, an A codon base was changed for a T codon base. As in the previous sequencing, the mutation did not affect the amino acid sequence because both GGT and GGA translate the same amino acid: Glycine.

4. PROTEIN PURIFICATION AND QUANTIFICATION

4.1 Protein purification

After fragments sequence verification, the correct sequence was inserted in BL21 E.coli strains to express de protein. The bacteria culture was done as explained in Chapter 2 section 6. The purification process was also explained in the same chapter and section.

The chromatograms obtained during purification for CAS and HB II are shown in Fig.73 and Fig.74 respectively. The first peak corresponds to the purified protein; the step line reflects the injection of the reduced glutathione elution buffer needed to eliminate the GST from the purification column. The last peak corresponds to the pure GST eluted.

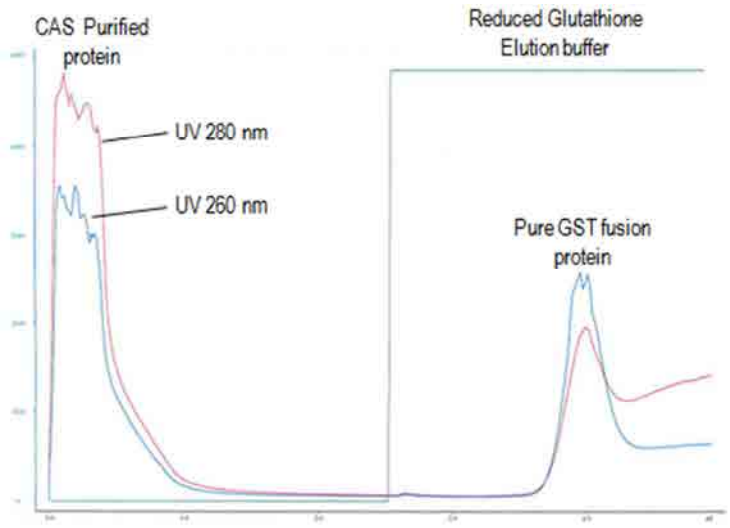

Fig.73 Chromatogram obtained during protein purification of the CAS fragment with the equipment ÄKTApurifier 10 by General Electric Healthcare.

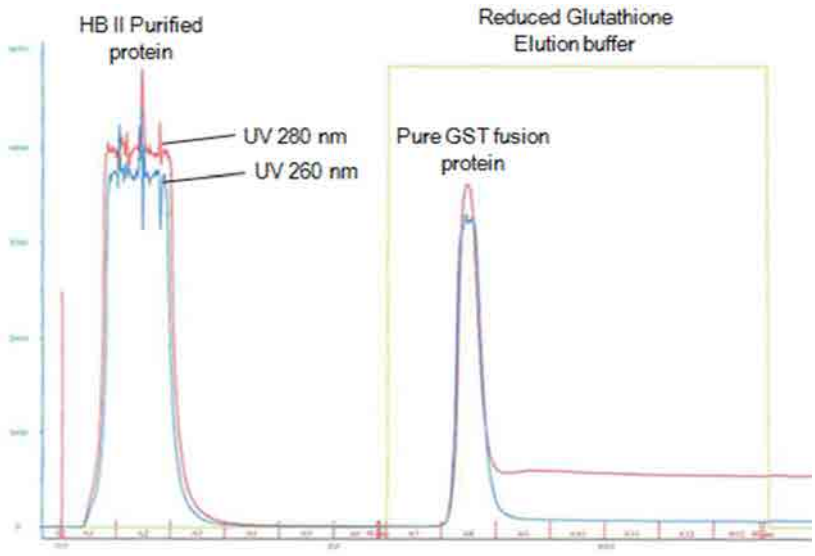

Fig.74 Chromatogram obtained during protein purification of the HB II fragment with the equipment ÄKTApurifier 10 by General Electric Healthcare.

Both CAS and HB II sequences have a molecular weight of 31kDa and 32kDa respectively. Figure 75 shows the SDS-PAGE for each fragment. There is more than one band, but the band of interest is located between the 37kDa and 25kDa. The other bands obtained might be attributed to other proteins synthesized by the bacteria which have affinity for our fragments, for the GST or even for the column. Despite this, the

intensity of our band of interest is much higher than the rest of bands; it is at least more than the 90% of the total

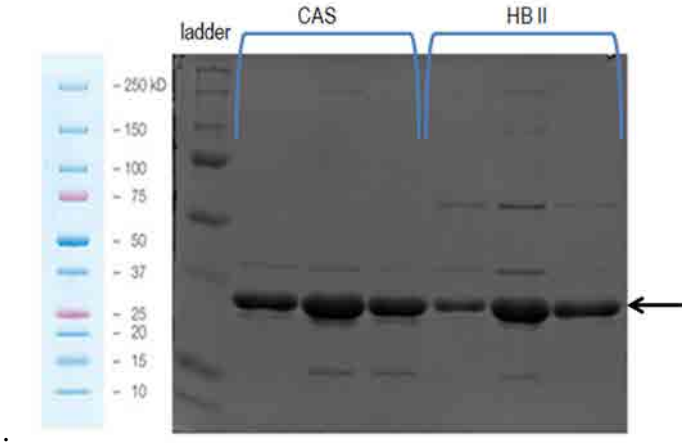

Fig.75 SDS-PAGE of the CAS and HBII fragments. The ladder used was *Precision Plus Protein™ Dual Color Standards* from BioRad.

4.2 Protein quantification

The quantification was done according to the *BCA Protein Assay Reagent* by *Thermo Scientific*. The absorbance is related with protein concentration according to the BSA standard curve prepared, as can be seen in Fig. 76.

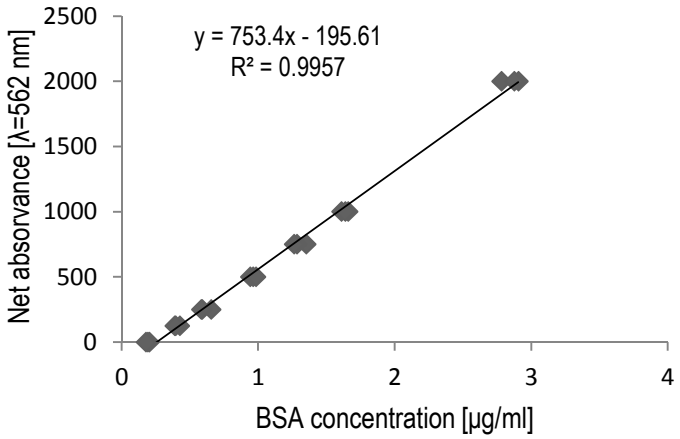

Fig.76 Standard curve for bovine serum albumin (BSA) obtained using the *BCA Protein Assay Reagent* by *Thermo Scientific* test to quantify the FN fragments CAS and HB II.

The values of the absorbance obtained for each fragment were substituted in the equation of the graph and translated into concentration. In the table 28 the concentration obtained in 1ml of eluted protein of each fragment is shown.

FRAGMENT	CONCENTRATION (µg/ml)
CAS d1-d3	3,78
HB2 d1-d3	6.92

Table 28. Concentration obtained by means of the *BCA Protein Assay Reagent* by *Thermo Scientific*.

Chapter 6

Optimization of the biofunctionalization process

As it was explained in the introduction, there are two main strategies to attach a molecule onto a surface: physisorption and covalent bonding. In this chapter both strategies were studied with the CAS and the HB II fragment. The aim was to determine the best technique to immobilise the molecules on the Ti25Nb21Hf alloy in terms of the efficiency of the technique to adhere protein and its conformation.

1. OPTICAL WAVEGUIDE LIGHTMODE SPECTROSCOPY SYSTEM (OWLS)

1.1 Physisorbed protein

The protein fragment was injected after base line stabilization. Immediately, the slope of the curve increased indicating the adsorption of protein onto the TiO_2 chip surface. Approximately 10 minutes after protein injection the adhesion rate started to diminish and it started to be less pronounced until almost reached a plateau. After 1h of incubation PBS was injected to remove the non-adsorbed protein (see Fig.77 and Fig.78). A change in the diffraction of the laser which was translated in a step on the curve can be observed. After PBS injection the line was stabilized again giving the mass adsorbed on the surface. In Fig.78 a valley instead of a step was seen after PBS injection. This was due to an air bubble trapped on the syringe that reached the flow cell.

The adsorbed mass for the CAS fragment was approximately 125 ng/cm^2 and for the HBII fragment was approximately 250 ng/cm^2.

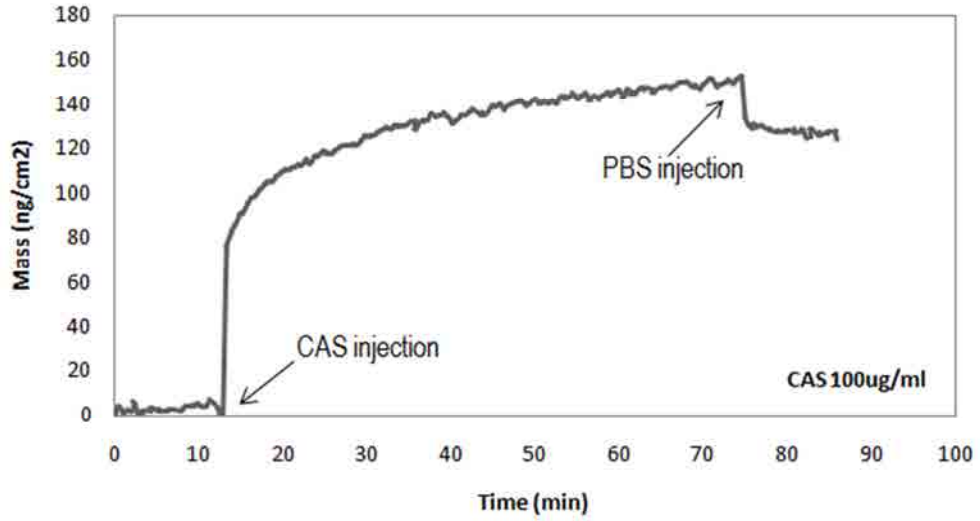

Fig.77 Adsorption curve obtained after CAS fragment injection onto bare TiO_2 chips. The baseline was made with PBS as buffer and the protein was injected 10 min after obtaining a linear baseline. After one hour of incubation PBS was injected and the non-adsorbed protein was removed from the chip surface.

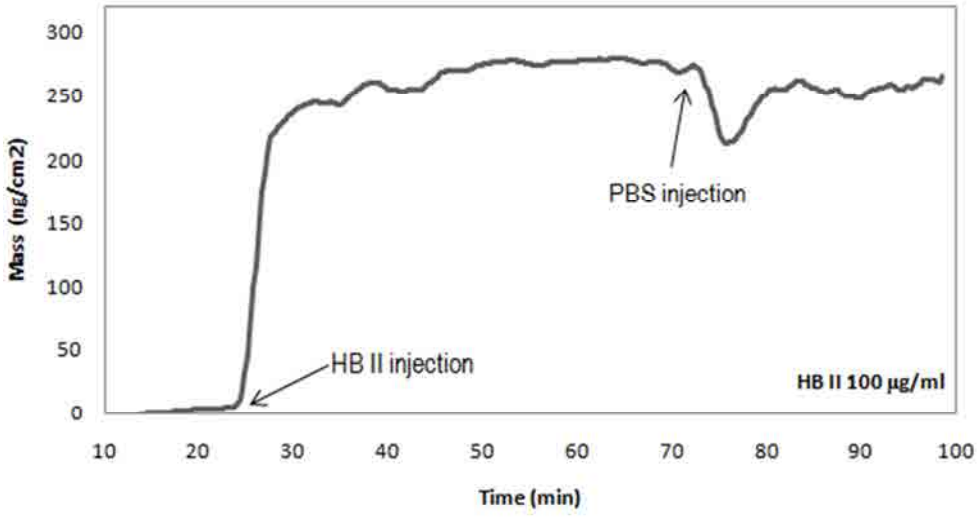

Fig.78 Adsorption curve obtained after HBII fragment injection onto bare TiO_2 chips. The baseline was made with PBS as buffer and the protein was injected 10 min after obtaining a linear baseline. After one hour of incubation PBS was injected and the non-adsorbed protein was removed from the chip surface.

1.2 Covalently bound protein

The protein fragment was injected after base line stabilization. Immediately the slope of the curve increased indicating the adsorption of protein onto the silanised TiO_2 chip surface. Less than 10 minutes after protein injection, the adhesion rate started to diminish and it was observed on the curve slope, it started to be less pronounced. In the covalently bound protein no plateau was observed after protein adhesion stabilization. After 1h incubation the PBS was injected to remove the protein that was not adsorbed onto the chip (see Fig.79 and Fig.80). There is then, a change in the diffraction of the laser which was translated in a step on the curve. After PBS injection the line was stabilized again giving the mass adsorbed on the surface.

The adsorbed mass for the CAS fragment was 280,34 ng/cm^2 and for the HBII fragment was 219,7 ng/cm^2.

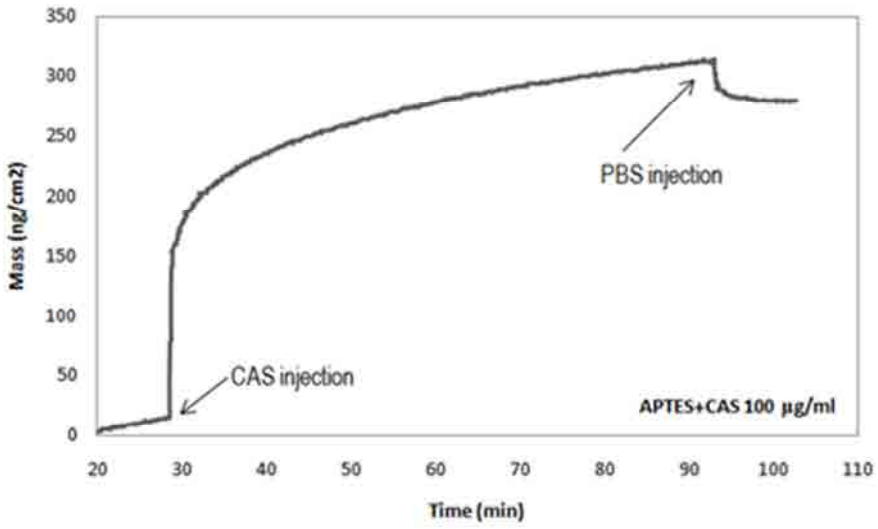

Fig.79 Adsorption curve obtained after CAS fragment injection onto silanised TiO_2 chips. The baseline was made with PBS as buffer and the protein was injected 10 min after obtaining a linear baseline. After one hour of incubation PBS was injected and the non-adsorbed protein was removed from the chip surface.

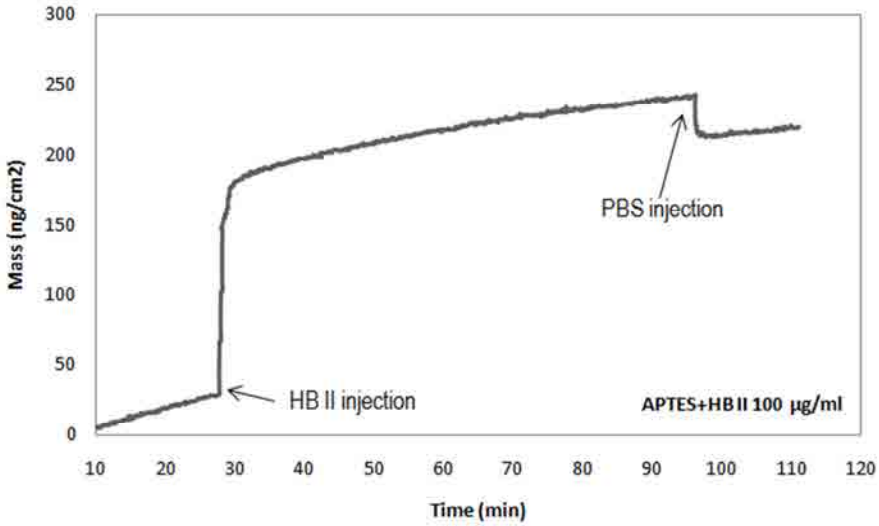

Fig.80 Adsorption curve obtained after HB II fragment injection onto silanised TiO_2 chips. The baseline was made with PBS as buffer and the protein was injected 10 min after obtaining a linear baseline. After one hour of incubation PBS was injected and the no- adsorbed protein was removed from the chip surface.

2. ATOMIC FORCE MICROSCOPY (AFM)

2.1 Physisorbed protein

Fig.81 shows the distribution of physisorbed CAS fragment onto the TiNbHf alloy. The surface was covered with the fragment and no aggregation areas were seen.

With the aim to determine the thickness of the protein layer adhered onto the surface a scratch was made (Fig.82) and five different points were measured. The values obtained are shown in Table 29.

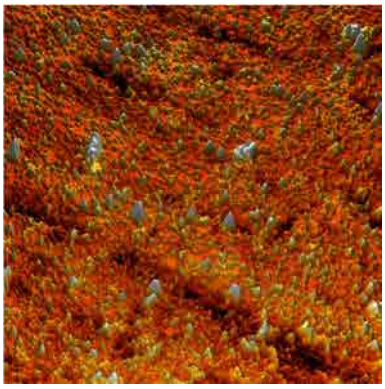

Fig.81 AFM tapping mode image in PBS at 37ºC of CAS fragment adsorbed onto TiNbHf alloy. The area scanned was 2 x 2 µm.

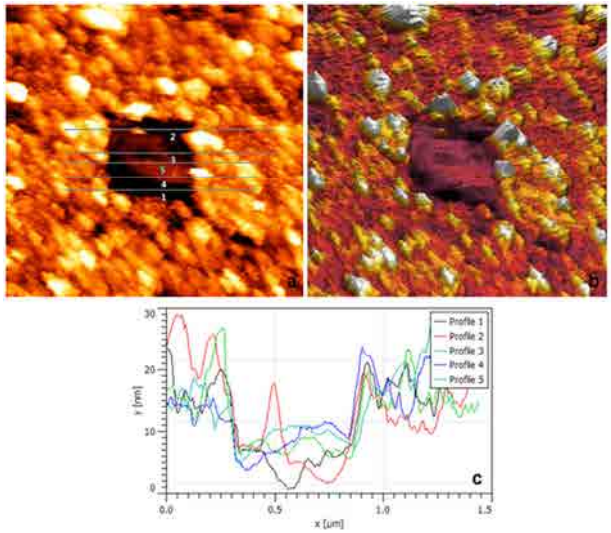

Fig.82 AFM tapping mode image of the scratch done on TiNbHf sample functionalized with the CAS fragment in 2D (a) and in 3D (b). The depth of the scratch was measured in five different points (c).

TiNbHf+CAS thickness [nm]		
profile	value	
1	7,00	
2	5,00	**Mean**
3	3,00	5 ± 1,58
4	4,00	
5	6,00	

Table 29. Values of the layer thickness obtained for each zone measured in the scratch.

2.2 Covalently bound protein

When the protein was adhered to the TiNbHf alloy by means of the silanes chemistry, the surface was also covered, but the topography observed was not granular. The fragment was disposed in fibrils (Fig. 83).

The layer thickness for the covalently bounded protein was also measured by means of a scratching (Fig.84). The values obtained are shown in Table 30.

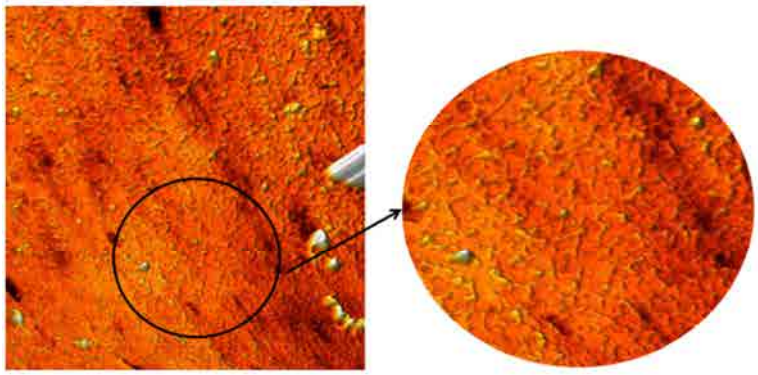

Fig.83 AFM tapping mode image in PBS at 37ºC of the CAS fragment covalently bound onto TiNbHf alloy by means of silanes chemistry. The area scanned was 2 x 2 µm.

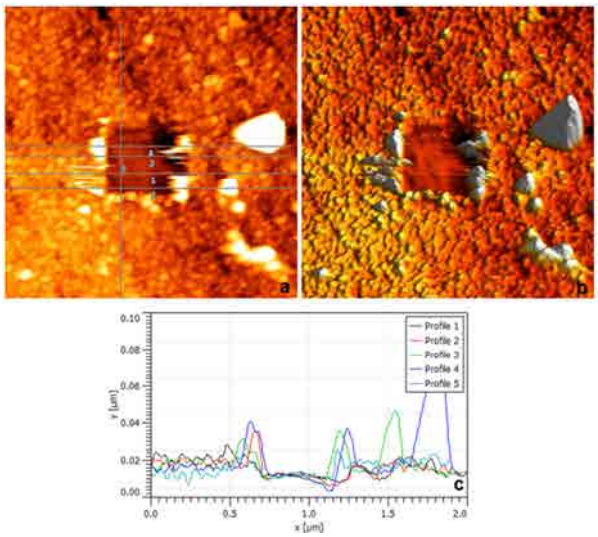

Fig.84 AFM tapping mode image of the scratch done on TiNbHf sample functionalized with the covalently bound CAS fragment in 2D (a) and in 3D (b). The depth of the scratch was measured in five different points (c).

TiNbHf+APTES+CAS thickness [nm]		
profile	value	
1	8,00	
2	6,00	
3	6,00	**Mean** 6,8 ± 0,83
4	7,00	
5	7,00	

Table 30. Values of the layer thickness obtained for each zone measured in the scratch.

Owing to the fact that the silanisation method gave better adhesion efficacy of the fragments and induces fibrilar conformation of the CAS fragment, the silanisation method was used to tether the molecules onto the surface in further studies.

4. BIBLIOGRAPHY

1. RICO, Patricia, et al. Molecular Assembly and Biological Activity of a Recombinant Fragment of Fibronectin (FNIII7–10) on Poly(Ethyl Acrylate). *Colloids and Surfaces B: Biointerfaces*, 7/1, 2010, vol. 78, no. 2. pp. 310-316. ISSN 0927-7765.

2. PATEL, Salima, et al. Urea-Induced Sequential Unfolding of Fibronectin: A Fluorescence Spectroscopy and Circular Dichroism Study. *Biochemistry*, 2004, vol. 43, no. 6. pp. 1724-1735.

3. MAO, Yong; and SCHWARZBAUER, Jean E. Fibronectin Fibrillogenesis, a Cell-Mediated Matrix Assembly Process. *Matrix Biology*, 9, 2005, vol. 24, no. 6. pp. 389-399. ISSN 0945-053X.

4. LIN, M. C., et al. Control and Detection of Organosilane Polarization on Nanowire Field-Effect Transistors. *Nano Letters*, 2007, vol. 7, no. 12. pp. 3656-3661.

5. VANDENBERG, Elaine T., et al. Structure of 3-Aminopropyl Triethoxy Silane on Silicon Oxide. *Journal of Colloid and Interface Science*, 1991, vol. 147, no. 1. pp. 103-118.

Chapter 7

Cell response to the biofunctionalised surfaces

1. CELL ADHESION FORCE

1.1 Cell adhesion force plots

The cell adhesion experiments were done as stated in Chapter 2, section 7.3.3.2.

During the experiments, the cantilever was coated with biotin and streptavidin. The biotin-streptavidin system is the strongest non-covalent biological interaction known and is one of the most widely used affinity pairs in cellular assays. Owing to the biotin-straptavidin system the cell was able to attach to the cantilever in a strong way and contact the surface functionalised with lRGD, cRGD and CAS.

In the assay, Ti was used as a control material owing to its well-known biofunctionalisation properties and cell response.

The following information was obtained from the generated curves:

a) the tip-cell approach to the surface
b) the cell adhesion
c) the cell adhesion force (determined as the lowest point of the adhesion curve)
d) the energy required to remove the cell from the surface (area enclosed by the force curve and the x-axis)
e) the membrane tethers pulled out from the cell surface (steps in the force curve)

Fig.85, Fig.86 and Fig.87 show representative cell adhesion curves obtained when cells were in contact with Ti biofunctionalised with lRGD, cRGD or CAS fragment, respectively. In all three cases, the curves showed steps when the cell was being pulled away from the surface. The initial part of the retraction curve shows deformation of the whole cell and many complex attachments removed at the same time whilst the cell is pulled off the surface.

When cells were in contact with lRGD functionalised surfaces (Fig.85), less steps were detected compared with the cRGD (Fig.86) or the CAS fragment (Fig.87). In the case of the CAS fragment, the steps began before that in the case of the cRGD. According to the graphics, the energy needed to detach the cells from the different biofunctionalised surfaces was of the same order of magnitude.

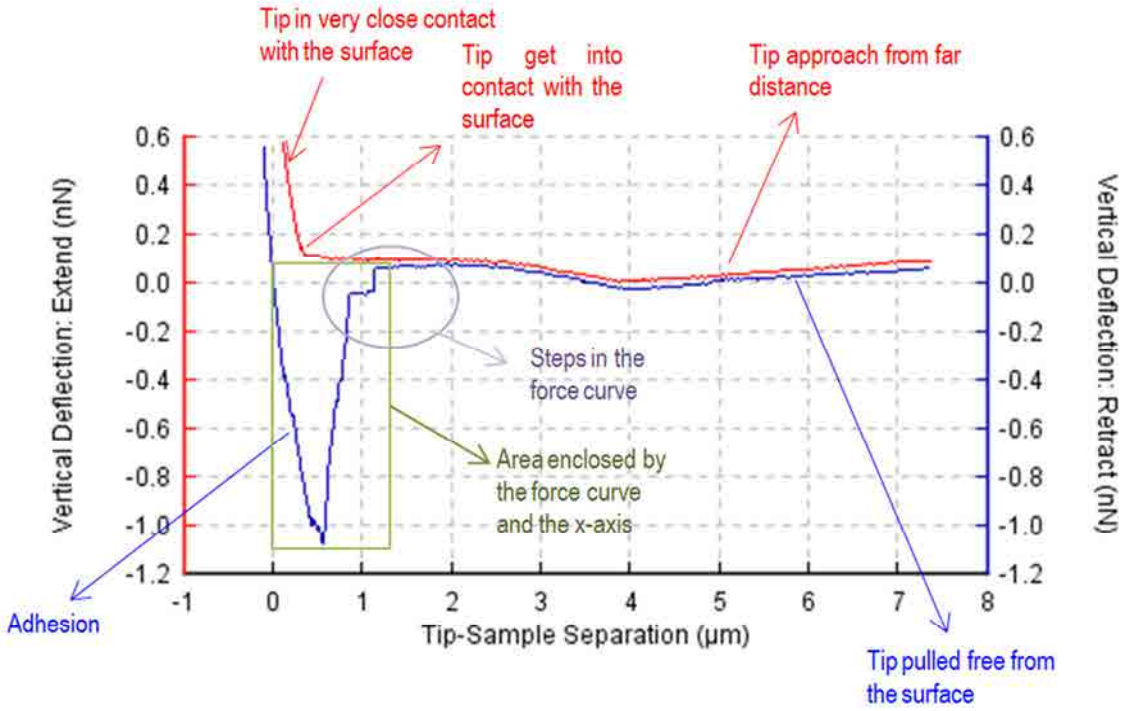

Fig.85 Cell adhesion force curve obtained for Ti functionalised with lRGD Ti. Different events are displayed such as the tip approach, the cell adhesion, the events related to cell membrane tethering and the energy needed to remove the cell from the surface.

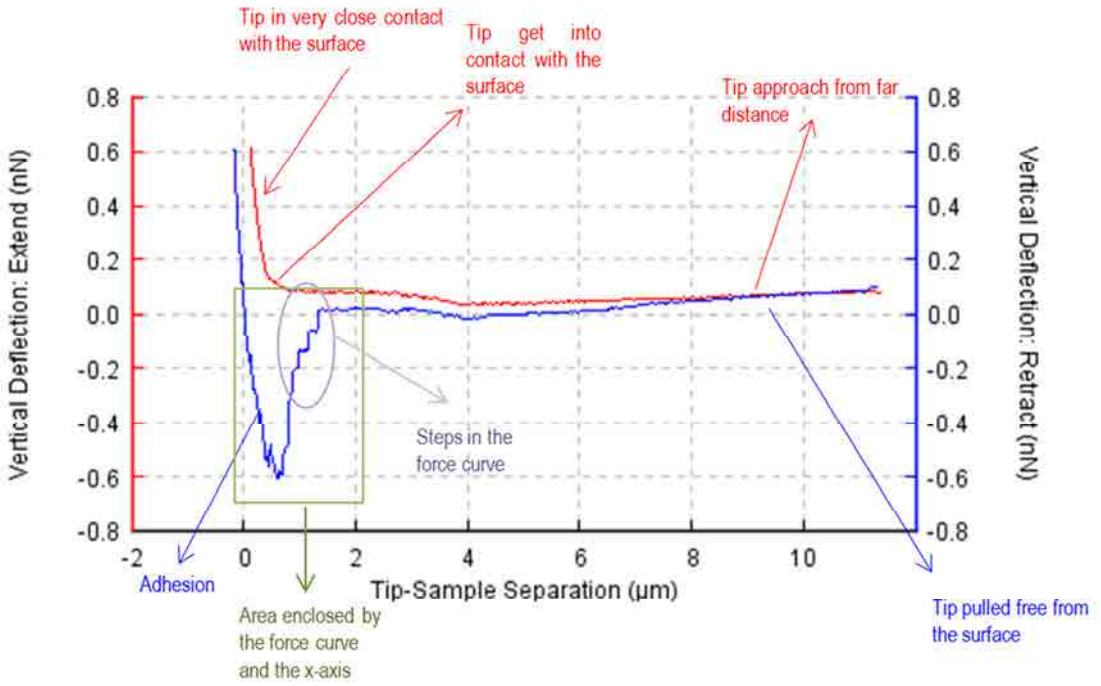

Fig.86 Cell adhesion force curve obtained for Ti functionalised with cRGD. Different events are displayed such as the tip approach, the cell adhesion, the events related to cell membrane tethering and the energy needed to remove the cell from the surface.

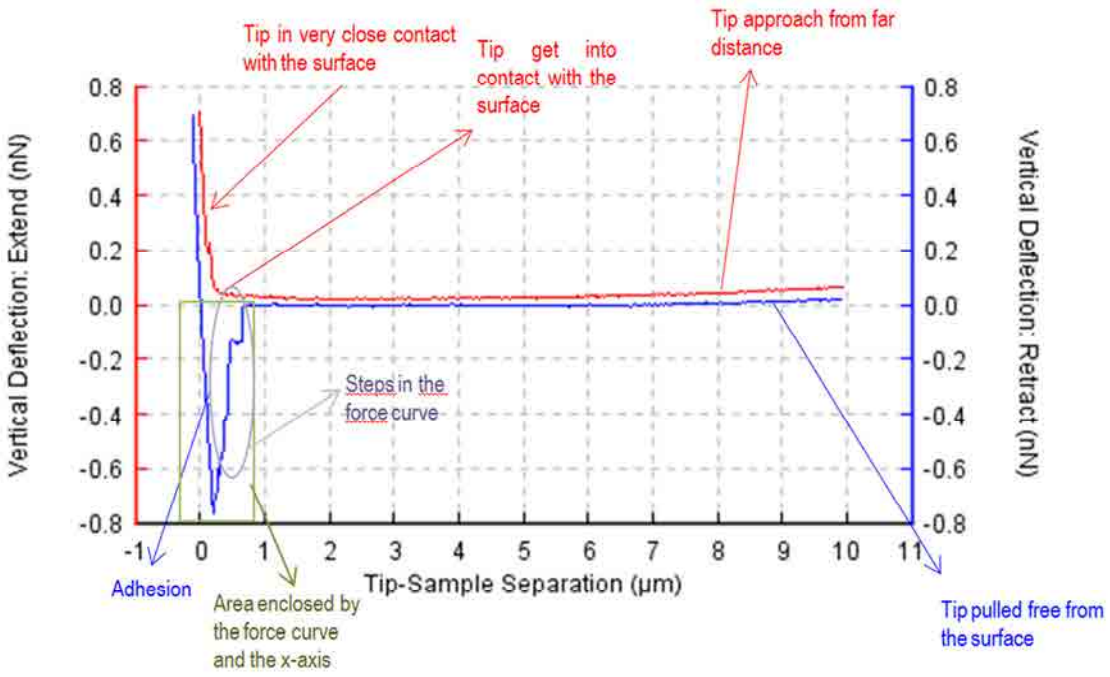

Fig.87 Cell adhesion force curve obtained for Ti functionalised with CAS. Different events are displayed such as the tip approach, the cell adhesion, the events related to cell membrane tethering and the energy needed to remove the cell from the surface.

Fig.88, Fig.89 and Fig.90 show representative cell adhesion curves obtained when cells were in contact with Ti25Nb21Hf alloy biofunctionalised with lRGD, cRGD or CAS fragment, respectively. In these curves the phenomenon related to the steps during pulling off cells was also seen, but with cells in contact with the biofunctionalised Ti25Nb21Hf alloy the steps were more pronounced.

As in the Ti biofunctionalised surfaces, the Ti25Nb21Hf functionalised with lRGD (Fig. 88), showed fewer steps than in the case of cRGD (Fig.89) or the CAS fragment (Fig.90). The CAS fragment showed more steps than the cRGD and more complex attachments at the initial part of the retraction curve. According to the graphics, the energy needed in this case to detach cells from the different biofunctionalised surfaces was of the same order of magnitude between the different motifs, but higher than in the case of the biofunctionalised Ti.

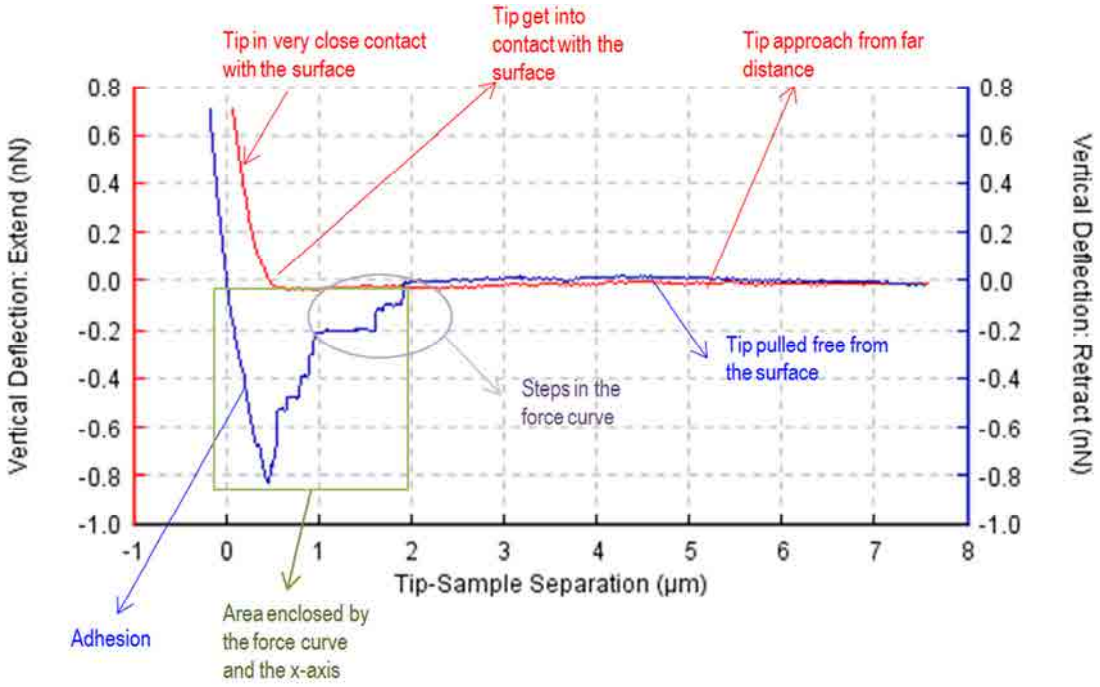

Fig.88 Cell adhesion force curve obtained for Ti25Nb21Hf functionalised alloy with lRGD. Different events are displayed such as the tip approach, the cell adhesion, the events related to cell membrane tethering and the energy needed to remove the cell from the surface.

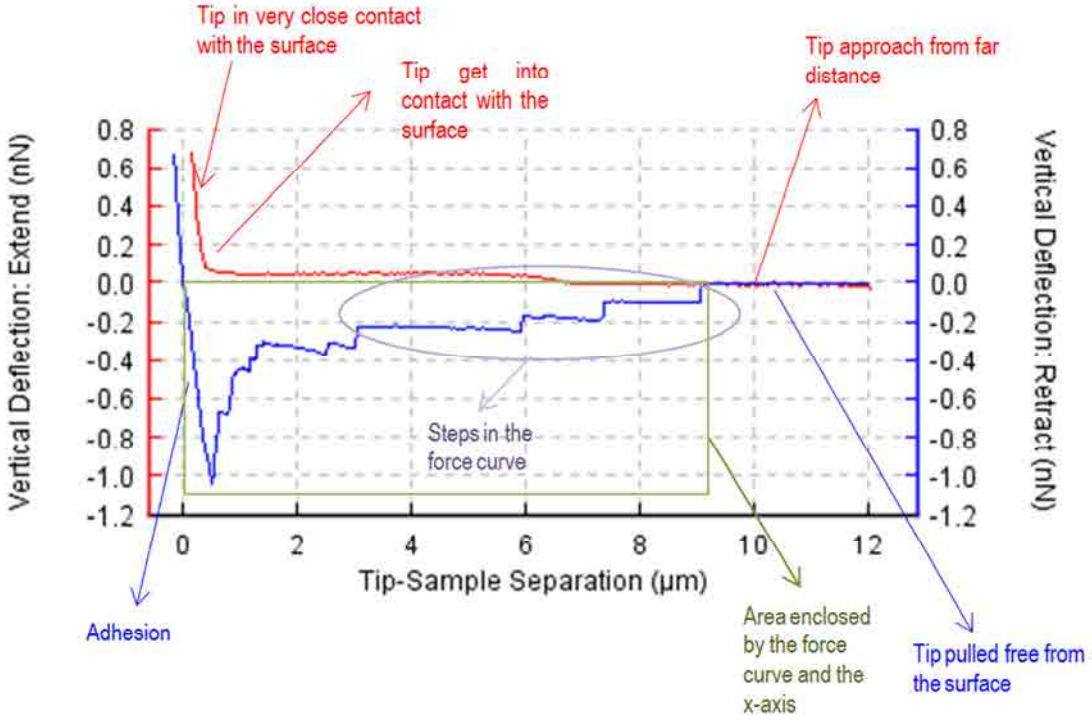

Fig.89 Cell adhesion force curve obtained for Ti25Nb21Hf functionalised alloy with cRGD. Different events are displayed such as the tip approach, the cell adhesion, the events related to cell membrane tethering and the energy needed to remove the cell from the surface.

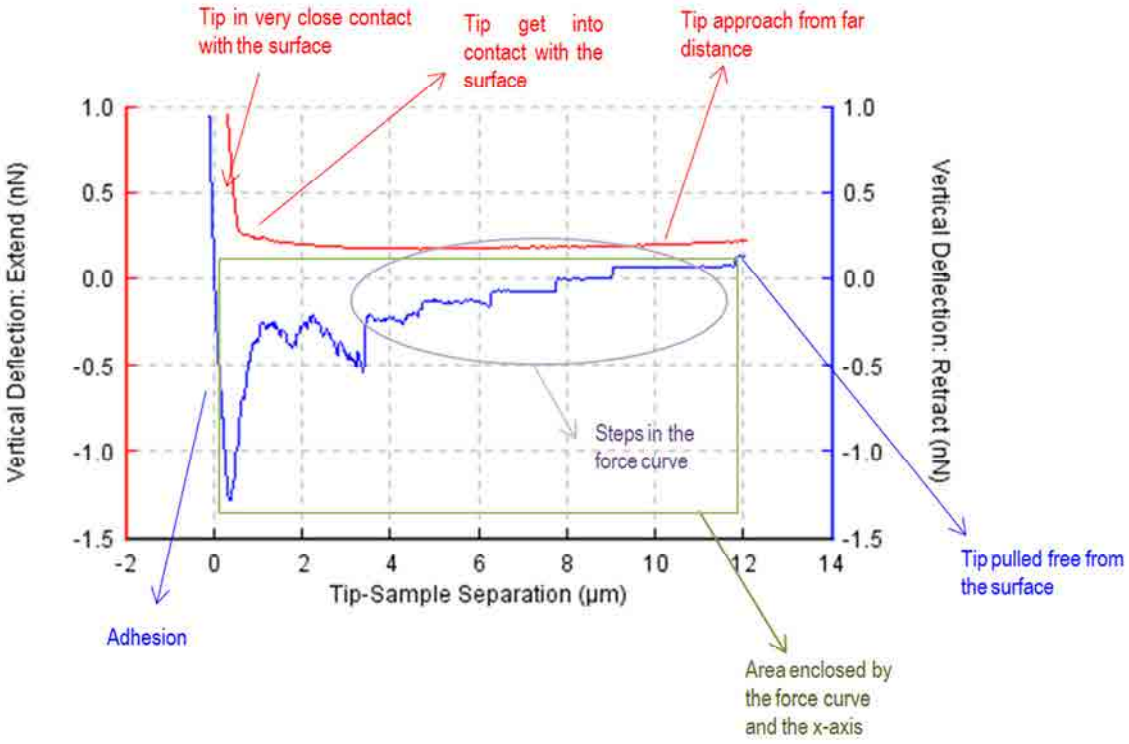

Fig.90 Cell adhesion force curve obtained for Ti25Nb21Hf functionalised alloy with CAS. Different events are displayed such as the tip approach, the cell adhesion, the events related to cell membrane tethering and the energy needed to remove the cell from the surface.

1.2 Cell adhesion force statistics

The adhesion force obtained for each material and each functionalized molecule was represented by a box and whisker plot. This statistic tool allows comparing at the same time different data groups with no information loosening. It is a representative graphic of a group of data distribution in which the descriptive measurements of the data are used. These descriptive measurements are the mean, the first quartile, the third quartile, maximum value and minimum value. This visual representation, associate the five measurements that usually are processed individually. At the same time gives information about the central trend, dispersion and symmetry of the data.

Fig.91 shows the box plots obtained for Ti functionalized with lRGD, cRGD or CAS. In all the studied cells, there are values that are distant from the others showing variability in the measurements. . In presence of cRGD or CAS there were cells that experienced forces with high deviation between the mean and the maximum and minimum values. On those cases, also high dispersion of results was shown. The adhesion forces obtained

with lRGD showed two trends, 3 of the six cells tested showed means under 50pN. For cRGD four of the six cells tested showed values under 50 pN. The values of the mean obtained for the cells studied under CAS effect, were above 50pN in all the cases. The number of cells with adhesion forces above 100 pN was one for lRGD, two for cRGD and three for CAS.

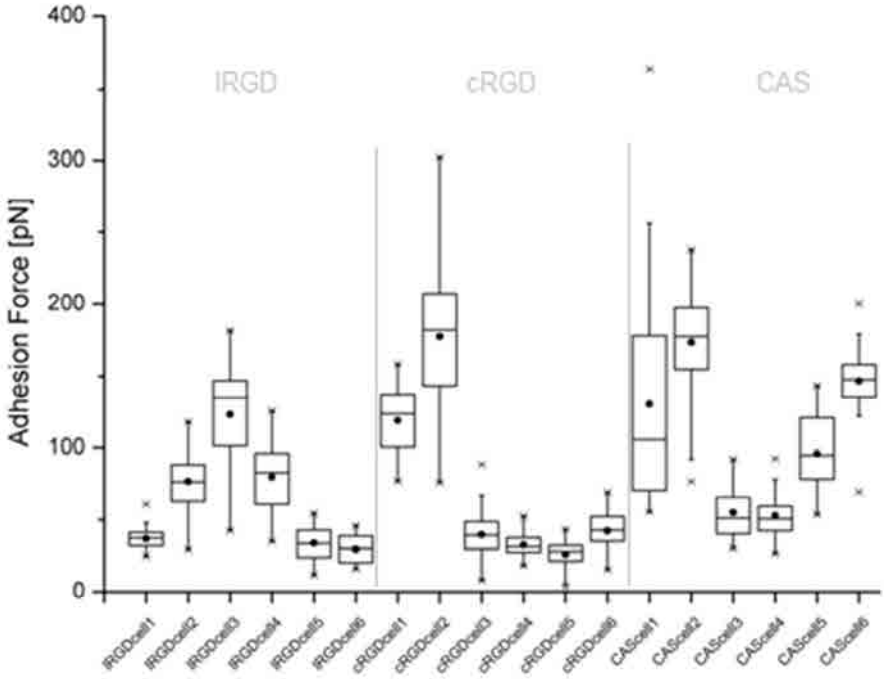

Fig.91 Box plot representing the adhesion force values obtained for each cell tested on titanium fuctionalized by means of covalent bonding with lRGD 100 µM , cRGD 100 µM and CAS 100 µg/ml.

Fig.92 shows the box plots obtained for Ti25Nb21Hf alloy functionalized with lRGD, cRGD and CAS. In all the studied cells, outliers were found and dispersion amongst results. One of the six cells tested on lRGD showed a mean value of adhesion force under 50pN. For cRGD three of the six cells tested showed values under 50 pN. The values of the mean obtained for the cells studied under CAS effect, were above 50pN in all the cases. The number of cells with adhesion forces above 100 pN was one for lRGD, two for cRGD and four for CAS.

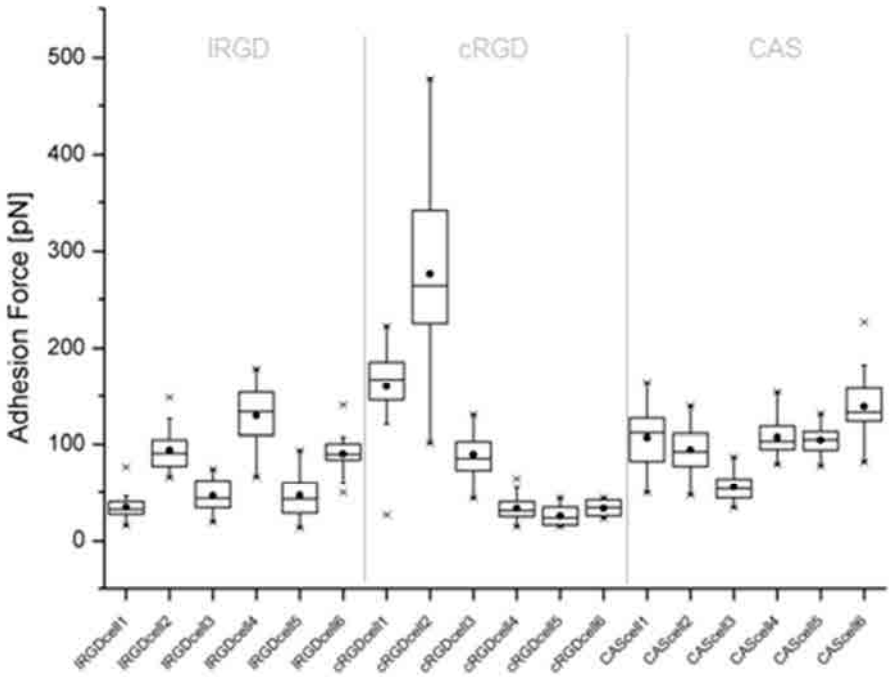

Fig.92 Box plot representing the adhesion force values obtained for each cell tested on TiNbHf alloy fuctionalized by means of covalent bonding with lRGD 100 µM , cRGD 100 µM and CAS 100 µg/ml.

All the tested cells showed higher adhesion forces when attached to the CAS biofunctionalised surfaces independently of the material used, Ti or Ti25Nb21Hf alloy. Cells tested on the new TiNbHf alloy functionalized with the same molecules as Ti showed less dispersion. Despite that, the data obtained for the cRGD still show a high dispersion.

2. CELL ADHESION RESPONSE

2.1 Number of cells adhered

The number of cells adhered was determined as stated in Chapter 2, section 8.2. Cell adhesion response was evaluated 4h after cell seeding on Ti25Nb21Hf alloy biofunctionalised with five different biomolecules: FN, lRGD, cRGD, CAS, HB II and

three different combinations of the CAS and HB II recombinant fragments fabricated in this thesis.

In Fig. 93 the number of cells adhered onto each biofunctionalised surface is shown. There were no significant differences between the adhesion triggered on the rMSC cells by the lRGD, cRGD and CAS. Surprisingly, the HB II fragment gave an adhesion response equivalent to that obtained with the aforementioned fragments and combinations.

The different combinations made with the CAS and HB II fragments triggered different cell adhesion responses. The CAS-HB II 70:30 combination showed an equivalent response to that obtained with lRGD, cRGD and CAS, whilst CAS-HB II 50:50 and CAS-HB II 30:70 combinations showed less adhesion efficiency. Being the last combination the one which promoted less cell adhesion.

Adhesion to the FN functionalised surfaces was less than the observed for all the fragments studied except for the CAS-HB II 50:50 and CAS-HB II 30:70 combinations.

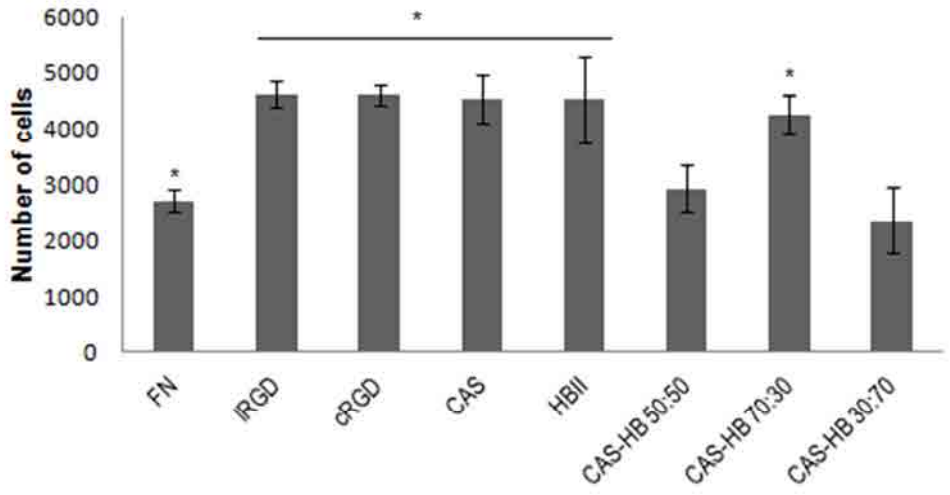

Fig.93 Adhesion of rMSC cells onto Ti25Nb21Hf alloy biofunctionalised with the different bio molecules after 4h of culture. The initial number of cells seeded was 10000. Error bars represent a standard deviation for n=3. The asterisk means differences between samples with $p<0,05$.

2.2 Cell spreading

Cell spreading was determined according to the area of the cells in contact with the different molecules. Fig. 94 show the area in μm^2 of the cells adhered on the different biofunctionalised surfaces. The area was measured according to the procedure given in Chapter 2, section 8.2.

According to Fig.94, the area of cells in contact with lRGD, cRGD, CAS or CAS-HB II 70:30 motifs showed no statistical differences. As expected, the higher spreading was obtained for the cells in contact with FN and the less spread cells were those in contact with the HB II fragment. .

When both CAS and HB II fragments were used to functionalise the surface, the cells in contact showed different spreading behaviour depending on the proportion of HB II present in the solution. The highest spreading was observed for cells in contact with CAS-HB II 30:70, whilst the less spreading was seen for cells in contact with CAS-HB II 70:30. There were no differences between cells in contact with the CAS-HB II 50:50 and CAS-HB II 30:70 combinations. These results are opposite to that observed in the number of cells adhered (Fig. 93).

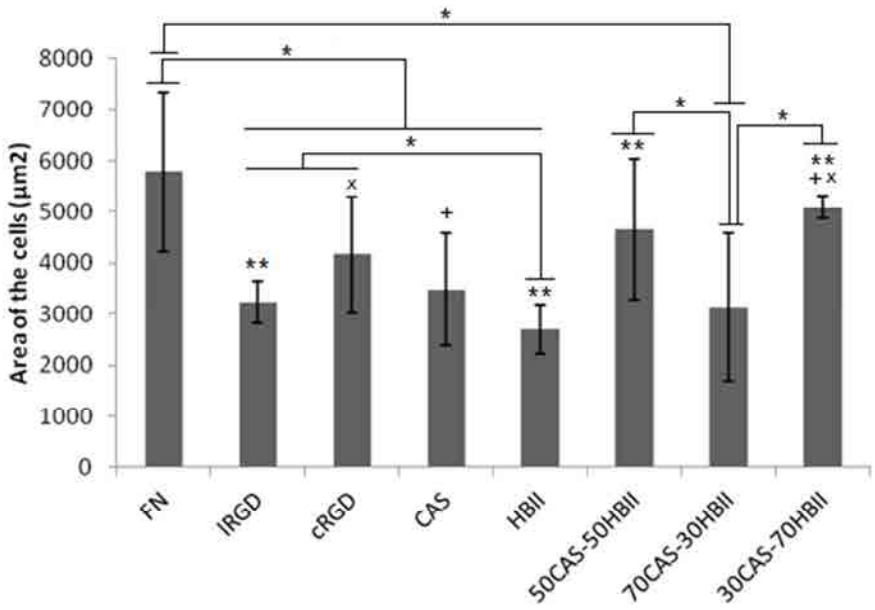

Fig.94 Spreading of rMSC cells onto Ti25Nb21Hf alloy biofunctionalised with the different biomolecules after 4h of culture. The initial number of cells seeded was 25000. Error bars represent a standard deviation for n=5. The asterisk means differences between samples with p<0,05.

2.3 Cell morphology

Immunofluorescence of the cells after 4 h of incubation was done according to the procedure given in Chapter 2, section 8.2. With this technique it was possible to see the cytoskeleton of the cells (in red) and the focal contacts (in green), indicators of a proper cell adhesion and spreading.

Fig. 95 shows the spreading and morphology of the representative rMSCs in contact with the different functionalized molecules.

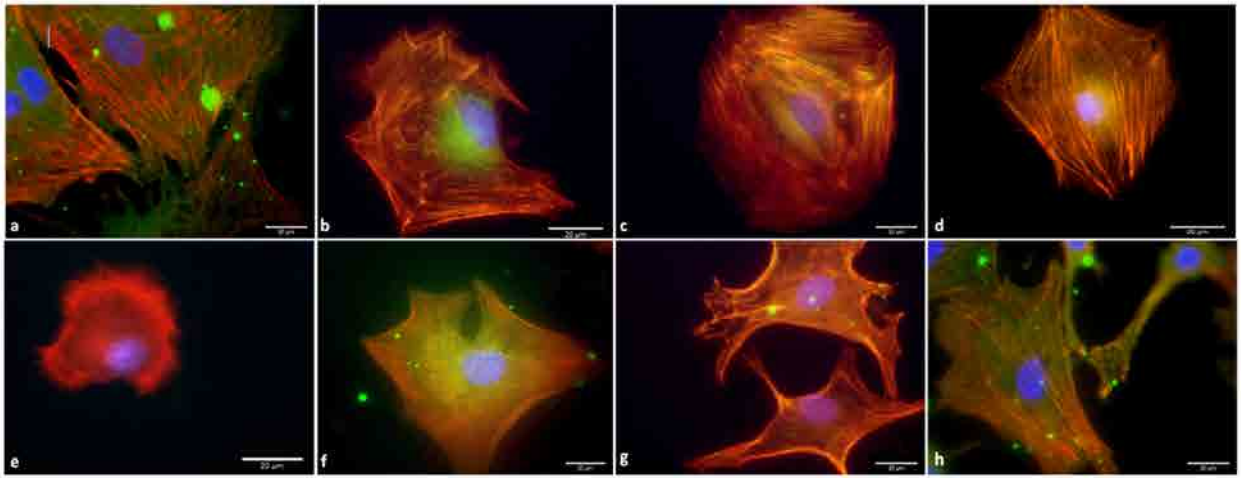

Fig.95 Representative images of rMSC cell spreading and morphology after 4h culture in contact with FN (a), lRGD (b), cRGD (c), CAS (d), HB II (e), CAS-HB 50:50 (f), CAS-HB 70:30 (g) and CAS-HB 30:70 (h) functionalized Ti25Nb21Hf alloy. Error bar corresponds to 20 µm.

The results obtained after cell area analysis showed no statistical differences between cells in contact with the lRGD, cRGD and CAS. According to the representative images obtained for lRGD (Fig. 95 b), cRGD (Fig. 95 c) and CAS (Fig. 95 d), cells showed similar size. In all three cases, a proper cytoskeleton was formed but there was no evidence of focal contacts formation.

The representative image for cells in contact with the HB II fragment (Fig. 95 e) agrees with the results obtained for area analysis, showing the less spread area, but there is a great difference with the rest of cells that were not evidenced in Fig. 94. The fragment was able to trigger certain cell spreading, but no actin filaments and no focal adhesions were formed. These were the only cells which showed ruffled borders. The representative images for cells in contact with the CAS-HB 50:50 (Fig. 95 f), CAS-HB

70:30 (Fig. 95 g) and CAS-HB 30:70 showed in all the cases a well formed cytoskeleton with focal contacts. Cell morphology resembles the morphology of cells in contact with FN (Fig. 95 a).

3. CELL PROLIFERATION RESPONSE

The cell proliferation response of rMSCs was determined as stated in Chapter 2, section 8.3.

In Fig.96 the proliferation of the rMSCs in terms of cells adhered on the different biofunctionalised substrates after 4h, 7days, 14 days and 21 days in culture is shown.

After 7 days in culture, cells adhered onto the different biofunctionalised surfaces increased considerably except for cells in contact with HB II and CAS-HB 70:30.

After 14 days in culture different behaviours were seen:

a) cells did not increment in number, making clear a steady state in the proliferation. As was the case for cells in contact with FN and CAS-Hb 70:30
b) cells were reduced in number, leading us to think in an spontaneous apoptosis. As was the case for cells in contact with lRGD, cRGD, CAS and HB II
c) cells increase slightly in number, suggesting a low proliferation rate. As was the case for the CAS-HB 50:50 and CAS-HB 30:70

In all the cases there was a recovery in the cell proliferation rate after 14 days in culture. In the case of cells in contact with lRGD, cRGD and CAS, the number of cells after 21 days in culture did not outrange the number of cells adhered after 7 days in culture. The less proliferative cells were those in contact with lRGD, cRGD, CAS, HB II and the CAS-HB 70:30 combination. The CAS-HB 50:50 and 30:70 combinations showed a proliferation equivalent to that to FN.

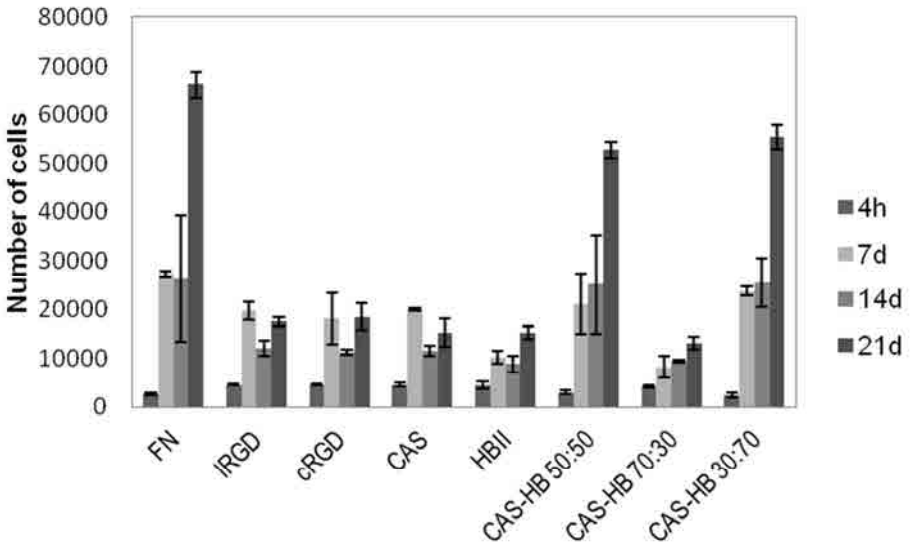

Fig.96 Proliferation of rMSCs onto Ti25Nb21Hf alloy biofunctionalised with the different biomolecules after 4h, 7 days, 14 days and 21 days culture. The initial number of cells seeded was 10000. Error bars represent a standard deviation for n=3.

In Fig.97 the duplication of the cumulative population was represented. After 7 days in culture, the cells in contact with FN, lRGD, cRGD, CAS, CAS-HB 50:50 and CAS-HB 30:70 duplicated its population. The slope for the lRGD, cRGD and CAS is less than in the case of the rest of fragments, meaning that the speed of proliferation is lower. After 7 days in culture, the proliferation started to diminish in all the cases, being the cells in contact with lRGD, cRGD and CAS the ones which experienced the most pronounced deceleration. At 14 days in culture, cells started to proliferate again. Cells in contact with the lRGD, cRGD and CAS were not able to regain the proliferation speed and they proliferated slowly than the cells in contact with FN, CAS-HB 50:50 and CAS-HB 30:70.

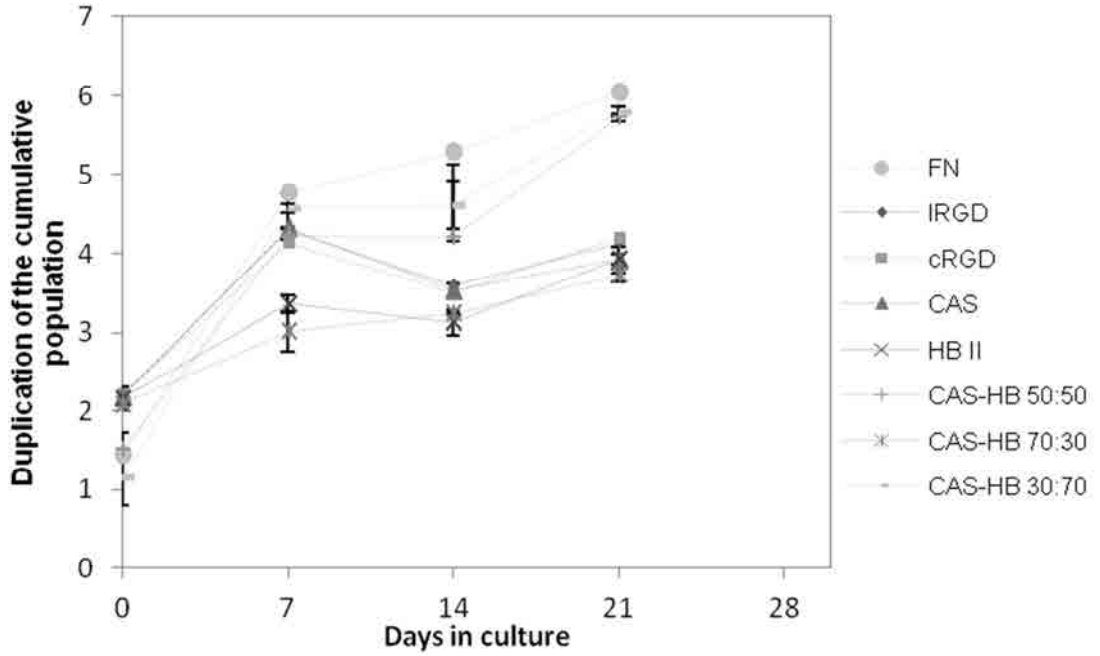

Fig.97 Duplication of the cumulative population of rMSCs onto Ti25Nb21Hf alloy biofunctionalised with the different biomolecules after 4h, 7 days, 14 days and 21 days culture. . The initial number of cells seeded was 10000. Error bars represent a standard deviation for n=3.

4. CELL DIFFERENTIATION RESPONSE

The cell differentiation response of the rMSCs was determined as stated in Chapter 2, section 8.4. Fig. 98 shows the differentiation in terms of ng ALP/num.cells x min released by cells after 4h, 7 days, 14 days and 21 days.

The fragments that promoted higher rates of differentiation were the HB II and the CAS-HB 70:30. Cells in contact with lRGD, cRGD and CAS showed certain differentiation. Cells in contact with lRGD, cRGD and CAS presented some osteoblastic differentiation. The RGD's were not able to make cells differentiate in the same manner as did the CAS fragment.

After 7 days in culture all the fragments triggered cell differentiation, although the higher obtained value was for the CAS-HBII 70:30 fragments combination. After 14 days in culture different behaviours were seen:

a) cells did not differentiate. As was the case of the RGD's
b) cells differentiation rate was reduced. As was the case of the CAS, HB II and CAS-HB 70:30

c) cells continued differentiating. As was the case of FN, CAS-HB 50:50 and CAS-HB 30:70

Cells in contact with the CAS-HB70:30 combination of fragments showed a peak of differentiation after 7 days in culture. The HB II fragment triggered such rate of differentiation after 21 days in culture, whilst for the other fragments this differentiation was not reached even after 21 days in culture.

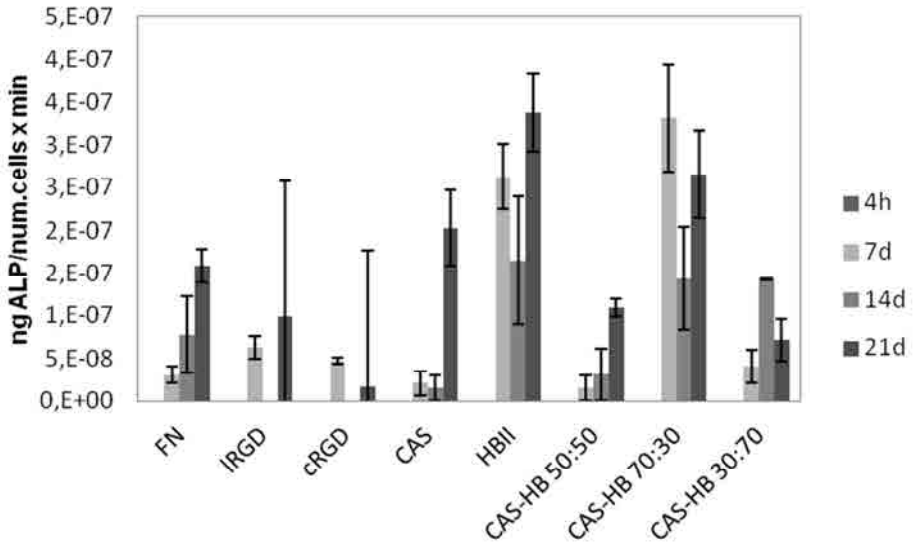

Fig.98 Differentiation of rMSCs onto Ti25Nb21Hf alloy biofunctionalised with the different biomolecules after 4h, 7 days, 14 days and 21 days of culture. . The initial number of cells seeded was 10000. Error bars represent a standard deviation for n=3.

5. BIBLIOGRAPHY

1. Pankov, R. & Yamada, K. M. Fibronectin at a glance. *J. Cell Sci.* **115,** 3861–3863 (2002).

2. Ruoslahti, E. Integrins. *J. Clin. Invest.* **87,** 1–5 (1990).

3. Borm, B., Requardt, R. P., Herzog, V. & Kirfel, G. Membrane ruffles in cell migration: indicators of inefficient lamellipodia adhesion and compartments of actin filament reorganization. *Exp. Cell Res.* **302,** 83–95 (2005).

IV

Discussion

Chapter 8

Discussion

1. CHAPTER 3: EFFECT OF THE ALLOYING ELEMENTS IN THE Ti-24.8Nb-16.2Hf-1Zr ALLOY

Despite the good properties of the Ti-based alloys used to replace bone, there is still a mismatch in the elastic modulus between bone and the implant that results in a stress shielding effect and implant failure. Different Ti-based alloys have been developed in the last years to overcome the problem of stress shielding effect [1]. One of these alloys is the ternary alloy Ti-Nb-Hf. In this chapter, the effect of the alloying elements in the mechanical properties of this ternary system has been studied.

Prior to the alloys fabrication, the quantum parameters were determined for all of them.

The quantum parameters range of the alloys with 20-29 wt % Nb was:

- $0.60992 \leq \overline{BO} \leq 0.61130$
- $0.15311 \leq \overline{OE} \leq 0.15258$
- $4.1314 \leq e/a \leq 4.2017$

The quantum parameters range of the alloys with 10-21 wt % Hf was:

- $0.60891 \leq \overline{BO} \leq 0.61212$
- $0.15312 \leq \overline{OE} \leq 0.15260$
- $4.1584 \leq e/a \leq 4.1760$.

In all the cases, the values of the quantum parameters were enclosed in the range established in Arciniega's map for the zone of low elastic modulus and shape memory effect. According to Arciniegas' map the alloys with shape memory properties are in the range $0.4688 \leq \overline{BO} \leq 0.6117$; $0.1518 \leq \overline{OE} \leq 0.1543$. The alloys with low elastic modulus are in the range $0.5970 \leq \overline{BO} \leq 0.6224$; $0.1523 \leq \overline{OE} \leq 0.1546$. There is a range in which the BO and OE parameters for the shape memory and low elastic modulus properties are overlapped. High OE values and intermediate BO values mark out the region for α-phase alloys region on the map; whereas the low values of OE and a wide range of BO mark out the β-phase alloys region. Those alloys in which both phases coexist are scattered in the central area of the map.

The electron/atom ratio have been reported as a key factor to obtain multifunctional beta-type titanium alloy with an ultra-low elastic modulus, high strength, superelastic-like elastic deformability and superplastic-like cold workability without work hardening at room temperature[2,3]. The e/a parameter found in the designed alloys ranged from 4.13 to 4.2, which is very close to the range between 4.15 and 4.24 reported to achieve multifunctional Ti alloys [2,3] .

After fabrication, the wt% of each alloying element was verified. It is important to check if the presence of each element after the melting process is correct, because if there is any inclusion or variation in the wt%, the mechanical characteristics of the alloy may vary. The alloys showed a deviation between experimental and theoretical results. This might be due to various causes: i) the presence of impurities in the alloying elements, ii) both sides of the sample are not totally parallel and iii) the arc melting furnace was not able to melt completely the materials and the buttons weren't homogeneous. As the technique accuracy was around 2%, according to the manufacturer, samples were considered as homogeneous.

Once it was known that the alloys concurred with the desired properties determined a priory and the composition, the influence of the composition in the microstructure was studied.

First of all, the microstructure was determined by means of optical microscopy. The microstructures obtained for the Ti-(20-29)Nb-16Hf showed an increase of the β-phase as the Nb content increased. The result agrees with previous studies that reported a needle-shaped α phases in a β-dominated matrix in Ti-Nb alloys [4] and a dependence of the β-phase presence on the Nb content. High content of Nb favours the β-phase [5].

The microstructures obtained for the alloys Ti-25Nb-(10-21)Hf agreed with Zhou et al. studies [6] This studies reported a lamellar α' martensite in Ti-Hf alloys with 10-40 %wt Hf. The organization of the martensite arrays was dependent on the Hf content. By increasing the Hf content, the martensite becomes finer and the arrays are rearranged from unidirectional to multidirectional. Studies made on Ti-40Nb-(1-7)Hf, showed a single β-phase[4]. There was an alloy that did not follow such tendency: the Ti-25Nb-15Hf alloy. This alloy showed a microstructure formed mainly by a β-phase with martensite plaques distributed randomly. The base alloy (Ti-24.8Nb-16,2Hf-1Zr)

showed a very similar microstructure. This similarity between microstructures was explained by similarity in composition of both alloys.

To confirm the microstructure observed by optical microscopy, XRD assays were conducted. The diffractogram obtained for the Ti-(20-29)Nb-16Hf alloys showed a gradually diminishing of the the α' and the α'' peaks as the Nb percentage increased in the alloys. The microstructure formed by martesite (α' phase), thermo elastic martensite (α'' phase) and retained β phase become a microstructure formed by β phase with areas of thermoelastic martensite. This behaviour agrees with the effect of Nb reported by Hon et al. which demonstrated the influence of Nb content on the phases present in the alloy[4]. As Nb content increases, the primary α peak diminishes gradually, that means the proportion of the α phase declines as the Nb content increases, and the original α phase dominated structure gradually transforms into a β phase-dominated structure. In this study was also demonstrated that when the content exceeds 34 mass%, only β-peaks remain. In our case, the mass % to obtain only β-peaks is 26% instead of 34%. It is well known that Nb and Hf are both β stabilisers and also reduce the Ms temperature [7], then it is not surprising that the α' phase and the α'' decreases enough to get only a β-phase, due to the effect of Hf which might enhance Nb β-stabilizing character

No ω-phase was detected with XRD which also agrees with Nobuito et al. studies.[8] which suggested the presence of ω phase formed during finally cooling process in Ti-Nb-Ta-Zr when the mass % of Nb ranges from 15 to 25%, but not detectable with XRD.

Previous studies on Ti-Hf (10, 20, 30, 40% Hf) reported the formation of an α' structured (HCP) after rapid quenching from the β field without the presence of any second phase[6,9]. This allotropic transformation of BCC to HCP structure is formed without a diffusion solute and designated as martensite. There are two different types of martensite depending on the chemical composition and the quenching rate from the β field. One is marteniste α'with HCP structure, and the other is marteniste α''with ortho-rhombic structure. According to Zhou et al.[9], the martensite present in quenched Ti-Hf alloys is exclusively α', although in some binary Ti alloys such as Ti–Mo, Ti–Nb and Ti–Ta only α'' martensite were found. Potavof et al.[10] studied the effect of the addition of 8-20 wt% Hf in a NiTi alloy showing that at room temperature, the microstructure was mainly martensitic although the alloys with 8- 11 at% Hf showed a small amount of the parent B2 phase. Our studies agree with the studies made by Zhou et al [9]., where

just α'' martensite were found. It leaded us to think that the Nb role in the formation of martensite is stronger than the influence of Hf.
Other studies demonstrated that the addition of Hf to a Ti-Nb alloy triggers ω phase[4]. The presence of ω phase is not desirable because it produces an increase in the brittleness, less ductility and less fatigue strength of the material[4]. Nevertheless, the α phase homogeneously precipitated may lead to an increase of the material strength without involve ductility[11]. In titanium alloys with beta-stabilizers which have been subjected to a quenching or aging treatment, the ω phase formation is common. The ωphase is metastable with respect to the quilibrium (α+β) or (α+ intermetallics)[12]. This is the case of our alloys and the presence of ω-phase is not unexpected.

As ω phase is of difficult detection by means of XRD, And Nobuito et al.[8] suggested the presence of ω phase in Ti-Nb-Ta-Zr alloys when the Nb mass percentage ranges from 15 to 25%, TEM images were done on our the alloys with Nb mass ranging from 20 to 23% demonstrating absence of ω phase. Alloys with 17% and 21% wt Hf showed a peak that could be identified either as an ω-phase or also as an α''-phase. TEM images were done on these two alloys confirming the presence of ω-phase. Thus it can be concluded that, the addition of Hf induced the formation of the ω-phase which concurs with previous studies. In Ti-alloys containing β-stabilisers that have been subjected to quenching or aging it is common the formation of ω-phase. This phase is metastable respect to the equilibrium (α+β) or (α+ intermetallics). This is the case of our alloys and it is not surprising the presence of such phase. The fact that it was only observed in the Ti-24.8Nb-(10-21)Hf alloys group and not in the Ti-(20-29)Nb-16.2Hf alloys group might be due to the fact that in some quenched Ti-Nb systems the transformation of the α' to the α'' phase took place before the ω-phase formation.

The microstructure also influences the alloy elastic modulus. Hon et al.[4] reported an α-phase modulus 1.5 times greater than the β-phase. Owing to the fact that β-phase has lower modulus; a β-phase microstructure is expected to decrease the modulus. According to that, the modulus obtained for the Ti-(20-29)-Nb-16Hf alloys should be lower that the modulus obtained for the Ti-25Nb-(10-21)Hf. The study of the modulus was done by means of nanoindentation. To determine the existence of phase transformation during loading and unloading process, 5 cycles of loading-unloading at an indentation depth of 300nm were done. To determine the elastic modulus and the

hardness, 10 cycles of loading-unloading at an indentation depth of 2000nm were done. In this case, the first 100nm of the loading curve were taken and the resultant curve was fit with the Hertz curve

The Ti-(20-29)Nb-16.2Hf alloys group showed loops that narrowed as the Nb content increased. Values from 20-23% wt of Nb showed α' martensitic plates which deform plastically and irreversibly. On each cycle, a remnant plastic deformation was seen due to the plastic deformation of the martensite plaques. When the % wt of Nb was above 23%, the microstructure was mainly formed by β-phase. In the nanoindentation curves a higher elastic recuperation were seen due to the susceptible transformation of this metastable β-phase (β_m) in α''-phase. The alloys with higher content in Nb composed by β_m, showed pop-in's associated to the β_m to α'' transformation. This behaviour agrees with the change observed in the microstructure of the alloys: a high content in Nb was translated in a less martensitic structure. The Ti-25Nb-(10-21)Hf alloys group showed wider loops as the Hf content increased. The microstructure observed in this group alloy was HCP martensite. There were no β_m to α'' transformation and thus, the elastic recuperation was lower than in the Ti-(20-29)Nb-16Hf alloys. This result agrees with the change observed in microstructure: a high content of Hf was translated in a more martensitic structure.

Regarding the modulus determination, addition of Nb above 22% wt increases the modulus drastically, whereas values above 27%wt of Nb decrease the elastic modulus. The values of the elastic modulus were in a range between 38 and 77 GPa, although no tendency could be established between the modulus' variation and the Nb wt % variation. This did not concur with the studies made by Hon et al. [13] which report a decrease in the modulus as the Nb content in the alloy increase except for the 30-34%wt of Nb. No correlation was found between the amount of Hf added to the alloys and the increment or decrease of modulus. Previous studies about the effect of Hf in the elastic modulus [6,9,13] reported that Hf had a slight effect or increased the value of the elastic modulus. The results obtained for the Ti-25Nb-(10-21)Hf alloys were in a range between 43 and 77 GPa. There was a variation in the modulus according to the different quantities of Hf although no tendency was observed which allowed to relate the modulus and the Hf wt %. This evidenced other factors affecting the elastic modulus and not just the phase as Hon et al.[4] studies reported.

According to the values of quantum parameters (very close to that reported for GUM Metal [2,3]), elastic behaviour (higher elastic regime that the other alloys) and elastic modulus (51,6 GPa), the chosen alloy to work with was the Ti-25Nb-21Hf.

2. CHAPTER 4: TI-25NB-21HF ALLOY CHARACTERIZATION

The effect of the alloying elements was studied making small buttons of each composition. As there were twelve compositions to study, this method was faster and allowed us to use the minimum material. Once the alloy was chosen, a bar was made in order to characterise it. The mechanical and physic-chemical properties of the material are decisive for the good integration of the implant.

The Ti-25Nb21Hf alloy was fabricated at *Fort Wayne Metals Research Corporation, Fort Wayne, Indiana, USA*. Bars of diameter 10mm and longitude 300mm were obtained by means of vacuum arc remelting (VAR) and drop casting. The bar was vacuum-homogenized and annealed at 650ºC. No further treatment such as quenching or hot work was done on the bar.

As was done with the buttons, the microstructure was firstly determined by means of optical microscopy. The study revealed a microstructure formed mainly of β-phase with grain size less than 20 microns.

To confirm the microstructure observed by optical microscopy, XRD assays were conducted. The novelty of the alloy was a handicap when dealing with XRD diffraction peaks identification. In an attempt to shed light to the multi-phase peaks and the unknown peaks, the studies of Zhou[6,9] and Hon[4,13] were reviewed. The diffractograms obtained on each study are shown in Fig.99 and Fig.100 respectively.

In the diffractogram obtained for our study alloy, there is an unknown peat at θ=36.5º. Zhou studied the ternary system with %wt of Hf between 1 and 7. The peak we found at θ=36.5º in our ternary alloy has no equivalent on peaks from Zhou's studies. But there is a peak at θ=35º found in Hon's studies, associated with α' phase in the plane (1 0 0)that could be equivalent to the peak found in our alloy.

The other unknown peak of our diffractogram was found at θ=41.3º. In Zhou's diffractograms there is a peak corresponding to θ=40º identified as α' phase. This peak is very close to the one obtained in our diffractogram θ=41.3º. The % wt of Hf is much lower in these alloys that in the one under study with 21 % wt of Hf and no peak around θ=40º was obtained.

The Ti25Nb21Hf alloy diffractogram, show two peaks that can be associated to more than one phase: θ=38.5º and θ=82.2º. According to Hon's diffractograms, the θ=38.5º corresponds to a β phase and the θ=82.2º, to a ω phase. In our diffractogram, the omega phase was not present at this angle, it was identified as β or α''.

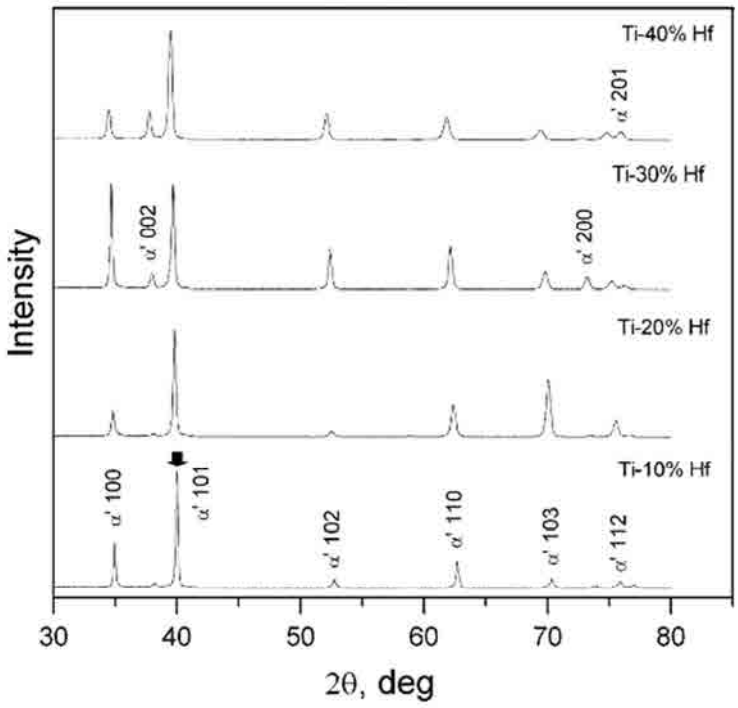

Fig.99 XRD patterns of bulk Ti–Hf alloys. Extracted from [6]

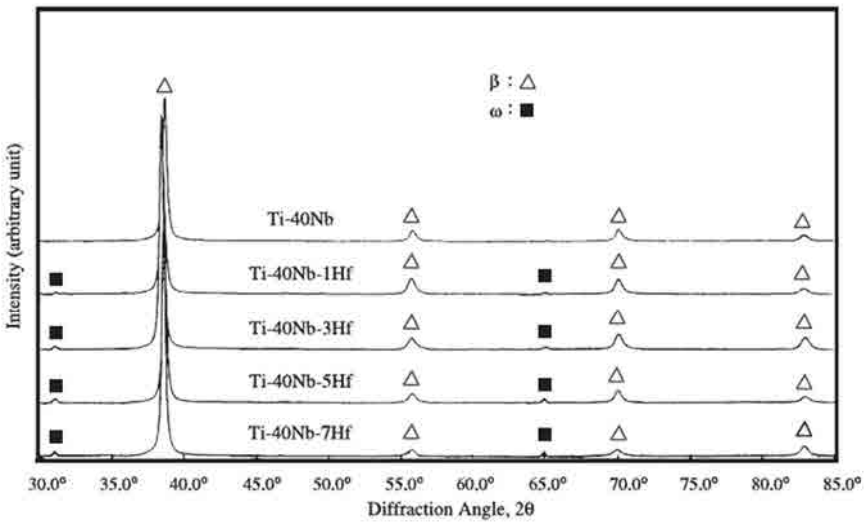

Fig.100 X-ray diffraction patterns of Ti–40Nb–xHf alloys. Extracted from [13]

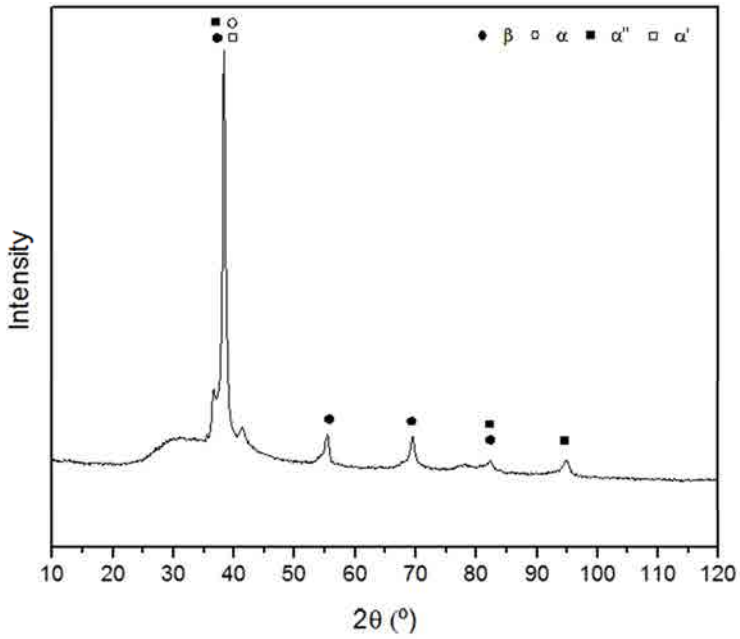

Fig.101 Diffractogram obtained for the Ti25Nb21Hf alloy. On each peak obtained, the possible phases are depicted.

All these data leaded us to conclude that the unknown peaks correspond to α' phase present in the alloy, the multi-phase peak at θ=38.5º corresponds to β phase and there is still a controversy with the θ=82.2º. The ω phase is difficult to detect with XRD technique. TEM images revealed an alloy microstructure composed mainly by equiaxial grains of β-phase with a high dislocations density and no ω-phase. These results agree with the results obtained in Chapter 3 where the Ti-25Nb-21Hf showed a martensite

structure and the presence of the ω-phase after quenching. As was said in Chapter 2, the Ti25Nb.21Hf bar was not heat treated after its fabrication.

After unknown peaks identification it can be state that the alloy was composed by a β-phase with α' martensite. Once the microstructure was defined, the elastic modulus was measured.

Two different methods were used to obtain the elastic modulus: nanoindentation and tensile test. The alloy was compared with Ti6AL4V alloy owing to the fact this is the most common Ti alloy used in bone replacement. With both methods, nanoindentation and tensile tests, the elastic modulus associated to the Ti25Nb21Hf showed lower values than the Ti6Al4V and the cp Ti as well. The elastic modulus of cp Ti is 102,7 GPa [14]; the elastic modulus obtained for the Ti6Al4V was 123 GPa with nanoindentation and 158 GPa with the tensile test. The values obtained for the alloy under study were 97 GPa and 85 GPa for nanoindentation and tensile test, respectively.

Ti alloys for biomedical applications are divided in α+β and β[15,16]. The lowest values correspond to the β-Ti alloys. The Ti25Nb21Hf alloy showed values of the elastic modulus close to the ones obtained for the β-Ti alloys. It is worthy to highlight that these values were obtained in alloys that were annealed or aged, whilst the alloy under study was not thermal treated.

Materials in contact with body fluids get oxidized releasing ions to the surrounding tissue and the body stream which can be hazardous for the body[17]. A material with good corrosion properties would minimize this effect and thus, improve biocompatibility. The corrosion resistance of the Ti25Nb21Hf alloy was compared with that of Ti and Ti6Al4V. All three materials showed a clear active to passive transition at E_{corr} near to 0V. This transition is translated in the formation of a passive protective oxide layer on the surface of the material. The values of E_{corr} obtained for the Ti25Nb21Hf alloy were the lower ones indicating a higher passivation potential. Ti25Nb21Hf alloy had current density smaller that the obtained for cp Ti and Ti6Al4V alloy, which indicates that the oxide layer formed on the surface, is stronger and more stable and can prevent in a more effective way the exchange of electrons and ions than the oxide layer of cp Ti and Ti6Al4V. These results agree with the studies done by Zhou et al. were the corrosion resistance and the biocompatibility of Ti-Ta alloys were studied showing a strong Ta_2O_5 oxide layer which might prevent ions exchange[18]. In the same line, β titanium alloys

composed by Ti-Nb-Ta-Zr were developed presenting a large passive potential range and good biocompatibility[19,20].

Proteins are prone to adsorb on hydrophobic surfaces compared to hydrophilic surfaces and cells behave in an opposite manner. The contact angle is an indicator of the hydrophilic or hydrophobic character of a surface. Moreover, the surface free energy (SFE) of a given material can be determined by the contact angle values. SFE is a more important surface characteristic than surface roughness for cellular adhesion strength and proliferation. Surface energy components were shown to be related to cellular adhesion strength [21].

The contact angle measurements and the surface free energy measurements revealed all three materials are moderately wettable surfaces and showed values of contact angle typical of hydrophilic surfaces. The contact angles for the Ti6Al4V (46±2º) and Ti25Nb21Hf (56±4º) alloys were similar, whilst the contact angle obtained for cp Ti was the highest one (85±3º). Cells tend to adsorb better on hydrophilic surfaces [17], thus the response of cell to our study would be better than for Ti6Al4V.. Previous studies suggested strong cell attachment on surfaces with high surface free energy [21]. In our study there were no differences between the SFE of Ti6Al4V and Ti25Nb21Hf, but there were between Ti and the alloys. Cell response could be affected by the different components (polar and dispersive) of the surface energy.

The electric charge of a material surface is considered to be one of the main physical factors involved in the biological evolution of the tissue around an implant. This charge depends on several factors, such as the chemical composition of the material surface in contact with the tissues, the inflammatory situation, the composition of the surrounding body fluid and the environmental pH value. Investigation of the relationship between surface chemistry, electric charge on a surface and protein adsorption is essential for understanding the mechanism of biological integrations with tissues. Consequently, it is beneficial to the improvement of the quality of prostheses and biomedical devices [22].

The value of the zeta potential determines the attraction of repulsion behavior of charged particles. Positive values of zeta-potential at a fixed pH indicate a positive charge of the surface meaning that negatively charged entities, such as anions or charged proteins, would be attracted[17]. cp Ti showed the highest IEP, which reflects less

dissociable surface groups and more unspecific adsorption of electrolyte ions compared with the other materials under study.

The IEP was also calculated at pH 7 (physiological pH) and the values of zeta-potential were also negatives. The lowest value was obtained for Ti25Nb21Hf alloy as in the IEP obtained after the protonation test. Previous studies[22] showed the relation between zeta-potential and protein adhesion. According to these studies, the lower the absolute value of zeta-potential of the surface, the lower driving force that brings proteins to adhere to the surface. In our case, the lower absolute value of zeta-potential was found for the Ti25Nb21Hf alloy, which could lead us to think that the alloy under study would trigger better protein adhesion if compared with Ti and Ti6Al4V.

3. CHAPTER 5: RECOMBINANT FRAGMENTS FABRICATION

One approach to improve osseointegration is the use of molecules that enhance the bioactivity of the material. There are different strategies based on the use of ECM proteins, fragments of proteins or small peptide chains [23]. In this thesis recombinant fragments of fibronectin were used. The fragments were expressed in an E.coli host. The cloning was carried out using a pGEX-6P-1 vector resistant to ampicillin engineered with an internal *lac*Iq gene.

The fragments were those corresponding to the cell attachment site and heparing binding domain of FN. The cell attachement site (CAS) spanned from the 8^{th} to the 10^{th} domain of FN III whilst the heparing binding domain (HBII) sppaned from the 12^{th} to the 14^{th} domain of FNIII.

The primary key to successful preparation of recombinant proteins in E. coli is the skilful combination of the utensils from the vast genetic toolbox. There is a vast variety of expression vectors, tags and promoters[24]. The FN fragment spanning the cell attachment site in Petri et al. [25] studies was inserted in an XA3 plasmid (Pinpoint System, Promega) and tagged with biotin at the amine terminus. The fragment was amplified in DH5α cells and expressed in JM109 bacterial cells. In Martino et al.[26] studies the vector used was a pGEX4T-1 (GE Healthcare, Chalfont St. Giles, UK) and

the fragment was GST tagged and amplified in BL21 *Escherichia coli* cells. The FN fragment spanning the heparin binding region in Kim et al.[27] studies was inserted in a pBAD-His-A multicloning site vector (Invitrogen) and poly-His tagged.

In this thesis we demonstrate that both fragments can be inserted in a pGEX-6P-1 (GE Helthcare, New Jersey, USA), both can be GST tagged and BL21 *Escherichia coli* cells were suitable for their expression.

4. CHAPTER 6: OPTIMIZATION OF THE BIOFUNCTIONALISATION PROCESS

Technological advancement in areas such as coating materials requires a chemical and physical understanding of surface processes. It is essential to conserve the biological activity and accessibility of active sites after immobilization. Ideally, immobilization must provide stability to their structure at different conditions of temperature or pH. Previous studies dealing with FN recombinant fragments immobilisation used physisorption[28], brushes[29] or SAMs of alkanethiols[25,30], but no use of the silanes chemistry was seen in previous studies to immobilise a recombinant fragment of FN onto a surface. For these reason the study of physisorption vs silanisation was studied to immobilise our fragments on the Ti25Nb21Hf alloy. Silanisation is a common technique to immobilise small peptide chains on surfaces. After silanisation, the surface of the material is covered with alkoxysilane molecules which are able to form strong bonds with titanium oxide layer TiO_2. The TiO_2 layer contains hydroxyl groups that attack and displace the alkoxy groups of the silane forming covalent -Si-O-Si bonds. The most commonly used aminosilane is the 3-Aminopropyltriethoxysilane (APTES) which have three ethoxy groups per molecule. Proteins interact with APTES at the primary amino groups or the carboxyl groups forming a covalent bonding between them and the material's surface.

The adsorbed mass results for CAS or HBII fragments varied depending on the strategy used to tether it onto the surface. The fragments behaved inversely: CAS gave better results with covalent bonding and HB II with physisorption.

In the case of physisorption, the HB II adsorbed mass was twice the mass adsorbed for the CAS. Both fragments present an isoelectric point at pH= 4.75 *(calculated by Protein Calculator V3.3; http://www.scripps.edu/~cdputnam/protcalc.html)*. The net charge on the molecule is affected by pH of its surrounding environment and the number of charged amino acids it contains. Working at pH= 7, both fragments have negative net charge, but each amino acid in the fragment has a different dissociation constant (K_D) and at physiological pH most of these amino acids are not fully ionized or fully unionized. Therefore, the different rate of adsorption between fragments might be due to its charge and also due to the hydrogen bonds and Van der Waals forces triggered by the different amino acids. After the Ti25Nb21Hf characterization, it was known that the zeta potential at pH7 was negative. After checking the charge of each amino acid in the fragments, the CAS showed more negative amino acids than the HBII, which explains the lower ratio of adhesion of the former fragment.

In the case of covalent bonding, the CAS adsorbed mass was 1.3 times the mass adsorbed for the HB II. As it was explained in Chapter 2, section 7.2; a crosslinker that converts the free amino groups of APTES into maleimide groups was used. Thus, the amino groups and other nucleophilic groups of the protein can react with the surface. Each amino acid contains an amino group prone to react with the silanised surface, but just two amino acids contain nucleophilic groups (Serine and Cysteine). The CAS fragment possesses 45 more amino acids than the HBII. Moreover, no Cysteines are present in either of the fragments, but CAS has the double number of Serines than the HBII. The higher mass adhered of CAS might be due to a higher content of amino and nucleophilic groups compared with HB II.

Together with a high quantity of protein adsorbed, it is also important a good distribution of the protein on the surface. For this reason, AFM topography studies were conducted on the functionalised surface after protein physisorption and silanisation. CAS was capable to form a continuous layer onto the surface both in physisorption or silanisation. The scratching tests confirmed the presence of this layer and its thickness. The layer obtained by physisorption was 5 ± 1.58 nm thick and the layer obtained by covalent bonding 6.8 ± 0.83 nm thick. According to previous studies[31,32], the thickness of the APTES layer is 0.7nm. Thus, one can conclude that the layer of protein formed in the silanised surface was higher than the layer formed by physisorption. This result agrees with the result obtained with OWLS, were higher protein adhesion was found

after silanisation. The conformation of the fragment was different if physisorbed or bonded by silanes chemistry on the TiNbHf alloy. The fragment showed a glomerular distribution when adhered by means of physisorption, but when it was adhered by means of the silanes chemistry the conformation was in fibrils. This fibril-like distribution was observed by Rico et al.[30] when studying the molecular assembly and biological activity of a recombinant fibronectin fragment $FNIII_{7-10}$ on poly(ethyl acrylate). FN has a compact conformation mediated by intramolecular interactions, although this conformation might change due to changes in the pH or ionic strength o by addition of detergent or denaturants or by surface chemistry[33]. As the FN binding sites are distributed along the length of the molecule, this extension plays an important role in exposing this binding sites and allowing intermolecular interactions[34].

The study of the immobilisation of the fragments by means of physisorption and silanisation demonstrated that silanisation gave better adhesion efficiency of the fragments and induced fibrilar conformation of the CAS fragment exposing its binding sites and allowing intermolecular interactions.

5. CHAPTER 7: CELL RESPONSE TO THE BIOFUNCTIONALISED SURFACES

In vitro studies were made to test the bioactivity of the fragments synthetized. Although this type studies did not reflect totally the implantation process, they are an indicative of how the tissue will respond to the new materials and it is an essential step previous to *in vivo* studies. There are different indicators of a good bioactivity such as cell adhesion, proliferation and differentiation.

Previous studies state that cell spreading is related with the strength of the initial binding[35]. One of the goals of this thesis was determine the differences regarding force adhesion between the CAS fragment and lRGD and cRGD. For this purpose, AFM cell adhesion force assays were conducted.

The AFM adhesion force obtained for each material and each functionalisation molecule was represented by a box and whisker plot. This statistic tool allows comparing at the same time different data groups with no information loosening. The

graphics showed less dispersion in the strength binding values for cells tested in Ti25Nb21Hf biofunctionalised alloy than for cells tested in biofunctionalised cp Ti. The force values obtained for the Ti25Nb21Hf alloy were higher than for the cp Ti. In both substrates, the higher forces obtained were for the CAS fragment.

Some studies state that lRGD have less specificity than the plasma proteins and integrins and it lacks RGD signals not connected to integrins[36,37]. Puleo et al.[38] demonstrated that adding flanking residues and constraining the conformation of the RGD motif to a loop the ligand specificity for integrins is improved. The CAS fragment spans the region from 8th to 10th type III of fibronectin which includes the sequences RGD (Arg-Gly-Asp) and PHSRN (Pro-His-Ser-Arg-Asn). The PHSRN sequence is needed to achieve full adhesive activity for the $\alpha_5\beta_1$ fibronectin receptor. Previous research showed that high affinity binding requires this synergic site to be engaged[39,40]. Kerssemakers et al.[41] identified the steps observed in the force curves as membrane tethers pulled out from the cell surface and the initial part of the retraction curve as the deformation of the whole cell and many complex attachments removed at the same time whilst the cell is pulled off the surface. In ours studies, the curves for the CAS fragment were the ones with more steps. According to these results, it is demonstrated that the presence of the PHSRN sequence in the CAS fragment enhanced the adhesive activity of cells compared with lRGD and cRGD.

Cell adhesion is important for the maintenance of tissue structure and the promotion of cell migration which are important for implant colonization. Cell adhesion determines the proliferation, differentiation and many other important cell behaviors. With the adhesion assay the ability of cells to adhere on the different functionalised substrates was tested.

Cell adhesion assays made by Martino et al.[26] showed similar adhesion between FN and FN $III_{9\text{-}10}$. On the other hand, Petrie et al.[25] states that FN $III_{7\text{-}10}$ improved cell adhesion when compared with RGD. In the adhesion assays conducted in this thesis, the CAS ($FNIII_{8\text{-}10}$) gave better adhesion than FN. The adhesion obtained for the CAS was equivalent to that obtained for the lRGD, cRGD. Such cell response might be due to the high concentration of RGD sequences on the surface if compared with the whole FN molecule, which covered more surface and then the final concentration of RGDs were lower. HB II fragment gave also an adhesion response equivalent to that obtained with

the aforementioned motifs. This result agreed with some studies that suggest that cell surface heparan sulfate proteoglycans may act as a receptor for the heparin binding fragment [27,42] . Other studies suggest that integrin receptors α4β1 and αvβ5 may interact with specific sequences in this region of FN[27,43] .

When both fragments CAS and HB II were used together, the cell adhesion response showed that CAS-HB II 70:30 combination adhesion triggered was equivalent to that of lRGD, cRGD, CAS and HB II. Whilst CAS-HB II 50:50 and CAS-HB II 30:70 combinations showed an adhesion efficiency equivalent to that of FN, being the latter combination the one that promoted less cell adhesion. This lead us to think of a possible competence between the fragments which diminishes the presence of signals for the integrins involved in adhesion.

Cells require a stretched morphology to maintain their normal phenotype and function. Cell spreading is an indispensable factor for their subsequent settlement and commitment owing to the fact that is an essential stage for cell proliferation and differentiation. Therefore a spreading study it is important to determine cell response to the different substrates.

Regarding cell spreading, previous studies [26] showed equivalent spreading between FN and FN $III_{9\text{-}10}$. In our studies, cells in contact with FN showed higher spreading than cells in contact with the lRGD, cRGD and the CAS and HBII fragments alone. The HBII showed a lowest spreading which. agrees with a previous study that demonstrated the ability of the HB domain to promote cell spreading in absence of the cell binding domain [42]. An important feature showed in cells in contact with the HB II fragment was the presence of ruffled borders. According to Borm et al. [44] conditions of suboptimal cell-substrate adhesion lead to a significantly reduced lamellipodia persistence and an inefficient cell migration resulting in a dramatic increase in ruffle frequency. The different combinations of CAS and HB II fragments showed equivalent spreading from that obtained for cells in contact with FN when the proportion of HB II was over 30% in the solution. In addition to the interaction between integrins and the RGD-PHSRN sequence from the cell binding domain, it is known that cell membrane heparan sulfate proteoglycans (HSPGs) interacts with fibronectin via the heparin binding domains promoting the formation of focal contacts which are responsible in a great extent of cell motility and spreading [23,42,45,46]. Our results made patent the role of the HB II fragment

in cell spreading. As it was said before, the HB domain of FN play important roles in various biological processes including reorganization of the cytoskeleton and the assembly of focal adhesions, [23,42,45,46], although without the cell-binding domain it promoted reduced spread area, no focal adhesions formation and absence of stress fibres. It is not surprisingly, that the presence of the HB fragment combined with the CAS fragment triggered a better cell response in terms of cell morphology. The results obtained in this thesis agree with a previous study by Kim J.H. et al. [27] who reported that the HB domain enhances the central cell-binding domain cell adhesion, spreading and proliferation. However, in that case the fragment used spanned the FN III $_{8\text{-}14}$, whilst in our case we used a combination of two fragments: FN III $_{8\text{-}10}$ and FN III $_{12\text{-}14}$. The results obtained after cell area analysis showed that when the proportion of HB II was over 30% in the solution, cells spreading was equivalent to that obtained for cells in contact with FN. Images obtained for cells in contact with CAS-HB 70:30 combination showed less focal contacts and a fewer dense cytoskeleton, which explains the lower spreading area observed for this fragment. In the FNIII$_{8\text{-}14}$ fragment the proportion of the CAS and HB domains is 1:1 whilst if both fragments are combined, there is an adsorption competence and the distance between fragments to be effective is not controlled. This might be the cause of the minimum percentage of HB needed to trigger a cell response equivalent to that of FN.

As was stated before, cell adhesion determines the proliferation, differentiation and many other important cell behaviors. The results obtained in this thesis reported that the fragments with higher proliferation where those with higher spreading. Proliferation is an indicative of the non-toxicity of the material as it allows the material integration. . Studies by Petry et al. demonstrated that RGD had less integrin specificity which reduces proliferation and differentiation [25]. This agreed with the results obtained for cells in contact with lRGD and cRGD. The CAS fragment spans the region from 8th to 10th type III of fibronectin which includes the sequences RGD (Arg-Gly-Asp) and PHSRN (Pro-His-Ser-Arg-Asn). The PHSRN sequence is needed to achieve full adhesive activity for the $\alpha_5\beta_1$ fibronectin receptor[39,40]. Owing to the fact that cell proliferation need signals from other integrins, the CAS fragment was not able to trigger a proper spreading response. The HB II showed the lower proliferation. This agrees with the fact that cells in contact with HB II had no focal adhesions, ruffling activity

and absence of stress fibers, which leads to a frustrate cell structure. When both fragments were combined, it seemed that there was a treshold value for HB II, Above 30% of HB II in the combiantion favoured cell proliferation achieving values equivalent to that observed for FN.. The highest proliferation was found for FN, CAS-HB 50:50 and CAS-HB 30:70. Once again, the role of HB II was demonstrated.

Besides to trigger a proper cell adhesion and proliferation, an implant material should favour osteoblastic differentiation to guarantee osseointegration.. It is important to know if the fragments would be able to trigger the proper differentiation in cells. Previous studies showed that a recombinant fragment of FN enhanced differentiation in comparison with RGD peptides [29] and that RGD had less integrin specificity which reduces proliferation and differentiation [25]. The results obtained in this thesis agree with that. The RGD's are not enough to stimulate differentiation whilst CAS seemed to trigger certain differentiation. It might be due to the presence of PHSRN sequence that made the adhesion with the $\alpha_5\beta_1$ integrins more strong.Cells were able to attach and differentiate on HBII functionalised surfaces unless they are not able to proliferate properly. The differentiation associated to this fragment might be due to its interaction with growth factors [47]. The low proliferation may be associated to its weak adhesion. . When both fragments were combined, the differentiation response was improved when the percentage of HBII was fewer than 50%. This result is opposite to cell proliferation results, where the highest rates were found when the percentage of HBII was higher than 50%. This proliferation response on behalf of rMSC cells agrees with the fact that differentiation inhibits proliferation. Regarding differentiation the role of the HB II was patent. Although it was not studied in this thesis, it would be interesting to study CAS and HBII combinations with a percentage of HBII ranging between 30% and 50% with the purpose to find a combinations with good proliferation and differentiation as occurs in FN.

6.BIBLIOGRAPHY

1. Niinomi, M. Recent Metallic Materials for Biomedical Applications. *Metall. Mater. Trans. A* **33,** 477 (2002).

2. Saito, T. *et al.* Multifunctional Alloys Obtained via a Dislocation-Free Plastic Deformation Mechanism. **300,** 464 (2003).

3. Hao, Y. L. *et al.* Super-elastic titanium alloy with unstable plastic deformation. **87,** (2005).

4. Hon, Y. H. & Wang Y.N, J. Y. and P. Composition/Phase Structure and Properties of Titanium-Niobium Alloys. *Mater. Trans.* **44,** 2384 (2003).

5. Li, S., Hao, Y., Yang, R., Cui, Y. & Niinomi, M. Effect of Nb on Microstructural Characteristics of Ti-Nb-Ta-Zr Alloy for Biomedical Applications. *Mater. Trans.* **42,** 2964–2969 (2002).

6. Zhou, Y.-L., Niinomi, M. & Akahori, T. Changes in mechanical properties of Ti alloys in relation to alloying additions of Ta and Hf. *14th Int. Conf. Strength Mater.* **483-484,** 153–156 (2008).

7. Raabe, D., Sander, B., Friák, M., Ma, D. & Neugebauer, J. Theory-guided bottom-up design of β-titanium alloys as biomaterials based on first principles calculations: Theory and experiments. *Acta Mater.* **55,** 4475–4487 (2007).

8. Nobuhito, S., Niinomi, M., Toshikazu, A., Takashi, S. & Tadahiko, F. Effects os Alloying Elements on Elastic Modulus of Ti-Nb-Ta-Zr System Alloy for Biomedical Applications. *Mater. Sci. Forum* **449-452,** 1269–1272 (2004).

9. Zhou, Y.-L., Niinomi, M. & Akahori, T. Dynamic Young's Modulus andMchanical Properites of Ti-Hf alloys. *Mater. Trans.* **45,** 1549 (2004).

10. Potapov, P. L. *et al.* Effect of Hf on the structure of Ni-Ti martensitic alloys. *Mater. Lett.* **32,** 247–250 (1997).

11. Cremasco, A. *et al.* Correlations between aging heat treatment, ω phase precipitation and mechanical properties of a cast Ti–Nb alloy. *Mater. Des.* **In Press, ,** (2010).

12. Hickman, B. S. The formation of omega phase in titanium and zirconium alloys: A review. *J. Mater. Sci.* **4,** 554–563 (1969).

13. Hon, Y. H., Wang, J. Y. & Pan, Y. N. Influence of hafnium content on mechanical behaviors of Ti–40Nb–xHf alloys. *Mater. Lett.* **58,** 3182–3186 (2004).

14. Setcos, J. C., Babaei-Mahani, A., Silvio, L. Di, Mjör, I. A. & Wilson, N. H. F. The safety of nickel containing dental alloys. *Dent. Mater.* **22,** 1163–1168 (2006).

15. Geetha, M., Singh, A. K., Asokamani, R. & Gogia, A. K. Ti based biomaterials, the ultimate choice for orthopaedic implants – A review. *Prog. Mater. Sci.* **54,** 397–425 (2009).

16. Niinomi, M. Mechanical properties of biomedical titanium alloys. *Mater. Sci. Eng. A* **243,** 231–236 (1998).

17. *Titanium in medicine :material science, surface science, engineering, biological responses, and medical applications*. (Springer, 2001).

18. Zhou, Y. L., Niinomi, M., Akahori, T., Fukui, H. & Toda, H. Corrosion resistance and biocompatibility of Ti–Ta alloys for biomedical applications. *Mater. Sci. Eng. A* **398,** 28–36 (2005).

19. Vasilescu, E. *et al.* In vitro biocompatibility and corrosion resistance of a new implant titanium base alloy. *J. Mater. Sci. Mater. Med.* **21,** 1959–68 (2010).

20. Xie, K. Y. *et al.* Nanocrystalline β-Ti alloy with high hardness, low Young's modulus and excellent in vitro biocompatibility for biomedical applications. *Mater. Sci. Eng. C. Mater. Biol. Appl.* **33,** 3530–6 (2013).

21. Ponsonnet, L. *et al.* Relationship between surface properties (roughness, wettability) of titanium and titanium alloys and cell behaviour. *Mater. Sci. Eng. C* **23,** 551–560 (2003).

22. Cai, K. *et al.* Surface functionalized titanium thin films: Zeta-potential, protein adsorption and cell proliferation. *Colloids Surfaces B Biointerfaces* **50,** 1–8 (2006).

23. Shekaran, A. & García, A. J. Extracellular matrix-mimetic adhesive biomaterials for bone repair. *J. Biomed. Mater. Res. Part A* **96A,** 261–272 (2011).

24. Sørensen, H. P. & Mortensen, K. K. Advanced genetic strategies for recombinant protein expression in Escherichia coli. *J. Biotechnol.* **115,** 113–128 (2005).

25. Petrie, T. A., Capadona, J. R., Reyes, C. D. & García, A. J. Integrin specificity and enhanced cellular activities associated with surfaces presenting a recombinant fibronectin fragment compared to RGD supports. *Biomaterials* **27,** 5459–5470 (2006).

26. Martino, M. M. *et al.* Controlling integrin specificity and stem cell differentiation in 2D and 3D environments through regulation of fibronectin domain stability. *Biomaterials* **30,** 1089–1097 (2009).

27. Kim, J.-H., Park, S.-O., Jang, H.-J. & Jang, J.-H. Importance of the heparin-binding domain of fibronectin for enhancing cell adhesion activity of the recombinant fibronectin. *Biotechnol. Lett.* **28,** 1409–13 (2006).

28. Salmerón-Sánchez, M. *et al.* Role of material-driven fibronectin fibrillogenesis in cell differentiation. *Biomaterials* **32,** 2099–2105 (2011).

29. Petrie, T. A. *et al.* The effect of integrin-specific bioactive coatings on tissue healing and implant osseointegration. *Biomaterials* **29,** 2849–57 (2008).

30. Rico, P., González-García, C., Petrie, T. A., García, A. J. & Salmerón-Sánchez, M. Molecular assembly and biological activity of a recombinant fragment of fibronectin (FNIII7–10) on poly(ethyl acrylate). *Colloids Surfaces B Biointerfaces* **78,** 310–316 (2010).

31. Lin, M. C. *et al.* Control and Detection of Organosilane Polarization on Nanowire Field-Effect Transistors. *Nano Lett.* **7,** 3656–3661 (2007).

32. Vandenberg, E. T. *et al.* Structure of 3-Aminopropyl Triethoxy Silane on Silicon Oxide. *J. Colloid Interface Sci.* **147,** 103–118 (1991).

33. Patel, S., Chaffotte, A. F., Goubard, F. & Pauthe, E. Urea-Induced Sequential Unfolding of Fibronectin: A Fluorescence Spectroscopy and Circular Dichroism Study. *Biochemistry* **43,** 1724–1735 (2004).

34. Mao, Y. & Schwarzbauer, J. E. Fibronectin fibrillogenesis, a cell-mediated matrix assembly process. *Matrix Biol.* **24,** 389–399 (2005).

35. Selhuber-Unkel, C., López-García, M., Kessler, H. & Spatz, J. P. Cooperativity in Adhesion Cluster Formation during Initial Cell Adhesion. *Biophys. J.* **95,** 5424–5431 (2008).

36. Hersel, U., Dahmen, C. & Kessler, H. RGD modified polymers: biomaterials for stimulated cell adhesion and beyond. *Synth. Biomim. Polym.* **24,** 4385–4415 (2003).

37. Sechler, J. L., Corbett, S. A. & Schwarzbauer, J. E. Modulatory Roles for Integrin Activation and the Synergy Site of Fibronectin during Matrix Assembly. *Mol. Biol. Cell* **8,** 2563–2573 (1997).

38. Puleo, D. A. & Bizios, R. *Biological Interactions on Materials Surfaces*. (Springer, 2009). doi:10.1007/978-0-387-98161-1-7

39. Aota, S., Nomizy, M. & Yamada, J. M. The Short Amino Acid Sequence Pro-His-Ser-Arg-Asn in Human Fibronectin Enhances Cell-adhesive Function. *J. Biol. Chem.* **269,** 24756–24761 (1994).

40. Dillow, A. K., Ochsenhirt, S. E., McCarthy, J. B., Fields, G. B. & Tirrell, M. Adhesion of α5β1 receptors to biomimetic substrates constructed from peptide amphiphiles. *Biomaterials* **22,** 1493–1505 (2001).

41. Kerssemakers, J. W. J. *et al.* Assembly dynamics of microtubules at molecular resolution. *Nature* **442,** 709–12 (2006).

42. Woods, A., Couchman, J. R., Johansson, S. & Höök, M. Adhesion and cytoskeletal organisation of fibroblasts in response to fibronectin fragments. *EMBO J.* **5,** 665–70 (1986).

43. Dalton, B. A., McFarland, C. D., Underwood, P. A. & Steele, J. G. Role of the heparin binding domain of fibronectin in attachment and spreading of human bone-derived cells. *J. Cell Sci.* **108,** 2083–2092 (1995).

44. Borm, B., Requardt, R. P., Herzog, V. & Kirfel, G. Membrane ruffles in cell migration: indicators of inefficient lamellipodia adhesion and compartments of actin filament reorganization. *Exp. Cell Res.* **302,** 83–95 (2005).

45. Ruoslahti, E. Integrins. *J. Clin. Invest.* **87,** 1–5 (1990).

46. Pankov, R. & Yamada, K. M. Fibronectin at a glance. *J. Cell Sci.* **115,** 3861–3863 (2002).

47. Hynes, R. O. The extracellular matrix: not just pretty fibrils. *Science* **326,** 1216–9 (2009).

V

Conclusions

Chapter 9

Conclusions

After studying the ternary system TiNbHf and the role of the CAS and HBII recombinant fragments of FN on cell adhesion, proliferation and differentiation it can be concluded that:

1. Effect of the alloying elements in the ternary system TiNbHf

1.1. The properties map is a useful technique to help on the designing of alloys. All the alloys show quantum parameters close to the values reported for Gum Metal.

1.2. The method of fabrication gives valid composition of the alloys.

1.3. The addition of niobium increases the β-phase in the alloys, whereas the addition of hafnium triggers the appearance of thermoelastic martensite and ω-phase which was due to thermal treatment.

1.4. Addition of Nb above 22% wt increases the modulus drastically, whereas values above 27%wt of Nb decrease the elastic modulus.

1.5. No correlation was found between the amount of Hf added to the alloys and the elastic modulus increase or decrease.

1.6. According to the values of quantum parameters, elastic behaviour and elastic modulus, the chosen alloy to work with was the Ti-25Nb-21Hf.

2. Properties of the Ti25Nb21Hf

2.1. Due to the novelty of the alloy the XDR diaffractograms were not available. Despite this, all the unknown peaks were identified by comparison with previous works.

2.2. TEM assays concluded that the alloy was composed mainly of β-phase with thermoelastic martensite (α’’). The β-phase was a cubic body centered structure (BCC). The value of the 'a' parameter was also determined, showing a value of 4,6 Å. Grain size was less than 20 microns.

2.3. Both nanoindetantion and tensile test showed similar values of the modulus demonstrating that Ti25Nb21Hf alloy has lower modulus than Ti6Al4V.

2.4. Ti25Nb21Hf alloy with any further heat treatment or cold work, showed an elastic modulus around 85 GPa, which is close to the elastic modulus obtained for β-Ti alloys such as Ti13Nb13Zr (aged), TMZF (annealed), Ti15Mo2.8Nb0.2Si (annealed) and Tiadyne 1610 (aged).

2.5. Ti25Nb21Hf improved the passivation potential of cp Ti and Ti6Al4V alloy.

2.6. Ti25Nb21Hf was able to generate a passive oxide layer stronger and more stable than the oxide layer or cp Ti and Ti6Al4V. Thus, the alloy developed in this thesis is able to prevent in a more effective way the exchange of electrons and ions.

2.7. The alloy showed values of contact angle typical of hydrophilic surfaces. The value of contact angle was slightly higher than the obtained for the Ti6Al4V alloy

2.8. At a physiological pH the Ti25Nb21Hf alloy showed lower values of the zeta-potential.

3. Optimization of the biofunctionalisation process

3.1. Ti25Nb21Hf alloy was successfully biofunctionalised with different motifs such as lRGD, cRGD, CAS, HBII and FN.

3.2. Silanisation increased by 124% the ng/cm^2 of CAS tethered onto the surface. Whilst the ng/cm^2 of HB II tethered onto the surface diminished by 12%.

3.3. AFM topography studies confirmed CAS was able to form a continuous layer onto the surface both in physisorption or silanisation. A layer of about 5nm in thickness was achieved when the motif was tethered to the surface by means of physisorption, when silanization was used, the thickness of the layer increased around 2nm compared to physisorption.

3.4. CAS fragment showed fibrilar conformation when silanes chemistry was used improving the glomerular conformation obtained by phisisorption. Fibrilar conformation allowed the fragment to expose its binding sites which favours intermolecular interaction.

3.5. Silanisation gave more molecule adhesion efficiency and a better conformation for the final purpose: improve cell response.

4. Cell response to the biofunctionalised surfaces

4.1. Ti25Nb21Hf silanised surfaces biofunctionalised with lRGD,cRGD and CAS gave higher cell adhesion forces than cp Ti biofunctionalised in the same manner.

4.2. The adhesion force triggered by the CAS fragment in rMSCs was higher than the force triggered by lRGD and cRGD and more focal contacts were shown.

4.3. Cell adhesion response to lRGD, cRGD, CAS and HBII showed higher number of adhered cells than FN

4.4. When the CAS and HB II fragments were combined with a proportion of HB II less than 50%, the adhesion was equivalent to that obtained with CAS.

4.5. Cells in contact with the HB II fragment showed ruffled borders which is an indicative of suboptimal cell-substrate adhesion

4.6. Immunofluorescence images showed very similar cell cytoskeleton for cells in contact with CAS and HB II fragments combinations and FN.

4.7. It seemed to be a threshold value at which HB II fragment increases cell spreading and proliferation and inhibits differentiation. A proportion above 30% of HB II in CAS and HB II combination of fragments increased cell spreading and proliferation to levels equivalents to those of FN.

4.8. The HB70:30 combination induced rMSC differentiation after 7 days in culture, reaching a value not achieved even after 21 days in culture for any of the motifs tested. This made us to conclude that this is the best combination to favour differentiation.

VI

Ongoing Research

Chapter 10

Effect of the cold work in the microstructure and mechanical properties of the Ti-25Nb-21Hf alloy

1. INTRODUCTION

Nanocrystalline materials, defined as polycrystalline materials with an average grain size less than 10^{-7} m, are currently of great interest due to their unusual mechanical and physical properties. This type of materials are structurally characterized by a large volume fraction of grain boundaries, which may significantly alter their physical, mechanical, and chemical properties in comparison with conventional coarse-grained polycrystalline materials which have grain sizes usually in the range of 10‑300 μm.

Two types of atoms can be considered in a nanocrystalline structure:

- crystal atoms with neighbour configuration corresponding to the lattice
- boundary atoms with a variety of interatomic spacing

The atomic structure of this type of materials is schematised in Fig.102. In the core of incoherent interfaces, the misfit between neighboring crystallites modifies the atomic structure by reducing the atomic density and by altering the coordination between nearest-neighbor atoms relative to the perfect crystal.

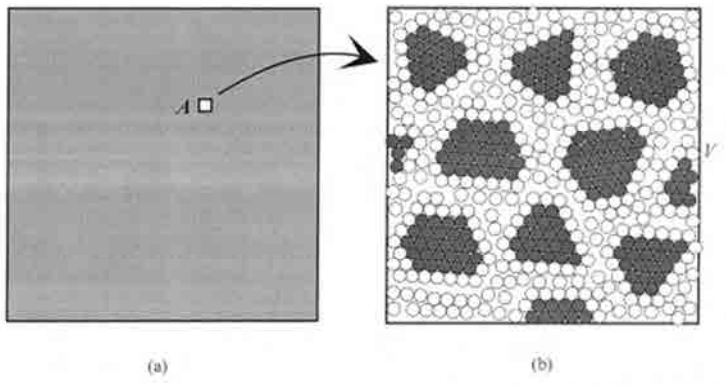

Fig.102 A macroscopically homogeneous nanocrystalline material (a) and its atomic microstructure (b). Adapted from [1]

Nanocrystalline materials contain high density of interfaces, thus a substantial fraction on atoms lie in the interfaces. If it is assumed that the atoms are sphere shaped, the volume fraction of interfaces in the nanocrystalline material may be estimated as $3\Delta/d$ (where Δ is the average interface thickness and d is the average grain diameter).

Thus, the volume fraction of interfaces can be as much as 50% for 5 nm grains, 30% for 10 nm grains, and about 3% for 100 nm grains [2].
The attractiveness of this type of materials rely on its increased strength/ hardness, improved toughness, reduced elastic modulus and ductility, enhanced diffusivity, higher specific heat, enhanced thermal expansion coefficient and superior soft magnetic properties in comparison with conventional polycrystalline materials.

Not surprisingly, in the last years owing to their unique, often greatly enhanced, mechanical and physical properties, nanocrystalline materials have shown a great promise for use in structural and device applications and have attracted an increasingly extensive attention.

Nanocrystalline materials can be synthesized either by consolidating small clusters or breaking down the polycrystalline bulk material into crystalline units with dimensions of nanometers. The principal synthesis methods are: inert gas condensation, mechanical alloying, crystallization from amorphous material, cold and hot work, plasma synthesis and chemical vapor deposition amongst others [2].

Previous studies reported a reduction in the elastic modulus of nanocrystalline material obtained by means of accumulative roll bonding [3] or severe plastic deformation [4] by 35% compared with the corresponding coarse-sized crystalline material. Other studies reported superelasticity and/or phase transformation in nanocrystalline materials [5–7].

These nanocrystalline alloys special properties lead us to study the effect of high rates of cold work in the microstructure and the mechanical properties of the Ti25Nb21Hf alloy.

2. MATERIALS AND METHODS

2.1 Sample fabrication

The Ti25Nb21Hf bar obtained by means of drop casting at Fort Wayne Metals facilities was extruded to 4.2 mm, then machined to 3mm and the fins were eliminated. The machined bar was drawn to 1.4mm and annealed. Thin 127 µm wires were produced by varying cold work (95% and 99%) and heat-treated at 650°C in a vacuum furnace. The

heat-treatments were done at 1s and 3s. After the heat-treatment the material was pre-strained at 0.7kN.

2.2 Other samples tested

Thin 125 μm wires of 316LV with 90% CW, NiTi wires with 40% CW SEA and Ti6/4 all of them supplied by Fort Wayne Metals.

2.3 Wire tensile testing

The tensile testing principles were explained in detail in Chapter 2, section 2.2.

Monotonic uniaxial tensile properties of the wires were measured at room temperature at a strain rate of 10^{-3} s^{-1} using an Instron Model 5565 Tensile test frame (Instron Corp., USA) equipped with pneumatic grips and a 1 kN load cell. Fine 600 grit abrasive cloth was used to line the pneumatic grips in order to prevent excessive sample slip outside of the test gage.

Cyclic tensile tests were also completed at 37ºC and 150ºC for the Ti25Nb21Hf wires on an equivalent tensile bench fitted with an environmental chamber capable of maintaining a temperature of 200ºC.

2.4 Rotary beam fatigue testing

Some common fatigue test methods are axial, bending and torsional testing. In this thesis rotary beam fatigue testing was used to determine the fatigue behaviour of the different Ti25Nb21Hf alloy wires. The aim of this study was determine how does the fatigue response is affected by microstructure.

During rotary beam fatigue testing, the mechanical deformation that takes place in a solid wire may be put on the same level as pure bending. In pure bending exists a longitudinal fiber which remains undeformable, called the neutral axis (Fig.103). Every point at a distance (y) from the neutral axis is under flexural loading. If the distance is positive, the fiber is in compression; if negative, the fiber is in tension.

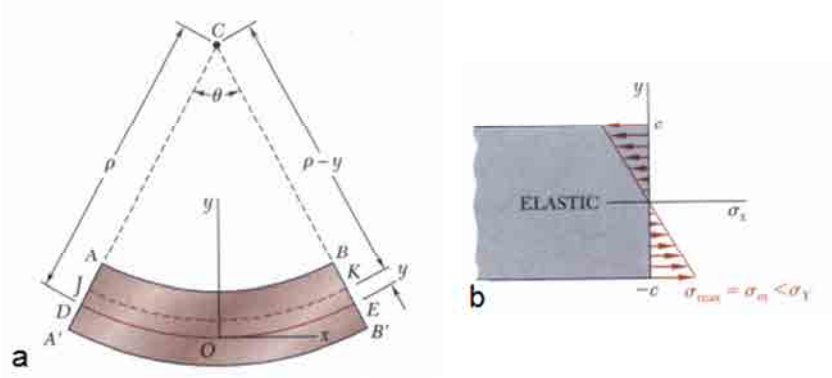

Fig.103 a) Specimen subjected to pure bending. DE denotes neutral axis, AB the compression zone, A'B' the tension zone and ρ the radius of curvature. b) Diagram of the forces experienced in the specimen. Adapted from [8]

Rotating the wire samples causes a reversing cyclic stress, where the wire surface experiences an alternating tension and compression state. During testing, the stresses are always maintained below the superelastic limit, so there is no permanent set present.

The equipment (Fig.104) consists of a motor-driven chuck and an adjustable bushing support that allows variable positioning of the free end of the specimens. The various holes in the bushing-bar provide strain adjustment to the specimen. Using a calculated distance from the chuck to form an arch, the design allows the axis of the chuck and the axis of the loose wire end in the bushing to be exactly parallel.

The specimen, with a known length, is mounted into the drive chuck system while the "non-driven" end is inserted into the free bushing. To prevent vibration, two support guides are positioned on the radius of the specimen, but outside of the apex, such that the guides do not affect the region of maximum strain. An electronic clock counts the number of cycles with a resolution of $1/100^{th}$ of a minute. A sensor is placed in contact with the specimen but not affecting the test in such a way that when the specimen breaks the clock stops.

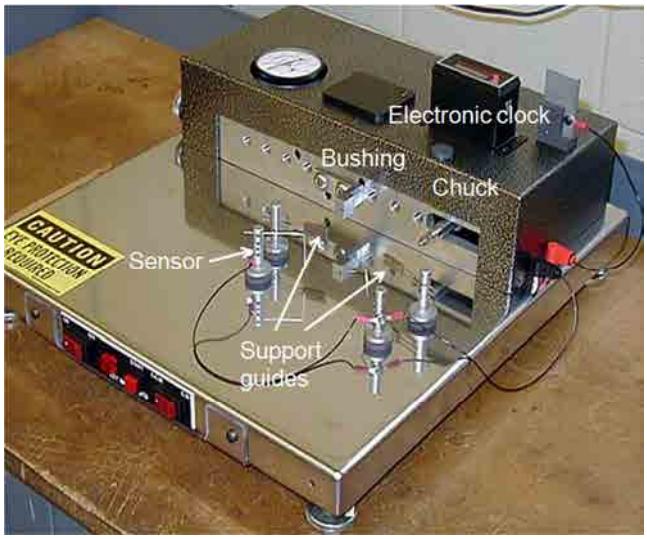

Fig.104 Valley Instruments model 10.040 test machine (USA). Adapted from http://www.positool.com/wftesters.htm

Rotating beam fatigue testing (RBT) was carried out using a Valley Instruments model 10.040 test machine (USA). Seven specimens were cycled to failure until a maximum of 10^9 cycles at a test rate of 60 s^{-1}. The strain was alternated from levels ranging from 0.8% to 1.6%. The specimens were tested under two different conditions: in air at room temperature and in phosphate buffered saline solution (PBS) at 37ºC. One of the extremes of the specimen was fixed in the chuck and the other extreme was inserted into the free bushing. Two support guides were positioned on the radius of the specimen, in a way that they did not affect the region of maxim strain, to avoid vibrations.

2.5 Transmission electron microscopy (TEM) assay

TEM technique was explained in detail in Chapter 2, section 2.4. Owing to the fact that the studied samples were small sized, the jet-polishing method to prepare the samples was not suitable. In this case, the focused ion beam (FIB) milling technique was used.

2.5.1 Focused ion beam (FIB) milling technique

A FIB instrument is very similar to a scanning electron microscope (SEM) regarding design and features, although it provides nanofabrication and site-specific sample preparation capabilities. Both instruments rely on a focused beam to create a specimen image; an ion beam for the FIB and an electron beam for the SEM. For both instruments, the intensity of the secondary electrons produced at each raster position of

the beam is displayed to create an image of the sample. In the FIB, secondary ions may also be detected and used to construct an image of the sample. Images having magnifications up to ∽100 000 times are available using a FIB with a very good depth of field. The operation of a FIB begins with a liquid metal ion source (LMIS). A reservoir of gallium (Ga) is positioned in contact with a sharp Tungsten (W) needle. The Ga wets the needle and flows to the W tip. A high extraction field (>10^8 V/cm) is used to pull the liquid Ga into a sharp cone whose radius may be 5‑10 nm. Ions are emitted as a result of field ionization and post-ionization and then accelerated down the FIB column. The use of Ga is advantageous for two reasons: (i) Ga has a low melting point and, therefore, near room temperature it is in liquid state and (ii) Ga can be focused to a very fine probe size (<10 nm in diameter). FIBs typically operate with an accelerating voltage between 5 and 50 keV. By controlling the strength of the electrostatic lenses and adjusting the effective aperture sizes, the probe current density (and therefore beam diameter) may be altered from tens of pA to several nA corresponding to a beam diameter of around 5nm to 0.5 μm.

Using this technique, thin lamellas of the material can be obtained. The lamellas have the proper thickness to be studied by TEM. The procedure starts with the deposition of a metal line on the area of interest to prevent damage and spurious sputtering of the specimen top portion and to also delineate the location of the interest area. The beam current is reduced and milling is performed on alternate sides of the specimen to reduce redeposition of sputtered material onto the specimen surface. Milling is continued until the membrane is thinned to almost 100 nm or less. After this process, the transparent portion of the sample has a dimension of about 5 μm×20 μm (Fig.105). Then, the electron transparent thin membrane is removed from the bulk specimen and analyzed directly by TEM.

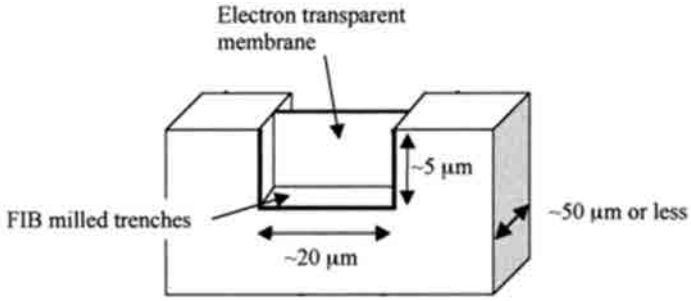

Fig.105 Schematic diagram of a prepared FIB TEM specimen. Adapted from[9]

Lamellas of the TiNbHf alloy wires for TEM studies were prepared by FIB. The equipment used was a FIB Neon 40 (Zeiss, Germany). . 10µm x 3µm lamellas were obtained by cutting the samples in the transversal direction. 500 µm of platinum were deposited on the sample surface to protect it from ion implantation. The TEM used was a JEM 1200 EXII (JEOL, Peabody, MA, USA) with a beam power of 120 kV and a calibrated chamber constant of λ_L=2.606 mm·nm. Both bright field and dark field images were obtained.

3. RESULTS

3.1 Tensile testing

3.1.1 Effect of the cold-work on the elastic modulus

The stress-strain curves obtained for the different materials tested (Fig.106) showed that the elastic modulus of the alloy under study with different grades of cold work (% cw) was similar to that of NiTi and much more lower than the elastic modulus of 316L and Ti6Al4V.

According to Fig.107, an increase in the % cold work was translated in an increment in the elastic modulus as well. The lower modulus was obtained for the samples cold worked at 75% which presented an equivalent value to that of NiTi.

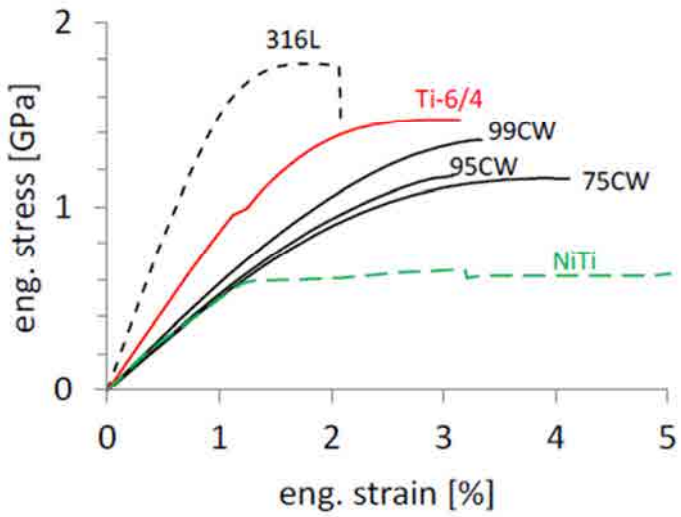

Fig.106 Tensile test curves obtained for the Ti25Nb21Hf at 75 %, 95 % and 99 % of cold work compared with Ti6Al4V, NiTi and 316L.

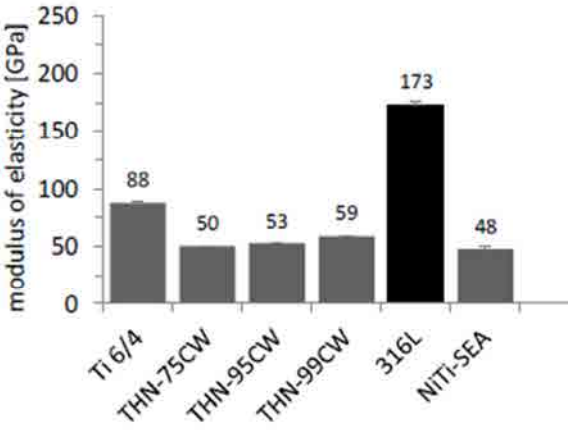

Fig.107 Modulus of elasticity obtained for the Ti25Nb21Hf at 75 %, 95 % and 99 % of cold work compared with Ti6Al4V, NiTi and 316L.

The engineering strain is expressed as the ratio of total deformation to the initial dimension of the material body in which the forces are being applied. In Fig.108 the strains during the plastic and the elastic deformation of the specimens are shown. As it was expected, the 316L specimen had the lower values of strain both in plastic and elastic deformation whilst NiTi had the higher values. Ti25Nb21Hf with 95 % cw showed the lowest value of both elastic and plastic strain. The elastic strain obtained for the 99% cw specimens showed a higher value of elastic deformation if compared with

the 75% cw and 95 % cw samples. Amongst the cold worked samples, the 75 % cw showed the higher plastic strain.

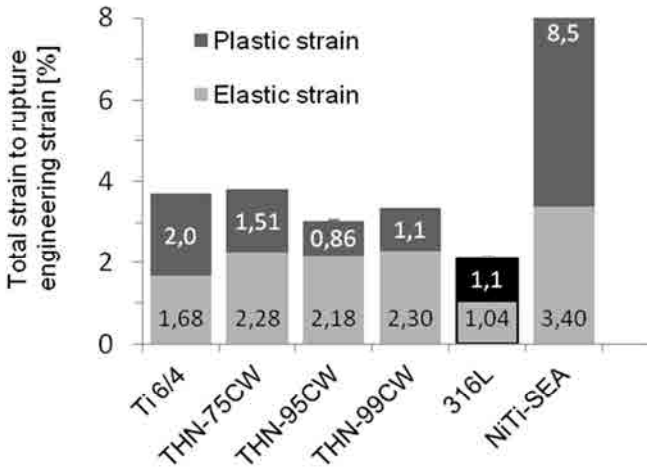

Fig.108 Values of the plastic and elastic strain obtained from the tensile test for each specimen tested.

3.1.1 Effect of the heat treatment on the elastic modulus

In Fig.109 the effect of the heat treatment in the elastic modulus is shown. Samples heat treated for 1s lowered its elastic modulus except for the samples with 75% cw which showed no variation. Samples with 75 % cw heat treated for 3s showed a modulus that exceeded the modulus prior to heat treatment. For the 95% cw and 99% cw, the modulus after 3s of heat treatment showed no differences with modulus before treatment.

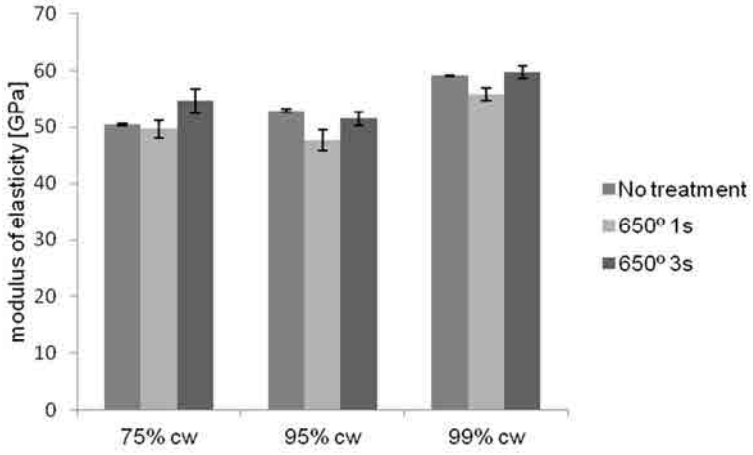

Fig.109 Effect of the heat treatments in the elastic modulus of the different wires.

3.1.3 Cyclic tensile testing

Fig.110 shows cyclic uniaxial tension tests that were performed at body temperature (37 ºC) and at 150 ºC on Ti25Nb21Hf wires after 99% cw.

When the Ti25Nb21Hf specimens were tested at body temperature, no evidence of reversibly performing was seen in either of the cycles. Although for tests conducted at 150ºC, when the magnitude of the external loading returned to zero in the three first cycles, the strain recovered fully returned to the initial level. This elastic behaviour was not seen in further cycles.

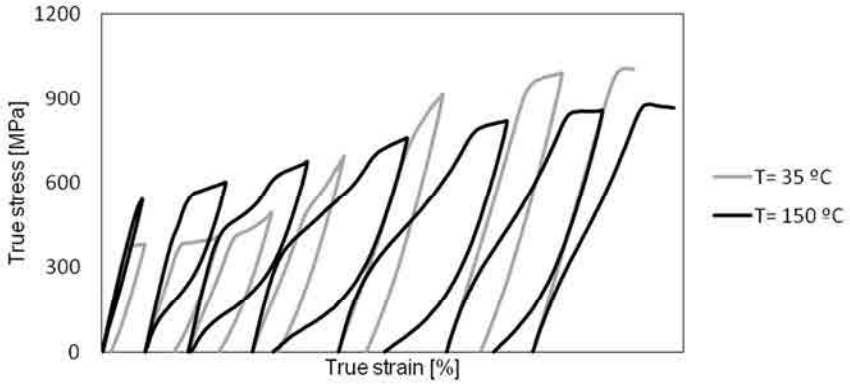

Fig.110 Graphic of the loading-unloading curves at different strain rates of the TiNbHf alloy at 37ºC and 150ºC

When the loading-unloading curves obtained for the Ti25Nb21Hf alloy at 150 ºC were compared with those of NiTi-SEA (Fig.111), it was seen that the behaviour of the Ti25Nb21Hf wire could be related in a certain way with NiTi behaviour.

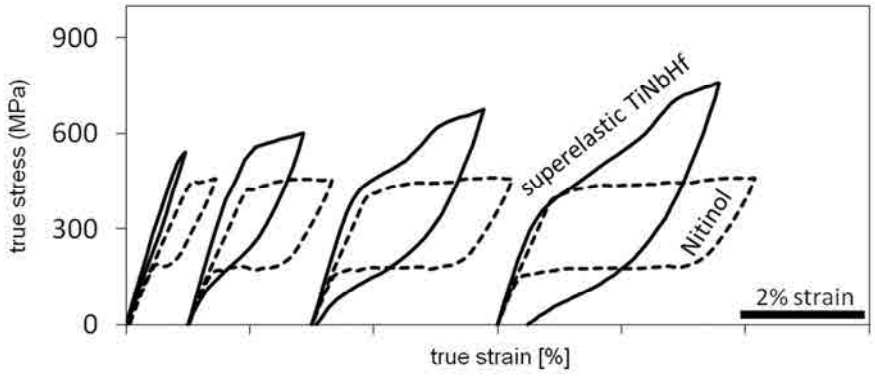

Fig.111 Comparison of the superelastic behaviour of the alloy Ti25Nb21Hf at 150ºC and the shape memory alloy NiTi at 25ºC.

3.2 Microstructure studies

Fig. 112 shows the microstructures obtained for the alloys at different % cw and heat-treated at 650ºC for 1 and 3 s. In all %cw conditions, the 3s heat treatment, lead to a microstructure composed by nanograined regions whilst the 1s heat treatment lead to a microstructure with a mixture of clearly defined grains and grains with not clearly defined boundaries. In all the cases, the bright field images confirmed the presence of austenite β (BCC), orthorhombic martensite α´´, ω-phase and an amorphous phase.

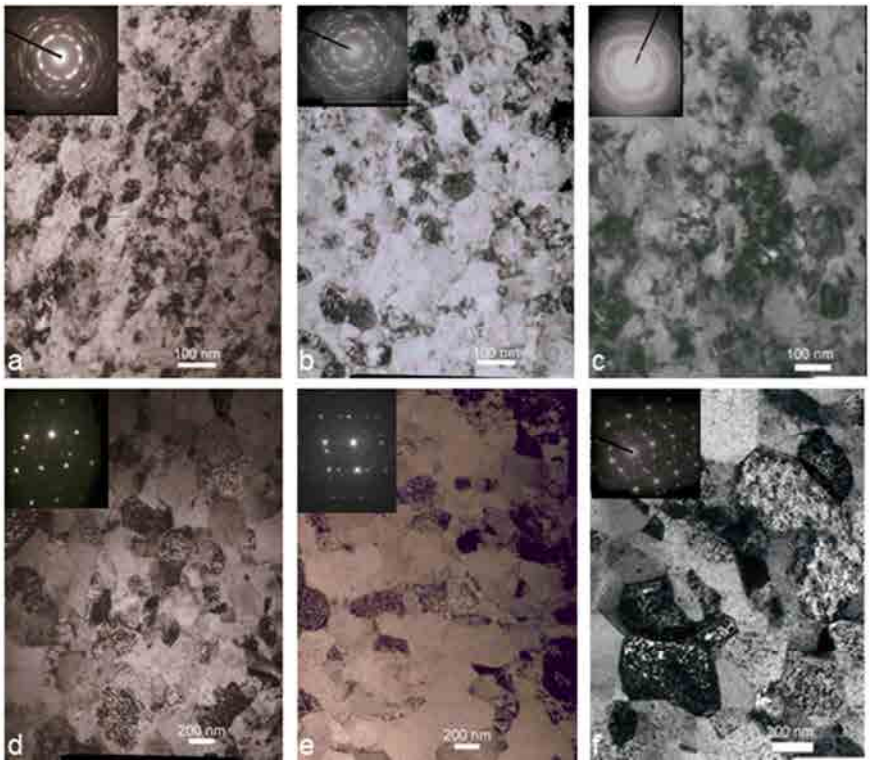

Fig.112 Microstructures obtained for the Ti25Nb21Hf cold worked at 75% heat treated at 650ºC for 1s (a) and for 3 s (d); cold worked at 95% heat trated at 650ºC for 1s b) and for 3s (e); cold worked at 99% heat trated at 650ºC for 1s (c) and for 3s (f).

3.3 Rotary beam fatigue testing

Fig. 113 shows the results obtained for rotary beam fatigue testing. In air and at room temperature, the Ti25Nb21Hf alloy showed better fatigue response than NiTi and 316L.

In air and at room temperature, Ti25Nb21Hf alloy was capable to perform at higher strain values until failure than the other two materials under study. The performed assays in PBS at body temperature showed fatigue strain amplitudes in excess of 0.5% at a greater cycle life than 10^7 cycles.

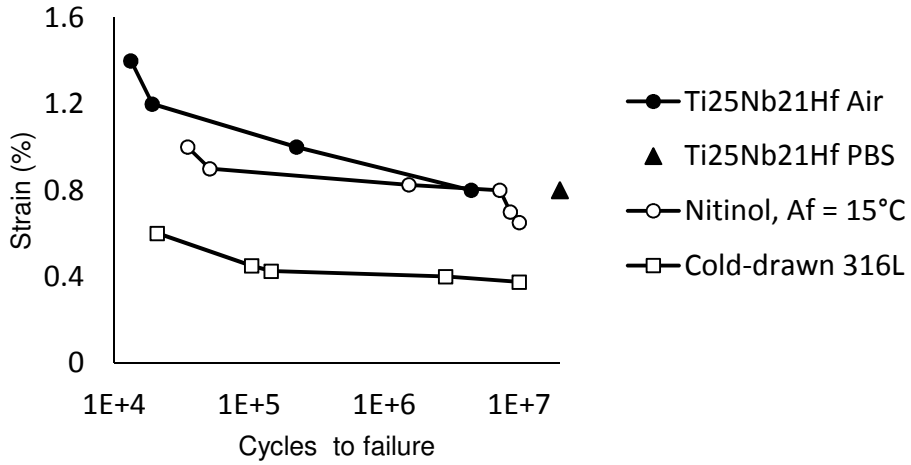

Fig.113 Results of the rotary beam fatigue testing at room temperature (25 ºC) in air for the Ti25Nb21Hf alloy, NiTi and 316L and in PBS and at body temperature (37 ºC) for the Ti25Nb21Hf alloy.

The cumulative distribution at 1% alternating strain for superelastic NiTi compared to Ti25Nb21Hf alloy is shown in Fig.114. According to the graphic, the Ti25Nb21Hf alloy would last more cycles than NiTi until failure.

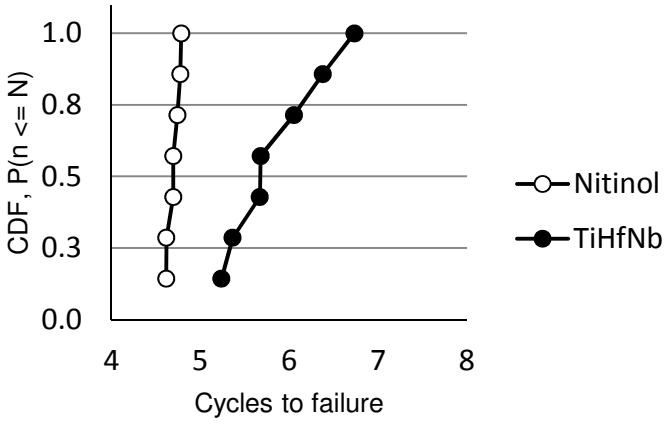

Fig.114 Cumulative distribution at 1% alternating strain for superelastic NiTi compared to Ti25Nb21Hf alloy.

4. DISCUSSION

During tensile testing was seen that higher percentages of cold work give raise to higher values of modulus as observed in other studies [10], but in all the cases the modulus obtained for the Ti25Nb21Hf alloy was between 50 GPa and 59 GPa. Since the modulus of elasticity obtained from the bar was close to 86GPa, then cold work induces an approximately 40% modulus reduction. In addition, the elastic modulus after cold work are close to the NiTi elastic modulus, although the elastic and plastic strain values are far from the ones seen in NiTi.

The thermal treatment had also had an effect on the elastic modulus values. An increase in the heat-treatment duration is translated in higher values of elastic modulus. This behaviour concurs with the results obtained by Wang et al. [11] on which a TiNbTaZr alloy rolled by 99% cold reduction ratios in thickness was treated at 873 K and 1223 K for 1.2 ks.

During cyclic tensile testing a modulus of elasticity lower than 60 GPa and axial recoverable strain greater than 3% were observed with stress hysteresis resembling a reversible stress-induced martensitic transformation at a test temperature of 150°C. Similar behaviour was observed in a Ti-35Nb-2Ta-3Zr alloy [11], but in this case the strain recovery did not fully returned to the initial level. A study by Miyazaki et al. [7] also reported shape memory effect and superelastic behavior in the Ti–22Nb–0.5O (at.%) alloy and Ti–22Nb–(1.0–2.0)O (at.%) alloys, respectively.

TEM studies revealed a microstructure composed of austenite β-phase (BCC), orthorhombic martensite α´´, ω-phase and amorphous phase. The bright field images were the typical ones of nano-grained microstructures. The strong crystalline reflections belong to the austenite phase whereas the weak martensite reflections indicate that only a small amount of martensite is retained. This results agree with the results reported by Xie et al. [4] except for the fact that they did not observed ω-phase. The presence of the ω-phase in our specimens might be explained owing to low β-phase stability that promoted ω-phase formation during cold working, as was reported by Tane et al. [10] when studying the Ti–Nb–Ta–Zr–O alloy. In this study was also found that 90% cold working induced an increase in the Young's modulus attributable to α″ martensite phase (0.09% O) and ω phase (0.09, 0.30, and 0.47% O) formation in the β phase matrix. This

could explain the fact that the modulus of the wires increased as the % of cold work increased too.

The fatigue testing revealed that the Ti25Nb21Hf alloy had better life expectancy than NiTi and 316L. Moreover, when the fatigue was tested in PBS at body temperature, negligible saline impact on fatigue results was observed.

5. CONCLUSION

The novel TiNbHf alloy presents superelasticity and phase transformation and there is no saline impact on fatigue results. These properties along with the fact that all components are biocompatible make TiNbHf alloy a potential product for nickel-free service as a superelastic material for medical device applications. TiNbHF alloy could be used in orthodontic wires for dental purposes, in intravascular stents, as bone fracture fixtures,staples for foot surgery etc.

A thorough study of the effect of the cold work on the microstructure should be done. It would be convenient to determine grain size triggered by the different grades of cold work done in the wires as well as have an indexation of the rings observed in the bright field images. A texture analysis would be also of interest.

Apart from the extensive microstructural characterization, further efforts should be directed to improve heat-treatment (variation of the temperature, combination of heat-treatments, etc.) and alloy composition improvement (addition of other elements) to achieve superelasticity at low temperatures and eliminate ω-phase. The addition of other alloying elements should be taken into account as well.

6. BIBLIOGRAPHY

1. Wang, G.-F., Feng, X.-Q., Yu, S.-W. & Nan, C.-W. Interface effects on effective elastic moduli of nanocrystalline materials. *Mater. Sci. Eng. A* **363,** 1–8 (2003).

2. Meyers, M. A., Mishra, A. & Benson, D. J. Mechanical properties of nanocrystalline materials. *Prog. Mater. Sci.* **51,** 427–556 (2006).

3. Raducanu, D. *et al.* Mechanical and corrosion resistance of a new nanostructured Ti-Zr-Ta-Nb alloy. *J. Mech. Behav. Biomed. Mater.* **4,** 1421–30 (2011).

4. Xie, K. Y. *et al.* Nanocrystalline β-Ti alloy with high hardness, low Young's modulus and excellent in vitro biocompatibility for biomedical applications. *Mater. Sci. Eng. C. Mater. Biol. Appl.* **33,** 3530–6 (2013).

5. Hou, F. Q., Li, S. J., Hao, Y. L. & Yang, R. Nonlinear elastic deformation behaviour of Ti–30Nb–12Zr alloys. *Scr. Mater.* **63,** 54–57 (2010).

6. Hao, Y. L., Li, S. J., Sun, S. Y., Zheng, C. Y. & Yang, R. Elastic deformation behaviour of Ti-24Nb-4Zr-7.9Sn for biomedical applications. *Acta Biomater.* **3,** 277–86 (2007).

7. Miyazaki, S., Kim, H. Y. & Hosoda, H. Development and characterization of Ni-free Ti-base shape memory and superelastic alloys. *Mater. Sci. Eng. A* **438-440,** 18–24 (2006).

8. Callister, W. D. & Rethwisch, D. G. *Materials science and engineering*. **8th,** (John Wiley & Sons, 2011).

9. Giannuzzi, L. A. & Stevie, F. A. A review of focused ion beam milling techniques for TEM specimen preparation. *Micron* **30,** 197–204 (1999).

10. Tane, M. *et al.* Low Young's modulus in Ti–Nb–Ta–Zr–O alloys: Cold working and oxygen effects. *Acta Mater.* **59,** 6975–6988 (2011).

11. Wang, L., Lu, W., Qin, J., Zhang, F. & Zhang, D. The characterization of shape memory effect for low elastic modulus biomedical β-type titanium alloy. *Mater. Charact.* **61,** 535–541 (2010).

Chapter 11

CASHB Fragment Fabrication

1. INTRODUCTION

One of the aims of this thesis was to synthesise fibronectin recombinant fragments to improve cell interaction and thus, biomaterial's integration. The recombinant protein technique [1,2] arises as a potential solution to the weak points of peptides. When dealing with recombinant proteins the signalling zone of the ECM protein of interest can be spanned and thus, their properties and functions [3]. Another strong point of recombinant proteins is that some characteristics as protein immobilization, orientation or activity may be modulated by modification of some amino acids without affecting their function. Moreover, there is the possibility to combine sequences, join different fragments, etc. As was seen in Chapter 7, the CAS and HBII fragments improved the activity of the linear and cyclic RGD peptides; as well as triggered a similar response to FN where they were combined. Previous works which worked with fibronectin fragments used fragments separatelly[4–9] or the sequence spanning from the FNIII8-14 [10]. In the present thesis two fragments of fibronectin were synthesized, the CAS and the HBII, and combined in an attempt to mimic fibronectin cell response. No evidence of research work regarding the union of both fragments was found. Thus, owing to the good results obtained with the fragments combination, and to go a step further, the fusion of both fragments was proposed.

2. MATERIALS AND METHODS

2.1 RNA extraction and reverse transcription

Since the fragments used were the CAS and the HBII, the RNA extraction and reverse transcription was done as explained in Chapter 2, section 4.1.

2.2 Primers design

The DNA sequences used to amplify the FNIII 8-10 and the FNIII 12-14 of Homo sapiens fibronectin were obtained from the nucleotide NCBI database (www.ncbi.nlm.nih.gov/). For each fragment, CAS or HB II, the primer, the reading

frame, the target, the added of the starting frame and the riding frame were the following:

A cleavage site was added to both fragments. The cleavage site was cut by the restriction enzyme forming the sticky ends, thus the DNA sequence was inserted in the plasmid. With the aim to allow the restriction enzyme to attach and cut the target, two nucleotides were added. It is important not to lose the reading frame of the protein of interest after any of the previous DNA sequence modifications. A restriction site for the same restriction enzyme (HindIII) was generated at the end of the CAS and at the beginning of the HBII, thus in the amino acid chain of the protein CAS will be placed before HBII as it is in FN. Primers were selected from the *Universal ProbeLibrary* by Roche (www.roche-applied-science.com) and ordered to *Invitrogen* .

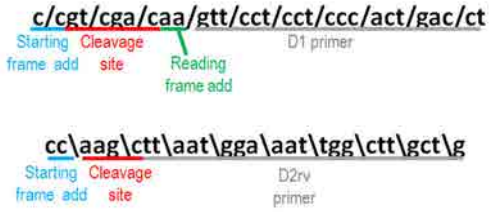

Fig.115 Primers D1 and D2rv corresponding to the CAS sequence with the starting frame add, the cleavage site and the reading frame add.

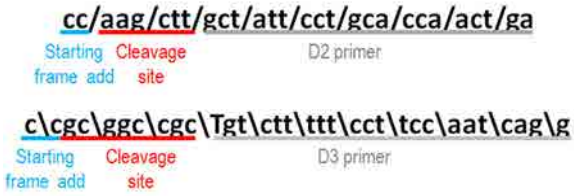

Fig.116 Primers D2 and D3 corresponding to the HBII sequence with the starting frame add and the cleavage site.

2.3 PCR amplification

The PCR cycle was conducted following the supplier's instructions as stated in Chapter 2, section 4.3. In Tab. 31 the cycles, times and temperatures of the process are shown. During the cycling phase, the first 5 cycles were done at 65ºC to amplify the DNA fragment without the restriction target, the following cycles were done at 70ºC and the target and the DNA were both amplified. Owing to the melting temperature of the D2rv primer, the annealing phase for CAS amplification was done at 67ºC instead of 70ºC.

State	Step	Temperature	Time
Holding	AmpliTaq Gold 360 Master Mix polymerase activation	95ªC	10 min
Cycling (40 cycles)	Denaturation	95ºC	30 s
	Annealing	65ºC	30 s
	Extend	72ºC	60s/kb
	Denaturation	95ºC	30 s
	Annealing	70ºC	30 s
	Extend	72ºC	60s/kb
Holding	Final extend	72ºC	7 min
Holding	Final hold	4ºC	∞

Table 31. Table with cycles, times and temperatures for each step of PCR reaction.

2.4 Fragments clonning procedure

The E.coli strains and the plasmid used were the same as stated in Chapter 2, section 5.1.

2.5 DNA fragments digestion

Prior to insert the CAS and HBII fragments into the plasmid, they were fused as one DNA sequence. The sticky ends in this case were at the end of the CAS DNA sequence and at the beginning of the HBII DNA sequence.

The CAS fragment was digested adding to the 30 µl purified PCR, 1 µl of HindIII, 7 µl of NE Buffer 3, 0.7 µl of BSA. The mixture was incubated at 37ºC for 2h.

The HBII fragment was digested adding to the 30 µl purified PCR, 1 µl of HindIII, 7 µl of NE Buffer 3, 0.7 µl of BSA. The mixture was incubated at 37ºC for 2h.

After digestion, DNA fragments were purified with the aim to eliminate the fragments cut during digestion. The purification process was the same described in Chapter 2, section 4.4.2. The aim of this purification was to eliminate the small target fragments which might be ligated again avoiding the fragment ligation; the restriction enzymes, the buffer, etc.

After purification, 3 µl of each fragment, 3 µl of ligase buffer, 1µl of ligase and 25 µl of RNAse free water were mixed and the reaction was incubated at 4ºC over night. The ligation product of both fragments was checked by electrophoresis following the procedure explained in Chapter 2, section 4.3.1.

In order to insert the fragment in the plasmid, the ends of the fragment and the plasmid have to be cut with the same restriction enzymes as stated in Chapter 2, section 5.1.

The plasmid was digested by mixing 1ug of plasmid with 1 µl of SalI, 1 µl of NotI, 7 µl of NE Buffer 3, 0.7 µl of BSA. The mixture was incubated at 37ºC for 2h.

The fused DNA was digested adding to the 30 µl resultant from the previous fusion, 1 µl of SalI, 1 µl of NotI, 7 µl of NE Buffer 3, 0.7 µl of BSA. The mixture was incubated at 37ºC for 2h.

After digestion, the DNA sequence and the plasmid were purified as described in Chapter 2, section 4.4.2.

2.6 Plasmid and fused DNA ligation

Once the DNA and the plasmid were purified, the ligation between them was carried out. In Tab. 32 the combinations of the different reaction mixture for ligation are shown.

COMBINATION 1	COMBINATION 2	COMBINATION 3
2 µl plasmid	3 µl plasmid	3 µl plasmid
2µl fused DNA	2µl fused DNA	3µl fused DNA
3 µl ligase buffer	3 µl ligase buffer	3 µl ligase buffer
1 µl ligase	1 µl ligase	1 µl ligase
22 µl H_2O RNAse free	21 µl H_2O RNAse free	20 µl H_2O RNAse free

Table 32. Quantities of each element that participate in the ligation for three different conditions.

When DNA and the plasmid get into contact they anneal through the sticky ends. After that, the DNA fragment and the plasmid are linked covalently by means of the T4 DNA Ligase (Roche, Manheim, Germany). The different combinations were left at 4ºC for 24h to allow the reaction to took place. After that, all of them were mixed resulting in one reaction.

Transformation of the E.coli DH5$_\alpha$ with the result of the fused DNA-Plasmid was conducted as explained in Chapter 2, section 5.1.5. The transformed E.coli BL21 culture was done as stated in Chapter 2, section 5.2. The verification of the transformations as well as the fragments sequencing was done following the procedure explained in Chapter 2, sections 5.3 and 5.4, respectively.

Protein expression and purification was done as stated in Chapter 2, section 6.

3. RESULTS

3.1 Amplification of the FN fragments

RNA was retrotranscribed to cDNA and specifically amplified using the primers for each fragment. After the amplification the molecular weight of each fragment was

checked by means of electrophoresis. The CAS d1-d2rv fragment consists of 832 pair of bases and the HBII d2-d3 fragment, of 831 pair of bases. As could be seen in Fig.117, the molecular weight is the correct one in both cases.

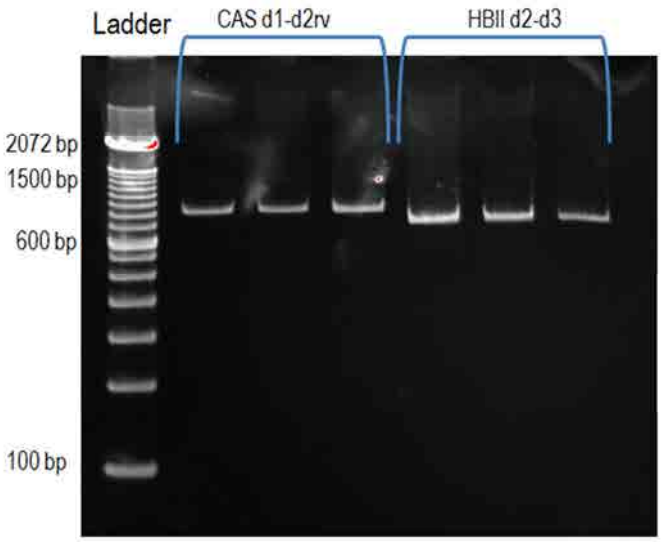

Fig.117 Electrophoresis of the amplified fragments CAS d1-d3 and HBII d1-d3 showing the pair of basis for each fragment.

3.2 Plasmid-fused DNA ligation

After fragments insertion in the pGEX plasmid, colonies of the DH5α E.coli strain were grown and it was checked which of them had inserted the correct fragment. To determine this, the molecular weight was determined by electrophoresis. A digestion of the plasmid ends (Chapter 2, section 5.3) was done to obtain the fused fragment.

Fig.118 shows the molecular weight of the fused DNA sequence inserted in each colony.

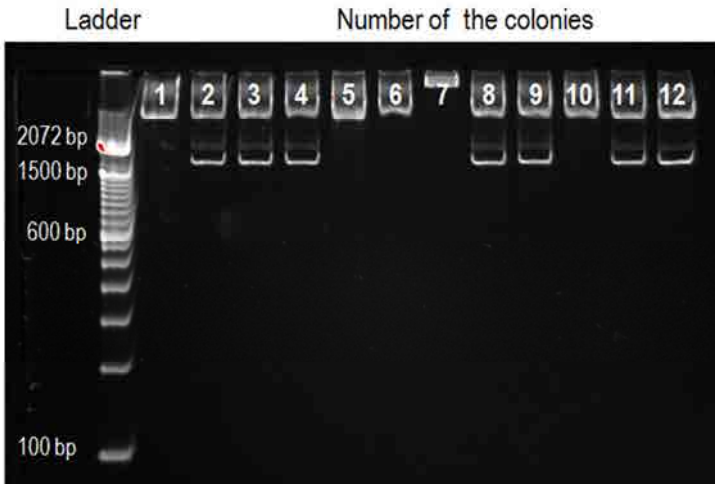

Fig.118 Electrophoresis gel showing the pair of basis of each picked colony with the inserted CASHBII sequence.

Only seven of the twelve colonies (2, 3, 4, 8, 9, 11 and 12) picked with the CASHBII fragment had inserted the fused DNA fragment in the plasmid. According to the ladder, all of the inserted fragments exhibited the theoretical molecular weight, approximately 1700 bp. All the inserted fragments gave the same intensity signal. The colony chosen to sequencing was number 2.

3.3 Fragment sequencing

Owing to the fact that a minimum amount of DNA is needed for the sequencing, the concentration of the inserted sequences was calculated. Table 33 show the results obtained for colony two of the DH5α cells transformed with the CAS_{d1-d3} fragment and for the colony two of the $HBII_{d1-d3.}$

FRAGMENT	CONCENTRATION (ng/µl)
CASHBII	81,75

Table 33. Concentration of the DNA fragment obtained after plasmid insertion and cell transformation.

As it was said in Chapter 2 section 5.4, the sequencing was done at the Genomic Services of the UB (http://www.ccit.ub.edu/CA/tb06.html). The sequence obtained was

in the 5' direction and in the 3' direction. To check the sequence in the 3' direction the DNA sequence obtained was transformed into the complementary form and was read in the reverse direction. First of all the primers were identified, then the targets and finally the DNA fragment sequence. Since the amplification process can introduce mutations, the nucleotides obtained were compared with the original ones. If there has been any change in the DNA sequence, this could lead to an amino acid substitution or to a truncated protein. Sometimes this mutation leads to no error in transcription because there is more than one amino acid that codifies the same protein as could be seen in Table 3 of Chapter 5.

The underlined zones correspond to the primers' sequence. The primer, the reading direction, the target, the added of the starting guideline and of the riding guideline are detailed in Fig.1. The d1 primer is marked in red; the d2rv primer is marked in green; the d2 primer is marked in orange; the d3 primer is marked in purple and the restriction enzyme targets in blue. The CASHBII sequence is underlined in grey and the mutations are in black.

The sequence for the pGEX 5' direction was:

AATCGGATCTGGAAGTTCTGTTCCAGGGGCCCCTGGGATCCCCGGAATTCCCGGGTCGACAAGTTCCTCC
TCCCACTGACCTGCGATTCACCAACATTGGTCCAGACACCATGCGTGTCACCTGGGCTCCACCCCCATCC
ATTGATTTAACCAACTTCCTGGTGCGTTACTCACCTGTGAAAAATGAGGAAGATGTTGCAGAGTTGTCAA
TTTCTCCTTCAGACAATGCAGTGGTCTTAACAAATCTCCTGCCTGGTACAGAATATGTAGTGAGTGTCTC
CAGTGTCTACGAACAACATGAGAGCACACCTCTTAGAGGAAGACAGAAAACAGGTCTTGATTCCCCAACT
GGCATTGACTTTTCTGATATTACTGCCAACTCTTTTACTGTGCACTGGATTGCTCCTCGAGCCACCATCA
CTGGCTACAGGATCCGCCATCATCCCGAGCACTTCAGTGGGAGACCTCGAGAAGATCGGGTGCCCCACTC
TCGGAATTCCATCACCCTCACCAACCTCACTCCAGGCACAGAGTATGTGGTCAGCATCGTTGCTCTTAAT
GGCAGAGAGGAAAGTCCCTTATTGATTGGCCAACAATCAACAGTTTCTGATGTTCCGAGTTGCTCTTAAT
GGCAGAGAGGAAAGTCCCTTATTGATTGGCCAACAATCAACAGTTTCTGATGTTCCGAGGGACCTGGAAG
TTGTTGCTGCGACCCCCACCAGCCTACTGATCAGCTGGGATGCTCCTGCTGTCACAGTGAGATATTACAG
GATCACTTACGGAGAAACAGGAGGAAATAGCCCTGTCCAGGAGTTCACTGTGCCTGGGAGCAAGTCTACA
GCTACCATCAGCGGCCTTAAACCTGGAGTTGATTATACCATCACTGTGTATGCTGTCACTGGCCGTGGAG
ACAGCCCCGCAAGCAGCAAGCCAATTTCCATTAAGCTTGCTATTCCTGCACCAACTGACCTGAAGTTCAC
TCAGGTCACACCCACAAGCCTGAGCGCCCAGTGGACACCACCCAATGTTCAGCTCACTGGATATCGAGTG
CGGGTGACCCCCANGGANAAAACGGGACCAATGAAAAAAATCAACCTTGCTCCTGANAGCTCATCCGGGG
NTGTNTCANGGACTTATGGGGGNCNNCNAAANNNGAANNNGAGNGTNTATNCTCTTAAGGAAACTTNGAA
AAGCAAAACANCTCAGGGGGTTGTCNCCNCTTTGNANAANGTCCCCCCCCAAAAAGGGNCNTGNNNANAA
ATNCTTTTGNAAACCCCCTCCCCTTTNNTGGGNAAACAAAAAGGAAAAAANCCNNGGNTTCCAAGTTGAG

GCCNTCCCCCCCAGGGGCAAACCCTTTCNAAAACCCTNNNCGANNTNAAANCNCCCCCCCNGGNTTAAAN
NGGNCGGNANAAAAAATCNNGNNCCTGGGAAAGGGG

The sequence for the pGEX 3' direction was:

CCTGNNNCGAAACGCGCGAGGCAGATCGTCAGTCAGTCACGATGGCGGCCGCTGTCTTTTTCCTTCCAAT
CAGGGGCTCGCTCTTCTGATTATTCTTCAGGGCAATGACATAAATTGTATATTCGGTTCCCGGTTCCAGG
CCAGTAATAGTAGCCTCTGTGACACCAGGGCGGGGCCGAGGGACCACTTCTCTGGGAGGAGACCCAGGCT
TCTCATACTTGATGATGTAGCCGGTAATCCTGGCACGTGGCGGCTGCCATGATACCAGCAAGGAATTGGG
TGTGGTGGCCAGGAAACGCAGGTTGGATGGTGCATCAATGGCAGTGGAGGCGTCGATGACCACAGGGGAG
CTCCGAGCATTGTCATTCAAGGTGTACAGGTAGATCTTGTAGTCAGTGCCTGGTTGTAAACCTGTGATGG
TGTAGCTTCTGACATCTGGCTTGATGGTTCTCTGGATTGGAGTCTGGCCATTGGCTGGAACGGCATCAAC
TTGGAAGCCAGTGATCGTCTCAGTCTTGGTTCTCCAGCTAATGGTGATGGTGGTCTCAGTAGCATCTGTC
ACACGAGCCCTTCTTGGTGGGCTGACATTCTCCAGAGTGGTGACAACACCCTGAGCTGGTCTGCTTGTCA
AAGTGTCCTTAAGAGCATAGACACTCACTTCATATTTGGTGGCCACCATAAGTCCTGATACAACCACGGA
TGAGCTGTCAGGAGCAAGGTTGATTTCTTATTGGTCCGTCTTCTCCTTGGGGGTCACCCGCACTCGATAT
CCAGTGAGCTGAACATTGGGTGGTGTCCACTGGGCGCTCAGGCTTGTGGGTGTGACCTGAGTGAACTTCA
GGTCAGTTGGTGCAGGAATAGCAAGCTTAATGGAAATTGGCTTGCTGCTTGCGGGGCTGTCTCCACGGCC
AGTGACAGCATACACAGTGATGGTATAATCAACTCCAGGTTTAAGGCCNCTGATGGTANCTGTAAACTTG
CTCCNAGGCACAGTGAACTCCTGGANAGGGCTATTTCCCCCTGTTTCCCCGNAANTGATCCTGNAAAATC
TCACTGGGAANANCAGGANCATCCCANCTGATCANNAGGCTGGNGGGGGTCCNAACAANANTTCCAGGTC
CCTCGGAAANATCAAAAACTGTTAATTGTNGGCCANCCAAAAGGNACTTNCCTCTTGCCATAAAAAAAAN
AAGCNAACCAAANCNTTTNCCNNGAANNAGTTTNNAANGGNAAAAANTCCAAAAGGGGGNNCCCATTTNT
CAAGNTNCCNNNAAAGNCCCGNAAAAAGGNAACCTNANCCNGNNGGGGCCNGAAAAACCCNGCNAAAAAA
AANTGGNAAAAAAAAAAANCCCNGGGAAAAAC

The results obtained showed one nucleotide change during the RT-PCR for the CASHBII in the pGEx 5' direction and another in the 3' direction. In the pGEX 5' direction, a G codon base was mutated into an A codon base, but this mutation did not affect the translation, because according to the codon chart both GAA and GAG translate the same amino acid: Glutamate. In the pGEX 3' direction, a T codon base was mutated into an A codon base, but as occurred in the pGEX 5' direction, the mutation did not affect the translation because both ACA and ACT translate the same amino acid: Tyrosine.

It is important to highlight the fact that the sequencing technique has a limitation in the number of bases read, so it was not possible to read the whole sequence CASHBII in only one direction. Despite this it is clear that in the pGEX5' direction the CAS

sequence was first, then the D2rv primer, the D2 primer (corresponding to the HBII sequence) and the first nucleotides of the HBII sequences. Taking a look to the pGEX3' direction, the D3 primer corresponding to the HBII fragment is present, then the HBII sequence joint with the D2 primer and the D2rv primer (corresponding to the CAS sequence) and finally the first nucleotides of the CAS fragment. This was an evidence of the fragments fusion.

3.4 CASHBII fragment expression and purification

The CASHBII sequence has a molecular weight of approximately 65kDa. After purification, the chromatograms showed no evidence of a peak related to protein elution. For this reason, a SDS-PAGE was done prior to purification.

After bacterial culture and protein induction, the culture was sonicated to extract the expressed proteins by E.coli. As one of the problems of the lack of CASHBII fragment expression might be insolubility, the pellet was also studied. Fig.119 shows the result of the SDS-PAGE done with the supernatant and the pellet. As can be seen, there is no evidence of a band at 65kDa, which is the molecular weight of the CASHBII fragment neither in the supernatant bands nor in the pellet bands.

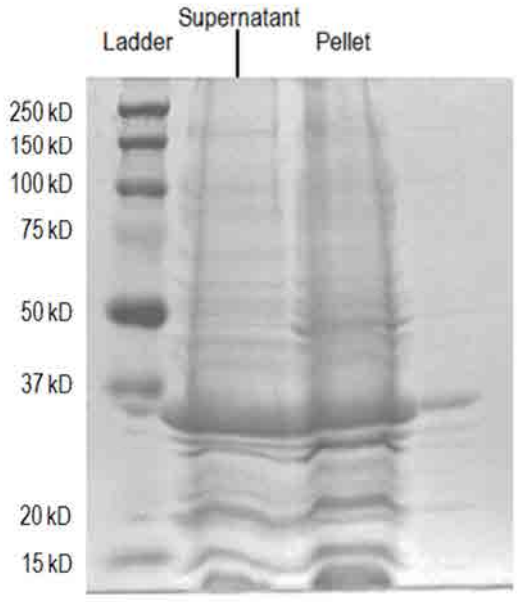

Fig.119 SDS-PAGE of the CASHBII fragment. Bans correspond to proteins obtained after sonication in the supernatant and in the pellet. The ladder used was *Precision Plus Protein™ Dual Color Standards* from BioRad.

According to *The Recombinant Protein Handbook from Amersham Pharmacia Biotech*, if no protein is detected in bacterial sonicate it might be needed an optimization of the culture conditions to improve yield. Then, the effect of cell strain, medium composition, incubation temperature and induction conditions should be studied. Exact conditions will vary for each fusion protein expressed.

This led us to study the expression of the fragment at different culture temperatures and with different concentrations of the promoter IPTG.

The culture was done at 25ºC and 30ºC. As can be seen in Fig.120, no bands corresponding to the CASHBII fragment were detected.

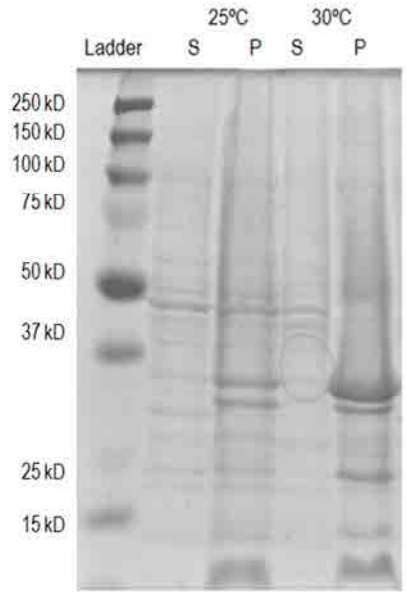

Fig.120 SDS-PAGE of the CASHBII fragment. Bans correspond to proteins obtained after sonication (S) in the supernatant and in the pellet (P) when cultured at 25ºC and 30ºC and at IPTG concentration of 1mM. The ladder used was Precision Plus Protein™ Dual Color Standards from BioRad.

Fig.121 shows the results obtained after induce the protein with IPTG at 1mM, 0,5mM, 0,2mM and 0,1mM. According to the bands obtained, these IPTG concentrations did not trigger the proper expression of the CASHBII fragment.

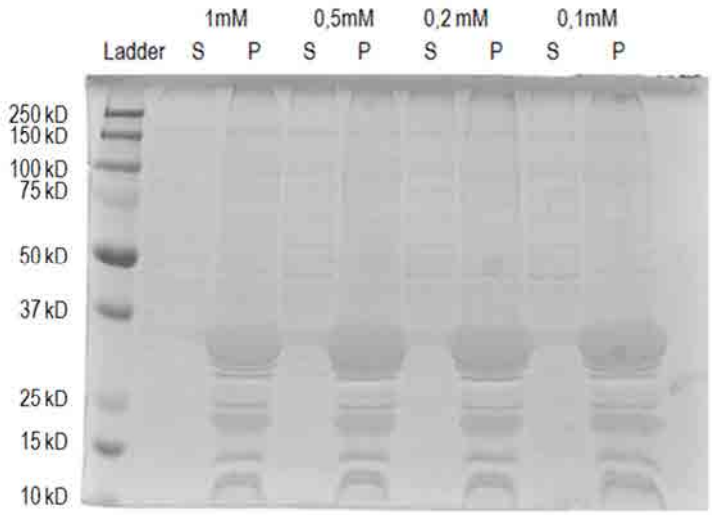

Fig.121 SDS-PAGE of the CASHBII fragment. Bans correspond to proteins obtained after sonication (S) in the supernatant and in the pellet (P) protein was induced at different IPTG concentrations and at 37ºC. The ladder used was *Precision Plus Protein™ Dual Color Standards* from BioRad.

5. CONCLUSION

Both the CAS and HBII fragments were fused successfully according to sequencing and the plasmids were able to insert the fused fragment. Despite this, the expression of the fragment was not successful. Different culture temperatures and inducer concentrations were studied without achieve protein expression.

Further studies should be done regarding alterations of the growth conditions to achieve protein expression such as try another growth temperatures within the range of +20° to +30°C to improve solubility, decrease IPTG concentration to <0.1 mM to alter induction level, alter time of induction, induce for a shorter period of time or induce at a higher cell density for a short period of time.

The disruption procedure (sonication) should be also checked. Cell disruption is seen by partial clearing of the suspension or by microscopic examination. Addition of lysozyme (0.1 volume of a 10 mg/ml lysozyme solution in 25 mM Tris™-HCl, pH 8.0) prior to sonication may improve results. Avoid frothing as this may denature the fusion protein.

Check for expression by immunoblotting would be another useful tool. Some fusion proteins may be masked on an SDS-polyacrylamide gel by a bacterial protein of

approximately the same molecular weight. Immunoblotting can be used to identify fusion proteins in these cases.

Ultimately, the E.coli strain and/or the plasmid could be changed.

6. BIBLIOGRAPHY

1. García, A. J., Schwarzbauer, J. E. & Boettiger, D. Distinct Activation States of α5β1 Integrin Show Differential Binding to RGD and Synergy Domains of Fibronectin†. *Biochemistry* **41,** 9063–9069 (2002).

2. García, A. J. & Reyes, C. D. Bio-adhesive Surfaces to Promote Osteoblast Differentiationand Bone Formation. *J. Dent. Res.* **84,** 407 (2005).

3. Sørensen, H. P. & Mortensen, K. K. Advanced genetic strategies for recombinant protein expression in Escherichia coli. *J. Biotechnol.* **115,** 113–128 (2005).

4. Petrie, T. A., Capadona, J. R., Reyes, C. D. & García, A. J. Integrin specificity and enhanced cellular activities associated with surfaces presenting a recombinant fibronectin fragment compared to RGD supports. *Biomaterials* **27,** 5459–5470 (2006).

5. Petrie, T. A. *et al.* The effect of integrin-specific bioactive coatings on tissue healing and implant osseointegration. *Biomaterials* **29,** 2849–57 (2008).

6. Petrie, T. A., Reyes, C. D., Burns, K. L. & García, A. J. Simple application of fibronectin-mimetic coating enhances osseointegration of titanium implants. *J. Cell. Mol. Med.* **13,** 2602–2612 (2009).

7. Rico, P., González-García, C., Petrie, T. A., García, A. J. & Salmerón-Sánchez, M. Molecular assembly and biological activity of a recombinant fragment of fibronectin (FNIII7–10) on poly(ethyl acrylate). *Colloids Surfaces B Biointerfaces* **78,** 310–316 (2010).

8. Woods, A., Couchman, J. R., Johansson, S. & Höök, M. Adhesion and cytoskeletal organisation of fibroblasts in response to fibronectin fragments. *EMBO J.* **5,** 665–70 (1986).

9. Dalton, B. A., McFarland, C. D., Underwood, P. A. & Steele, J. G. Role of the heparin binding domain of fibronectin in attachment and spreading of human bone-derived cells. *J. Cell Sci.* **108,** 2083–2092 (1995).

10. Kim, J.-H., Park, S.-O., Jang, H.-J. & Jang, J.-H. Importance of the heparin-binding domain of fibronectin for enhancing cell adhesion activity of the recombinant fibronectin. *Biotechnol. Lett.* **28,** 1409–13 (2006).